CHEMISTRY OF THE ADSORPTION OF CARBON DIOXIDE BY ARGONNE PREMIUM COALS AND A MODEL TO SIMULATE CO_2 SEQUESTRATION IN COAL SEAMS

by

Ekrem Ozdemir

BS, Chemical Engineering, Hacettepe University, 1990

MS, Biochemical Engineering, Drexel University, 1997

Submitted to the Graduate Faculty of

the School of Engineering in partial fulfillment

of the requirements for the degree of

Doctor of Philosophy

University of Pittsburgh

2004

UNIVERSITY OF PITTSBURGH

SCHOOL OF ENGINEERING

This dissertation was presented

by

Ekrem Ozdemir

It was defended on

September 21, 2004

and approved by

Götz Veser, Ph.D., Assistant Professor, Department of Chemical and Petroleum Engineering

Joseph J. McCarthy, Ph.D., Associate Professor and William Kepler Whiteford Faculty Fellow,
Department of Chemical and Petroleum Engineering

Turgay Ertekin, Ph.D., Professor and Program Chair in Petroleum and Natural Gas Engineering
and George E. Trimble Chair in Earth and Mineral Sciences, PennState University

Karl Schroeder, Ph.D., Research Chemist, U.S. Department of Energy (U.S. DOE), National
Energy Technology Laboratory (NETL)

Robert M. Enick, Ph.D., Professor and Macleod Faculty Fellow, Department of Chemical and
Petroleum Engineering
Dissertation Director

CHEMISTRY OF THE ADSORPTION OF CARBON DIOXIDE BY ARGONNE PREMIUM COALS AND A MODEL TO SIMULATE CO_2 SEQUESTRATION IN COAL SEAMS

Ekrem Ozdemir, PhD

University of Pittsburgh, 2004

The interactions of CO_2 with coal were investigated under a set of conditions to determine the effects of the nature of the coal and the sequestration environment including parameters such as rank and moisture content of the coal, the temperature, pressure, and pH. A mathematical model was also developed to simulate the coal bed methane production and the CO_2 sequestration processes.

The excess adsorption and desorption isotherms of CO_2 on eight Argonne Premium coal samples were measured using the volumetric method. The isotherms were found to be rectilinear and fit to the conventional adsorption model equations poorly due to the coal swelling. An adsorption isotherm equation was derived to account for the volumetric changes and significantly better fits were obtained. Upon drying, the volume of coals was determined to shrink, which was about 2% to 5% for medium and high rank coals, and up to 40% for the low rank coals. The swelling of coals during adsorption isotherm measurements in CO_2 was estimated to be about the same as the shrinkage that occurred during the moisture loss. If the swelling was not included in the adsorption isotherm equation, the reported adsorption capacities and surface areas of the coals were overestimated by about 15%. The adsorption capacities of moisture-free Argonne coals were found to be about 2.2 ± 0.8 mmole/g-coal, daf basis and to be lower in wet coals. The isosteric heat of adsorption for CO_2 on Argonne coals was estimated to be about 25±2 kJ/mole, regardless of the coal rank. The adsorption capacity of CO_2 on the weak solutions of acid leached coals was higher than both the base leached and untreated coals, possibly due to the removal of ash content of the coals.

The modeling results developed to simulate the CO_2 injection process suggest that the CO_2 can be injected at a rate of about $10*10^3$ standard m^3 per day. The injected CO_2 will reach the production well, which is separated from the injection well by 826 m, in about 30 years. During this period, about $160*10^6$ Sm^3 of CO_2 can be stored within a 2.14 $(km)^2$ coal seam.

DESCRIPTORS

Adsorption

Adsorption Isotherm Model

Argonne Premium Coal

Carbon Dioxide

CO_2

Helim Density of Coal

High-Pressure Adsorption Isotherms

Hysteresis

Leached Coals

Manometric Gas Adsorption Apparatus

Modeling

Moisture content

Rank

Rectilinear Adsorption Isotherm

Shrinkage

Swelling

Temperature Effect

Transport Phenomena

Volumetric change

Volumetric Method

TABLE OF CONTENTS

DESCRIPTORS v

TABLE OF CONTENTS vi

LIST OF TABLES xiii

LIST OF FIGURES xv

ACKNOWLEDGMENTS xxii

NOMENCLATURE xxiii

1.0 INTRODUCTION 1

1.1 ANTHROPOGENIC CO_2 AND COAL SEAM SEQUESTRATION 1

1.2 PROBLEM STATEMENT 6

1.3 OBJECTIVES 10

2.0 LITERATURE REVIEW 12

2.1 STRUCTURE OF COAL 12

2.1.1 Origin and Formation of Coal 12

2.1.2 Organic Structure of Coal Macerals 15

2.1.3 Physical Structure of the Coal Matrix 18

2.1.3.1 Layered Structure of the Coal Matrix 19

2.1.3.2 Pore Size in the Coal Matrix 20

2.1.3.3 Density and Porosity of the Coal Matrix 21

2.1.3.4 Open and Closed Porosity in Coals 23

2.1.3.5 Surface Area of the Coal Matrix 25

2.1.4 Coal Swelling 28

2.2 STORAGE OF CO_2 IN COAL 32

2.2.1 Gas Adsorption 33

2.2.1.1 Adsorption Isotherms 34

2.2.1.2 Mechanisms of Adsorption 36

2.2.2 Construction of an Adsorption Isotherm 38

2.2.2.1 Modeling the Adsorption Isotherms 38

2.2.2.2 Density of the Adsorbed Phase (ρ^a) 41

2.2.2.3 Model Equations for the Absolute Adsorption (n^{abs}) 44

2.2.2.4 Saturation Pressure for CO_2 (P_s) 45

2.2.3 Adsorption of Gases on Coals 47

2.2.4 Adsorption Capacity and Stability of CO_2 on Coal 49

2.2.4.1 Low-temperature, low-pressure adsorption of CO_2 49

2.2.4.2 Adsorption of CO_2 under Geological Conditions 50

2.2.5 Factors affecting the coal adsorption capacity and CO_2 stability 51

2.2.6 Coal Structural Changes upon CO_2 Adsorption 59

2.3 TRANSPORT PHENOMENA IN COAL SEAMS 60

2.3.1 Reservoir Characteristics of Coal Seams 62

2.3.2 Gas Storage in Coal Seams 65

2.3.3 Mass Transport in Coal Seams 66

2.3.4 Enhanced Coalbed Methane Production 69

3.0 EXPERIMENTAL 72

3.1 COAL SAMPLES USED 72

3.2 SAMPLE PREPARATION AND HANDLING 73

3.3 EXPERIMENTAL SETUP 74

3.4 EXPERIMENTAL METHODS 77

3.4.1 Drying of Coal Samples 77

3.4.2 Estimation of the Void Volume in the Sample Cell 77

3.4.3 Measurement of CO_2 Adsorption Isotherms 78

3.4.4 Measurement of Densities of the As-Received and Dried Argonne Premium Coals 79

3.4.5 Determination of the Moisture Content of the Coals 79

3.4.6 pH Treatment of Coals 80

3.4.6.1 Initial Acid Treatment 81

3.4.6.2 Base Treatment 82

3.4.6.3 Neutralization 82

3.4.6.4 Acid Treatment 82

4.0 RESULTS AND DISCUSSION 84

4.1 EXCESS ADSORPTION ISOTHERMS OF CO_2 ON COALS (n^{ex}) 84

4.1.1 Interpretation of Excess Adsorption Isotherms (n^{ex}) 85

4.2 VOLUMETRIC CHANGES DUE TO DRYING OF COALS 91

4.2.1 Densities of the As-Received and Dried Argonne Premium Coals 91

4.2.2 Shrinkage of Coals upon Moisture Loss 93

4.3 DEVELOPMENT OF AN ADSORPTION ISOTHERM MODEL ACCOUNTING FOR VOLUME CHANGES 97

4.3.1 Volumetric Changes in Coal Samples Associated with Adsorption Isotherms 97

4.3.2 Model Development ... 99

4.3.3 Interpretation of the Excess Adsorption Isotherms of CO_2 on Coals Accounting for Volume Changes ... 101

4.3.4 Modified Dubinin-Astakhov Equation for the Interpretation of the Excess Adsorption Isotherms of CO_2 on Coals Accounting for Volume Changes ... 107

4.3.5 Excess (n^{ex}) and Absolute (n^{abs}) Adsorption Isotherms of CO_2 on Coals ... 109

4.3.6 Comparison of the Modeling of the Excess Adsorption Isotherms with and without Including the Volume Effects ... 112

4.3.7 Expansion Coefficient, γ, of Powdered Coals under CO_2 Atmosphere ... 113

4.3.8 Storage Capacity of CO_2 on Dried Coals: Effect of Rank ... 115

4.4 EFFECT OF MOISTURE ON CO_2 ADSORPTION CAPACITY OF COALS ... 117

4.4.1 Adsorption and Desorption Isotherms of CO_2 on As-Received and Dried Argonne Coals ... 117

4.4.2 Variation of Physical Constants with Coal Rank and Moisture Content ... 119

4.4.2.1 Adsorption Capacity of CO_2 on As-Received and Dried Argonne Coals ... 119

4.4.2.2 Surface Areas of As-Received and Dried Argonne Coals ... 120

4.4.2.3 Isosteric heat of Adsorption ... 122

4.4.2.4 Average Pore Sizes of As-Received and Dried Argonne Coals Obtained with CO_2. ... 124

4.4.2.5 Volumetric Effects ... 125

4.4.3 Absolute Adsorption Isotherms of CO_2 on Coals (n^{abs}) ... 128

4.4.4 Quantifying the Effect of Moisture on the Adsorption Capacity of Coals ... 129

4.4.5 Implication to the Mechanism of CO_2 Adsorption on Moist Coals ... 136

4.4.6 Significance to the CO_2 Sequestration Modeling ... 138

4.5. EFFECT OF TEMPERATURE ON ADSORPTION ISOTHERMS AND ADSORPTION CAPACITY OF CO_2 ON COALS ... 140

4.6. EFFECT OF pH ON ADSORPTION ISOTHERMS AND ADSORPTION CAPACITY OF CO_2 ON COALS 146

4.6.1 pH Treatment/Leaching of Coals 146

4.6.2 Adsorption Isotherms of CO_2 on Leached Coals 151

4.6.3 Effect of pH on the Physical Parameters 153

4.6.3.1 CO_2 Adsorption Capacity of the Leached Argonne Coals 153

4.6.3.2 Isosteric Heat of Adsorption 155

4.6.3.3 Average Pore Sizes of the Leached Argonne Coals Reported by CO_2 156

4.6.3.4 Volumetric Effects 157

4.6.3.5 Importance of pH to the CO_2 Sequestration 158

4.7. SUPERCRITICAL CO_2 ADSORPTION ON COALS 159

4.7.1 Physical Constants Obtained from Supercritical CO_2 Adsorption on Argonne Coals 165

4.7.1.1 Adsorption Capacity of Supercritical CO_2 on Dried Argonne Coals 165

4.7.1.2 Isosteric Heat of Adsorption 167

4.7.1.3 Average Pore Sizes of Dried Argonne Coals Obtained from Supercritical CO_2 Adsorption Isotherms 168

4.7.1.4 Expansion Coefficient and the Volume Change for the Dried Argonne Coals 169

4.8 MODELING OF CO_2 SEQUESTRATION IN COAL SEAMS 173

4.8.1 Modeling of Fluid Flow in Coal Seams 173

4.8.1.1 Flow Geometry 173

4.8.1.2 Assumptions 175

4.8.1.3 Derivation of the Continuity Equation 175

4.8.1.4 Flow in Cleats 177

4.8.1.5 Flow in Coal Matrix 184

4.8.1.6 Dependence of Coefficients in the Governing Equations on Pressure and Solubility 189

4.8.2 Solution of the Governing Equations 190

4.8.3 Calculation of the Flow Rates at the Wells 191

4.8.4 Modeling of Dewatering and Degasification of a Coal Seam 193

4.8.5 Validation of the Two-Phase Fluid Flow Model 196

4.8.6 Dewatering and Degasification of a Coal Seam 206

4.8.7 Modeling of CO_2 Sequestration in the Previously Dewatered and Degasified Coal Seam 215

4.8.8 Effect of Coal Seam Properties on CO_2 Sequestration: Parametric Studies 222

4.8.8.1 Effect of Coal Thickness on CO_2 Sequestration 223

4.8.8.2 Effect of Permeability on CO_2 Sequestration 224

4.8.8.3 Effect of Compressibility of Coal on CO_2 Sequestration 225

4.8.8.4 Effect of Cleat Porosity on CO_2 Sequestration 226

4.8.8.5 Effect of Cleat Spacing or Sorption Time Constant on CO_2 Sequestration 228

4.8.8.6 Effect of Adsorption Capacity on CO_2 Sequestration 229

5.0 CONCLUDING REMARKS 231

6.0 FUTURE WORK 234

APPENDIX A. COMPRESSIBILITY FACTORS FOR HELIUM (He) AND CARBON DIOXIDE (CO_2) 236

APPENDIX B. MEASUREMENTS OF THE CO_2 ADSORPTION ISOTHERMS ON COALS USING THE EXPERIMENTAL APPARATUS 256

APPENDIX C. ERROR ANALYSIS OF THE ADSORPTION ISOTHERMS AS DETERMINED BY THE VOLUMETRIC METHOD 273

APPENDIX D. DEPENDENCE OF COEFFICIENTS IN THE GOVERNING EQUATIONS ON PRESSURE AND SATURATION 281

APPENDIX E. SORCE CODE IN FORTRAN 77 FOR THE MODELING OF FLUID FLOW IN COAL SEAMS 288

REFERENCES 321

LIST OF TABLES

Table 1. ASTM classification of coal rank (65) 14

Table 2. Wide angle X-ray scattering measurement of the layered structure of Argonne Premium coals(86) 20

Table 3. The pore size of selected Argonne Premium Coals 21

Table 4. Constant density approximation for the adsorbed phase 42

Table 5. Model equations(135) used to represent the absolute adsorbed amount, n^{abs} where n_o is the adsorption/monolayer/micropore capacity, K_i is a constant related to the heat of adsorption differently in each adsorption model, and j_i is an exponent related to the heterogeneity of the solid adsorbent 45

Table 6. Relationships for saturation pressure of CO_2 46

Table 7. Proximate and Ultimate Analyses of the Argonne Premium Coal Samples(207) 73

Table 8. The components and description of the high-pressure manometric gas adsorption apparatus 76

Table 9. The adsorbed phase density (ρ^a) and saturation pressure (P_s) for CO_2 used in the interpretation of its excess adsorption isotherms on coals 87

Table 10. Best-fit parameters at 22 °C obtained from Eq.(10) 90

Table 11. Best-fit parameters at 4 MPa and 22 °C obtained from Eq.(45) 106

Table 12. Effect of temperature on the adsorption capacity (n_o) of CO_2 on Argonne Premium coals, (mmole/g-coal, daf) 143

Table 13. Effect of temperature on the characteristic heat of adsorption (E_o) for CO_2 adsorption on Argonne Premium coals, (kJ/mole) 143

Table 14. Effect of temperature on the Dubinin exponent (*j*) ... 144

Table 15. Effect of temperature on the average pore sizes of coals estimated from the CO_2 adsorption isotherms, (Å) ... 144

Table 16. Effect of temperature on the percent volume change ($\Delta V_{coal}\%$) for CO_2 adsorption on Argonne Premium coals ... 145

Table 17. Ash Content of Leached Coals ... 148

Table 18. Metals removed from coals (mg/g-coal) ... 150

Table 19. Physical parameters used in the model ... 197

Table 20. Default (base case) parameters for CO_2 injection in a coal seam ... 218

Table 21. Coefficients n_{ji} and γ of the Angus-EOS for helium ... 237

Table 22. Compressibility factor for helium at various temperatures and pressures ... 238

Table 23. Compressibility Factors for CO_2 calculated from the PR-EOS ... 243

Table 24. Coefficients n_{ji} of the Angus-EOS for CO_2 ... 245

Table 25. Compressibility Factors for CO_2 calculated from the Angus-EOS ... 246

Table 26. Compressibility Factors for CO_2 calculated from the Span and Wagner-EOS ... 253

Table 27. The parameters for experimental apparatus and the limits of error, Δx_n, for each experimental variable ... 276

Table 28. Experimental pressure values obtained for the adsorption isotherm of CO_2 at 55 ^oC and the compressibility factor along with the derivatives of the compressibility factor with respect to pressure and temperature ... 278

Table 29. Limit of error for each variable, Δx_n, and the contribution of each variables to the total expected error ... 279

Table 30. Adsorption isotherm data for CO_2 on the Pocahontas No.3 coal with the total calculated error on an absolute and percentage basis ... 280

LIST OF FIGURES

Figure 1. A schematic representation of the coal seam sequestration of CO_2 4

Figure 2. Areas of study of CO_2 sequestration in coal seams 5

Figure 3. Parameters that affect the adsorption isotherm, adsorption capacity, and stability of CO_2 adsorbed on coal.. 7

Figure 4. Conceptual representations of the average molecular structure of the vitrinite maceral: (a) Shinn (1984)(74) model, (b) Marzec (1986)(75) model, and (c) Jones et al. (1999)(68) model 17

Figure 5. The percent difference in coal volume estimated by helium and methanol (calculated from Ref. (16)) 24

Figure 6. Surface areas of Kentucky No.12 coal obtained at 298 ^oK from various sorbate vapors with different swelling parameters(35) 27

Figure 7. Equilibrium expansion and contraction response of a Kentucky coal specimen (~1 cm long and 0.4 cm in diameter) under vacuum and exposed to He, N_2, CO_2, and Xe, at 20 psig and 298 K(113) 29

Figure 8. Expansion of selected coals in elevated pressures of CO_2 as measured by dilatometry in a packed bed(101) 30

Figure 9. The types of adsorption isotherms(103) 35

Figure 10. A schematic representation of adsorption mechanisms (a) Langmuir's monolayer adsorption model (b) BET's multilayer adsorption model (c) Dubinin's pore filling model38

Figure 11. Construction of an adsorption isotherm: (a) estimation of the empty volume of the sample cell (V_S), (b) estimation of the volume of the adsorbent, from the change in the volume of the sample cell (V_o), and (c) measurement of the adsorption isotherm during which the void volume (V_o) in the sample cell decreases (to V_i) due to the volume occupied by the adsorbed phase (V^a)... 39

Figure 12. Proposed adsorbed phase densities of CO_2 at various temperatures 43

Figure 13. Suggested saturation pressure for CO_2 at below and above its critical temperature ... 47

Figure 14. Cleat spacing and aperture data from Northeast Blanco Unit No. 403, San Juan Basin.(190) ... 65

Figure 15. Coal bed methane production by pressure depletion method(200) ... 67

Figure 16. A schematic of the manometric gas adsorption apparatus: G: Gas Cylinder, I: ISCO Syringe Pump, D: Data Aqcuision, R: Reference Cell, S: Sample Cell, P: Pressure Transducer, V: Vacuum Pump T: Thermocouples B: Constant Temperature Water Bath .. 75

Figure 17. Schematic showing the preparation of the leached coal samples ... 81

Figure 18. Excess adsorption (○) and desorption (●) isotherms of CO_2 on dried Argonne Premium coals ... 86

Figure 19. Best-fit curves obtained from Eq.(10) using the model equations in Table 5 for the absolute adsorption term, n^{abs} ... 88

Figure 20. Densities of as-received and dried Argonne Premium coal samples ... 92

Figure 21. Specific volumes of as-received and dried Argonne Premium coals ... 93

Figure 22. Comparison of the volume change and percent shrinkage of the Argonne Premium coals upon drying with the volume of the removed water ... 94

Figure 23. Comparison between the percent volume change (this work) and percent shrinkage (Suuberg et al.(218)) of the Argonne Premium coals upon drying ... 95

Figure 24. Best-fit curves obtained from Eq.(45) using the model equations in Table 5 for the absolute adsorption term, n^{abs} ... 103

Figure 25. Deviation plots comparing (a) the conventional Dubinin-Astakhov and (b) modified Dubinin-Astakhov equations for each of the Argonne Premium coals ... 104

Figure 26. Fit of the adsorption isotherm data of CO_2 on Argonne Premium coals using the modified Dubinin-Astakhov equation (Eq.46) to account for volume effects ... 111

Figure 27. Comparison of the conventional and modified Dubinin-Astakhov equation for the estimation of (a) the adsorption capacity (n_o), (b) characteristic heat of adsorption (E_o), (c) average pore size, and (d) volume changes ... 113

Figure 28. Comparison of the expansion coefficient or pore compressibility, γ, for coals under a CO_2 atmosphere as obtained from the adsorption isotherms (this study) and the bulk compressibility obtained from the dimensional changes reported by Walker et al.(101) 115

Figure 29. The absolute adsorbed CO_2 on Argonne coals and the expected volume change with pressure 116

Figure 30. Excess adsorption (open symbols) and desorption (closed symbols) isotherms of CO_2 on as-received and dried Argonne Premium coals (numbers in parenthesis show the percent moisture content in coals) 118

Figure 31. Adsorption capacities of as-received and dried Argonne Premium coals 120

Figure 32. Surface areas of Argonne Premium coals as a function of carbon content 122

Figure 33. Isosteric heat of CO_2 adsorption on as-received and dried Argonne Premium coals 123

Figure 34. Average Pore sizes of Argonne Premium coals estimated from CO_2 adsorption isotherms at 22 °C 125

Figure 35. Estimated volume change during the adsorption measurements at 3.8 MPa 126

Figure 36. Comparison of the percent volume change estimated from the adsorption isotherms of CO_2 on Argonne coals to the shrinkage of these coals as a result of the moisture loss estimated from the helium expansion method (Volume change for the Illinois No.6 was not included in the regression analysis) 127

Figure 37. Calculated absolute adsorption (n^{abs}) and volumetric changes for CO_2 adsorption onto (a) as-received and (b) dried Argonne Premium coals 129

Figure 38. Effect of moisture content on the adsorption capacity of CO_2 on coals 130

Figure 39. The linear relationship between the inverse of the adsorption capacity of partially dried coals, $1/(n_o)_w$, *vs.* moisture content of coals, m 132

Figure 40. Effect of moisture content on the adsorption capacity of CO_2 on coals 133

Figure 41. Comparison of the coefficient, A, and slope, α, and the adsorption capacities of dry coals, $(n_o)_d$, obtained from Figure 39 employing Eq.(54), suggested by Ettinger et al.$^{(41)}$, and Figure 40 employing Eq.(55) 134

Figure 42. Moles of water lost per mole of CO_2 adsorbed with coal rank 136

Figure 43. Proposed mechanism of gas adsorption onto a moist coal 138

Figure 44. Adsorption isotherms of CO_2 on Argonne Premium coals at 22, 30, 40, and 55 °C and pressures upto 4 MPa 141

Figure 45. Adsorption isotherms of leached and non-leached Argonne Premium coals 152

Figure 46. Adsorption capacity of CO_2 on leached Argonne Coals 154

Figure 47. Isosteric heat of CO_2 adsorption on leached Argonne Premium coals..................... 156

Figure 48. Average Pore sizes of leached coals estimated from CO_2 adsorption isotherms 157

Figure 49. Estimated volume change during the adsorption measurements at 4 MPa 158

Figure 50. High-pressure adsorption (○) and desorption (●) isotherms of CO_2 on Argonne Premium coals at 55 ^{o}C.. 161

Figure 51. Comparison of the adsorption isotherm of CO_2 on coals at high pressures 163

Figure 52. Expected error in the estimation of the adsorption isotherms of CO_2 on Argonne Premium Pocahontas No.3 coal 164

Figure 53. Adsorption capacities of dried Argonne Premium coals at 55 ^{o}C and over increasing pressure ranges.. 166

Figure 54. Isosteric heat of CO_2 adsorption on dried Argonne Premium coals with increasing pressure 167

Figure 55. Average Pore sizes of Argonne Premium coals with increasing pressure estimated from supercritical CO_2 adsorption isotherms... 169

Figure 56. Expansion coefficient for coals with increasing pressures estimated from supercritical CO_2 adsorption isotherms 170

Figure 57. Volume change with increasing pressure calculated from expansion coefficient..... 171

Figure 58. The layout for a coal seam... 174

Figure 59. Representation of material balance for a fluid on a differential volume element in cylindrical coordinates 176

Figure 60. Cross section of a coal seam for fluid flow. Left corner: the image for cleats and the coal matrix. Right corner: representation of fluid flow within the cleats, instant equilibrium at the surface of the coal matrix and diffusion through the coal matrix 178

Figure 61. Cross-section of the coal matrix: Flow occurs by convection in cleats and by diffusion in coal matrix. Instantaneous equilibrium establishes at the surface of the coal matrix..... 186

Figure 62. Model coal seam dewatering/degasification set-up.. 194

Figure 63. Adsorption Capacity of Coal used in the present model 198

Figure 64. The Parameters for gas and water phases used in the models (a) relative permeability (b) Viscosity (c) Capillary pressure, and (d) Formation volume factor............................. 198

Figure 65. Comparison of results produced from the present model and the model developed by Sung(251) for the case of constant pressure constraint at the well. (a) Gas production rate (b) Water production rate (c) Cumulative production rate for gas (d) Cumulative production rate for water 200

Figure 66. Validation runs for the case of constant total flow rate at the well. (a) Gas production rate (b) Water production rate (c) Cumulative production rate for gas (d) Cumulative production rate for water... 202

Figure 67. Bottomhole pressure for the case of constant total flow rate at the well.................. 202

Figure 68. Validation of the present model with the model developed by Sung(251) for the case of constant pressure at the well while the source term was excluded. (a) Gas production rate (b) Water production rate (c) Cumulative production rate for gas (d) Cumulative production rate for water 204

Figure 69. Validation of the present model with the model developed by Sung(251) for the case of constant pressure at the well while the source term was included. (a) Gas production rate (b) Water production rate (c) Cumulative production rate for gas (d) Cumulative production rate for water 205

Figure 70. Bottomhole pressure for the case of constant total flow rate including the source term 206

Figure 71. Effect of bottomhole pressure specification at the internal boundary on the gas and water production rates and the cumulative productions (a) Gas production rate (b) Water production rate (c) Cumulative production rate for gas (d) Cumulative production rate for water.. 208

Figure 72. Effect of constant total flow rate specification at the internal boundary on the production rate and the cumulative production for the gas and water phases (a) Gas production rate (b) Water production rate (c) Cumulative production rate for gas (d) Cumulative production rate for water 210

Figure 73. Bottomhole pressure for the case of constant total flow rate (the source term was included) 211

Figure 74. Pressure distribution during the dewatering and degasification of a coal seam........ 213

Figure 75. Gas saturation within the coal seam during the degasification process 213

Figure 76. Effect of well spacing on the duration of the degasification and dewatering of a coal seam (a) Gas production rate (b) Water production rate (c) Cumulative production rate for gas (d) Cumulative production rate for water 215

Figure 77. Layout for the CO_2 injection in a coal seam 217

Figure 78. CO_2 injection in a coal seam without the source term (a) CO_2 injection rate and the cumulative injected CO_2, (b) mole fraction of CO_2 in the gas phase (c) pressure (d) gas saturation 220

Figure 79. CO_2 injection in coal seam including the source term (a) CO_2 injection rate and the cumulative injected CO_2, (b) mole fraction of CO_2 in the gas phase (c) pressure (d) gas saturation 222

Figure 80. Effect of coal seam thickness on the CO_2 sequestration 224

Figure 81. Effect of permeability on the CO_2 sequestration 225

Figure 82. Effect of coal compressibility on the CO_2 sequestration 226

Figure 83. Effect of cleat porosity on the CO_2 sequestration 227

Figure 84. Effect of cleat spacing or sorption time constant on CO_2 sequestration 229

Figure 85. Effect of adsorption capacity of coal on the CO_2 sequestration 230

Figure 86. Compressibility factor for helium calculated from the Angus-EOS at various temperature and pressures 239

Figure 87. Comparison of the compressibility factor of CO_2 obtained from the PR-EOS, the Angus-EOS, and the Span and Wagner-EOS 255

Figure 88. Typical gas expansion procedure 265

Figure 89. Thermal and pressure equilibrium during the gas expansion process 267

Figure 90. Estimation of the empty volumes of the reference and sample cells 269

Figure 91. Estimation of the void volume of the sample cell, from which the volume of the sample is calculated 270

Figure 92. Construction of the adsorption and desorption isotherms of CO_2 on Argonne Premium Pittsburgh No.8 Coal 271

Figure 93. Repeatability of the adsorption measurement using the manometric adsorption apparatus shown in Figure 16 272

Figure 94. The derivatives of the compressibility factor for CO_2 with respect to pressure and temperature at 55 °C.. 277

ACKNOWLEDGMENTS

I would like to express my sincere gratitude to Dr. Karl Schroeder at the U.S. Department of Energy (U.S. DOE) – National Energy Technology Laboratory (NETL) for his guidance and constant support throughout this research. Without him, this work could not be achieved. Yes Karl, you are a good man and I thank you for everything! I would also like to extend my appreciation to my adviser Dr. Robert M. Enick for his guidance and help in accomplishing this dissertation. I would like to thank Dr. Curt White at NETL for his continuous encouragements to achieve more: “Keep up the good work!” Not finished! I would like to thank Dr. Alan J. Russell for his guidance, support, and the discipline in the research. I would also like to thank the committee members, friends, and colleagues at the University of Pittsburgh and at the NETL, especially, my group mates, Romaine, Arsam, Yannick, Jean-Philipe, Laurent, and Dr. Badie I. Morsi, and Dr. Yee Soong, Dr. Angela Goodman, Dr. Robert Warzinski, Dr. Kenneth Jones, Dr. Terry Ackman, and others such as those with whom we have enjoyed playing soccer. I would also like to thank Dr. Turgay Ertekin and Dr. Ozgen Karacan at the PennState University for their valuable discussions. Furthermore, my thanks go to those I met during the conferences and meetings for their valuable discussion and encouragements. In separate, my dedication goes to my parents for their constant support and encouragements throughout all my school years. I send you all my love and warm hugs from the distance. The last but not the least, my sincere appreciation goes to my wife, Sevgi. I could not survive without your constant guidance, support, and love.

NOMENCLATURE

a	ash content in coal	wt%
A	area perpendicular to the flow	m^2
A	a coefficient in Eq.(28)	moisture wt%
b	Langmuir constant	MPa^{-1}
B_g	formation volume factor for the gas phase	m^3/Sm^3
B_w	formation volume factor for the water phase	m^3/Sm^3
C	BET constant	-
C	concentration	mole/ m^3
C_a	concentration of gas in the cleat	mole/m^3
C_i	concentration within the coal matrix	mole/ m^3
C_{ie}	equilibrium gas concentration	mole/m^3
C_m	matrix compressibility	MPa^{-1}
C_o	concentration in the coal matrix initially	mole/ m^3
C_p	pore compressibility	MPa^{-1}
D	Dubinin coefficient	-
D_a	macropore diffusion coefficient	m^2/day
D_i	micropore diffusion coefficient	m^2/day
d_p	diameter of pores	Å
E	characteristic adsorption energy	kj/mole
E_o	characteristic heat of adsorption	kj/mole
g	gravitational force	m/s^2
h	thickness of the formation	m
H_V	molar enthalpy of vaporization	J/mole
j	Dubinin's structural heterogeneity parameter	-
k	a constant in Eq.(51) (= 3.145 for CO_2)	$kJnm^3mol^{-1}$

k	absolute permeability	md
k_D	dissolution coefficient	mmole/g
k_g	permeability to gas phase	md
K_i	affinity coefficient between the adsorbent and adsorbate	-
k_{rg}	relative permeability for gas phase	fraction
k_{rgc}	relative permeability for gas phase at critical water content	md
k_{rw}	relative permeability for water phase	fraction
k_{rwc}	relative permeability for water phase at critical gas content	md
k_o	absolute permeability initially	md
k_T	thermal expansion coefficient	$^oK^{-1}$
m	moisture content of coal	wt%
M	molecular weight	g/mole
m_c	critical moisture content	wt%
m_g	flow rate for the gas phase	m^3/day
n	degree of surface coverage or micropore filling	mmole/g-coal
N	Avogadro's number	molecules/mole
N_c	exponent for permeability-cleat porosity relationship	-
n_d	amount of adsorbed gas on fully dried coal	mmole/g-coal
n_o	the adsorption/micropore capacity	mmole/g-coal
n^{abs}	absolute adsorbed amount	mmole/g-coal
n^{ex}	Gibbs (experimentally measured) excess adsorption	mmole/g-coal
$(n_o)_d$	adsorption capacity of moisture-free coals	mmole/g-coal
n^t	total moles of gas transferred into the sample cell	mmole
$(n_o)_w$	adsorption capacity of moist coal	mmole/g-coal
n_w	amount of adsorbed gas on wet coal	mmole/g-coal
P	pressure	MPa
P_{atm}	pressure at the ground surface	MPa
P_{cgw}	capillary pressure between gas and water phases	MPa
P_e	pressure at the equivalent well block radius, r_e	m
P_{ob}	overburden pressure	MPa
P_r	reduced pressure	fraction

P_s	saturation pressure	MPa
P_{sc}	pressure at standard condition	MPa
P_{well}	pressure at the well-bore	MPa
q_f	adsorption/desorption (source) term	kg/day
q_{gi}	adsorption/desorption (source) term for gas	$Sm^3/day/m^3$
q_{go}	adsorbed gas at the initial in-seam pressure, P_{go}	Sm^3/m^3-coal
q_g	adsorption/desorption (source) term for gas	kg / day/m^3
q_w	adsorption/desorption (source) term for water	kg / day/m^3
q_{wi}	adsorption/desorption (source) term for water	$Sm^3/day/m^3$
Q_g	gas production/injection rate	Sm^3/day
Q_{st},	isosteric heat of adsorption	kJ/mole
Q_T	total of gas and water production/injection rate	Sm^3/day
Q_w	water production/injection rate	Sm^3/day
r_e	average pore size	nm
r_e	equivalent well block radius	m
r_{sw}	dissolved gas in water	kg/ kg-water
r_w	radius of the well bore	m
R	the universal gas constant (=0.082)	Latm/mole/K
R_{sw}	dissolved gas in water	Sm^3/Sm^3
S	specific surface area of coal	m^2/g
S_f	saturation of the fluid in the cleat porosity	fraction
S_g	gas saturation	fraction
S_{girr}	critical gas content	fraction
S_w	water saturation	fraction
S_{wirr}	critical water content	fraction
T	temperature	^oK
T_b	boiling temperature	^oK
T_c	critical temperature	^oK
T_g	glass transition temperature	^oK
T_r	reduced temperature	fraction
T_{sc}	temperature at standard condition	^oK

V^a	volume of the adsorbed phase	cm^3
V_s	empty volume of the sample cell	cm^3
V_{coal}	volume of the coal	cm^3
V_i	free volume (void volume) in the sample cell	cm^3
V_{icoal}	volume of the coal initially	cm^3
V_o	void volume in the sample cell	cm^3
y_i	mole fraction for i^{th} component	fraction
z	compressibility factor for gas	-
Z_c	the half of the cleat spacing	m

Greek Letters

α	slope in Eq.(55).	mmole/g/moisture%
α	unit conversion factor for permeability	$(m^3/day)cP/m^2/(MPa/m)/md$
α_1	unit conversion factor	m^3/Sm^3
β	affinity coefficient between adsorbate and the adsorbent ($\beta = 0.35$ for CO_2)	
γ	volumetric expansion coefficient	MPa^{-1}
σ	cross-sectional area of the adsorbate (0.253 nm^2 for CO_2)	nm^2/molecule
σ_e	effective stress	MPa
σ_{OB}	overburden pressure	MPa
ε	adsorption potential	kj/mole
λ	experimental uncertainty	-
μ_g	viscosity of the gas phase	cP
μ_w	viscosity of the water phase	cP
Γ	the gamma function	-
ϕ	cleat porosity	fraction
ϕ_o	cleat porosity initially	fraction
ρ^a	density of the adsorbed phase	g/cm^3
ρ_b	density at its boiling temperature	g/cm^3
ρ_c	density at critical point	g/cm^3

ρ_{coal}	density of the coal	g/cm^3
ρ_{f}	density of the fluid	g/cm^3
ρ_{liq}	density at its liquid phase	g/cm^3
ρ_{MeOH}	density measured using methanol	g/cm^3
ρ_{wsc}	density of water at standard conditions	g/cm^3
ρ_{solid}	density at its solid phase	g/cm^3
ρ_{vdw}	density w.r.t. van der Waals volume ($1/b$)	g/cm^3
ρ_{w}	density for water	g/cm^3
δ	solubility parameter	$MPa^{1/2}$
υ	molar volume	$cm^3/mole$
ν_{f}	superficial velocity of the fluid	m/day
ν_{g}	superficial velocity of the gas phase	m/day
ν_{w}	superficial velocity of the water phase	m/day
ΔC_o	concentration difference	Sm^3/ m^3
ΔP_o	pressure difference	MPa
$\Delta V/V$	volumetric strain	Fraction
ΔV_c	volumetric changes due to the compression or shrinkage	cm^3
ΔV_d	volumetric changes due to dissolution of the adsorbing gas	cm^3
ΔV_o	volumetric changes due to the sieving effect	cm^3
ΔH_v	enthalpy of vaporization	kJ/mole
ΔV_x	overall volumetric changes	cm^3

Subscripts

1	initial
2	final
b	boiling point
c	critical condition
d	dissolved
d	dry

f	fluid
gb	glass beads
Hg	mercury
i	void volume in the sample cell representing the actual void volume
liq	liquid phase,
o	void volume in the sample cell containing the solid adsorbent as reported by helium
R	reference cell
s	saturation condition
S	sample cell
vdw	van der Waals
x	sum of all volume effects
w	moist

Superscripts

a	adsorbed phase
abs	absolute or real adsorbed gas
ex	excess or experimentally estimated gas
T	total
t	exponent

Acronyms

ARI	Advanced Research Institute
ASTM	American Standard Testing Method
BET	Brunauer, Emmett, and Teller equation
BETn	Modified BET Equation
CBM	Coalbed Methane
CFCs	Chlorofluorocarbons
CT	Computerized Tomography
D-A	Dubinin-Astakov Equation
daf	Dry, Ash Free Basis
DOE	Department of Energy
ECBM	Enhanced Coalbed Methane
EOS	Equation of State
FTIR	Fourier Transform Infrared Spectroscopy
GHGs	Green House Gas
HRTEM	High-Resolution Transmission Electron Microscopy
IAS	Ideal Adsorbed Solution Theory
IR	Infrared Spectroscopy
IUPAC	International Union of Pure and Applied Chemistry
maf	Moisture, Ash Free Basis
mmmf	Moisture and Mineral Matter Free Basis
NETL	National Energy Technology Laboratory
NMR	Nuclear Magnetic resonance Spectroscopy
ppm	Parts per Million
ppmv	Parts per Million by Volume
SEM	Scanning Electron Microscopy
TEM	Transmission Electron Microscopy
WAXRS	Wide-Angle X-Ray Scattering

1.0 INTRODUCTION

1.1 ANTHROPOGENIC CO_2 AND COAL SEAM SEQUESTRATION

Atmospheric concentrations of carbon dioxide (CO_2) along with other greenhouse gases (GHGs) such as methane (CH_4), chlorofluorocarbons (CFCs), and nitrous oxide (N_2O) are increasing due to human (anthropogenic) activities.(1) Among these, CO_2 is the most abundant greenhouse gas. It is produced mainly by the burning of fossil fuels including coal, oil, and natural gas. The atmospheric concentration of CO_2 increased from 280 ppm during the preindustrial era to 365 ppm in 1998 with an accumulation rate of about 1.5 ppmv per year.(2) Model predictions show that the emissions of CO_2 will continue to increase over the coming decades as fossil fuels continue to be the major source of energy.(3) Currently, CO_2 accounts for about 64% of the anthropogenic greenhouse effect and is the most important GHG contributor.(4) Because of the large contribution of CO_2 to climate change, large reductions in CO_2 emissions will be necessary to stabilize the atmospheric CO_2 concentration.

The 1997 Kyoto Protocol calls for industrialized nations to reduce their CO_2 emissions to 95% of 1990 levels by 2012.(5) In this regard, many national and international programs have been initiated towards understanding the magnitude and mitigation options of the greenhouse gases. U.S. Department of Energy (U.S. DOE) – National Energy Technology Laboratory (NETL) has established energy research and development programs in carbon sequestration science in order to address the potential impact of increasing GHGs in the atmosphere during the 21st century. The potential methods and options as routes to carbon sequestration were summarized in the DOE – Office of Fossil Energy Report and in many other international references.(6)

The CO_2 concentration in the atmosphere can be controlled either by reducing its production and release into the atmosphere, or by capturing and disposing of the produced CO_2 in a safe manner (sequestration).(6,7) Various CO_2 sequestration options have been proposed, including placement in the deep oceans; placement in geologic formations (deep saline aquifers, abandoned oil or gas reservoirs, and unmineable coal seams) and consumption via advanced chemical and biological processes.(6,7,8,9) Presently, these options are still under investigation to determine their feasibility in terms of their storage capacity, safety, and costs.

CO_2 sequestration in deep unmineable coal seams is one of the geologic strategies. Coal seam sequestration of CO_2 is particularly attractive in those cases where the CO_2 can be stored in the coal seam in an adsorbed state that is expected to be stable for geologically significant periods.(10) Injection of CO_2 may also enhance the production of the coalbed methane (CBM) to generate a profit to help offset the expense of the sequestration. If so, long-term sequestration of CO_2 in coal seams might be more cost-effective. Additionally, many power plants are located near coal seams, which would reduce the transportation costs. However, a better understanding of the chemistry of the coal-CO_2 interaction is needed in order to determine which, if any, of the coal seams might be good disposal sites and under what environmental conditions the adsorbed CO_2 would remain stable.

Figure 1 shows a schematic representation of the coal seam sequestration of CO_2. Coal is a naturally fractured porous solid, which is characterized by a dual porosity consisting of both micropores and macropores.(11) The microporosity of coal is contained within the macromolecular network of the coal matrix. The macroporosity of a coal seam consists of the naturally occurring fractures called cleats.(12) Coals also contain a range of microstructures of various shapes and sizes between the micropores and the cleats.(13) While the storage of gas is dominated by adsorption within micropores, the cleat system provides the conduit for mass transfer through the formation.(14)

The flue gas itself or a captured stream of concentrated CO_2 can be injected into a coal seam. The flue gas product of the coal combustion usually contains CO_2, water vapor, nitrogen (N_2), excess oxygen (O_2), SO_x and NO_x. Because the oxidant commonly used in coal-fired power plants is air, only about 10% to 14% of the flue gas is CO_2; the majority of the remaining flue gas is N_2. There are disadvantages injecting the flu gas into the coal seam. For example, the compression of the flue gas to injection pressures is costly due to the large quantity of N_2; the storage of the flue gas within the coal seam reduces the amount of CO_2 actually stored within the coal seam, and information about the flue gas-coal interaction is limited. Thus, in most scenarios, CO_2 is captured from the CO_2-lean flue gas and injected directly into the coal seams as concentrated CO_2. When CO_2 is injected into a coal seam, several phenomena are expected to occur.(15) These include (1) the transport of gasses through the cleat system, (2) diffusion into the coal matrix, (3) storage within the micropores, (4) coal swelling, (5) extraction of small molecules and water trapped within the coal, (6) softening the coal matrix in the presence of CO_2, (7) closing the cleat apertures as a result of coal swelling, (8) opening the microporosity in the coal matrix that will lead to increases in the diffusion coefficients, and (9) a decrease in pH as the CO_2 dissolves in the cleat water. All of these may influence the adsorption capacity and transport phenomena in the coal seam.

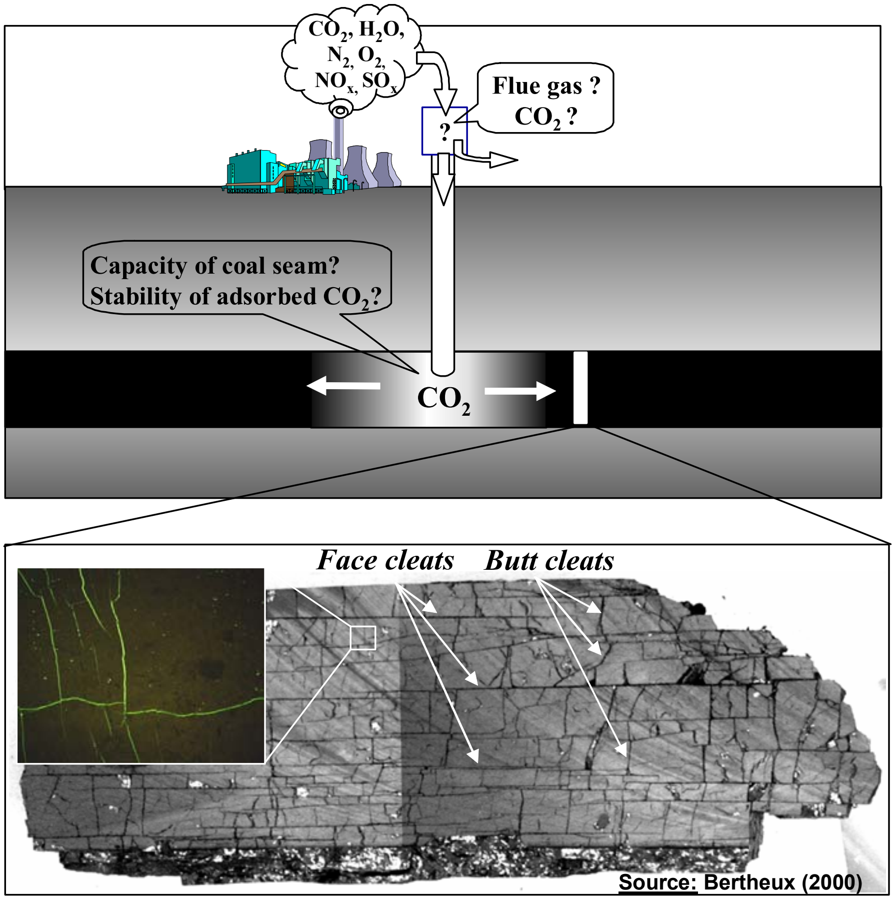

Source: Bertheux (2000)

Figure 1. A schematic representation of the coal seam sequestration of CO_2

The studies in coal seam sequestration of CO_2 have focused mainly on two areas: the transport in the coal seam and the storage within the coal matrix as shown schematically in Figure 2. The transport in the coal seam usually includes the flow of CO_2 through the naturally fractured porous network (cleats), diffusion into the organic coal matrix, and storage within the micropores in an adsorbed state. Nevertheless, there is a lack of understanding of what happens when the CO_2 is injected into a coal seam because the transport properties of the coal are highly related to the chemical and physical changes that occur during the adsorption and desorption processes.

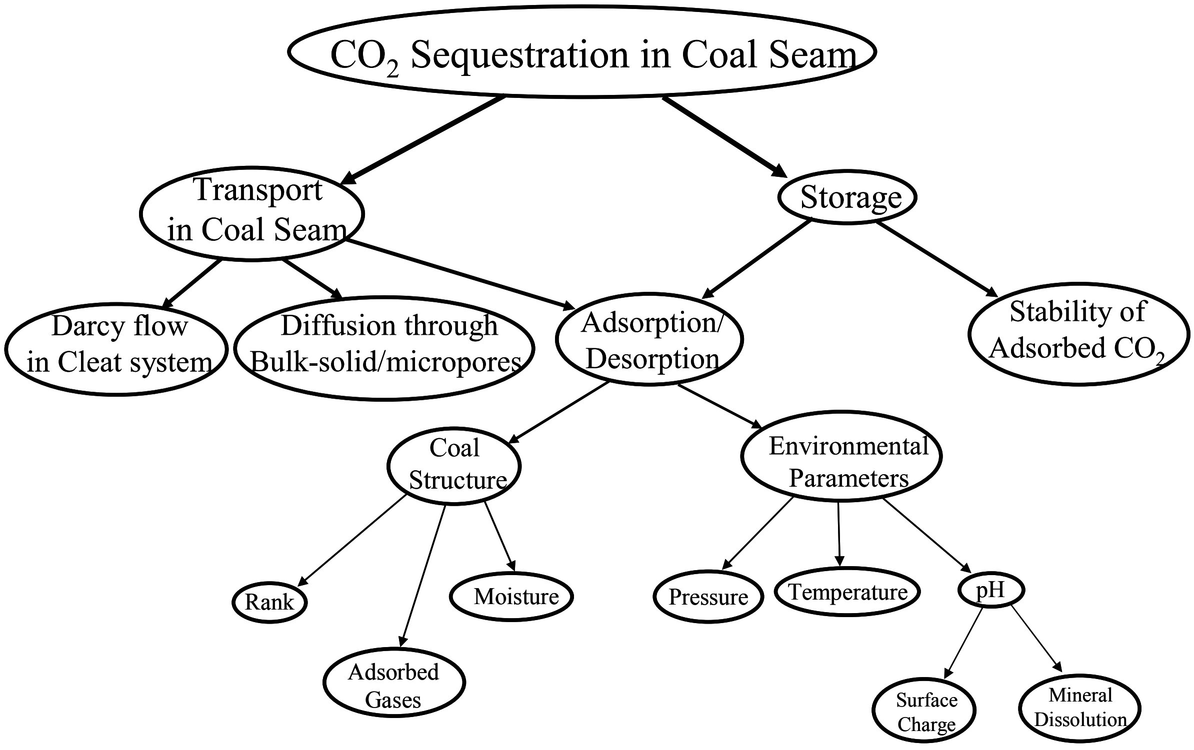

Figure 2. Areas of study of CO_2 sequestration in coal seams

The storage of CO_2 in the coal includes the adsorption and desorption of gases on and from the coal matrix, as well as the stability of the adsorbed CO_2 on the coal. Both adsorption capacity and stability of adsorbed CO_2 can be affected by the nature of the coal and the environmental parameters, such as rank and moisture content of the coal, temperature, pressure, and pH. The prediction of the adsorption capacity and the long-term stability of the sequestered gas require knowledge of how the gas is held in place and what factors might induce its release. In order to evaluate the long-term storage capacity of a coal seam, possible changes in the sequestration environment should be anticipated and understood. The nature of the coal will determine its maximum adsorption capacity, but the dynamic nature of the sequestration environment will determine the extent to which that capacity can be realized.

1.2 PROBLEM STATEMENT

Adsorption isotherms are one of the most important tools for the characterization of solid adsorbent materials. As shown in Figure 3, the adsorption capacity, heat of adsorption, surface area, volumetric changes, and average pore size can all be estimated from adsorption isotherms. Adsorption isotherms are affected by the nature of the coal itself and environmental parameters as depicted in Figure 3. In order to develop an efficient strategy for coal seam sequestration, variables that affect the CO_2-coal interactions need to be investigated.

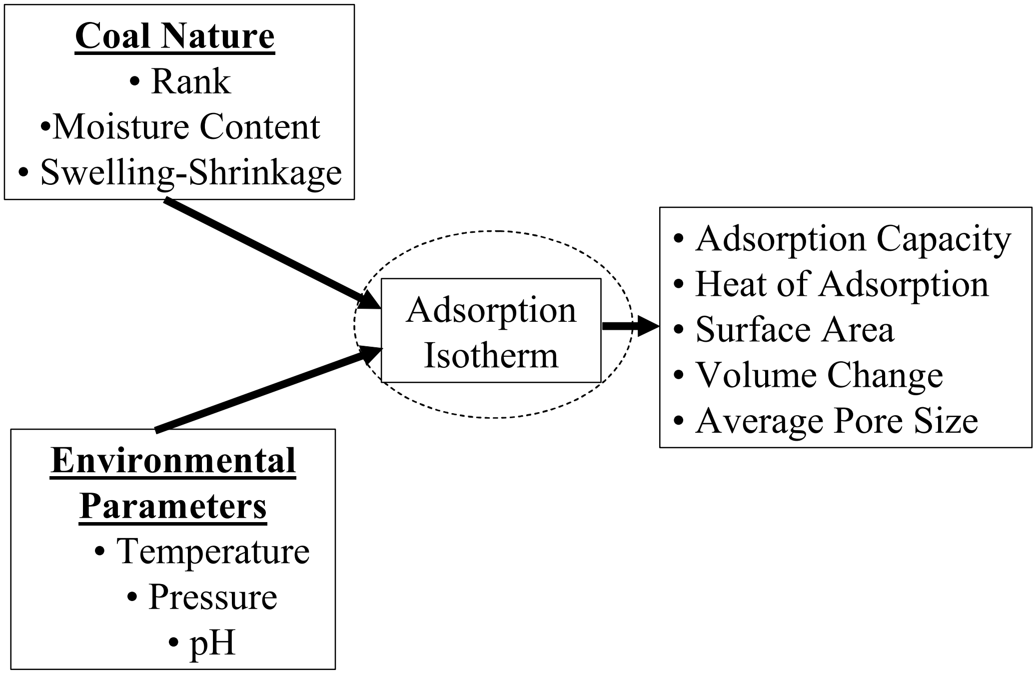

Figure 3. Parameters that affect the adsorption isotherm, adsorption capacity, and stability of CO_2 adsorbed on coal

Coal is an extremely complex material in terms of its pore structure and surface area. It has been recognized that the densities of coals measured by helium displacement are significantly higher than those measured by mercury displacement.(16) Coal has been described as a 'highly porous, glassy solid rock' below its glass transition temperature ($T_g \sim 600\ ^{o}K$).(17) However, the glassy macromolecular network is transformed into a rubbery material at temperatures above its glass transition temperature. A similar effect has also been observed when organic solvents(18) and adsorbate gases(19,20) and vapors(21,22) were brought into contact with coal. The nature of the microporosity of coal, particularly whether it is closed or part of an open pore network, has been the subject of discussion in the literature.(23,24,25,26,27,28) Some report that coal contains an interconnected pore network of high surface area with slit-shaped pores having constricted openings of molecular dimensions.(26,27) Others report that coal does not contain an interconnected pore network as generally accepted; on the contrary, pores in the coal are isolated from each other and they can only be reached by diffusion through the solid coal matrix.(28,24) These contradictory views of the porous structure of coal lead to several consequences for the interpretation of coal adsorption isotherms.

The adsorption of CO_2 on coals has been used to estimate surface areas,(29,30) and micropore structures of coals,(31) but, these measurements have been conducted at low pressures (usually below atmospheric) and low temperatures (-78 ^{o}C).(30) Although information obtained from measurements such as these is important to current sequestration efforts, low-pressure, low-temperature adsorption isotherm data do not represent geologic, in-seam conditions. In addition, traditional interpretation of coal adsorption isotherm data does not consider the noticeable volumetric changes due to coal swelling,(32,33,34,20,35) which range from 0.36% to 4.18%(36,37) at high pressure. The information obtained by fitting the empirical high-pressure isotherm data to one of the typical model equations may be misleading because these models are based on a rigid adsorbent structure.(38) Therefore, there is a need for a more rigorous mathematical model based on an analysis of the physical phenomena occurring in the coal-sorbate systems.

Moisture plays an important role in the adsorption of gases on coal. It has been shown that the presence of moisture reduces the CH_4 adsorption capacity of coals.(39,40,41) Yet, there have been few studies on the CO_2 adsorption on moist coals. In order to predict the CO_2 storage capacity of a candidate coal seam and to model its long-term stability, the intrinsic adsorption capacity of the organic matrix of the coal and how this capacity may change with a changing sequestration environment must be known accurately. There are a number of properties, such as shrinkage due to moisture loss, sorption induced swelling, and dissolution in the coal, which clearly shows that coal is an elastic material. Thus, the adsorption isotherms of CO_2 on coal need to be treated carefully in order to obtain the desired information.

When CO_2 is injected into a coal seam, it is expected that it will flow through the natural fractures within the seam and will diffuse into and be adsorbed by the organic matrix of the coal.(15) It is also expected that the injected CO_2 will lower the pH of any water entrained in, or wetting the surface of the coal due to the high-pressure dissolution of CO_2. In addition, some sequestration scenarios, such as co-sequestration of the acidic gases, including SO_X and NO_X, would depress the pH further.(42) Post-sequestration scenarios may also include the influx of fresh water or brines long after the sequestration field has been abandoned, which could lead to alterations of the pH.(43) It is recognized that the adsorption capacities of coals are dependent on a number of factors, including temperature, pressure, rank and moisture content.(44,41) Yet, the effect of the pH of the surrounding media on the adsorption capacity of the coal matrix and the stability of the adsorbed CO_2 has not been extensively studied.

Because CH_4 is the dominant gas in coal seams, the CBM reservoir capacity and the parameters that affect the adsorption capacity of CH_4 at high-pressures have been investigated in order to accurately determine the gas-in-place and to enhance the safety of coal mining.(44,41,45) The adsorption of other gases, such as ethane,(46) hydrogen,(47,48) and their mixtures on coals have also been investigated at elevated temperatures and pressures. However, data relating the CO_2

capacity of coals under in-seam conditions are limited.(49) The recent proposal of CO_2 injection into coal seams as a viable option to mitigate the increasing worldwide CO_2 emissions has stimulated interest in developing a better understanding of the CO_2-coal interactions at high pressures.(50,51,52,53) However, the adsorption isotherms of CO_2 on coals at high pressures have been reported to display unusual behavior that has not yet been explained adequately(54,55,56)

CO_2 sequestration in coal seams with concomitant recovery of CH_4 is a new technology that has been practiced in a few places but it is not well developed. Off-the-shelf technology is available to perform CO_2 sequestration - enhanced coalbed methane (ECBM) recovery. For instance, Burlington Resources has performed CO_2-ECBM production in deep unmineable coal seams in the San Juan Basin in New Mexico since 1996.(57) However, very little information has entered the public domain from this or similar projects. Therefore, there is a very incomplete understanding of what happens when CO_2 is injected into a coal seam.

1.3 OBJECTIVES

CO_2 sequestration in deep coal seams can be strongly affected by the coal rank and other environmental parameters, including moisture content, swelling/shrinkage properties of coal, pressure, temperature, and pH. In order to understand the effects of these parameters on the CO_2 adsorption capacity and CO_2 storage stability, the main objectives of this research are:

1. to measure the adsorption isotherms and sorption capacities of CO_2 on various ranks of coals under in-seam conditions including pressures up to 15 MPa and temperatures up to 55 ^{o}C for gaseous and supercritical CO_2;

2. to estimate the effect of the coal moisture content on the adsorption isotherms and sorption capacities of CO_2 on coal;

3. to estimate the role of pH on the CO_2 adsorption;

4. to assess the effect of coal swelling on the adsorption isotherms of CO_2 on coals; and

5. to develop a mathematical model for the CO_2 sequestration process in a coal seam.

2.0 LITERATURE REVIEW

2.1 STRUCTURE OF COAL

2.1.1 Origin and Formation of Coal

The origin, formation, and structure of coal have been studied and an enormous amount of literature is available.(58,59) Coal is an extremely heterogeneous material consisting of organic matter, mineral matter, moisture, and a complex pore network. It is generally accepted that the organic portion of coal was formed from concentrated deposits of swampy organic matter originally derived from terrestrial plants.(60) Plant structures (leaf, stem) were converted into coal through complex biological, chemical, and geochemical processes driven initially by selective microbial action and later by the temperature and pressure generated by overlaying sediments over several hundred millions of years. The organic sedimentary rock is composed of these fossilized plant remains called macerals and mineral inclusions. The macerals are the microscopically distinct areas in coal and are mainly classified as vitrinite, liptinite, and inertinite.(61) Vitrinite is derived from woody plant material and is the most common maceral. Liptinite is formed from lipids and waxy plant substances whereas the inertinite probably originates from char formed by prehistoric pyrolysis processes, such as forest fires. The process of conversion of the plant matter into lignite, bituminous coal, and anthracite is called "coalification". During the coalification process, large volumes of volatiles principally CH_4, CO_2, and water were liberated.(62) Although CO_2 is more strongly adsorbed to the coal matrix than the other volatiles, it is more easily dissipated because of its solubility in the water present throughout the coalification.(63) Therefore, CH_4 is the dominant gas in coal beds (about 95%).(64)

Coals are classified into ranks, which are used to define discrete points in the maturation process. Vitrinite reflectance (R%), fixed carbon content (C%), and percentage volatile matter (VM%) are used to distinguish higher-rank coals, while calorific heating value and moisture content may be used to distinguish lower-rank coals.(65) The rank system used in the United States is the American Standard Testing Method (ASTM) rank classification as shown in Table **1**.(65) The ASTM classification of coal is based on the behavior of coal as a fuel rather than the carbon content of coal. The ASTM analysis is based on the volatile matter content, fixed carbon content, and the calorific value reported on a moisture- and mineral matter- free basis (mmmf). As coal progresses through the maturation process, its physical and chemical properties change. As the rank increases from lignite to anthracite, the carbon content increases; the oxygen content decreases; the hydrogen content decreases, slowly at first, then rapidly during the late stages of coalification; the volatile matter decreases; and the calorific value generally increases (maf basis).(66,59) In addition, as rank increases, aromaticity and molecular cluster size increase; vitrinite reflectance increases; moisture content decreases, rapidly in the early stages, but slowly in the later stages of coal formation.(59)

Table 1. ASTM classification of coal rank (65)

Rank	Group	Fixed Carbon % (mmmf)	Volatile Matter % (mmmf)	Calorific Value (mmmf) (Btu/lb)
Anthracitic	Metanthracite	>98	<2	>14,000
	Anthracite	92-98	2-8	“
	Semianthracite	86-92	8-14	“
Bituminous	Low volatile			“
	Medium Volatile	78-86	14-22	“
	High volatile A	69-78	22-31	>14,000
	High volatile B	<69	>31	13,000-14,000
	High volatile C			10,500-13,000
Subbituminous	Subbituminous A			10,500-11,500
	Subbituminous B			9,500-10,500
	Subbituminous C			8,300-9,500
Lignite	Lignite A			6,300-8,300
	Lignite B			<6,300

Standard tests:

Calorific value : measuring the heat liberated into a surrounding water jacket by burning a weighted sample of coal in a high pressure oxygen atmosphere

Moisture content : the weight loss of coal when heated to 105 °C in an inert atmosphere

Volatile matter : the weight loss of coal when heated to 950 °C in an inert atmosphere

Fixed carbon : *FC%=100-(moisture content% + volatile matter% + Ash%)*

2.1.2 Organic Structure of Coal Macerals

Coal is an extremely complex mixture of organic material and inorganic components.(61) Due to its extreme heterogeneity, coal does not have a unique molecular structure. Instead, many 'average molecular structures' have been constructed based on the elemental analysis and chemical functionality determined by various analytical methods. These methods include spectroscopy (i.e. IR, FTIR, NMR, TEM), proximate and ultimate analysis, X-ray diffraction, solvent swelling and extraction, and adsorption methods.(67,68) Before the 1960s, coal structures were viewed as large almost graphite like sheets. The model proposed by Given(69) in 1960 illustrated the importance of functionality and the three dimensional structure of coal. But, the Given structure was still based on a large array of connected polycyclic aromatic systems. In 1973, Wiser(70) proposed a very different structure emphasizing much smaller aromatic ring systems with moderately reactive cross-links. More refined models have been, and continue to be, proposed.(71,72,73)

Figure 4 shows the average molecular models of vitrinite proposed by Shinn (1984),(74) Marzec (1986)(75), and Jones (1999).(68) The Shinn model (Figure 4a) depicts islands of aromatic and hydroaromatic clusters cross-linked with the etheric, methelenic, and sulfidic bonds. These relatively small aromatic clusters may contain substituents that are attached by aliphatic or aliphatic-heteroatomic bridges. The relative sizes of the islands, bridges, and substituents depend on the rank of coal.(67) The Marzec model (Figure 4b) contains a two-phase structure of coal. A three-dimensional covalently cross-linked macromolecular network traps a small amount of low molecular weight components within the network. The non-covalently bound volatiles and solvent extractable compounds are constrained within the macromolecular structure *via* either associative forces (hydrogen bonds, electrostatic forces, ionic linkages, van der Waals forces, and π-π interactions)(76) or trapped within entangled macromolecular clusters. The Jones model (Figure 4c) shows a three dimensional representation of the randomly oriented small aromatic clusters. All these models show that the coal is made up of clusters of aromatic units, chemical and reactive functional groups, and small molecular weight moieties which are entrapped within the macromolecular structures of coal. Those aromatic clusters are more or less randomly oriented and associated with each other by both covalent bonding and associative or secondary forces.

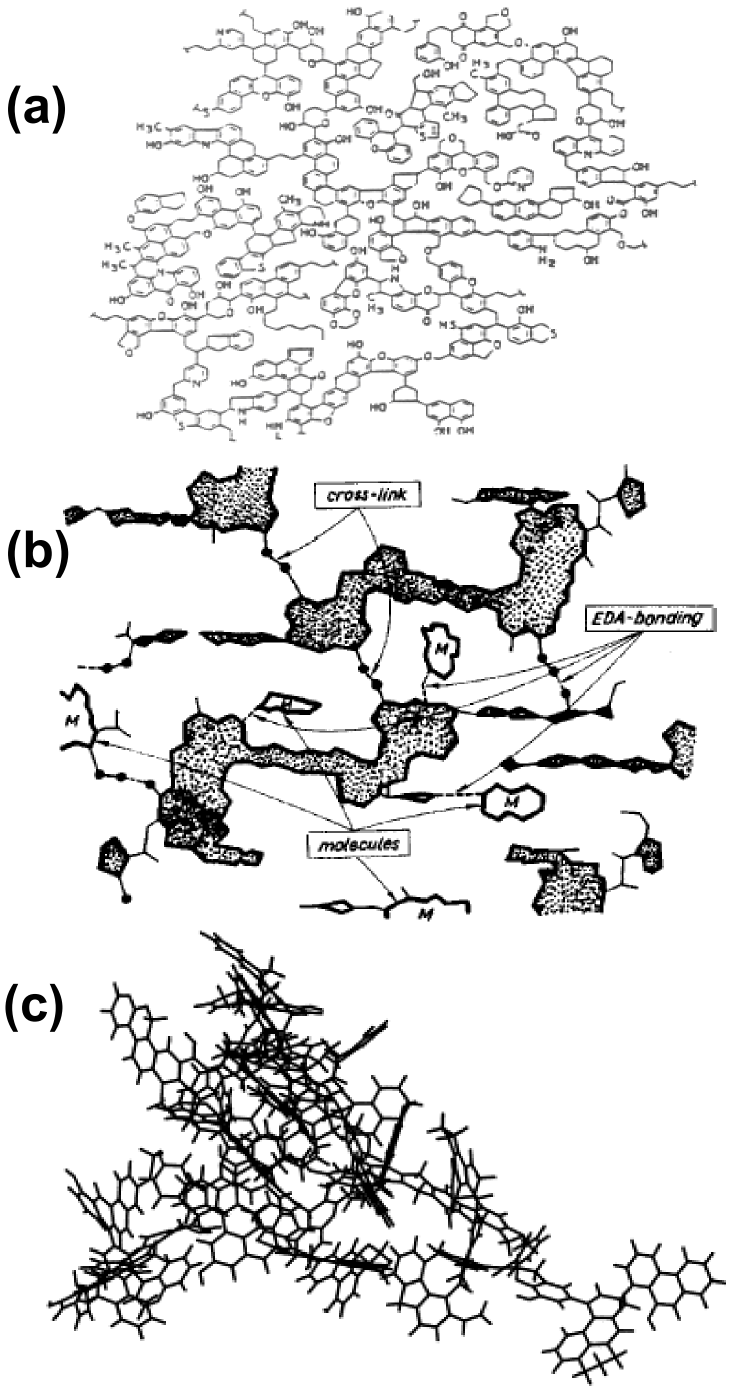

Figure 4. Conceptual representations of the average molecular structure of the vitrinite maceral: (a) Shinn (1984)(74) model, (b) Marzec (1986)(75) model, and (c) Jones et al. (1999)(68) model

2.1.3 Physical Structure of the Coal Matrix

Coal is a highly porous, 'glassy solid rock' below its glass transition temperature (T_g = 580 - 623 ^oK).(17) However, the glassy macromolecular network structure is transformed into a rubbery material at temperatures above its T_g. A similar effect is also observed when organic solvents(77) and adsorbate gases(78,20) and vapors(21,33) are contacted with the coal. Thus, coal is characterized as either a 'porous rock' or a 'pseudo-polymer'.

Coals as mined are anisotropically strained and glassy.(79) They are compressed perpendicular to bedding planes due to overburden pressure and expanded in the bedding plane as a result of tectonic movements.(80) Larsen et al.(79) stated that "when a coal is mined, this strain cannot spontaneously be relieved because the coal is a glassy solid and the macromolecular chain segments have very limited freedom of motion". When coals swell, this strain is relieved as the coal structure rearranges to a lower free energy state.(79)

Coal as a 'porous rock' is in a glassy state. Many coal properties are therefore similar to those of glassy polymers.(81) For instance, the structure of a glassy polymer is hard and brittle. The mobility of the macromolecular chains is severely limited. The structure is very dense and there is very little void space in the structure. Therefore, diffusion in the glassy state is low. However, upon exposure to a swelling solvent, coal behaves as a 'pseudo-polymer' and its structure has been described as rubbery.(82) In the rubbery state, the macromolecular chains are highly flexible. Large segments of the macromolecular network become mobile and occupy a larger portion of the free volume due to chain rotation, translation, and vibration. These aid in the diffusion process, as diffusion in the rubbery state is considerably higher than in the glassy state.

2.1.3.1 Layered Structure of the Coal Matrix: The layered structure of covalently linked polycyclic aromatic units in coal has been established earlier(83) and evidenced by high-resolution transmission electron microscopy (HRTEM)(84,85) and wide-angle X-ray scattering (WAXRS)(86) studies. Sharma et al.,(84) for the first time, have successfully imaged the lattice fringes of raw coals by viewing the thin edge of the coal samples. The lattice fringes and the individual layers can be seen clearly. Some small condensed aromatic units can also be seen as forming stacks parallel to each other. Their preliminary results show that the two macerals differ from each other such that vitrinite shows the presence of fewer stacked layers than the inertinite, which is more oriented and contains many stacked layers. The distance between the aromatic layers in stacks is between 3.3 and 4.0 Å. The average sizes of the layers are 10.0-13.0 Å and larger for the high rank coals.(85)

The number of layers and the distance between the layers in an average structural domain for various ranks of Argonne Premium coals were also reported by Wertz and Quin(86) after wide-angle X-ray scattering (WAXRS) studies. As shown in Table 2, the number of layers in an average structural domain is about 2.3, 3.0, and 4.5-5.0 and the average inter-layer distance is 4.1, 4.0, and 3.7 Å, for Wyodak, Pittsburgh No.8, and Pocahontas No.3 coals, respectively. The results indicate that the inter-layer structuring is rank dependent. As shown in the table, as the degree of maturation increases, the stacking number and the average length of the layers increase whereas the distance between the layers decreases.

Table 2. Wide angle X-ray scattering measurement of the layered structure of Argonne Premium coals(86)

Coal	Number of layers in an average structural domain	Distance between layers (Å)
Pocahontas No.3	5.0	3.7
Pittsburgh No.8	3.0	4.0
Wyodak	2.2	4.1
Beulah-Zap	2.0	4.1

2.1.3.2 Pore Size in the Coal Matrix: Coal is composed of highly cross-linked and entangled networks of macromolecular chains whose poor alignment in three dimensions produces an extensive porosity. According to IUPAC classification,(87) pores are classified with respect to their sizes as macropores $d_p > 500$ Å, mesopores $d_p = 20\text{-}500$ Å, micropores $d_p = 8\text{-}20$ Å and submicropores $d_p < 8$ Å. The distance between the layers of macromolecular units, which is about 3.5-4.1 Å, is thought to be responsible for most of the porosity in coals. However, as shown in Table 3, different techniques and probes reported different pore sizes, most probably, due to the pseudo-polymeric nature of the coal. For instance, an appreciable fraction of the pores in coals have pore sizes of 5.2-6.7 Å as estimated by ^{129}Xe-NMR method.(88,89) Tsiao and Botto(89) found the pore sizes of Argonne Premium Upper Freeport, Illinois No.3, and Wyodak coals to be about 5.8-6.7 Å. For Illinois No.6 coal, an additional pore structure was discerned having larger pore diameter of approximately 10 Å. The pores estimated by CO_2 adsorption and ^{1}H-NMR of pore water showed larger pore sizes. Amarasekera et al.(90) estimated the pore sizes of four brown coals, one medium-volatile subbituminous coal, one high-volatile subbituminous coal, and one low-volatile bituminous coal by CO_2 adsorption and found the pore sizes to be 13-14 Å independent of coal rank. Hayashi et al.(91) estimated the pore sizes of Yallourn brown coal (water content; 1.46 g-water/g-daf coal) and Beulah-Zap lignite coal (water content; 0.53 g-water/g-daf coal) by ^{1}H-NMR method of the *in-situ* pore water. They found that the pore sizes of these coals were 28 and 22 Å, respectively. These values indicate that coals are indeed submicroporous and the pore size is not a unique property of the coal but varies with the measurement technique and probe used. Moreover, coals are dried before pore sizes are estimated, which causes shrinkage and collapse of some pores as evidenced by ^{1}H-NMR measurements of the *in-situ* pore water.(91)

Table 3. The pore size of selected Argonne Premium Coals

Coal	Avg. Pore Size, (Å)		Method	Ref.
Upper Freeport	6.3 ± 0.7	-	^{129}Xe NMR	(89)
Illinois No.6	5.2	-	^{129}Xe NMR	(88)
Illinois No.6	5.8 ± 0.4	9.4 ± 1.9	^{129}Xe NMR	(89)
Wyodak	6.7 ± 0.2	-	^{129}Xe NMR	(89)
Pittsburgh	19.1	-	CO_2 Adsorption	(92)
Beulah-Zap	16.8	-	CO_2 Adsorption	(92)
Beulah-Zap	22.0	-	^{1}H-NMR	(91)

2.1.3.3 Density and Porosity of the Coal Matrix: The density and porosity of coals have been well studied and a number of reviews are available.(27,93,94,95,96) The most common methods used to characterize the porous structure of coals were summarized by Senel et al.(97) There are basically two density definitions. First is the 'true' density, which is defined as the weight of a unit volume of pore-free solid. The second is the ‘apparent’ density defined as the weight of a unit volume of solid including pores. The ’true’ density is generally measured by helium with the assumption that helium is a small molecule and able to access all of the pore volume with negligible adsorption. However, X-ray studies with anthracites have shown that there is some porosity in these high-rank coals, which is inaccessible to helium.(29) Therefore, the helium density of coal determined in this fashion would be lower than its ‘true’ density.

Mahajan(94) showed that the helium density of coals decreases with increasing carbon content up to 82 %C, passes through a minimum in the range of 82-86 %C and increases sharply with further increases in carbon content. Other investigators have also reported similar trends.(98,29,99) The bulk, or apparent density of coals, which includes micropores, macropores, and interparticle voids, is obtained by a fluid displacement method. Toda(16) measured the apparent densities of various ranks of coal in methanol, n-hexane, and mercury and compared them with the helium density. All of the densities were higher for lower and higher rank coals and displayed a minima at ~ 85%C. Walker et al.(99) also measured the densities and porosities of coals in helium, mercury, methanol, water, and carbon dioxide. They found that densities measured in MeOH, water, and CO_2 were frequently greater than those measured in helium. The authors account these discrepancies both to the penetration of some solvents into pores inaccessible to He and to imbibition into the coal structure, which results in swelling. It is clear that when coals are exposed to some fluids, they swell and expand to some extent resulting in their structure and their porosity being altered.

2.1.3.4 Open and Closed Porosity in Coals: The total open pore volume of coals was calculated from their moisture content by King and Wilkins(100) in 1944. They showed that the porosities of coals range from a high of 25-30% in lignites through a minimum of about 1%-3% in coals with 87-90% carbon, to higher values of about 10% in anthracites. The porosity of coals can also be estimated from the difference between their densities in mercury and another fluid, e.g. helium.

$$V_{pore} = \frac{1}{\rho_{Hg}} - \frac{1}{\rho_{fluid}} \qquad (1)$$

For instance, as reported by Toda(16), the specific volume of coals in methanol ($1/\rho_{MeOH}$) is lower than those in helium, n-Hexane, and mercury. In other words, methanol reports higher pore volume than n-hexane and mercury. Because the density was so much higher in MeOH than in helium, it was suggested that helium may be restricted from penetrating very narrow pore entrances, while MeOH can penetrate these pores by virtue of an imbibition effect.(101) As can be seen in Figure 5, the closed porosity in coals was calculated to be about 11% for lower rank coals and decreases with rank. Therefore, it is clear that some of the pores in coal are inaccessible.

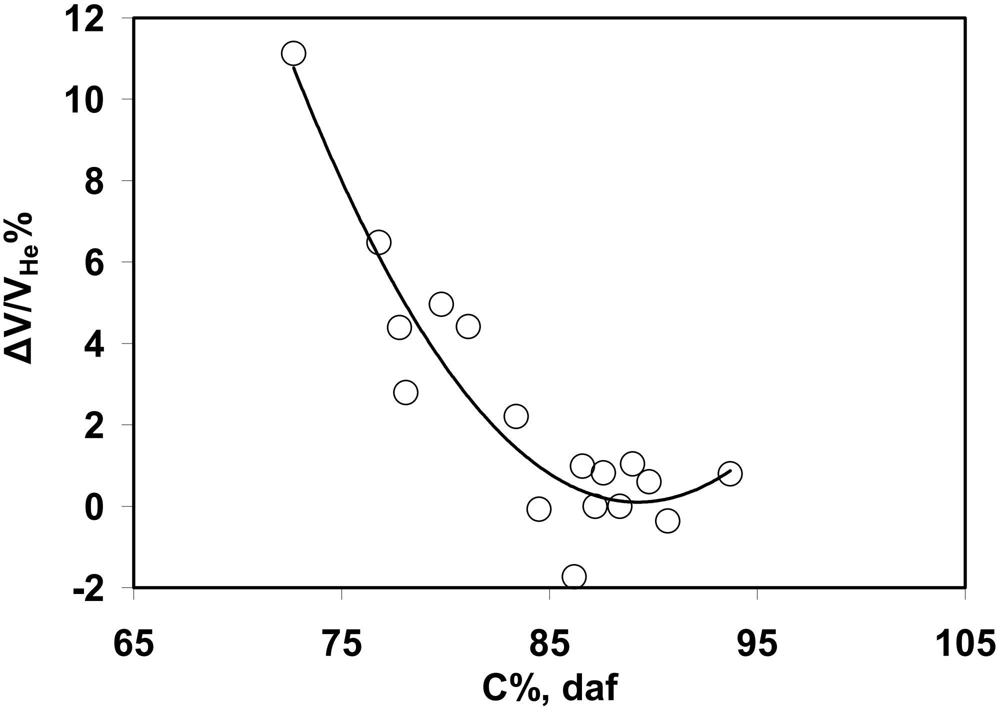

Figure 5. The percent difference in coal volume estimated by helium and methanol (calculated from Ref. (16))

Whether the micropores are closed or part of an open pore network has been the subject of much discussion in the literature. One school of thought has claimed that coals contain an interconnected-pore network of high surface area with slit-shaped, constricted openings of molecular dimensions. Another school of thought has argued that coals do not contain interconnected-pore network but that the pores in the coal are isolated from each other and that they can be only reached by diffusion through the solid coal matrix. Alexeev et al.(102) have recently shown the presence of closed porosity in coals. They found that most of the pores in coals are isolated. According to these authors, the closed porosity is greater than 60% of the total porous volume in coals. Larsen and coworkers(24,28) have studied the adsorption of CO_2 and a series of aliphatic hydrocarbons with various cross-sectional areas on the Argonne Premium coals. Large differences in the uptake of gases of similar molecular dimensions, including CO_2, ethane, and cyclopropane, are observed for Argonne Premium coals. They attributed this to a 'molecular sieving' effect. They concluded that coal does not contain an interconnected network of bottlenecked pores. Instead, they proposed that the pores in coal are isolated and can only be reached by diffusion through the solid coal matrix.

2.1.3.5 Surface Area of the Coal Matrix: Surface areas of porous adsorbents are generally determined by the conventional BET method employing the N_2-adsorption isotherm measured at –196 °C.(97,103,104) The BET surface areas of coals, however, are very low because of: (1) an activated diffusion phenomenon;(105) and (2) a thermal shrinkage of the pores at –196 °C.(106) In order to overcome this drawback, the use of CO_2 adsorption for measuring surface areas of coals was proposed several decades ago.(107,108)

Good reviews are available on the CO_2 surface area of coals.(109,94) Carbon dioxide adsorption measurements are usually conducted at 195, 273, and 298 K. Because these temperatures are much higher than those for nitrogen adsorption, and because the CO_2 molecule has a slightly smaller dimension than N_2, activated diffusion of CO_2 was not a problem.(110) Therefore, CO_2 may be considered a good candidate for measuring micropore volumes and total surface areas of microporous adsorbents. However, the validity of coal surface areas measured by CO_2 is affected by the swelling phenomenon. Swelling occurs as a result of the imbibition of the CO_2 molecules into the coal structure and the capillary pressure exerted by the adsorbed CO_2 as it forms a liquid layer.(111) But, it has been shown that the volume expansion (swelling) from

CO_2 uptake is much less than the volume of CO_2 taken up under these conditions.(99) Therefore, it has been concluded that the high CO_2-surface areas of coals are at least semi quantitatively correct.(101)

Gan et al.(112) compared the N_2 and CO_2 surface areas of coals as a function of the carbon content and showed that coals with higher N_2 surface areas fall in the carbon content range of 75.5 to 81.5 %. Coals with carbon contents <75.5% and >81,5% showed a negligible N_2 surface area of less than 8 m^2/g. CO_2 surface areas of anthracites are high. Generally, the CO_2 surface areas display a broad minimum at about 80 %. Many of the physical properties of the coal show a ‘U-shaped’ curve with a minimum or a maximum in the mid-bituminous coal rank. The trend is similar in the quantity decreasing with increases in carbon content up to 82 %C, going through a minimum in the carbon content range of 82-86 %C and increasing sharply with further increases in carbon content.

Reucroft and Patel(35) studied the sorption of a range of vapors on a Kentucky No.12 coal and compared the surface area and swelling parameter, defined as swollen volume/unswollen volume, of this coal with respect to solubility parameter of each adsorbate. The solubility parameter (δ) for organic vapors is defined as

$$\delta = \left(\frac{H_V - RT}{\upsilon} \right)^{1/2} \tag{2}$$

where H_V is molar enthalpy of vaporization (J/mole) and υ is molar volume (cm^3/mole). They found that the surface area and swelling parameter showed a sharp increase with increasing solubility parameter up to a maximum at $\delta = 20$ $MPa^{1/2}$ and then a decrease with increasing solubility parameter. Interestingly, the surface area is highly related to the swelling parameter, not the molecular area of each sorbate, as depicted in Figure 6. As shown in the figure, the surface area depends on the swelling parameter of the sorbate: the bigger the swelling parameter, the higher the surface area. It can be figured out that the coal is initially in its glassy state and the entrance of the adsorbate molecules into the pores is restricted by the layered structure of the coal which has been reported to have opening of only about 4 Å.(86) Depending on the magnitude of the swelling parameter, the sorbate molecules can open up such restrictions and access the bulk structure of the coal. Thus, the surface area reported is independent of the molecular size. Rather, the surface area depends on the swelling power of the adsorbate probe.(35) Nitrogen, for example, which has a very small swelling parameter, reports a very low surface area.

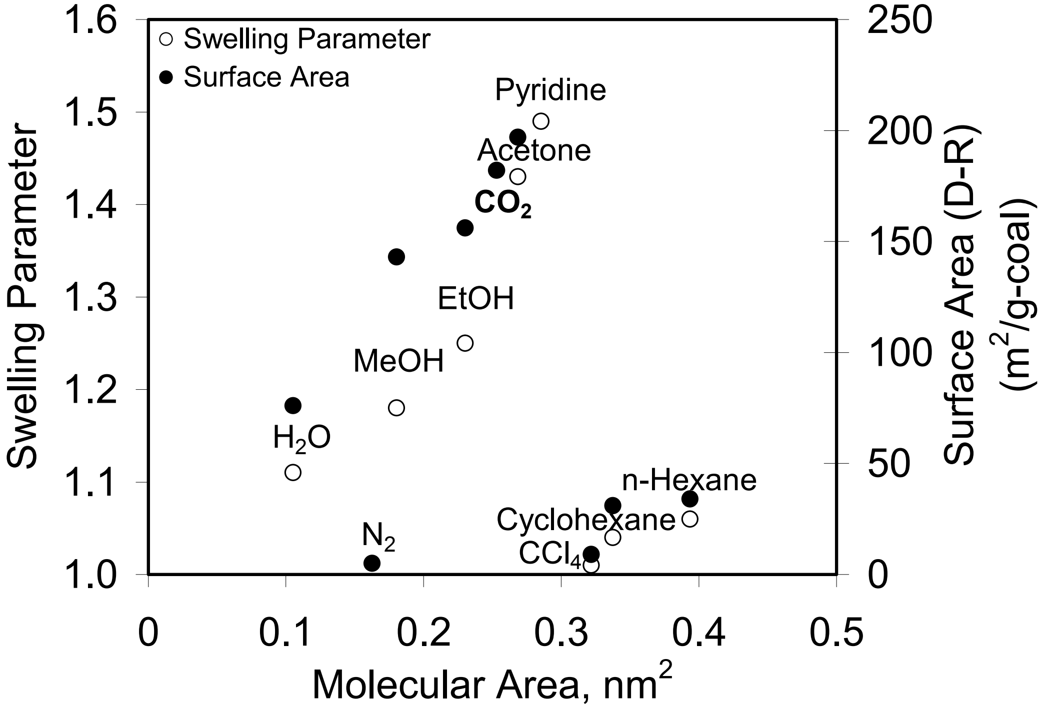

Figure 6. Surface areas of Kentucky No.12 coal obtained at 298 ^{o}K from various sorbate vapors with different swelling parameters(35)

2.1.4 Coal Swelling

The swelling of coal upon the sorption of liquids or gases is a well-known phenomenon.(113,36,58,101) Toda (1972)(16) measured the variation of the difference in volume of coal estimated by CO_2 and that estimated by helium for different coal ranks. His results showed that the volume of the coal measured by CO_2 was always lower than that by He indicating that the CO_2 could penetrate into micropores which were inaccessible to He.

Reucroft and Patel (1986)(113) studied the expansion and contraction of a pencil-shaped specimen (~1 cm long and 0.4 cm in diameter) of Kentucky coal in several gases, including He, N_2, CO_2, and Xe, and also in a vacuum. The dilatometer containing the specimen was initially evacuated and then exposed to a gas at atmospheric pressure and room temperature. They measured directly the change in length of the coal specimen while it was in equilibrium with the gaseous atmosphere at 20 psig. Figure 7 shows the expansion and contraction of the specimen produced by exposure to a gas or vacuum. The sample was initially evacuated leading to sample contraction. The value was recorded and then used as a baseline for the next step and so on. The evacuated sample was then exposed to He, N_2, and CO_2. Helium and nitrogen did not produce any significant effect on the coal. However, CO_2-induced expansion was significant. When CO_2 was evacuated, the contraction observed was also significant. Finally, when Xe was introduced into the evacuated specimen, little expansion was produced.

Reucroft and Sethuraman (1987)(36) extended the dilatometric studies to CO_2 pressures up to 15 atm. They found that the evacuation of the coal samples resulted in contraction, apparently due to moisture loss. The extent of the contraction was larger for coals with high initial moisture content. Atmospheric pressures of He and N_2 resulted in negligible changes, however, CO_2 caused considerable expansion. The volume change calculated from the length change, assuming isotropic swelling, was from 0.36% to 4.18% at pressures from vacuum to 15 atm. They also found that the extent of expansion in a CO_2 atmosphere was rank dependent as the lower-rank coals swell more than the higher rank coals.

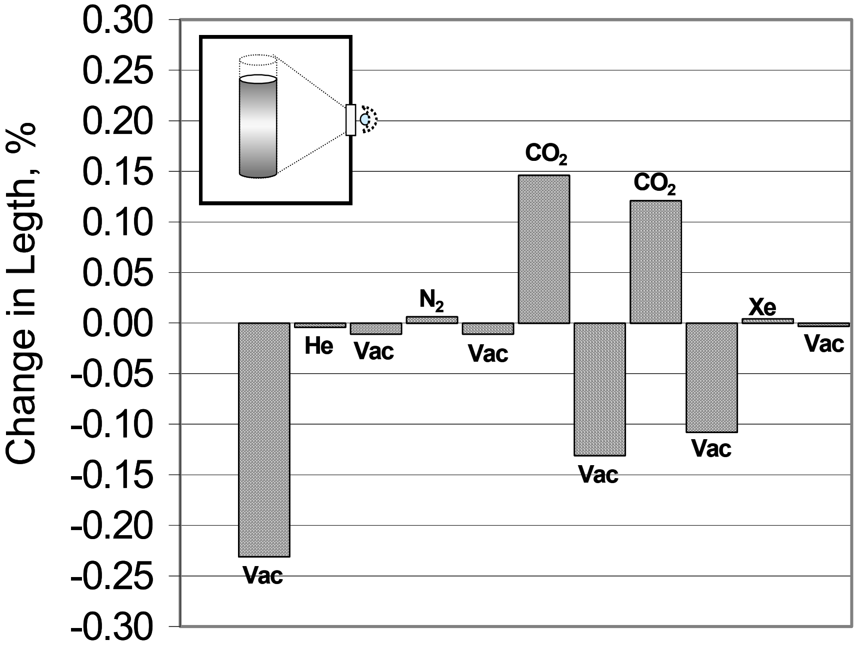

Figure 7. Equilibrium expansion and contraction response of a Kentucky coal specimen (~1 cm long and 0.4 cm in diameter) under vacuum and exposed to He, N_2, CO_2, and Xe, at 20 psig and 298 K(113)

Walker et al.(101) measured the expansion of coals and macerals induced by carbon dioxide and methanol in a dilatometer. Their measurements were made on minus 20 mesh samples. They used a probe rod, which exerted a mechanical pressure of 10 g/cm^2, to measure the changes in height of the bed. Attainment of equilibrium was much more rapid in CO_2 than in methanol. On the other hand, the extent of expansion was significantly greater in methanol than in CO_2, especially for low-rank coals. Figure 8 shows the expansion of selected coals under elevated pressures of CO_2 as measured by dilatometry. In each case, expansion increases with increasing CO_2 pressure. The expansion is also rank dependent. As was seen by Reucroft,(36) the expansion was greater for lower rank coals. The authors concluded that most of the CO_2 uptake was not due to imbibition of CO_2 into the coal structure, but rather to CO_2 uptake in the open and closed (to He) micropores.

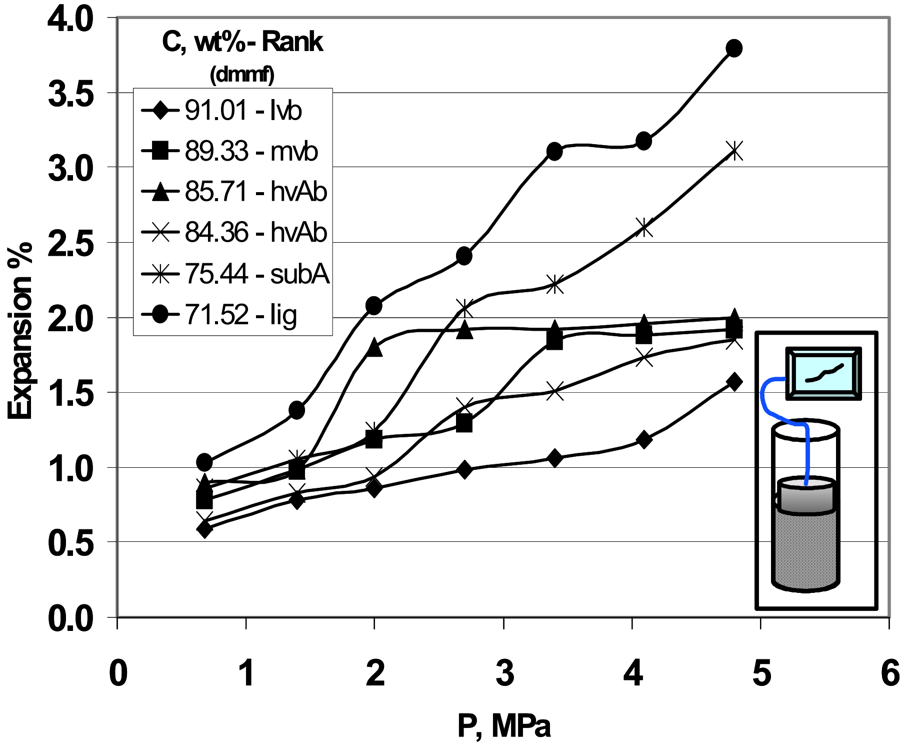

Figure 8. Expansion of selected coals in elevated pressures of CO_2 as measured by dilatometry in a packed bed(101)

Recently, George and Barakat(37) have investigated the change in effective strength associated with the shrinkage of coal as a result of desorption of gases. They monitored the volumetric changes of the coal matrix with the adsorption and desorption of methane, carbon dioxide, nitrogen and helium. Helium did not induce swelling because no adsorption occurred. The swelling due to CO_2 adsorption was 12 times greater than that for N_2 and 8 times greater than for CH_4. As the gas pressure was decreased from 4.0 MPa to atmospheric pressure, the resulting volumetric strain ($\Delta V/V$) due to desorption of CO_2, CH_4 and He was +4.5%, +2.2%, and -0.1%, respectively. Here, the positive sign shows shrinkage in volume upon desorption whereas the negative sign shows an expansion in volume.

Mechanism of Swelling: Upon exposure of a porous solid, such as coal to a fluid, swelling can be produced by at least two mechanisms:(58,114) First, the sorption of a liquid-like layer on the pore walls can create a pressure gradient that is large enough to cause measurable structural changes in the solid.(115) At elevated pressures, CO_2 is expected to behave as a high-density liquid especially inside microporous materials. The force exerted by the adsorbed layer will create a force to move the macromolecular clusters apart. In the second mechanism, the imbibition of fluid into the solid structure can cause an expansion of the porous material. In this case, interaction of the fluid with the solid through hydrogen bonding, electron transfer, etc. can result in relaxation of the molecular layers in the coal. It is suggested that the expansion of coals in high-pressure CO_2 is attributed to a combination of these mechanisms. However, it has been difficult to properly account the amount of expansion due to the extent of chemical versus physical interaction of the fluid with the solid.

2.2 STORAGE OF CO_2 IN COAL

The CO_2-holding capacity of coal seams is an important area of research both for an economic assessment of candidate coal seams and for an understanding of the gas-coal interactions. Because CH_4 is the dominant gas in coal seams, the coalbed CH_4 reservoir capacity and the parameters that affect the adsorption capacity of CH_4 have been investigated extensively in order to accurately determine the gas-in-place and to enhance the safety of coal mining.(41,116,45) However, data relating the CO_2 capacity of coals under in-seam conditions are limited.

The CH_4 capacity of a candidate coal seam can be estimated by: (1) direct methods which measure the volume of CH_4 released from a coal sample sealed into a desorption canister; or (2) indirect methods based on the adsorption/desorption isotherms obtained in the laboratory. A review of the estimation of the CH_4 content of coals by direct methods is readily available.(117) The adsorption/storage capacity of a coal for CO_2 is generally estimated indirectly from the adsorption isotherm data employing an empirical correlation. The most widely used adsorption equations, which are used to represent the adsorption isotherms of microporous adsorbents, are Langmuir's monolayer equation and Dubinin's pore filling equations.(118)

2.2.1 Gas Adsorption

When a solid is exposed to a gas or vapor, adsorption of gas onto the surfaces of the solid adsorbent occurs. Adsorption is a complicated process and different expressions are used interchangeably to define it. For instance, while the term 'adsorption' is used to imply the condensation of gases on free surfaces, the term 'absorption' or 'imbibition' is used to describe the penetration of gas molecules into the mass of the absorbing solid. Likewise, the term 'sorption' is used to emphasize the adsorption on a surface, absorption by penetration into the lattice of the solid, and/or capillary condensation within the pores.(103) The IUPAC definition is generally accepted for the 'adsorption' as the enrichment of one or more components in an interfacial layer.(119)

Adsorption is generally classified as chemical adsorption (chemisorption) and physical adsorption (physisorption). In chemisorption, the adsorbate becomes bound to the solid surface by a direct chemical bond. The energy generated is the same order of magnitude as the heat of reaction, which ranges between 60 and 4000 kJ/mole.(120) The surface coverage in chemisorption is monolayer. In physisorption, the adsorption takes place mainly by van der Waals and electrostatic forces between adsorbate molecules and the atoms, which compose the adsorbent surface. Because there is no chemical bond between adsorbate molecules and the solid surface, physical adsorption is a reversible process. Physisorption is exothermic and the energy involved is not much larger than the energy of condensation of the adsorbate ranging from 8 to 40 kJ/mole.(120) It is most likely that the adsorption occurs as a monolayer at low pressures and as multilayers at relatively higher pressures depending on the type of adsorbent and the adsorbate used.

2.2.1.1 Adsorption Isotherms: The amount of gas adsorbed by a solid sample is a function of the mass of the sample, the temperature and pressure, and the nature of both the solid and the gas.(103) The adsorption of a given gas on a particular solid can be represented by an adsorption isotherm, which is a plot of the amount adsorbed as a function of pressure at constant temperature. The shape of adsorption isotherms can provide information about the adsorption process, and the porosity as well as the surface area of the adsorbent. According to the IUPAC classification,(87) there are six significantly different adsorption isotherms describing the physical adsorption as shown in Figure 9.(103) A Type I isotherm generally occurs when a monolayer of adsorbate molecules is adsorbed on a non-porous solid or when adsorption is dominated by a micropore filling process. This type of isotherm is often called a Langmuir type isotherm. Type II is displayed by a nonporous or macroporous adsorbent. This isotherm is characterized by an inflection point, which represents the completion of the monolayer and the beginning of the formation of multilayers. Type III adsorption isotherm is typical for a non-porous or macroporous adsorbent and is observed for weak adsorbent-adsorbate interactions. Types IV isotherm, which is similar to the Type II, is typical for a mesoporous adsorbent. It displays a hysteresis loop due to capillary condensation. Type V is typical for non-porous or macroporous adsorbents and is observed for weak adsorbent-adsorbate interactions. Type VI isotherms or stepped isotherms are included in the classification although they are rare.(103)

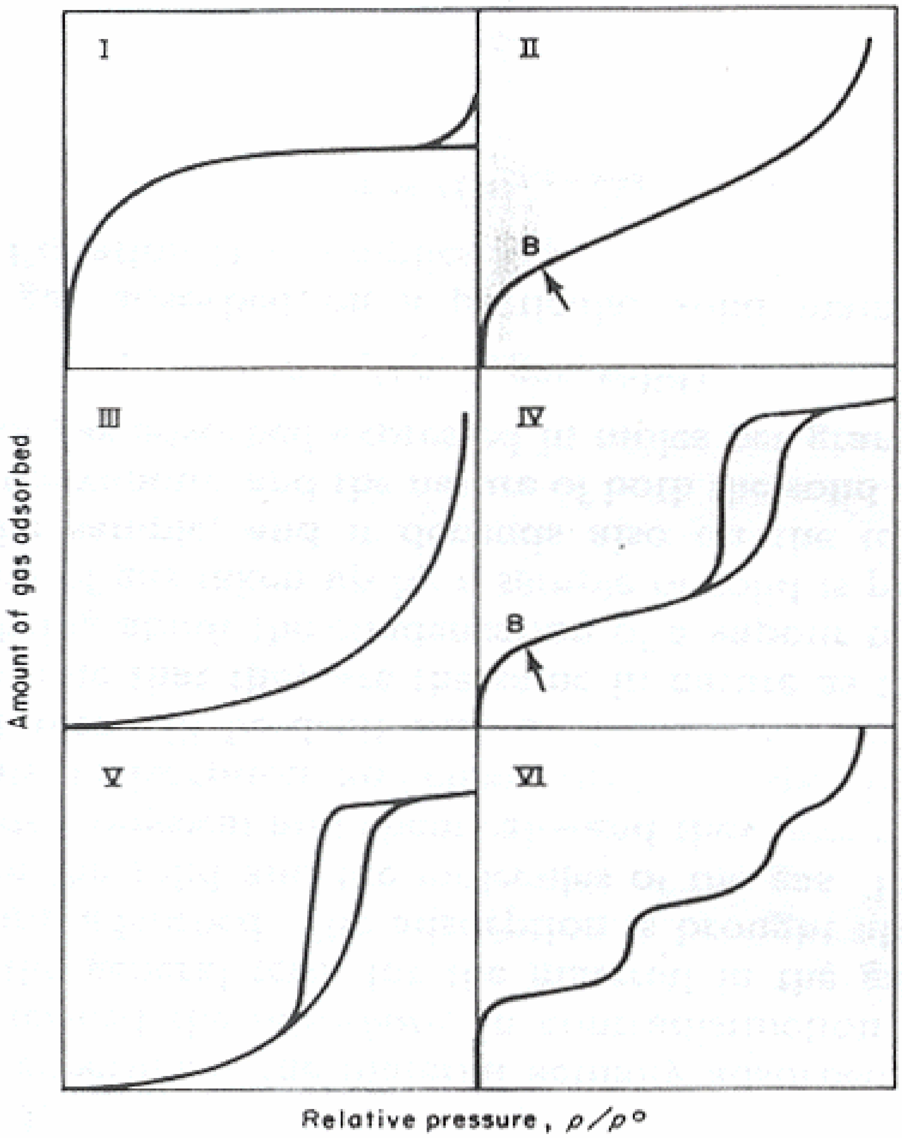

Figure 9. The types of adsorption isotherms(103)

Because coal is a microporous solid, the adsorption isotherms of gases, including N_2, CH_4, and CO_2, would be expected to follow a Type I isotherm. However, various isotherms have been reported in the literature for CO_2.(32,33)

2.2.1.2 Mechanisms of Adsorption: Various modes of adsorption of gases on coals have been suggested. Adsorption on the surface with a monolayer, a multilayer, and a pore filling mechanism have most commonly appeared in the literature. The Langmuir monolayer adsorption is the simplest isotherm model. It has been derived theoretically from both kinetic and statistical mechanical concepts.(121) The mechanism of the Langmuir model is depicted in Figure 10a. In the Langmuir model, it is assumed that the adsorbate molecules are adsorbed on a fixed number of well-defined, localized sites, each of which can hold only one adsorbate molecule. All sites are energetically equivalent and there is no interaction among the adsorbate molecules adsorbed on neighboring sites.

Brunauer, Emmett, and Teller (BET)(122) extended the Langmuir model in 1938 by introducing a multilayer adsorption model as shown in Figure 10b. The BET model assumes that, in addition to the assumptions made for the Langmuir model, each adsorbate molecule in the first layer serves as an adsorption site for an adsorbate molecule into the second layer, the second layer to the third layer, and so on. The attractive forces between the adsorbate molecules are negligible. The heat of adsorption of the second and subsequent layers is assumed to be equal to the heat of liquefaction of the adsorbate and different from the heat of the adsorption of the first layer.

Generally, the Langmuir and BET models are applied to adsorption on a single flat surface or on a pore surface when the radii of the pores are large. The theory is not applicable to microporous adsorbents in which the pore sizes are only few molecules wide.(123,124) The adsorption potentials associated with dispersion forces are strongly enhanced in micropores due to overlap of the adsorption fields from the opposite pore walls. Instead, the adsorption mechanism in microporous adsorbent is explained by a pore filling mechanism as shown in Figure 10c. Polanyi$^{(125)}$ defined the adsorption potential, ε, of an adsorbate molecule within the attractive force field of an adsorbent as the work required to bring an adsorbate molecule from the gas phase to the adsorption space with the adsorption forces

$$\varepsilon = \int_{P}^{P_S} VdP = RT\,\mathbf{ln}\left(\frac{P_s}{P}\right) \tag{3}$$

Dubinin$^{(126)}$ then proposed that the degree of micropore filling could be expressed as a function of the adsorption potential, ε, characteristic adsorption energy, E, and a constant, j, which depends on the homogeneity of micropore system:

$$\frac{n}{n_0} = e^{-\left(\varepsilon/E\right)^j} \tag{4}$$

The characteristic adsorption energy is further defined as

$$E = \beta E_o \tag{5}$$

where β is affinity coefficient ($\beta = 0.35$ for CO_2)$^{(31)}$ and E_o is the characteristic heat of adsorption. Therefore, the physical adsorption of gases or vapors by microporous solids can be described by Dubinin's pore filling theory.

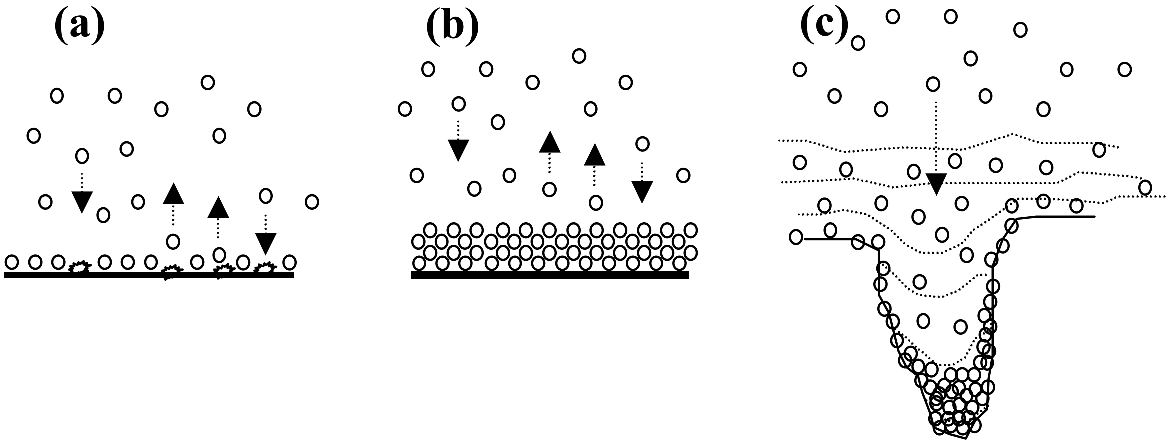

Figure 10. A schematic representation of adsorption mechanisms (a) Langmuir's monolayer adsorption model (b) BET's multilayer adsorption model (c) Dubinin's pore filling model

2.2.2 Construction of an Adsorption Isotherm

2.2.2.1 Modeling the Adsorption Isotherms: Gravimetric and volumetric methods are widely used for the construction of adsorption isotherms. Both require an accurate estimate of the volume of the solid adsorbent, in the former method, to make a buoyancy correction and, in the later one, to calculate the free gas space in the sample cell. Using the volumetric method to construct an adsorption isotherm requires the three steps shown in Figure 11. In the first step, the empty volume of the sample cell, V_s, is estimated. In the second step, the volume of the adsorbent, or the free volume (void volume) remaining in the sample cell after adding the adsorbent, V_o, is measured. These two volumes are usually measured using the helium displacement method. The density and volume of the adsorbent can also be estimated from these two measurements. In the third step, the adsorption isotherm is measured using the adsorbate gas of interest. The V-shaped notch in the adsorbent in Figure 11 represents the pores that are occupied to various extents, depending on the pressure, during the adsorption experiments.

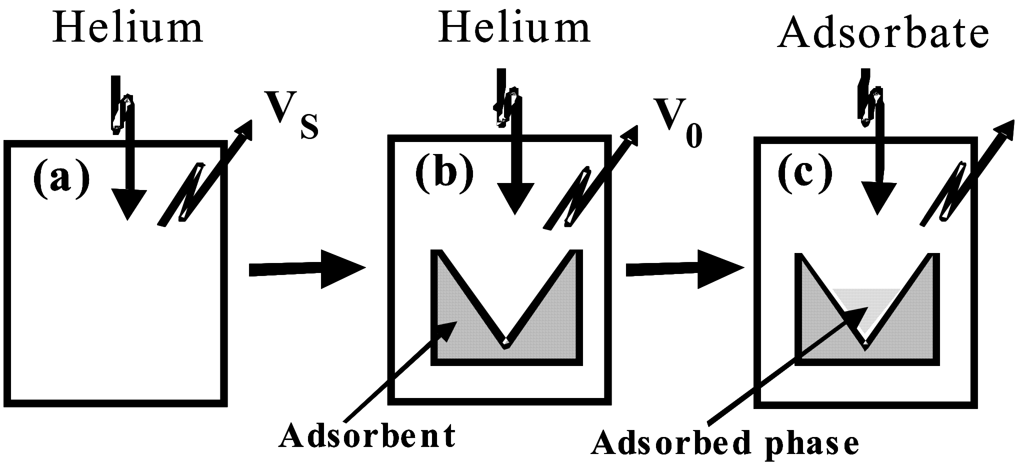

Figure 11. Construction of an adsorption isotherm: (a) estimation of the empty volume of the sample cell (V_S), (b) estimation of the volume of the adsorbent, from the change in the volume of the sample cell (V_o), and (c) measurement of the adsorption isotherm during which the void volume (V_o) in the sample cell decreases (to V_i) due to the volume occupied by the adsorbed phase (V^a)

As shown in Figure 11c, the adsorbed phase occupies volume and this volume needs to be included in the calculation of the remaining free volume in the cell. From the Gibbs definition,(127) the absolute adsorbed amount, n^{abs}, can be calculated by subtracting the moles of free-gas in the sample cell void volume (V_i) from the total moles of gas transferred into the sample cell, n^t. The total moles of gas transferred into the sample cell from the reference cell, n^t, is known in these experiments and must equal to the moles in the gaseous phase plus the moles adsorbed on the substrate:

$$n^{abs} = n^{t} - \rho V_{i} \tag{6}$$

where ρ is the molar density of the gas in the free space and V_i is the "true" void volume in the sample cell, that is, the volume occupied by neither the solid adsorbent nor the volume of the adsorbed phase (V^a). However, this leaves two unknowns, n^{abs} and V_i and in order to overcome this problem, the Gibbs excess adsorption (n^{ex}) is defined employing the void volume initially estimated by He expansion, V_o:

$$n^{ex} = n^{t} - \rho V_{0} \tag{7}$$

where n^{t} and ρ are as defined above.

The excess adsorption is the amount of gas calculated to have been adsorbed when the volume of the adsorbed phase, V^a, is ignored. The relationship between the experimentally measured excess adsorption, n^{ex}, and the absolute adsorption, n^{abs}, can be obtained from the difference between Eq.(7) and Eq.(6) such that

$$n^{ex} = n^{abs} + \rho \Delta V \tag{8}$$

where ΔV, is the difference between the void volumes in the presence and absence of the adsorbed phase, respectively, and is defined as

$$\Delta V = V_{i} - V_{0} = -V^{a} = -\frac{n^{abs}}{\rho^{a}} \tag{9}$$

where V^a and ρ^a are the volume and molar density of the adsorbed phase, respectively. Thus, the excess adsorption isotherm can be represented by the well-known adsorption equation for a rigid solid,(127) Eq.(10), which includes the correction for the volume occupied by the adsorbed phase:

$$n^{ex} = \left(1 - {\rho}/{\rho^{a}}\right) n^{abs} \tag{10}$$

The unknowns in Eq.(10) are the density of the adsorbed phase, ρ^a, and the absolute adsorption term, n^{abs}. The density of the adsorbed phase cannot be measured but it is estimated from suggested relationships. The approximations used to estimate the adsorbed phase density, ρ^a, and the model equations used to estimate the absolute (real) adsorbed amount, n^{abs}, are summarized in the following sections.

2.2.2.2 Density of the Adsorbed Phase (ρ^a): Because the density of the adsorbed phase cannot be measured directly, several approximations have been used, some of which are shown in Table 4. The approximations are based on one of two assumptions: either that the density of the adsorbed phase remains constant and additional adsorbate occupies additional volume, or that the volume available for adsorption remains constant and additional adsorption causes an increase in the density of the adsorbed phase. The first class of approximations can be further divided depending on whether the temperature at which the adsorption occurring is below or above the critical temperature of the adsorbate. For temperatures below the critical point, the liquid density at the boiling point,(128) a linear interpolation between the densities at the boiling and critical temperatures,(129) the density of the super-heated liquid,(130,128) and the density at the critical point(130) have been used as the adsorbed phase density. At temperatures above the critical temperature, the inverse of the van der Waals volume(130,128) and, rarely, the density of the solid adsorbate(55) have been used as the density of the adsorbed phase. For the cases involving the constant volume approximation, the adsorbed phase has been assumed to fill the pore volume of a microporous adsorbent,(131) which is considered to be constant, and an effective film thickness(132) has been assigned to describe the adsorbed phase volume. These latter two approximations view the solid and the pore volume as a rigid structure that does not change during the adsorption process. For this reason, they were not considered here further.

Table 4. Constant density approximation for the adsorbed phase

	Approximation	Relationship	Eq. No.
$T < T_c$	Liquid Density(128)	$\rho^a = \rho_{liq}$	(11)
	Linear Approximation(129)	$\rho^a = \rho_b - (\rho_b - \rho_{vdw})\left(\frac{T - T_b}{T_c - T_b}\right)$	(12)
	Superheated Liquid(132)	$\rho^a = \rho_{liq} e^{-k_T (T - T_b)}$	(13)
$T > T_c$	Inverse Van der Waals Volume(130,133)	$\rho^a = \rho_{vdw} = \frac{8MP_c}{RT_c}$	(14)
	Critical Density(130)	$\rho^a = \rho_c$	(15)
	Solid Density(55)	$\rho^a = \rho_{solid}$	(16)

The conditions used for measuring CO_2 isotherms often include both the subcritical and supercritical regions. Figure 12 shows a number of proposed adsorbed phase densities of CO_2 at various temperatures. As can be seen in the figure, the estimates of the density of the adsorbed phase generally decrease as the temperature is increased to the critical temperature. Extrapolation into the supercritical region would result in even smaller densities. For example, the saturated liquid density decreases almost exponentially and equals the critical density at the critical temperature. If this were the true adsorbed phase density, adsorption would occur in neither the liquid state nor above the critical temperature. However, Humayun and Tomasko(133) have shown that this is clearly not the case. Using a microbalance technique, they estimated adsorbed phase densities at temperatures higher than T_c and found that the adsorbed phase densities were higher than the saturated liquid density (12.78 mmole/cm^3), and the compressed liquid density (20.19 mmole/cm^3), and were very near the van der Waals density (23.45 mmole/cm^3).

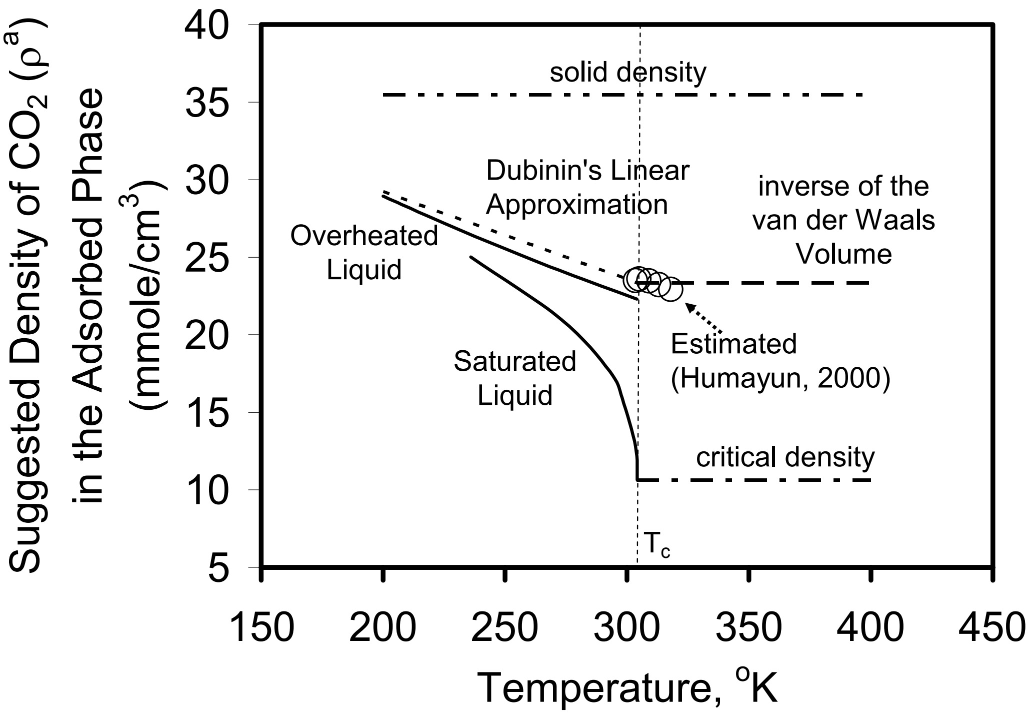

Figure 12. Proposed adsorbed phase densities of CO_2 at various temperatures

Although numerous approximations are used to estimate the density of the adsorbed phase, a systematic study showing the effect of the choice of the adsorbed phase density on the calculation of the absolute adsorption from the excess adsorption isotherms is not available. Also, the extent of unknown volume changes would confound the problem such that a single best-fit solution to the adsorption isotherm model might not exist.

2.2.2.3 **Model Equations for the Absolute Adsorption (n^{abs}):** The absolute adsorption, n^{abs}, is the amount of material actually adsorbed on a solid adsorbent. Many adsorption-model equations have been proposed to represent the absolute adsorption amount. Some of these equations are based on a theoretical foundation, such as the Langmuir,(121), BET,(122) Erying,(134) and virial equation of state,(134) while others are derived to provide empirical curve fits, such as the Langmuir-Freundlich,(135) Toth,(135) UNILAN,(135) modified BET (BETn),(122) and Dubinin(126) equations. Empirical equations, which are not related to physical factors, however, do not allow extrapolation beyond the range of the variables for which the parameters have been determined.(136) Table 5 shows some of the model equations used to represent the amount of gas in the adsorbed phase grouped according to the mechanism of adsorption and the surface properties of the solid adsorbent. For instance, the Dubinin equation is based on a pore filling rather than surface adsorption mechanism. The modified BET (BETn) is based on *n* numbers of adsorbed layers rather than the monolayer adsorption or infinite numbers of adsorbed layers as in the Langmuir and BET equations, respectively. When a particular adsorption equation is used for the n^{abs} term, in Eq.(10), the fit of the experimental adsorption data provides physically meaningful constants, such as the adsorption capacity (n_o), the affinity coefficient (K_i), and the heterogeneity parameter (j_i), from which the surface area, the heat of adsorption, and the average pore size of the solid adsorbent can be calculated.

Table 5. Model equations$^{(135)}$ used to represent the absolute adsorbed amount, n^{abs} where n_o is the adsorption/monolayer/micropore capacity, K_i is a constant related to the heat of adsorption differently in each adsorption model, and j_i is an exponent related to the heterogeneity of the solid adsorbent

Mechanism of Adsorption	Surface of the adsorbent	Model	Model Equation Representing the absolute adsorption (n^{abs})	Eq. No.
Monolayer Surface Adsorption	Homogenous	1.Langmuir	$n^{abs} = \frac{n_o P}{K_1 + P}$	(17)
	Heterogeneous	2.Langmuir-Freundlich	$n^{abs} = \frac{n_o P^{j2}}{K_2 + P^{j2}}$	(18)
		3.Toth	$n^{abs} = \frac{n_o P}{\left(K_3 + P^{j3}\right)^{1/j_3}}$	(19)
		4.UNILAN	$n^{abs} = \frac{n_o}{2j_4} \ln\left(\frac{K_4 + Pe^{j4}}{K_4 + Pe^{-j4}}\right)$	(20)
Multilayer Surface Adsorption	Heterogeneous	5.Modified-B.E.T (BETn)	$n^{abs} = \left(\frac{n_o K_5 (P/P_s)}{1-(P/P_s)}\right)\left(\frac{1-(j_5+1)(P/P_s)^{j5} + j_5 (P/P_s)^{j5+1}}{1+(K_5-1)(P/P_s) - K_5 (P/P_s)^{j5+1}}\right)$	(21)
Pore Filling	Heterogeneous	6. Dubinin-Astakhov	$n^{abs} = n_o e^{-\left[K_6 \ln\left(P_s/P\right)\right]^{j6}}$	(22)

2.2.2.4 Saturation Pressure for CO_2 (P_s): Some of the model equations to interpret the adsorption isotherms include the saturation pressure (P_s). For instance, the D-A equation, which is used to interpret the adsorption isotherms for microporous adsorbents according to a volume filling mechanism, contains the saturation pressure. While the saturation pressure can be defined at temperatures below the critical temperature, it does not have a physical meaning at temperatures greater than the critical temperature. However, as shown in Table 6, several relationships were suggested to represent the saturation pressure at temperatures greater than the critical temperature for data interpretation purposes.

Table 6. Relationships for saturation pressure of CO_2

	Relationship	Ref.	Eq.
$T < T_c$	$P_s = P_c \mathbf{exp}[A(T_r) + wB(T_r)]$ *where* $A(T_r) = 5.92714 - 6.09648T_r^{-1} - 1.28862\mathbf{ln}(T_r) + 0.169347T_r^6$ $B(T_r) = 15.2518 - 15.6875T_r^{-1} - 13.4721\mathbf{ln}(T_r) + 0.43577T_r^6$	(137)	(23)
	$P_s(CO_2, MPa) = -155.4953 + 1.75862T - 6.829149 * 10^{-3}T^2 + 9.231018 * 10^{-6}T^3$	(138)	(24)
$T > T_c$	$P_s = P_c\left(\frac{T}{T_c}\right)^2$	(129)	(25)
	$f_s = P_c\left(\frac{T}{T_c}\right)^t$	(139)	(26)
	$P_s(CO_2, MPa) = 7.382\,\mathbf{exp}\left(9.98144 - {}^{3036.254}\!/_{T}\right)$	(138)	(27)

Figure 13 shows the suggested saturation pressure for CO_2 below and above its critical temperature. Although the saturation pressure has no physical meaning at temperatures above the critical temperature, the suggested saturation pressure relationships have been used for modeling purposes. Good fits have been reported for supercritical adsorption using them.(129,124,140,141)

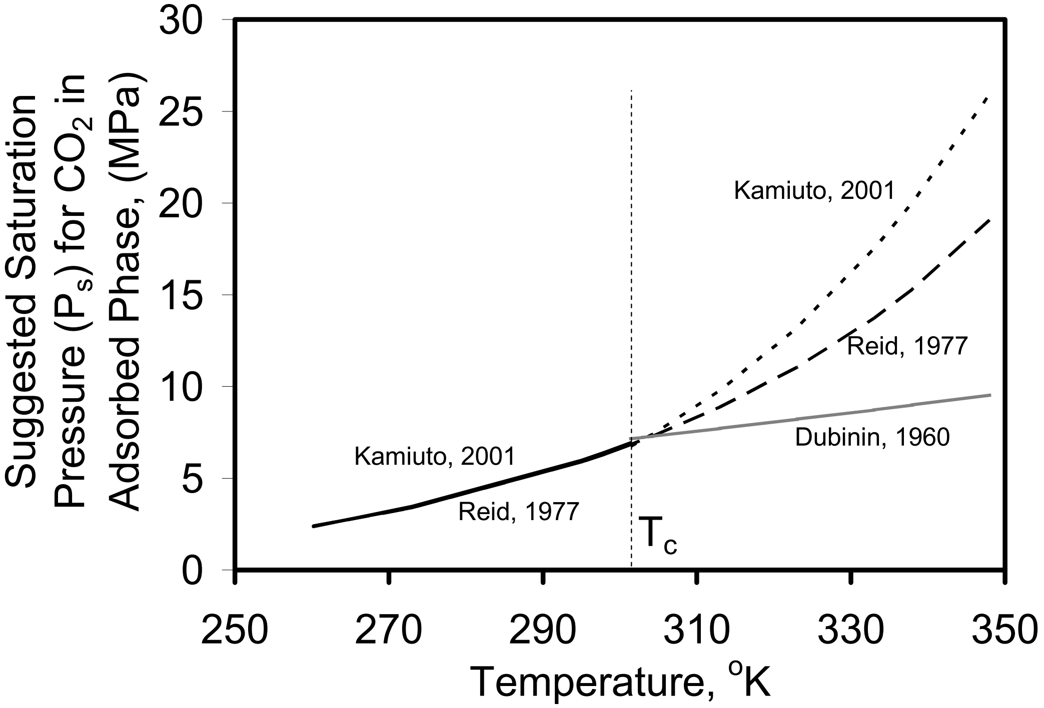

Figure 13. Suggested saturation pressure for CO_2 at below and above its critical temperature

2.2.3 Adsorption of Gases on Coals

A considerable literature is available on the physical adsorption of gases and vapors on microporous adsorbents, especially for activated carbon.(142,143,140) The adsorption/desorption isotherms have been studied for methane,(41,116,45), ethane,(46) hydrogen,(47,48) and other gases as well as their binary mixtures, at elevated temperatures and pressures. Martinez et al.(144) studied the adsorption mechanisms of CO_2 in the micropores of activated anthracite with pre-adsorbed n-nonane. Because n-nonane was retained within pores of different sizes, the adsorption mechanism of CO_2 could be interpreted in the narrow micropores from its adsorption isotherms.

They concluded from these isotherms that the adsorption in narrow micropores with molecular dimensions is a micropore filling process, and produces a curved CO_2 isotherm. The adsorption that occurs in pores larger than two molecular diameters occurs via surface coverage and is associated with a rectilinear isotherm. Clarkson et al.(118) applied the monolayer (Langmuir), multilayer (BET), and the potential (D-R or D-A) theories to the high-temperature, high-pressure (up to 10 MPa) CH_4 adsorption isotherms and low-pressure CO_2 isotherms in order to determine which best represented the experimental data. They found that the three-parameter D-A equation yielded the best fit to the high-pressure CH_4 isotherms. They concluded that one of the postulates of the Langmuir theory, the assumption of the energetically homogenous adsorption surface, does not apply to coal. They also concluded that, although the adsorption potential theory applies to low-pressure CO_2 isotherms, high-pressure adsorption isotherms of CO_2 needed further testing.

DeGance et al.(145) investigated pure and multicomponent adsorption isotherms of CH_4, N_2 and CO_2 on a wet coal sample under high pressures. They applied a two-dimensional equation of state, (2-D EOS),(146) the ideal adsorbed solution theory (IAS),(147) and an extended Langmuir equation to the data.(148) They concluded that although the EOS approach had some difficulty matching the experimental data for wet coals, the simplicity of the viral EOS made it useful for modeling efforts. Chaback et al.(134) measured the sorption isotherms of N_2, CH_4 and CO_2 on wet bituminous coals at in-situ conditions (46 ^{o}C and pressures up to 11 MPa). They concluded that the Langmuir equation and its extended form satisfactorily represent the adsorption isotherms of both pure components and gas mixtures. They also showed that the relative adsorption capacities of CO_2:CH_4:N_2 are 4:2:1, respectively.

As a matter of fact, there is a good agreement between the Langmuir's monolayer and Dubinin's pore filling models. In 1972, Toda and Toyoda(149) applied the Langmuir and Polanyi-Dubinin equations to the CO_2 on coal adsorption isotherms at 298 K. They found that there was a linear relationship between the monolayer adsorption capacity and the micropore volume as well as between the Langmuir constant, K_1, and the inverse of the Dubinin constant, $1/K_6$. The correlation indicated that the monolayer adsorption capacity was smaller than the micropore capacity by approximately 60%.

2.2.4 Adsorption Capacity and Stability of CO_2 on Coal

2.2.4.1 Low-temperature, low-pressure adsorption of CO_2: Adsorption of CO_2 on coals has been studied extensively since 1900s,(150) however, many of these studies have been performed at low pressures (usually below atmospheric) and often low temperatures (-78 ^oC) in order to estimate the surface area(29,30,106) and micropore structure(151,31,152,153) of coals. Although these low-pressure data have provided information, which is still relevant to today's sequestration projects, they do not properly represent the high pressures (up to 30 MPa) and high temperatures (up to 55 ^oC) environment for coal seam sequestration processes.(6) Under these conditions, CO_2 may be in gas, liquid, or supercritical phase ($T_c =$ 31.1 ^oC and $P_c = 7.38$ MPa) depending on the change in pressure during the adsorption-desorption processes in the coal seam. Unfortunately, high-pressure, high-temperature CO_2 adsorption data on coal are limited and require additional investigation.

2.2.4.2 Adsorption of CO_2 under Geological Conditions: Studies of the high-pressure adsorption/desorption isotherms of CO_2 is important for determining the coals ultimate CO_2 sequestration capacity, especially under in-seam conditions. The information provided by the adsorption/desorption isotherms is used as one of the primary inputs to the simulations of coalbed sequestration processes. Such adsorption isotherms are usually obtained by one of the commonly used methods, including gravimetric,(133) manometric (volumetric),(46,154) and chromatographic(155) methods. In the gravimetric technique, the adsorption isotherms are constructed by measuring the weight change recorded by a microbalance, after accounting for the buoyancy. In the manometric technique, the adsorption isotherms are obtained by calculating the adsorbed amount of gas from an appropriate gas equation at each equilibrium pressure. In the chromatographic method, the adsorption isotherm can be obtained by frontal analysis of the breakthrough curves. It should be mentioned that the accuracy of each method strongly depends on the careful design of the measurement apparatus and experimental conditions.

Although the adsorption/desorption isotherms have been studied extensively for CH_4 and other gases at elevated temperatures and pressures, a comprehensive study of CO_2 isotherms on coals under in-situ conditions is scarce, although several studies have appeared in the literature lately.(50,51,52,53) Clarkson and Bustin(51) studied the low- and high-pressure adsorption isotherm of CO_2 and CH_4 on four dried bituminous coals of the Cretaceous Gates Formation at pressures up to 5 MPa. They concluded that the CO_2 isotherms have a slight inflection at high-pressure, possibly as a result of multilayer adsorption. They also stated that the isotherm data are better fitted by the Dubinin-Astakhov (D-A) equation. However, coal swelling, a phenomenon that occurs when coal is contacted with adsorbing gases and vapors,(113,36,101) was not considered and could result in such an inflection in adsorption isotherms at higher pressures. As a matter of fact, as will be shown in section 4.3, change in the accessible pore volume in the coal gives rise to such an inflection, especially at higher pressures.(156) Therefore, the adsorption capacity of coals obtained in the presence of volume effects could be inaccurate.

2.2.5 Factors affecting the coal adsorption capacity and CO_2 stability

The adsorption capacity of coal and the stability of the adsorbed CO_2 can be affected by a number of factors, including those related to coal composition, i.e. rank and moisture content of the coal, and those related to the environmental variables, i.e. temperature, pressure, change in pH, and underground water floods through the coal seam. The sorption behavior of coal and the effect of temperature, moisture content, and particle size on sorption capacity have been investigated for CH_4 and comprehensive reviews are available in the literature.(41,116,45) Here, some of the parameters that can affect the adsorption capacity and the stability of the adsorbed CO_2 are summarized:

1. Coal Rank: Coal contains a wide variety of organic and mineral matters in a complex, porous, three-dimensional network, which varies from one coal deposit to another and from one location to another within the same seam. The general belief is that the CH_4 adsorption capacity of coal increases with increasing coal rank. However, Bustin and Clarkson(116) have shown that there was no or little correlation between coal rank and CH_4 adsorption capacity on the coal globally although there were general trends with rank and composition in particular basins. The organic portion of the coal is thought to capture CO_2 via surface adsorption, pore filling, and solid solution.(24) Less recognized is the possibility that the mineral matters present in the coal may assist via mineral carbonate formation. Thus, the nature of the coal seam itself is an important variable to be considered in the coal seam sequestration of CO_2.

2. Temperature: In the absence of external factors, underground temperature tends to be constant, but increases with depth. Ruppel et al.(46) showed that there was a significant decrease in the CH_4 adsorption with increasing temperature from 0 to 50 ^oC. Levy et al.(41) showed a linear decrease in the methane adsorption capacity on moisture equilibrated Boven Basin coal with increasing temperature. The average degrease in capacity was 0.12 mL/g-coal for each degree Celsius increase in temperature. This corresponds to a 0.45 mmole decrease in CH_4 adsorption per g-coal for 100 ^oC rise in temperature. Because the adsorption of CO_2 is exothermic,(157) it will provide a heat source, at least during the active pumping phase of sequestration. Also, some sequestration scenarios would provide additional heating mechanisms, such as by the dissolution of co-sequestered acid gases (SO_x, NO_x) or by reaction with residual oxygen in the flue gas.(42) Therefore, temperature is an important parameter to affect the adsorption capacity of coals.

3. Moisture Content: Deep coal seams are naturally wet and will undergo recharge from surface water more rapidly during the sequestration as a result of drilling operations, fracturing of the coal bed and over-lying strata, and the injection of flue gas which may contain residual water of combustion.(158) Thus, an aqueous phase will be present and will vary in composition according to its source and the nature of the coal bed and the surrounding minerals with which it is in contact. Joubert et al.(39) studied the effect of moisture on the sorption isotherm of CH_4 on a bituminous coal at a temperature of 30 ^{o}C and pressures up to 6.1 MPa. For all rank of coals studied, the adsorbed amount of CH_4 decreased with the moisture content up to a critical value which is characteristics of the coal type. Moisture in excess of the critical value appeared to have no effect on the methane sorption. The methane adsorption in the presence of moisture content, m, less than the critical moisture content, m_c, is represented by an empirical equation, Eq.(28),(41) developed originally by Ettinger at al.(150):

$$\frac{n_w}{n_d} = \frac{1}{1 + A\,m} \tag{28}$$

where n_{w} and n_d are the adsorbed amount of methane adsorbed on wet and fully dried coal at any pressure, respectively, and A is a coefficient. The magnitude of the coefficient (A) was not consistent for different coals as reported, for instance, to be 0.23 by Joubert et al.(39), 0.39 by Levy et al.(41), 0.64 and 0.84 by Gruneklee and Peters(39), and 0.31 by Ettinger et al.(150). Joubert et al.(39) also found that there was no further reduction in CH_4 adsorption when the moisture content was greater than m_c. Furthermore, the coefficient was also shown to be pressure dependent decreased from 0.28 to 0.19 as pressure increased from 1 MPa to 6 MPa.(40) Nevertheless, data to show the coefficient for CO_2 is limited.

4. Change in pH: The change of pH can affect the coal and CO_2 sequestration process in coal seams in several ways. A decrease of pH can dissolve and extract mineral matter associated with the coal.(159,160) Change in pH can alter the surface charge of the coal,(161) which, in turn, can affect the intermolecular interactions responsible for the 3-dimentional structure of the macromolecular network.(162) Because the aperture size of a pore in the coal is important for gases to access within the pores and because the maximum adsorbed amount is related to the pore volume,(93) all of these may affect the storage capacity of the coal and the stability of the adsorbed CO_2.

Injected CO_2 into a coal seam can decrease the pH and dissolves and extracts the mineral matter. Mineral matter in coal takes two forms: inherent mineral matter and extraneous mineral matter. Inherent mineral matter is found in relatively minor amounts in the coal.(163) These minerals, once present as nutrients in the original plant matter, were trapped in microscopic amounts during the coalification process and, as a result, have become part of the organic matrix.(164) The inherent mineral matter is generally found embedded within the micropore system of the coal, associated with the organic matrix, and cannot be easily removed.(165) The second type of mineral matter is referred to as extraneous mineral matter. These minerals have entered the seam via aqueous seepage during the coalification process.(12) Because they tend to fill larger cleats and fissures, extraneous deposits can range in size from a few hundred microns to several cubic feet.(166) The bulk of extraneous mineral matter is composed mainly of pyrite, calcite, quartz, and aluminosilicate clays.(166) With the possible exception of quartz, these minerals are affected by either acidic or basic surroundings through dissolution or ion-exchange. Calcite is particularly sensitive to acidic aqueous surroundings.

In addition to the extraction of mineral matter, changes in pH can alter the overall surface charge of coals.(161) It is well known that solids in contact with solutions with a pH above their isoelectric point acquire a net negative surface charge; those in contact with solutions with a pH below their isoelectric point acquire a net positive surface charge. The isoelectric point was reported to be about pH $\approx$ 3.8 for coals.(161) The isoelectric point for demineralized coal is lower than that of its mineral matter.(161) Consequently, the untreated coal in the presence of mineral matter is more hydrophilic than the carbonious coal. The CO_2 sequestration in water-saturated coal seam will certainly decrease the pH in the sequestration environment. Thus, the acidic pH would replace the carboxylic salts with the $R\text{-}CO_2H$ form.(167) Similarly, less reactive, and less common, phenolic groups in the coal matrix would be affected, transforming Ar-O-M to Ar-O-H. Ubiquitous nitrogen-containing groups, which are almost always found in heterocyclic forms, usually take the form of basic pyridine groups in higher-rank coals, and acidic pyrrole derivatives in lower ranks.(168) Sulfur also plays a role in the organic matrix; however, most of it is in the form of –SH groups.(166) Nitrogen and organic sulfur groups typically do not interact with mineral matter in coal and therefore cannot be removed by acid or base treatment although their chemical attributes can be changed. The properties of surface of a coal may change due to inherent surface charge and the chemical composition of coal. The three dimensional structure of coal is mainly maintained by the covalent bonding as well as the secondary forces such as hydrogen bonding, van der Waals interaction, electrostatic forces, and ionic interactions.(169,170) Disturbances in such interactions may alter the 3-D structure of coals.

The sudden decrease in pH during the CO_2 injection may enhance the CO_2 storage. For instance, removal of inorganic matter from coals by acid treatment brings about random and significant changes in surface areas measured by adsorption of N_2 and CO_2.(171) Changes in surface areas of raw coals have been attributed to physical removal of inorganic matter from the aperture cavity system.(171) It has been documented that CO_2 adsorption on demineralized coal increases proportionally to the concentration of carboxylic groups present on the coal's surface.(172) Nevertheless, studies of the effects of acidic and basic solutions on coal have frequently focused on the demineralization of the coals.(162,173,174,159) Most of these investigations have involved leaching the mineral matter in coal with concentrated acid and base solutions at elevated temperatures. Results gathered from these studies are of questionable applicability to carbon sequestration science because the coals have been exposed to more extreme pH values than they would be in a natural sequestration setting. Additional studies, which attempt to simulate environmental levels of acid and base, should better reflect the chemistry under *in situ* conditions.

5. Pre-adsorbed Components: Depending on the capture technology, the gas stream may be nearly pure CO_2, combustion gas, or something in between. Gases, such as hydrogen, methane, ethane, and higher hydrocarbons may be present in the coal seam(175) and act to inhibit or enhance the CO_2 sequestration. In the case of a gassy coal seam, it may be advantageous to displace and capture CH_4 as a profit-making part of the operation.(176) This displacement may be enhanced by secondary combustion gases, such as SO_x and NO_x. The composition of the post sequestration gas or liquid may change with time. Even slow reactions can become important over geologic-sequestration time scales. Also, microbes have an uncanny ability to adapt to many environments and are known to populate even deep geologic strata, at least to 9000 feet below the surface.(177) Under oxic conditions, gases such as SO_x, NO_x, and carbon monoxide (CO) may be produced either chemically or biologically. Under anoxic conditions, CH_4 and hydrogen sulfide (H_2S) may be produced by anaerobic microbes. These gases may displace CO_2 and thus limit the durability of the sequestration.

6. Adsorption at High-Pressures: Historically, the adsorption of CO_2 on coal has been used to estimate surface areas(29,30) and micropore structure.(31) Usually, these measurements have been conducted under low pressures (usually below atmospheric) and low temperatures (-78 °C).(30) Although the information obtained from such measurements is important to current sequestration efforts, low-pressure, low-temperature adsorption isotherm data do not represent geologic, in-seam conditions. On the other hand, the high-pressure adsorption isotherms of CO_2 on coal are scarce and have not been extensively studied. Krooss et al.(56) has recently reported CH_4 and CO_2 adsorption isotherms on dry and moisture-equilibrated Pennsylvanian coals at temperatures of 40, 60, and 80 °C and at pressures up to 20 MPa. From their measurements, it is clearly shown that the CH_4 adsorption isotherms are Langmuir-like and did not show any discrepancies at pressures up to 20 MPa. On the other hand, the CO_2 adsorption isotherms showed a very unusual behavior. They reported that the excess and absolute adsorption isotherms of CO_2 increased first monotonically as pressure increased up to 8 MPa, then, at pressures between 8 and 10 MPa, the excess adsorbed amount suddenly increased, and then, decreased to even negative excess adsorption values, and then, at pressures higher than 10 MPa, the excess adsorbed amount showed an increasing trend. Regrettably, they couldn't compare their high pressure adsorption isotherm data with the literature due to the lack of high pressure CO_2 adsorption isotherm data on coals, except the Hall et al.'s work.(54) They concluded that the unusual shape of the high pressure adsorption isotherm of CO_2 is due to the voluminous adsorbed phase at high pressures, and/or, to swelling of the coal matrix. Nonetheless, the "negative absolute adsorbed amount" has no meaning.

The adsorption isotherms of CO_2 on coals at high pressures are different. For instance, for a rigid solid, the measured adsorbed amount generally increases monotonically with pressure at low-pressures, and then, decreases as the pressure further increases, exhibiting a maximum. The adsorption of CO_2 on activated carbon is an example.(178,133) On the other hand, the adsorption isotherms of, not only CO_2,(32) but also H_2O,(179) CH_3OH,(179) and organic vapors(35,33) on coals showed monotonically increasing trend and exhibited almost a rectilinear shape. The adsorption and desorption isotherms of these adsorbates typically show hysteresis(35) which was related to coal swelling. Therefore, there is a need for an adsorption isotherm model to account the noticeable volume change for the evaluation of the high-pressure adsorption isotherm data on coals.

7. Coal Swelling: Coal swelling upon adsorption of gases or liquid solvents is a well-known phenomenon.(36,101) However, the adsorption capacities of coals are usually obtained by fitting the experimental data to one of the adsorption equations such as the Langmuir, Brunauer, Emmett and Teller (BET), Dubinin-Radushkevich (D-R), and Dubinin-Astakhov (D-A), none of which account for the coal swelling. In order to extract valuable information from the adsorption isotherm data, it is necessary to delineate the effect of coal swelling on the adsorption isotherms and adsorption capacity of coals.

The technical feasibility of CO_2 sequestration in coal seams can be assessed by defining the parameters that affect both the capacity and stability of the adsorbed CO_2. The effect of these parameters on the adsorption of CO_2 under in-seam conditions, however, needs further investigation due to lack of sufficient data.

2.2.6 Coal Structural Changes upon CO_2 Adsorption

Astakhov and Shirochin(115) studied the weakening of coals during their interaction with CO_2 and CH_4 gases. They introduced these two gases into a sample chamber at a temperature higher than the critical temperatures of the gases. After equilibrium had been established, they cooled the chamber quasi-statistically to a temperature below the critical temperature of the adsorbates, and continuously monitored the deformation of the sample. They estimated the compressive strength of the samples after they isothermally released the gas from the sample cell. The compressive strength of the anthracite coal starts to noticeably decrease at CO_2 pressures of 2.5 MPa and methane pressures of 1.5 MPa. They suggested that the adsorbed phase in the pores condenses due to the force field below the critical temperature of the adsorbate and the liquid inclusion which weakens the coal by disintegrating its three dimensional structure.

Khan(19) studied the thermoplastic properties of a Lower Kittanning coal in a dilatometer in both helium and CO_2 atmospheres. The softening temperature for this coal is determined to be 693 K in He and it remains almost constant when the helium pressure is increased because helium does not interact with the coal. But, when CO_2 is introduced into the dilatometer, the softening temperature is dramatically reduced as the pressure exceeded 3.0 MPa and at a pressure of 5.5 MPa, the softening temperature decreases to 328 K. From this behavior, the authors concluded that CO_2 acted as a plasticizer, dissolving in the coal and lowered its softening temperature.(24)

2.3 TRANSPORT PHENOMENA IN COAL SEAMS

Coalbeds are naturally fractured porous solid, which are generally characterized by dual porosity, containing both micropore and macropore systems. The microporosity of coal is mainly buried within the macromolecular network of the coal matrix. The macroporosity of a coal seam consists of naturally occurring cracks, called cleats.(12) While the storage of gas is dominated by adsorption within micropores, the cleat system provides the conduit for fluid flow through the formation.(14) The following questions need to be addressed to ensure a safe, cost-effective sequestration of large volumes of CO_2 in coal seams:

- How much CO_2 can be injected into a candidate coal seam?
- How would the injected CO_2 distribute along the coal seam?
- What would the injection rate be?
- How would the coal swelling influence the injection process?, and
- How stable is the adsorbed CO_2 during the post injection periods?

Effective modeling of the sequestration process is essential both for an understanding of the complex interactions which occur during CO_2 storage and methane production, and for predicting of the economic viability of sequestration under the particular conditions of a given site. Many commercial and research numerical models have been developed to simulate the coalbed methane (CBM) recovery processes.(180,181,182,183,184,185) In a three part survey, King and

Ertekin(180,181,182,183) reviewed the coalbed methane models which had been developed and published. They classified the models as empirical, equilibrium, and non-equilibrium sorption models. The equilibrium models assume that the adsorption and desorption processes are so rapid that the kinetics of the process is negligible. In non-equilibrium models, the adsorption and desorption processes are time dependent and the movement of the distributing component into and out of the coal matrix is retarded. These models took into account many of the factors important to coal seam sequestration including the dual porosity nature of coalbeds; multiphase Darcy flow of gas and water in the natural fracture system; single component gas diffusion in the natural fracture system; adsorption and desorption processes of a single and multi gas components on the coal surface; and coal matrix shrinkage due to gas desorption.

Sequestration of CO_2 in coal seams with concomitant recovery of coalbed methane is a new technology that has been practiced in a few places but it is not well developed. Off-the-shelf technology is available to perform CO_2-enhanced coalbed methane recovery/sequestration (CO_2-ECBM/sequestration). For instance, Burlington Resources have been performing CO_2-ECBM production in deep unmineable coal seams in the San Juan Basin in New Mexico since 1996.(57) Very little information has been available from this or similar projects.(186) Also, as a matter of fact what happens when CO_2 is injected into a coal seam is not yet understood. Here, a brief review on general reservoir characteristics, forms of gas storage, transport mechanisms in a coal seam, and modeling methodology, is given in the following.

2.3.1 Reservoir Characteristics of Coal Seams

The coal seams have adual porosity nature.(187) The microporosity of coal is contained within the macromolecular network of the coal matrix and has been previously discussed in Section 2.1.3. Briefly, high-resolution transmission electron microscopy (HRTEM)(85,84) and wide-angle X-ray scattering (WAXRS)(86) measurements demonstrated that some coal matrices have a layered structure of covalently linked polycyclic aromatic units.(83) The distance between the layers of the macromolecular units is about 3.5- 4.1 Å. This spacing is thought to be responsible for most of the porosity in coal matrix and for the restricted flow associated with the coal pores. However, other measurement techniques which use different molecular probes report different pore sizes, possibly, because of the pseudo polymeric nature of the coal. For instance, ^{129}Xe-NMR(88,188) accounts an appreciable fraction of the pores in coals to sizes of 5.2-6.7 Å. The pore sizes estimated by CO_2 adsorption and ^{1}H-NMR of pore water provide even larger pore sizes, 13-14 Å(90) and 22-28 Å(91), respectively. It appears that micropore sizes are not a unique property of a coal but vary with probe used. Because of the dimensions of the micropores, water in the micropore system was generally assumed to be immobile in simulators.(189)

The macroporosity of a coal seam consists of naturally occurring cracks, called cleats.(12) The characteristics and origins of the cleat structure of coal have been reviewed by Laubach et al.(190) There are mainly two types of cleats in coal beds: face cleat and butt cleat. These are primary and secondary avenues, respectively for gas and water flow in coal seam The two are commonly mutually orthogonal, and essentially perpendicular to the bedding surfaces.(191) The face cleat is laterally extensive, vertical, and continuous throughout the seam.

The butt cleat is also vertical, and in most cases discontinuous, ending with an intersection at the face cleat, generally with a right angle. As evidenced by SEM studies, coals also contain a range of microstructures between the micropores and the cleat system consisting of a variety of shapes and sizes.(13) While the storage of gas is dominated by adsorption within micropores, the cleat system provides the conduit for mass transfer through the formation.(14)

Coal cleats are characterized by their height, length, aperture, and connectivity, where permeability is dependent on. It should be mentioned that data on cleat characteristics are very limited and also vary from seam to seam. Here, some of the definitions are summarized for cleats: The *length* is defined as the dimension parallel to the cleat surface and parallel to bedding; *height* is the dimension parallel to the cleat surface and perpendicular to bedding; *aperture* is the dimension perpendicular to fracture surface; and *spacing* between the same set of two cleats is the distance between them at right angles to cleat surface.(190)

Estimates show that the length of cleat pathways varies from several centimeters to up to several meters.(190) Butt cleat length generally intersects at the face cleat and thus is limited with face cleat spacing.(190) Face and butt cleats are likely to cut the coal into rhombus- or cube-shaped coal matrix blocks.(192) Su et al.(192) reported that the cleat length in North China is commonly less than 10 m; the height is less than 30 cm; and the cleat apertures range from 0.001 to 8 mm. The microscopic examination of coal samples showed that the cleat aperture varies from 0.001 to 20 mm.(13) However, because cleat apertures may change as effective stress is altered in coalbeds, few reliable data on cleat apertures are available in the subsurface. The parallel-plate fracture permeability model showed that the cleat apertures range from 3 to

40 μm.(190) Karacan and Okandan(193) studied the fracture system in two medium volatile and one high volatile bituminous coals from Zonguldak Basin of Northwestern Turkey employing X-ray computerized tomography (CT), light microscopy image analysis, and scanning electron microscopy (SEM) analysis. They reported aperture sizes from 10 to 60 μm for cleats and from 2 to 10 μm for microfractures.

Cleat spacing is on the order of centimeters and is known to be affected by coal rank, ash content, and bed thickness. Cleat spacing generally decreases with increasing coal rank from bituminous to anthracite coal; coals with higher ash content show larger cleat spacing; and cleat spacing generally decreases with decreasing layer thickness. The rank dependent cleat spacing of North American coals was reported by Law (1993)(194). Ash content was not reported although ash content varies among coals and affects cleat spacing. He showed that the spacing of face cleats ranges from 22 cm in lignites and 0.2 cm in anthracites. The spacing for butt cleats also shows similar trend ranges from 20 cm in lignite to about 0.2 cm in anthracite. The average face and butt cleat spacings of a high volatile bituminous coal (Average vitrinite reflectance $\%R_o$ = 0.7) were also reported by Massarotto et al.(195) as 1.37 cm and 1.36 cm and the mean unstressed apertures were 0.246 mm and 0.212 mm, respectively.

Figure 14 shows the relationship between cleat spacing and aperture size from Northeast Blanco Unit No.403, San Juan Basin.(190) The plotted spacings represent averages of all measured spacings having a specific aperture measurement. As shown in the figure, the average spacing of the cleats is proportional to aperture size, and the ratio of aperture opening to the spacing is less than 3%. This finding is consistent with the literature as cleat-fracture porosity in coal was estimated to be between 0.5 and 2.5%.(196,197,198)

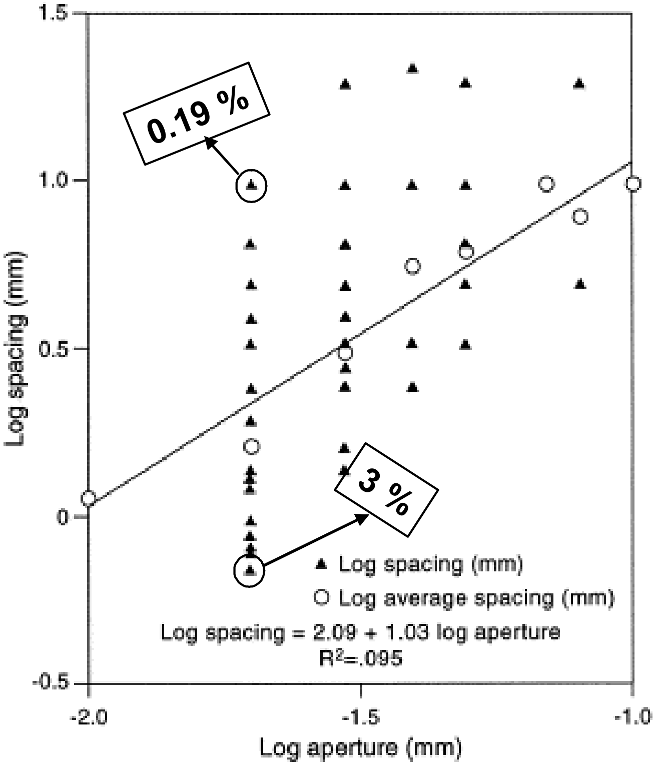

Figure 14. Cleat spacing and aperture data from Northeast Blanco Unit No. 403, San Juan Basin.(190)

2.3.2 Gas Storage in Coal Seams

Coals have been recognized as an important resource for a substantial amount of methane(64) and a reservoir for anthropogenic CO_2 sequestration;(6) both are important greenhouse gases.(9) Gases in coal are primarily composed of CH_4 (98%), CO_2, trace amount of hydrocarbons and other gases. Gases present in coalbeds exist mostly in adsorbed state within the micropores. Gases may also be present in coal seam in other forms such as in free gaseous phase within pores and fractures, and in dissolved form in resident brines to a lesser extent.(199) The storage capacity of the gas in a coal seam can be given as

$$Storage\ Capacity = Adsorbed\ \ Gas + Free\ Gas \tag{29}$$

or

$$Storage \quad Capacity = V_{coal}\rho_{coal}(1-\phi)n^{ads}(1-a-m)+ {}^{V_{coal}\phi S_g}\!\big/_{B_g} \tag{30}$$

where V_{coal} is the volume of the coal, ρ_{coal} is the density of the coal, ϕ is the cleat porosity, n^{ads} is the adsorption estimated from adsorption isotherms at in seam condition, a is the ash content, m is the moisture content, S_g is the gas saturation, and B_g is the formation volume factor for the gas phase. Because the bulk porosity of the coal cleat system is small, and the initial gas saturation in the cleat system is typically low, about 90% of the coalbed methane is stored in adsorbed state in the coal.

2.3.3 Mass Transport in Coal Seams

The transport of gas from the surface of the micropores to the well bore or *vice versa* can be described by the three different processes: Sorption/desorption process, diffusion process, and convection process. Figure 15 shows the schematics of the three transport processes.**(200)**

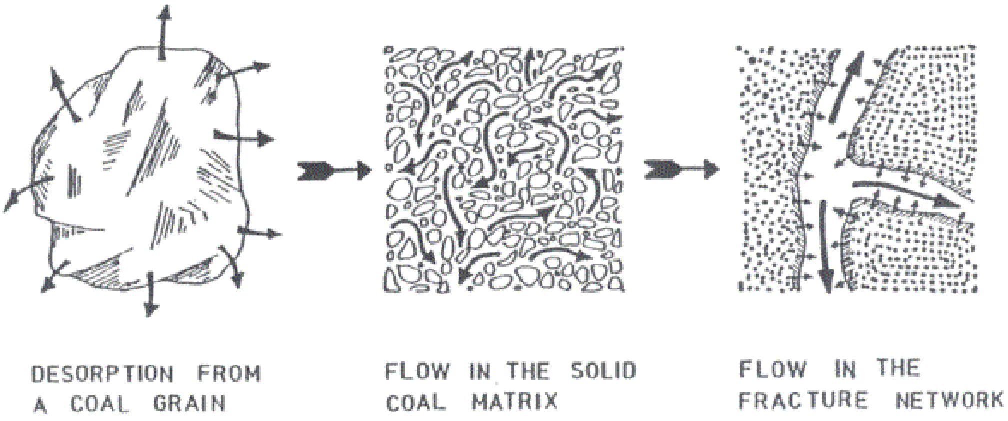

Figure 15. Coal bed methane production by pressure depletion method(200)

It is generally assumed that the adsorbed gas phase is in contact with the surrounding free gas phase and that these two phases are in equilibrium. Because the cleat porosity is assumed to be 100% saturated with brine initially, the pressure decline during the water production forces the adsorbed methane to be desorbed and diffuse through the microporous matrix to the macrospore system. The gas, along with the brine, is then transported through the cleat to the drainage well. In the micropore system, the permeability is negligible and diffusion is the dominant mode of transport.(201) The micropore transport of gas is expressed by the Fick's law of diffusion under the concentration gradient

$$\frac{m_g}{A} = -MD_i \nabla C_i \tag{31}$$

The diffusion coefficients for most coals have been experimentally determined to be between 10^{-7} and 10^{-11} m^2/day.(189,51)

In the fractured system, the gas flow through the cleats to the well bore is a laminar process and obeys Darcy's law.(201) The Darcy's law states that the apparent velocity of a flowing fluid in a porous media is directly proportional to the applied pressure gradient. The proportionality constant is related to the permeability of the medium divided by the viscosity of the fluid, i.e. the gas phase.

$$\frac{q_g}{A} = -\frac{k_g}{\mu_g} \nabla P_g \tag{32}$$

The permeability is a macroscopic property of the porous medium regardless of the flowing fluid. The relationship between the permeability and porosity is

$$\frac{k}{k_o} = \left(\frac{\phi}{\phi_o} \right)^{N_c} \tag{33}$$

where the value of the exponent (N_c) is usually 3 or greater. Due to the natural fracture network in coal seams, both the macropore porosity and permeability are dependent on the effective stress (σ_e)(202)

$$k = k_o \left(e^{-C_p \sigma_e} \right)^3 \tag{34}$$

where C_p is the pore compressibility and the effective stress is defined as the difference between the overburden pressure (σ_{OB}) and gas pressure

$$\sigma_e = \sigma_{OB} - P_g \tag{35}$$

Therefore, an increase in the confining stress or, equivalently, a reduction in the pore pressure causes cleat closure, and thus, a reduction in the permeability. The absolute permeabilities have been attributed to American coals to be in the range from 0.1 to 250 millidarcies (md), for Australian coals from 1 to 10 md, and for European coals ranging from 1 to 50 md.(96) It should be emphasized that the permeability values decrease with the burial depths.

2.3.4 Enhanced Coalbed Methane Production

The natural depletion method has been reported to be inefficient because a maximum recovery of only 30% to 50% of the original gas-in-place can be achieved.(203,204) Reznik et al.(203) conducted a set of experiments injecting CO_2 into large cores of methane- and water-saturated bituminous coals at pressures up to 5.44 MPa in order to simulate enhanced recovery of *in-situ* methane. They showed that CO_2 injection increased the methane recovery by a factor of two to three over that achieved using simple desorption. At high pressures, CO_2 was shown to produce 100% of the methane from the coal core. Puri and Yee(204) performed similar experimental studies using N_2 as the injection fluid. They showed that almost all of the CH_4 adsorbed on the coal could be recovered using N_2 injection.

It has been suggested that the mechanism of CH_4 recovery differs for the two gases. The injection of CO_2 results in CH_4 being displaced by the strongly adsorbing CO_2 whereas N_2, a gas that is less strongly adsorbed than CO_2, causes desorption by simply lowering the partial pressure of CH_4. The adsorption of a mixture of gases is controlled by both the adsorption capacity of the coal and the partial pressure of the gases.(205) When nitrogen is injected into a methane saturated coal seam, it is expected that the nitrogen will reduce the partial pressure of methane by sweeping it from the vicinity of the desorbing surface leading to desorption of more methane. In this manner, thermodynamic equilibrium cannot be reached and methane continues to desorb. For the injection of CO_2, CO_2 is expected both to displace the adsorbed methane and to reduce the partial pressure of the methane in the free gas phase, leading to increased production of methane.

Since 1996, Burlington Resources have conducted a commercial pilot application of CO_2 injection in the Allison production unit of the northern San Juan basin in north-central New Mexico.(57) The significance of the preliminary test results from the Allison unit was summarized as follows:(206)

(1) Injection of CO_2 began in 1995 at a rate of $141*10^3$ Sm^3/day; since then a loss of injectivity has reduced injection rates to about $85*10^3$ Sm^3/day;

(2) A sharp increase in water production was observed immediately and during the initial 6-month period of CO_2 injection; and

(3) Minimal breakthrough of CO_2 during the 5-years of CO_2 injection.

It appears that the reduction in the injection rate could be due to closing of the cleat structure as a result of the coal swelling or to the reduction in relative permeability in the presence of increasing water content in the cleat porosity. Simulators for CO_2 injection should have the ability to handle complicated mechanisms. A better understanding of these process mechanisms both in the field and in the laboratory will lead to improvements in the numerical simulators and in the understanding of the complex processes occurring during the sequestration of CO_2 in coal seams.

The ideal scenario in CO_2 sequestration in coal seams is that when CO_2 is injected into a coal seam it will flow through the coal cleat system and be stored within the coal matrix.(201) The experience gained from CBM production over the last two decades can be employed for an efficient, cost-effective, and continuous CO_2 sequestration in coal seams.(186) It should be emphasized that although CH_4 production from coalbeds has been studied extensively, much remained to be investigated for the CO_2 sequestration in actual unmineable coal mines.

3.0 EXPERIMENTAL

3.1 COAL SAMPLES USED

The interaction of CO_2 with coals was studied under a variety of conditions. Coals were obtained from the Argonne National Laboratory through the Premium Coal Sample Program.(207) Argonne Premium coal samples include representative of most coal types and they are among the most widely studied coals in the world. The full set of eight Argonne Premium coals used includes a lignite (Beulah-Zap), a subbituminous (Wyodak), a high volatile bituminous (Illinois No.6), a medium volatile bituminous (Upper Freeport), a low volatile bituminous (Pocahontas No.3), a liptinite-rich (Blind Canyon), an inertinite-rich (Lewiston-Stockton), and a cooking (Pittsburgh No.8) coal.(208) The Argonne Premium coal samples were selected by the Argonne Lab on the basis of their C, H, S, and O contents as well as their maceral contents and geological age. The proximate and ultimate analyses of the Argonne coals used are shown in Table 7.(207)

Table 7. Proximate and Ultimate Analyses of the Argonne Premium Coal Samples(207)

Coal Sample		Proximate Analysis (wt%)				Ultimate Analysis (wt%, daf)				
Seam	State	Rank	Moisture	Ash[a]	VM[a]	C	H	O	S	N
Pocahontas No.3	VA	Low Vol. Bit.	0.65	4.74	18.48	91.05	4.44	2.47	0.50	1.33
Upper Freeport	PA	Med. Vol. Bit.	1.13	13.03	27.14	85.50	4.70	7.51	0.74	1.55
Pittsburgh No.8	PA	High Vol. Bit.	1.65	9.10	37.20	83.20	5.32	8.83	0.89	1.64
Lewiston-Stockton	WV	High Vol. Bit.	2.42	19.36	29.44	82.58	5.25	9.83	0.65	1.56
Blind Canyon	UT	High Vol. Bit.	4.63	4.49	43.72	80.69	5.76	11.58	0.37	1.57
Illinois No.6	IL	High Vol. Bit.	7.97	14.25	36.86	77.67	5.00	13.51	2.38	1.37
Wyodak-Anderson	WY	Subbit.	28.09	6.31	32.17	75.01	5.35	18.02	0.47	1.12
Beulah-Zap	ND	Lignite	32.24	6.59	30.45	72.94	4.83	20.34	0.70	1.15

[a] dry basis

3.2 SAMPLE PREPARATION AND HANDLING

In all experiments, a 0.6-1.3 g of 150 μm size (-100 mesh) coal samples were used. The sample handling was performed in an inert gas (helium) flushed glove bag under a positive pressure of the inert gas. Because coals rapidly and irreversibly adsorb atmospheric oxygen,(209) efforts were devoted to maintain an oxygen-free environment. Vials of the Argonne Premium coals were opened after they were well-mixed in accordance with the provided mixing instructions.**(207)** Coal samples were removed from the glove bag only after they had been placed in the sample cell and capped. Each sample was dried in-situ at 80 °C for 36 hours before measurements were performed. The volume of the coal samples, and thus, the void volume of the sample cell, was estimated using helium expansion method before the measurement of the adsorption isotherms.

CO_2 and He gases used in the adsorption isotherms were purchased from Valley Co. (Pittsburgh, PA, USA) with a purity of 99.999% and 99.997%, respectively.

3.3 EXPERIMENTAL SETUP

In order to estimate the sorption capacity of CO_2 on coals, a high-pressure manometric gas adsorption apparatus was designed and constructed. A schematic diagram of the high-pressure manometric gas adsorption apparatus is shown in Figure 16. A brief description of the components of the high-pressure manometric gas adsorption apparatus is given in Table 8.

The manometric adsorption apparatus was designed to include four separate reservoirs and sample cells so that the apparatus is capable of collecting adsorption isotherm data for four samples simultaneously. The major advantages of the high-pressure manometric gas adsorption apparatus designed are

1. The size of the sample cell is small, about 6 ml, which is more appropriate for the small sample sizes especially for the Argonne Premium Coals
2. Reaching in equilibrium is fast.
3. The adsorption and desorption isotherms can be measured at pressures up to 20.4 MPa,

4. It can collect the adsorption and desorption isotherms of four different samples simultaneously, and
5. It can be used for either in gas phase or in supercritical phase adsorption and desorption isotherms.

The only disadvantage of using high-pressure manometric gas adsorption apparatus is that the volumetric method cannot measure the adsorption and desorption isotherms in liquid phase.

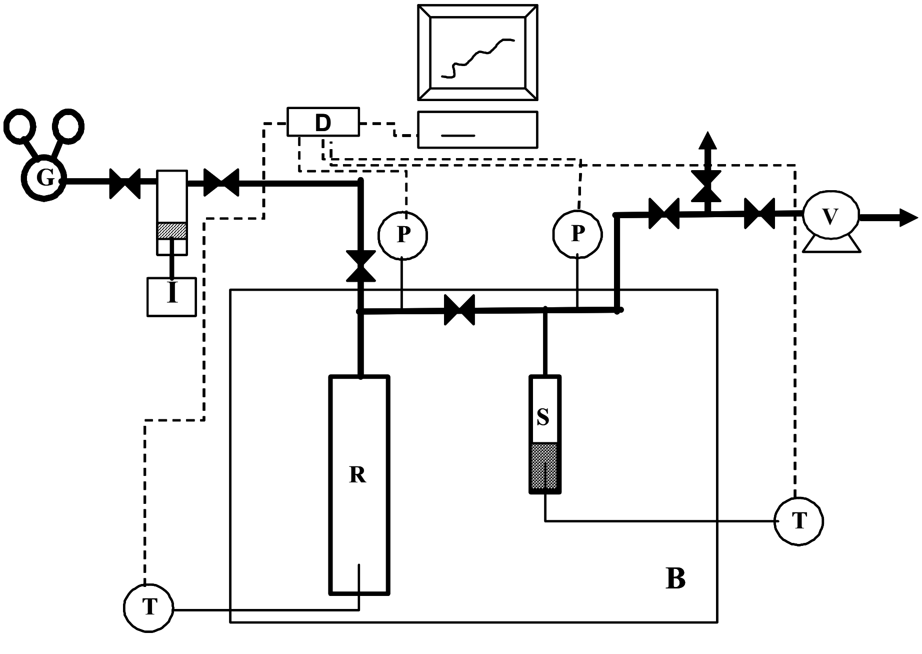

Figure 16. A schematic of the manometric gas adsorption apparatus: G: Gas Cylinder, I: ISCO Syringe Pump, D: Data Aqcuision, R: Reference Cell, S: Sample Cell, P: Pressure Transducer, V: Vacuum Pump T: Thermocouples B: Constant Temperature Water Bath

Table 8. The components and description of the high-pressure manometric gas adsorption apparatus

Components	Description
Gas Cylinders	Two gas cylinders, He and CO_2, were purchased from Valley Co. to the purity of 99.997 and 99.999, respectively.
ISCO Pump	ISCO Syringe pump (Model 500D) was used to pressurize the gas to the desired pressure levels (up to 20.4 MPa).
Tubing and Fittings	A Stainless Steel (SS) 1/8'' and a 1/16'' tubing, SS-reducing unions, SS-Tees, etc. purchased from Swagelok®, were used in construction.
Valves	Valves were two-way SSI valve, purchased from *AllTech, Co*. These valves were designed for high pressure, low volume systems and they are resistant to solvents and corrosion. The pressure rating for these valves was up to 68 MPa.
Reference and Sample Cells	Reference and sample cells were constructed from a ½" SS-tubing rated at 34 MPa, purchased from Swagelok®. The tubing was cut into 12 and 6 cm-pieces to construct the reference and sample cells, respectively. The bottom of each piece was capped with a ½" SS-cap, purchased from Swagelok®. The other end of each piece was capped with a ½" to 1/16" SS-reducing union. The reducing union was equipped with a 1μm frit.
Pressure Transducers	A 30 mV output gage pressure transducers (PX300), purchased from Omega, were used in pressure measurements. The pressure transducers have an excitation of 10 Vdc (5 to 15 Vdc limits) and output of 3 mV/V ratio metric 30 mV ±1mV at 10V. Operating temperature for the pressure transducers were between 0 to 160 °F (-18 to 71 °C). Gage type of the pressure transducers was stainless steel diaphragm with silicone oil filled semiconductor sensor. Quoted full-scale accuracy of the transducers was 0.25%FS.
Data Acquisition	The data acquisition was performed by a computer using an *InstruNet* A/D box and *iNet100-HC* board, both purchased from Omega, with a software package.
Water Bath	The constant temperature water bath was purchased from NesLab, model RTE 111, accurate to ± 0.1 ^{o}C.
Vacuum Pump	A Vacuum pump, *HayVac-2*, was purchased from HayVac products Co.

Details of procedures for the characterization of the experimental setup and for the measurement of the adsorption and desorption isotherms of CO_2 on coals are given in Appendix B.

3.4 EXPERIMENTAL METHODS

3.4.1 Drying of Coal Samples

Because the adsorption capacity and other properties such as the surface area, pore size, density, and porosity for coals could be affected by the presence of moisture within the coal sample, we dried the coal samples before the measurements, unless otherwise is indicated. After coal samples were placed in the sample cell and capped in an oxygen-free glove bag, each sample was dried under vacuum in-situ at 80 ^{o}C for 36 hours before the measurements were performed.

3.4.2 Estimation of the Void Volume in the Sample Cell

The empty and void volumes before and after the sample was placed in the sample cell, respectively, were estimated by the helium expansion method as described in Appendix B.

3.4.3 Measurement of CO_2 Adsorption Isotherms

The reservoir cell was first pressurized with CO_2. Ten minutes were allowed to achieve thermal equilibrium although a stable temperature reading was achieved in about 3 minutes. Then, a portion of the gas was transferred from the reference cell into the sample cell. Pressure and temperature were monitored in both cells to verify thermal and kinetic equilibration. In initial tests of up to 20 hrs, it was found that 20-30 min was sufficient for the adsorption of CO_2 to reach equilibrium. The amount of CO_2 in gas phase within both the reference and sample cell were calculated using the real gas law, which accounts for the gas compressibility. The compressibility factor for CO_2 was calculated using Span and Wagner equation of state(210) as summarized in detail in Appendix A. The excess adsorbed amount was calculated from the mass balance between the reference and sample cells at each gas expansion step using Eq.(36)

$$\Delta n^{ex} = \left(\frac{P_{R_i}}{z_{R_i}} - \frac{P_{R_f}}{z_{R_f}} \right) \frac{V_R}{wRT} - \left(\frac{P_{S_f}}{z_{S_f}} - \frac{P_{S_i}}{z_{S_i}} \right) \frac{V_o}{wRT} \tag{36}$$

where the indices, *i* and *f*, represent the values before and after the gas expansion, the indices, *R* and *S,* represent the reference and sample cells, respectively, *P* is pressure, *z* is compressibility factor, V_R and V_o are the volume of reference cell and the void volume in the sample cell, respectively, *w* is the weight of the sample, *R* is the universal gas constant, and *T* is temperature.

The above procedure was repeated incrementally for increasing pressures of gas. Finally, the estimate of the total amount of excess adsorbed gas, n^{ex}, at the end of the j^{th} step is determined from Eq.(37)

$$n^{ex} = \Delta n_1^{ex} + \Delta n_2^{ex} + \Delta n_3^{ex} + \cdots\cdots + \Delta n_j^{ex} \qquad (37)$$

The adsorption isotherms were plotted as the total excess amount of CO_2 adsorbed versus the measured equilibrium pressure.

3.4.4 Measurement of Densities of the As-Received and Dried Argonne Premium Coals

The densities of as-received and dried Argonne Premium coals were measured by helium displacement method before introducing CO_2. A known amount of coal sample was placed within the sample chamber in the volumetric apparatus and degassed under vacuum for 10 to 20 minutes in order to evacuate any preadsorbed gases. Then, the density of the coal samples were estimated at 22 ^{o}C by helium displacement method. The moisture content of each sample was estimated after completing the density (or void volume) and CO_2 adsorption isotherm measurements at 22 ^{o}C. The same procedure was repeated for the dried coal samples. Briefly, the Argonne Premium coal samples were placed in the sample cell of the volumetric apparatus and dried at 80 ^{o}C under vacuum for 36 hours. Then, the density of the dried coal samples were estimated at 22 ^{o}C by helium displacement method.

3.4.5 Determination of the Moisture Content of the Coals

The moisture content of the coal samples was estimated from Thermal Gravimetric Analysis (TGA) purchased from TA Instruments. About 30 mg of coal sample was loaded in the weighting pan. The pan automatically loaded into the furnace and the temperature ramp was run up to the desired temperature, 105 ^{o}C. The inert gas used to carry out the evaporated water was nitrogen at a pressure of 0.14 MPa. The weight change was monitored up to 60 min at 105 ^{o}C. The moisture content was calculated from the weight change of the sample as

$$Moisture\ \% = \frac{w_1 - w_2}{w_1} \cdot 100 \tag{38}$$

where w_1 and w_2 is the initial and final weights of the coal sample in the weighting pan, respectively.

3.4.6 pH Treatment of Coals

Two acid solutions were prepared by diluting 1.0 and 5.0 ml portions of ~36 N H_2SO_4 with 125.0 ml of de-ionized and de-aerated water. Similarly, two NaOH solutions were prepared by diluting 1.0 and 5.0 ml portions of 50 wt % NaOH solution with 125.0 ml of de-ionized water. The coal samples were treated in the weak acid, neutral, and weak base solutions as shown in Figure 17.

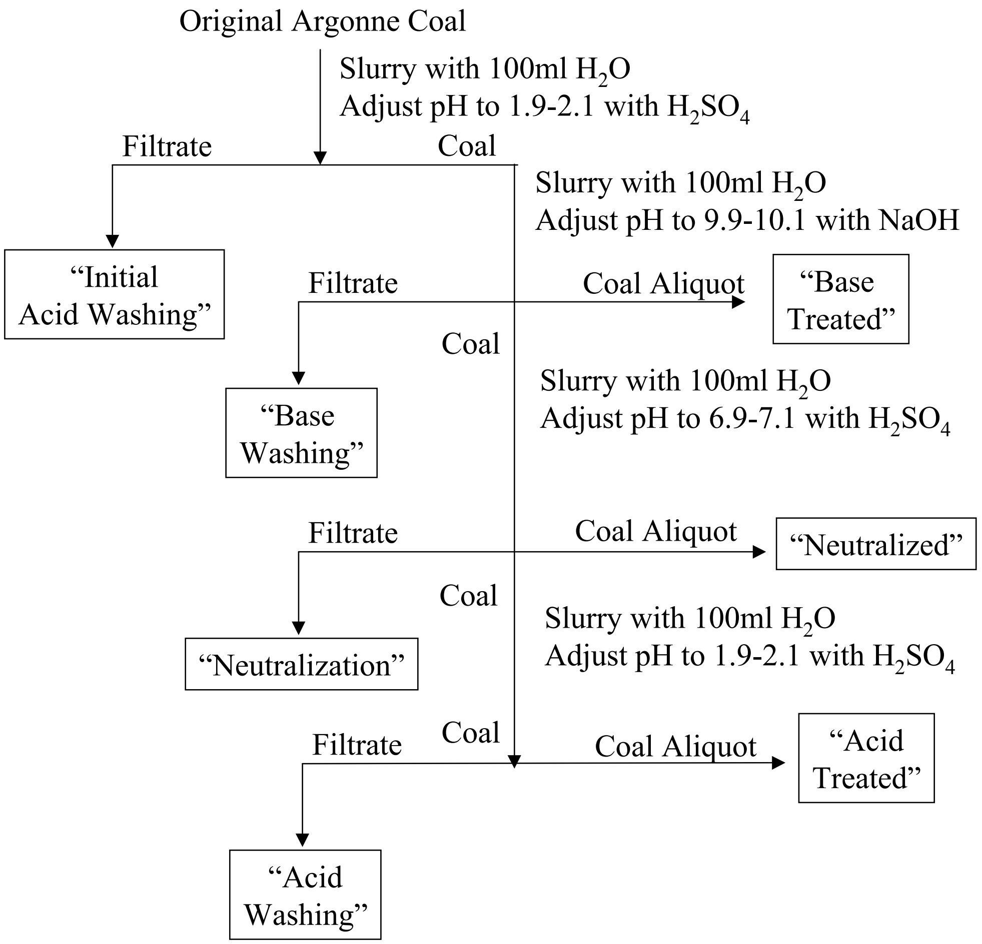

Figure 17. Schematic showing the preparation of the leached coal samples

3.4.6.1 Initial Acid Treatment: Each coal sample was added to a 100 ml of de-ionized water (resistivity 18.2 MΩ) and magnetically stirred to form a slurry. The slurry was then titrated to an equilibrium pH range of 1.9 – 2.1 with H_2SO_4 solution delivered in 1.0-ml increments with an auto pipette at room temperature. A more concentrated acid was used initially then a dilute acid was used as the desired end point approached. The pH was measured frequently using an Orion Ross Ag/AgCl electrode, and the final two readings were normally several hours apart to ensure complete equilibration. The acid-washed coal was vacuum filtered, using sterile 45 μm cellulose nitrate filters. The filtrate was saved for later analysis.

3.4.6.2 Base Treatment: The coal was transferred to a clean beaker, where it was again slurried with 100 ml of de-ionized water. The slurry was then titrated to an equilibrium pH range of 9.90 - 10.1 with NaOH solutions delivered in 1.0ml increments with an auto pipette at room temperature. A more concentrated base was used initially then a dilute base was used as the desired end point approached. Slow reaction times, especially for the lower-rank coals, often necessitated several days to achieve complete equilibration. The coal was vacuum filtered, and allowed to dry under the inert gas atmosphere for about 4 hours and approximately one-third of the coal was reserved for measurements as the "Base-Treated" coal.

3.4.6.3 Neutralization: The remainder of the base-treated coal was slurried with 100 ml of de-ionized water in a clean beaker. The slurry was neutralized by titrating with the acid solutions to attain an equilibrium pH in the range of 6.9-7.1. Because the previous washings had removed much of the buffering capacity, back titrations with NaOH were sometimes necessary to achieve equilibrium in this pH range. The lower buffering capacity also resulted in a faster equilibration time. After treatment, the coal was vacuum filtered and allowed to partially dry. Approximately half of the coal samples were reserved as the "Neutralized" coal sample.

3.4.6.4 Acid Treatment: The remaining coal sample was slurried with 100 ml of de-ionized water in a clean beaker. The slurry was then titrated to an equilibrium pH in the range of 1.9 - 2.1

with H_2SO_4 solutions delivered in 1.0-ml increments with an auto pipette at room temperature. The coal was vacuum filtered, and allowed to dry under the inert gas atmosphere for about 4 hours. The coal sample was then reserved for measurements as the “Acid-Treated” coal.

Finally, all of the treated coal samples were placed in a vacuum oven contained within a glove bag for an air-free environment and dried. The coals were dried at 75 ^{o}C repeatedly for four-hour periods until a constant weight (± 1%) was obtained for two subsequent weightings.

4.0 RESULTS AND DISCUSSION

4.1 EXCESS ADSORPTION ISOTHERMS OF CO_2 ON COALS (n^{ex})

Excess adsorption and desorption isotherms of CO_2 on the Argonne Premium Pocahontas No.3, Upper Freeport, Pittsburgh No.8, Lewiston Stockton, Blind Canyon, Illinois No.6, Wyodak, and Beulah Zap coals were measured at 22 °C and pressures up to 4 MPa by the volumetric method. Before the adsorption measurements were performed, coal samples were dried *in-situ* at 80 °C under vacuum for 36 hrs. Figure 18 shows the excess adsorption and desorption isotherms of CO_2 on these eight Argonne coals. The error bars represent the standard deviation calculated for the experimental apparatus (Appendix D).

The excess adsorption (n^{ex}) is the amount experimentally estimated from a mass balance neglecting the volume of the adsorbed phase and other volume changes, and it does not represent the absolute (real) adsorbed amount (n^{abs}). Consequently, the estimation of the absolute adsorption from the excess adsorption isotherms is a challenging question, especially at high pressures.(130,211,131) There are several issues specific to the excess adsorption isotherms of swelling agents on 'non-rigid' solids, e.g. CO_2-coal or organic solvent-polymer systems. As can be seen in Figure 18, the shape of the adsorption isotherms of CO_2 on coals are more-or-less rectilinear. The adsorption of not only CO_2,$^{(32,51)}$ but also of H_2O,$^{(34,20)}$ CH_3OH,$^{(35)}$ and organic vapors$^{(21,33)}$ on coals have been shown to have a rectilinear shape. The shape of the adsorption isotherm progresses from Langmuir-like to rectilinear as the rank of the coal decreases. Hysteresis is often seen between adsorption and desorption isotherms and typically the hysteresis becomes larger as the coal rank decreases. Although hysteresis is generally associated with mesoporous adsorbents,$^{(103)}$ at the low CO_2 pressures studied here ($P/P_s < 0.95$), this origin of the hysteresis is unlikely.$^{(115)}$ These observations are in agreement with the literature.$^{(106,212,213)}$

4.1.1 Interpretation of Excess Adsorption Isotherms (n^{ex})

The excess adsorption isotherms of CO_2 on coals were evaluated by fitting the adsorption isotherm data to the general conventional equation, Eq.(10). This equation assumes that the only change in volume is due to the free volume decreases accompanying the accumulation of the adsorbed phase. In order to fit the curves to the adsorption isotherms, each of the model equations shown in Table 5 were substituted for the n^{abs} term in Eq.(10), representing the real adsorbed amount. The free gas phase density (ρ), the adsorbed phase density (ρ^a), and the saturation pressure (P_s) for CO_2 used in the interpretations of the excess adsorption isotherms were calculated at various temperatures from the Span and Wagner-EOS, and the approximations suggested by Dubinin$^{(129)}$ and Reid et al.$^{(137)}$, as shown in Appendix A and as listed in Table 9, respectively. Then, each of the adjustable parameters such as the adsorption capacity (n_o), the affinity coefficient (K_i), and the exponent (j_i), defined for each model equations individually, was estimated using *SigmaPlot*® spreadsheet regression data analysis.

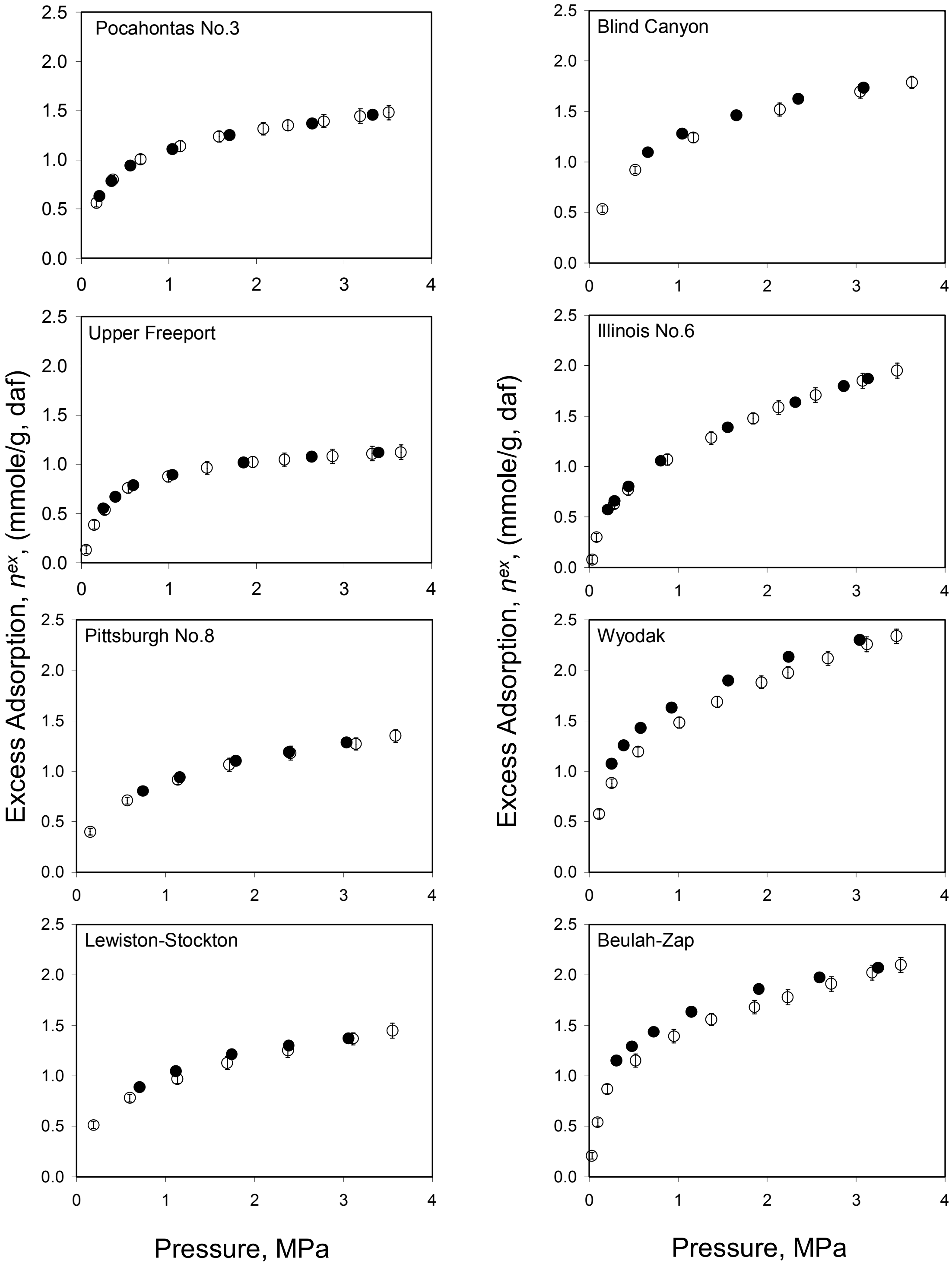

Figure 18. Excess adsorption (○) and desorption (●) isotherms of CO_2 on dried Argonne Premium coals

Table 9. The adsorbed phase density (ρ^a) and saturation pressure (P_s) for CO_2 used in the interpretation of its excess adsorption isotherms on coals

Temperature (^oC)	Density of the Adsorbed Phase (ρ^a)(129) (mmole/cm^3)	Saturation Pressure (P_s)(137) (MPa)
22	23.866	5.886
30	23.416	7.084
40	22.852	8.868
55	22.007	12.317

The SigmaPlot curve fitter uses the Marquardt-Levenberg algorithm(214) to find the coefficients (parameters) of the independent variables that give the best fit of the equation to the data. This algorithm seeks the values of the parameters that minimize the sum of the squared differences between the values of the observed and predicted values of the dependent variable.

Figure 19 shows the best fit of the experimental adsorption isotherm data to Eq.(10). With the exception of the Langmuir and UNILAN equations, the agreement between the calculated and experimental values was good. The two-parameter Langmuir equation described the adsorption behavior poorly and became worse as the coal rank decreased. The three-parameter UNILAN equation was acceptable for the high rank coal but not for the lower rank coals. The other equations provided good agreement with the experimental data; however, reasonable fits alone do not provide assurance that the parameter solutions obtained are accurate.

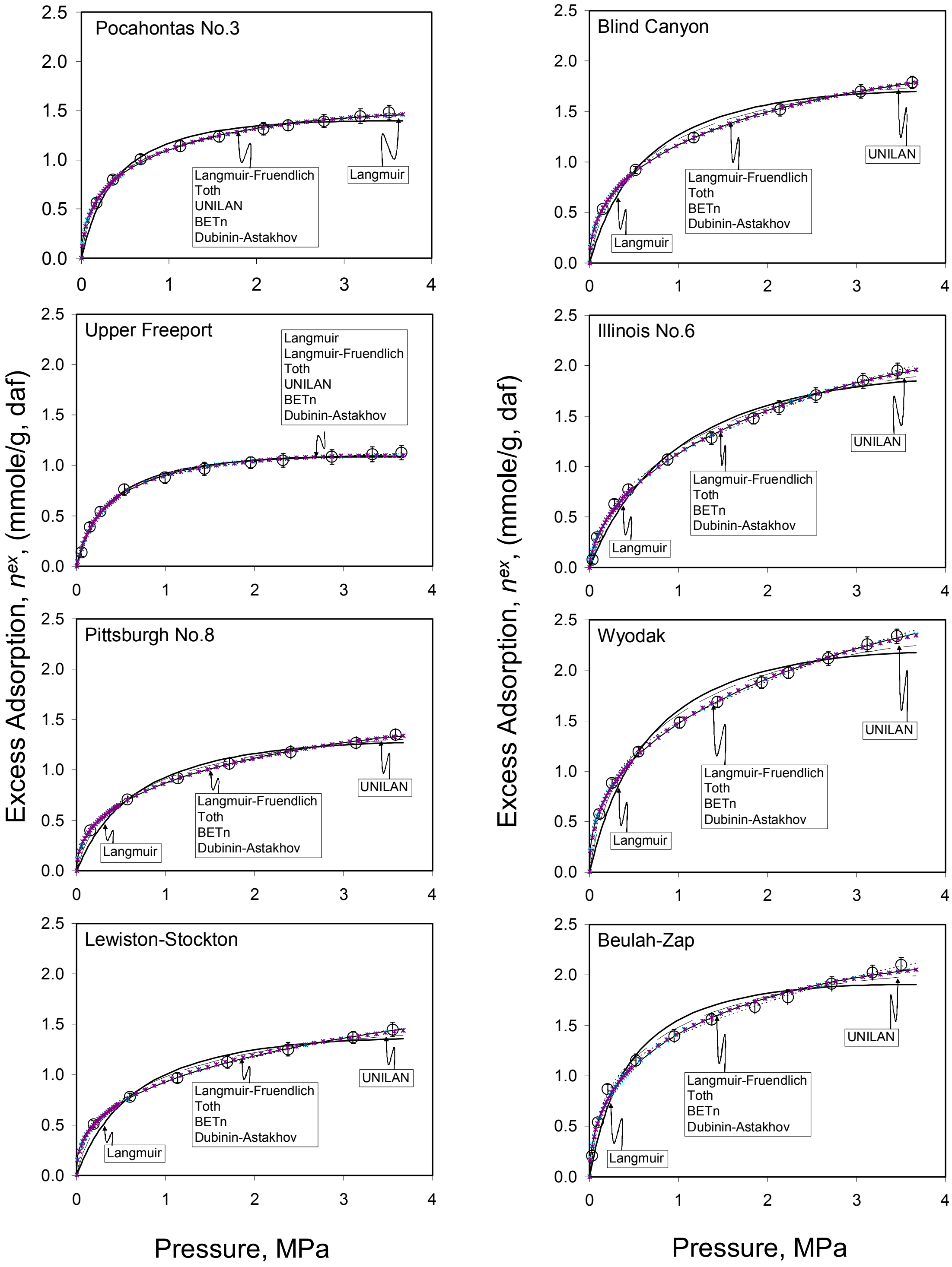

Figure 19. Best-fit curves obtained from Eq.(10) using the model equations in Table 5 for the absolute adsorption term, n^{abs}

Table 10 lists the values obtained for each of the parameters in each of the model equations shown in Table 5. The best-fit solutions are very different or misleading, as for example, the very large capacities obtained for the Langmuir-Freundlich, Toth, and UNILAN equations. This might be considered a drawback of the adsorption model and interpreted as proof for or against a particular adsorption mechanism. However, closer examination leads to the conclusion that the parameter solution was affected by volumetric changes to be discussed below.

Eq.(10) has been derived assuming a rigid solid and that no volume change occurs in the sample cell except that due to the adsorbed phase. The fact that coals shrink upon drying and swell during re-adsorption is a well-known phenomenon. However, changes in the actual void volume, which may occur upon swelling or shrinkage of the sample, are not considered in traditional formulations. There is a need to account for these volume changes in the interpretation of the excess adsorption isotherm data. The shrinkage reported in the literature is generally the physical shrinkage with respect to the dimensional changes of the coal (see Figure 8). Nevertheless, the effect of the swelling and shrinkage on the adsorption measurements is not due only to the dimensional changes but also the volumetric changes, including the opening or closing of the pores as well as the accessibility within the pores in the coal. The following section evaluates the volumetric changes due to the drying of coals.

Table 10. Best-fit parameters at 22 °C obtained from Eq.(10)

	1.Langmuir	2.Langmuir-Freundlich	3.Toth	4.UNILAN	5.BETn	6.Dubinin-Astakhov
			Pocahontas No.3			
n_o	1.69	2.79	3.79	4.63	1.10	1.71
K_i	0.43	1.49	0.45	28.86	33.78	0.20
j_i	-	0.52	0.30	6.49	2.33	1.32
			Upper Freeport			
n_o	1.30	1.39	1.45	1.12	0.99	1.21
K_i	0.39	0.50	0.42	0.20	23.54	0.09
j_i	-	0.88	0.76	-0.01	1.71	1.98
			Pittsburgh No.8			
n_o	1.68	7.50	197.08	5.05	0.88	1.71
K_i	0.77	7.44	0.66	59.54	28.95	0.35
j_i	-	0.45	0.09	6.29	3.09	1.08
			Lewiston-Stockton			
n_o	1.78	3.49E+06	1.50E+08	5.15	0.91	1.98
K_i	0.74	3.67E+06	0.63	46.56	34.37	0.44
j_i	-	0.38	0.03	6.11	3.33	0.90
			Blind Canyon			
n_o	2.20	9.77	232.37	6.65	1.17	2.27
K_i	0.71	7.20	0.64	58.41	30.22	0.35
j_i	-	0.45	0.09	6.36	3.10	1.08
			Illinois No.6			
n_o	2.67	8.32	58.18	7.71	1.21	2.55
K_i	1.20	6.24	1.00	43.32	19.32	0.42
j_i t	-	0.59	0.18	-5.16	3.68	1.13
			Wyodak			
n_o	2.86	4.50E+06	2.74E+08	8.51	1.45	3.17
K_i	0.76	3.01E+06	0.70	50.99	31.26	0.44
j_i	-	0.41	0.03	6.09	3.51	0.96
			Beulah Zap			
n_o	2.35	5.67	13.73	6.12	1.33	2.50
K_i	0.48	2.93	0.57	20.47	42.53	0.28
j_i	-	0.50	0.20	5.84	3.23	1.20

n_o: mmole/g-coal, daf; K_1: MPa; K_2: MPa^t; K_3: $MPa^{1/t}$; K_4: MPa; K_5 and K_6, j_i: dimensionless

4.2 VOLUMETRIC CHANGES DUE TO DRYING OF COALS

In order to delineate the volumetric changes, the densities of the as-received and dried Argonne Premium coals were estimated.

4.2.1 Densities of the As-Received and Dried Argonne Premium Coals: The densities of the as-received and dried Argonne Premium coals were measured using the helium expansion method. Figure 20 compares the densities of the as-received and dried Argonne coals to the densities for the same set of Argonne coals reported by Huang et al.(98). The densities of dried non-Argonne coals reported by Gan et al.(29) are also included. The agreement between the measured densities of the dried Argonne Premium coals and the literature data for the dried coals is excellent. The densities of the dried coals decrease from about 1.40 to 1.22 g/cm^3 as the carbon content increases from 70% to 78%, display a shallow minimum at about 1.22 g/cm^3, as the carbon content increased from 78% to 83%, and then increase from 1.22 back to 1.40 g/cm^3, daf, as the carbon content increases from 83% to 92%. In contrast, the densities of the as-received coals show a very different trend. The densities of the as-received coals increase continuously from 0.80 g/cm^3, daf, at a carbon content of about 72% to 1.35 g/cm^3, daf, at a carbon content of about 92%. The densities of the as-received coals are consistently smaller than the densities of the dried coals. The difference is especially large for the low rank coals.

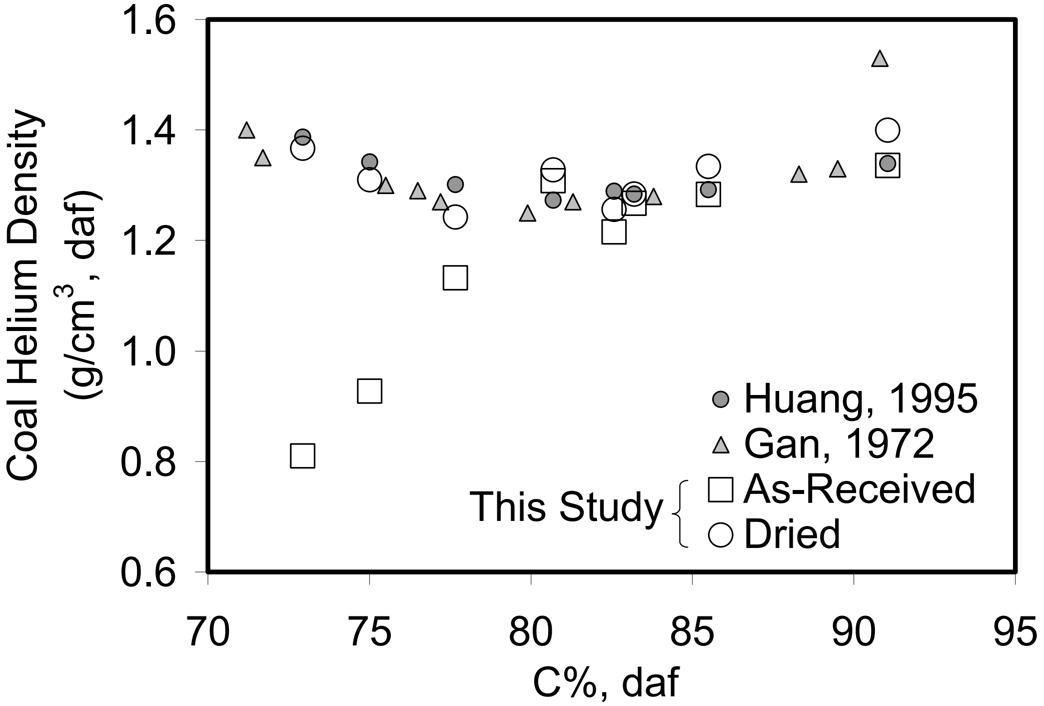

Figure 20. Densities of as-received and dried Argonne Premium coal samples

The effect of moisture can be seen more effectively by plotting the specific volumes as shown in Figure 21. All of the dried coals have specific volumes between 0.7 and 0.8 cm^3/g regardless of rank. The volume change upon water removal is very small for the higher rank coals. For the lower rank coals, loss of moisture causes the coal structure to shrink so that a gram of dried coal occupies less than 60% of the volume occupied by the as-received coal. The loss in volume can be related to two volumetric effects. One is the shrinkage of the coal matrix resulting in collapsing the pore structure(215) and the other is the increase in the accessibility of helium to those pores which were initially occupied by the moisture.

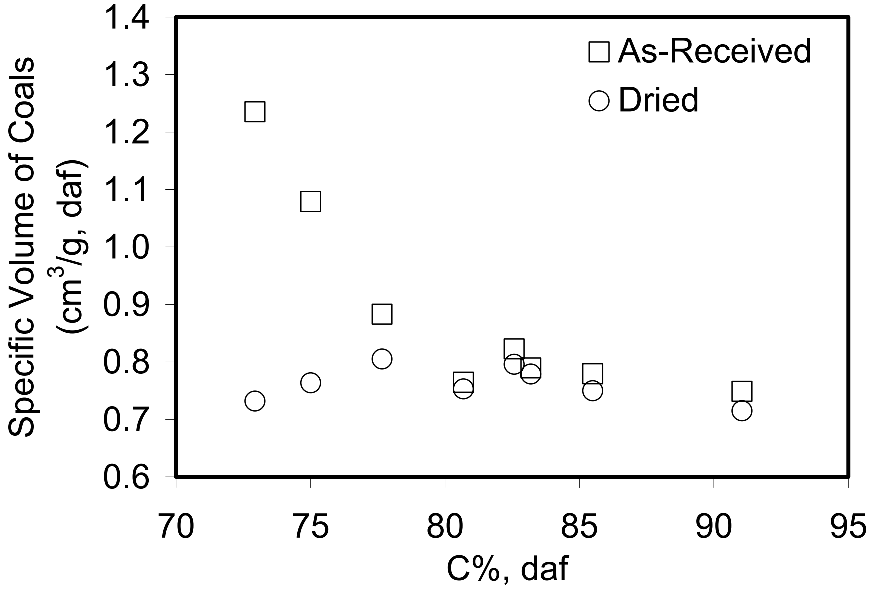

Figure 21. Specific volumes of as-received and dried Argonne Premium coals

4.2.2 Shrinkage of Coals upon Moisture Loss: Figure 22 shows the volume change and the percent shrinkage of the Argonne coals upon drying, as well as the volume of the removed water when the density of the water is assumed to be 1 g/cm^3. As shown in the figure, the high rank coals, which contain little moisture, lose almost no water whereas the low rank coals, which have high moisture contents, lose a considerable amount of water. The volume change upon water removal is very small for the higher rank coals. This is consistent with the prevailing theory that higher rank coals behave as glassy polymers and that water fills pores in this rigid structure.(216,217) Below about 80% C, loss of moisture causes the coal structure to shrink. The microscopic shrinkage was calculated from the densities of the as-received (ρ_w) and dried (ρ_d) coal as

$$\text{Shrinkage } \% = \frac{\rho_d - \rho_w}{\rho_d} \, x \, 100 \tag{39}$$

As shown in Figure 22, a 2% to 5 % shrinkage was observed for the high rank coals as a result of moisture lost, and up to 40% shrinkage was observed for the low rank coals. The volume change of the coals upon moisture loss is greater than the volume of removed water.

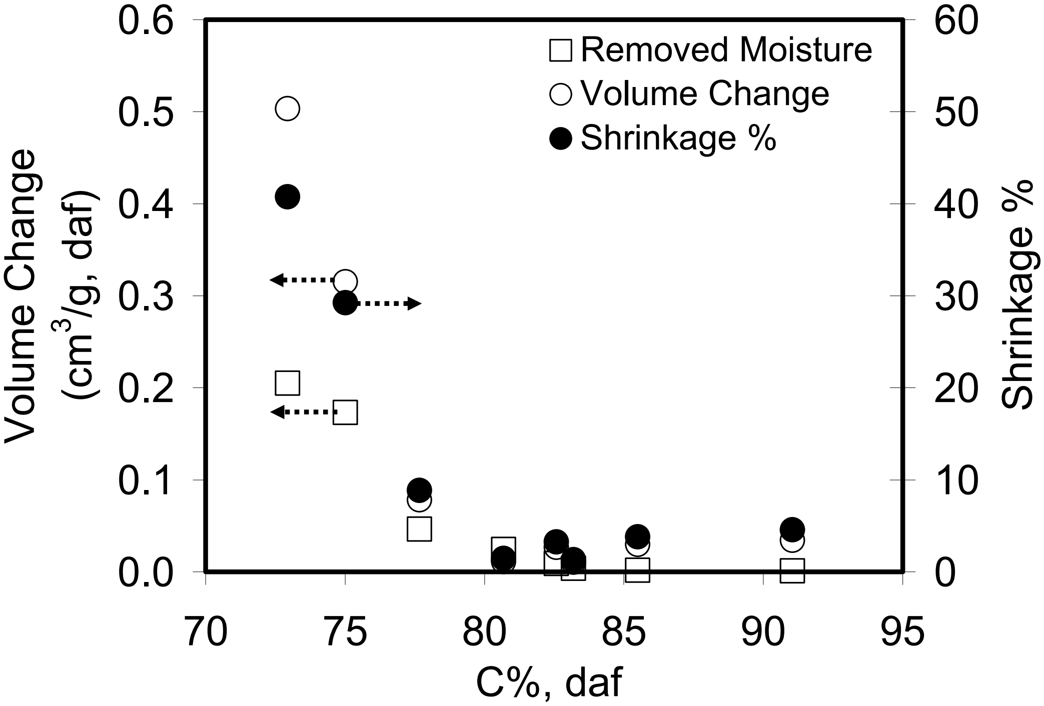

Figure 22. Comparison of the volume change and percent shrinkage of the Argonne Premium coals upon drying with the volume of the removed water

Figure 23 compares the microscopic shrinkage calculated from the change in the specific volume, Eq.(39), with the macroscopic shrinkage obtained by Suuberg et al.(218) using a bed-height technique. The agreement is much better than would be expected based on the different volume losses being measured by the two techniques. Qualitatively, the macroscopic shrinkage reported by Deevi and Suuberg(215) and the microscopic decrease in specific volume seen here are in agreement. In the case of Suuberg,(215) the volume loss upon drying reflects the shrinkage of the bed of particles. If one assumes spherical particles, then the particle-size decreases from the original diameter of about 600 microns to about 530 microns when the bed shrinks by 30%, which is about the largest shrinkage reported by Suuberg et al.(218) In the current case, the shape and size of the particles is irrelevant because the He reports all of the available volume around, between, and within the individual pieces of coal. Thus, helium reports the loss of microscopic porosity that has been proposed as the root-cause of the macroscopic shrinkage. As can be seen in Figure 23, the extent of loss of microporosity is about twice the loss of macroscopic volume (slope of 1.773 vs. 0.863). The correlation with moisture loss is good for the low rank coals in both cases but becomes poorer for the higher-rank coals.

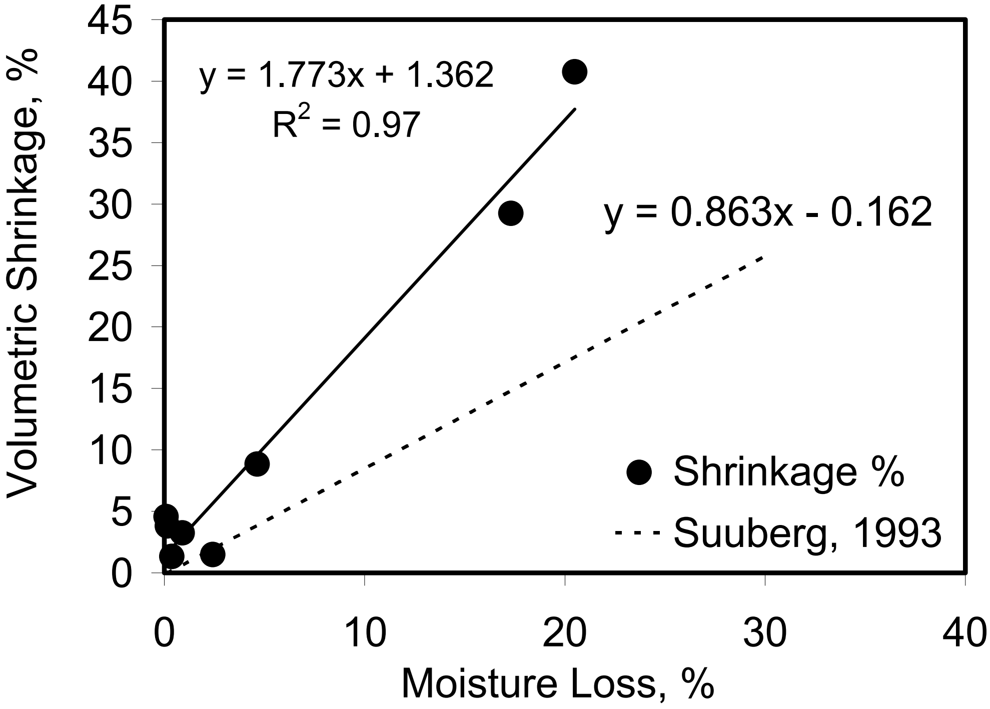

Figure 23. Comparison between the percent volume change (this work) and percent shrinkage (Suuberg et al.(218)) of the Argonne Premium coals upon drying

Changes in coal volume upon adsorption and desorption are not unique to water. It is well recognized that a number of compounds, including CO_2, act as swelling agents for coals.(21,33,219,101) A 40% volume change upon drying and re-adsorption is important to the estimation of the adsorption isotherm because any volume change affects the calculations (see discussion under ‘model development’ in section 4.3.2). This demonstrates the need either to rigorously control the moisture content of the coal during an adsorption isotherm measurement, or to use an adsorption model which allows for volumetric changes during the isotherm measurements. The model described in the next section was developed to account for such volume changes.

4.3 DEVELOPMENT OF AN ADSORPTION ISOTHERM MODEL ACCOUNTING FOR VOLUME CHANGES

The model developed here is based on the assumption that the swelling phenomenon affects not only the measured surface area but also the volume of the adsorbent and the void volume that is accessible to CO_2. This is of particular importance to the development of adsorption isotherms using both the gravimetric and the volumetric (manometric) techniques. All of the gravimetric and the volumetric calculations are based on the assumption that the volume of the adsorbent or the void volume of the sample cell, that is, the volume not occupied by the adsorbent, is accurately determined using He or other “inert” gas. Because of the swelling properties and accessibility problems discussed earlier, this assumption is questionable in the case of coal and other swelling adsorbents. Unlike previously derived adsorption isotherm models, which are based on a rigid adsorbent structure and constant adsorbent and void volumes, the equations derived here allow the sample-cell void volume to change.

4.3.1 Volumetric Changes in Coal Samples Associated with Adsorption Isotherms

In addition to the swelling-shrinkage behavior of the coal, there are several sources of volumetric changes during an adsorption isotherm measurement. Helium is generally used for the estimation of volume of the solid adsorbent. The selection of helium is based on the assumptions that helium is not adsorbed and that it can reach the smallest pores so that it yields the "true" density of the solid adsorbent.(220) If the small molecular size of helium allows it to penetrate the smallest pores, then larger, inert molecules that are unable to access such pores, would report a lower density for the solid adsorbent because part of the helium-accessible volume would be excluded. This is called the "sieving effect".(24) Conversely, helium has been reported to adsorb on solid adsorbents at low temperatures and high pressures(221,222) indicating that the measured void volume or the volume of the adsorbent may be subject to a change at other temperatures and pressures. When both molecular sieving and adsorption are present, the apparent density may be higher or lower than that observed in helium. Therefore, both assumptions about the behavior of helium may result in errors in the estimation of the actual void volume accessible to the adsorbing gas. Here, this change of void volume is called $\pm \Delta V_o$.

Another source of the volumetric changes in the coal sample is due to the compression or shrinkage at high pressures.(223,224) This is especially important for porous solids because the calculated volume of the solid may be affected in two opposing ways. First, there is a dimensional change as the solid is compressed at high pressures resulting in a net decrease in sorbent volume. Second, the constriction of pore entrances upon compression may prohibit gas molecules from accessing pores that were accessible initially, resulting in an apparent increase in solid volume. The expansion or swelling of adsorbents considered above may also result in a change in volume. Again, the volume of the solid may be affected in two opposing ways. The dimensional increase as the solid swells results in a net increase in sorbent volume. However, the widening of the previously constricted pore entrances may enable more gas molecules to access those pores that were initially inaccessible, resulting in a net decrease in solid volume. Here, this volumetric change is called $\pm \Delta V_c$.

Dissolution of the adsorbing gas in the coal sample is another source for the volumetric changes. A number of phenomena, such as sorption induced swelling(113,35) and dissolution of coals(24) have indicated that the coal is an elastic material. The adsorption on coal is generally explained with a dual sorption model describing adsorption on the surface and absorption within the coal matrix as two interacting subprocesses.(33,33,21,32,225) Dissolution of the adsorbing gas within the coal matrix may result in a volume change. Here, this volumetric change is called $\pm \Delta V_d$.

Another source of volume change is due to the volume occupied by the adsorbed phase which is called $\pm V^a$ or $\pm n^{abs}/\rho^a$. However, the volume change due to the volume of the adsorbed phase has been considered in the literature (i.e. Eq.(10)) and almost all high-pressure excess adsorption isotherms have been corrected to account for the adsorbed phase volume by assigning an adsorbed phase density.(223,211,146,128)

4.3.2 Model Development

In light of these volumetric changes, ΔV in Eq.(8) must be reconsidered. While still defined as the difference between the void volume in the sample cell (V_i) and the initially estimated void volume (V_o), the void volume actually includes not only the volume of the adsorbed phase (V^a), but also the volume created by the swelling or shrinkage of the solid adsorbent (ΔV_c), the over- or under- estimation of the void volume due to adsorption of helium and/or the extra volume due to sieving effect (ΔV_o), the volume change due to the dissolution of the adsorbing gas (ΔV_d), etc.. Collectively, these may be called the overall volumetric change in the sample cell (ΔV_x). Thus, the change in the void volume in the sample cell can be expressed as:

$$\Delta V = V_i - V_0 = -V^a \underbrace{\mp \Delta V_c \mp \Delta V_o \mp \Delta V_d \mp \cdots}_{-\Delta V_x} = -\frac{n^{abs}}{\rho^a} - \Delta V_x \tag{40}$$

The excess adsorption originally defined for a rigid solid in Eq.(10) now can be written for a non-rigid solid as:

$$n^{ex} = \left(1 - {\rho}/{\rho^a}\right) n^{abs} - \rho \Delta V_x \tag{41}$$

The equation, Eq.(41), suggested for the adsorption on non-rigid solids can be extended further assuming that the volumetric changes due to sieving effect and solid dissolution are too small and can be neglected. In this case, the following equation, suggested for the relative change of the volume of a coal sample per unit original volume with the pressure changes at isothermal condition, could be employed$^{(226)}$

$$\gamma = \mp \frac{1}{V_{coal}} \left(\frac{\partial V_{coal}}{\partial P} \right)_T \tag{42}$$

where γ is the expansion coefficient, MPa^{-1}, and V_{coal} is the volume of the coal sample at any pressure, cm^3/g. Integrating Eq.(42) from initial pressure of P_o to the any pressure of P and from initial volume of the coal sample, V_{icoal}, to any volume, V_{coal}, yields

$$V_{coal} = V_{icoal}\, e^{\gamma (P - P_o)} \tag{43}$$

Assuming the original volume of the coal sample is the volume of the coal initially measured by the helium expansion method, and the initial pressure, P_o, is sufficiently small to be negligible compared to P, the difference between the final and the initial volumes of the coal sample, ΔV_{coal}, which is the negative of the void volume change in the sample cell as assumed, *i.e.* $-\Delta V_x$, becomes

$$\Delta V_{coal} = V_{icoal}\left(e^{\gamma P} - 1\right) = -\Delta V_x \tag{44}$$

Inserting Eq.(44) in Eq.(41), the general modified equation will take the form

$$n^{ex} = \left(1 - {\rho}/{\rho^a}\right) n^{abs} + \rho V_{icoal}\left(e^{\gamma P} - 1\right) \tag{45}$$

where ρ, ρ^a, and V_{icoal} are as defined before. Eq.(45) can now be used to interpret the adsorption isotherms accounting for the volume changes.

4.3.3 Interpretation of the Excess Adsorption Isotherms of CO_2 on Coals Accounting for Volume Changes

The adsorption isotherm data discussed in the previous section were evaluated using Eq.(45), which explicitly accounts for influences of coal swelling and shrinkage which affect the measurements. Figure 24 shows the fit of the adsorption isotherm data to Eq.(45) employing each of the adsorption model equations shown in Table 5 for n^{abs} term. All the equations now provide very good fits to the adsorption isotherm data except the Langmuir equation. The Langmuir equation deviations are small or unobservable for the high rank coals. While still small, they are discernable for the low rank coals. All of the other model equations used fit the excess adsorption isotherm data well. For instance, Figure 25 compares the deviation plots obtained using the conventional D-A equation, i.e. Eq.(45) with γ=0, and the modified D-A equation, Eq.(45). Deviations were calculated as the difference between the measured excess adsorption and that obtained from the model. The deviations in the first case (Figure 25a) are larger with a range of about ± 0.04 mmole/gram versus about ± 0.02 mmole/gram for the modified equation. Also, the deviations obtained using the conventional equation display a regular, sinusoidal-like pattern for the entire set of Argonne coals. The deviations in the later case (Figure 25b) appear to be randomly distributed about the zero-axis.

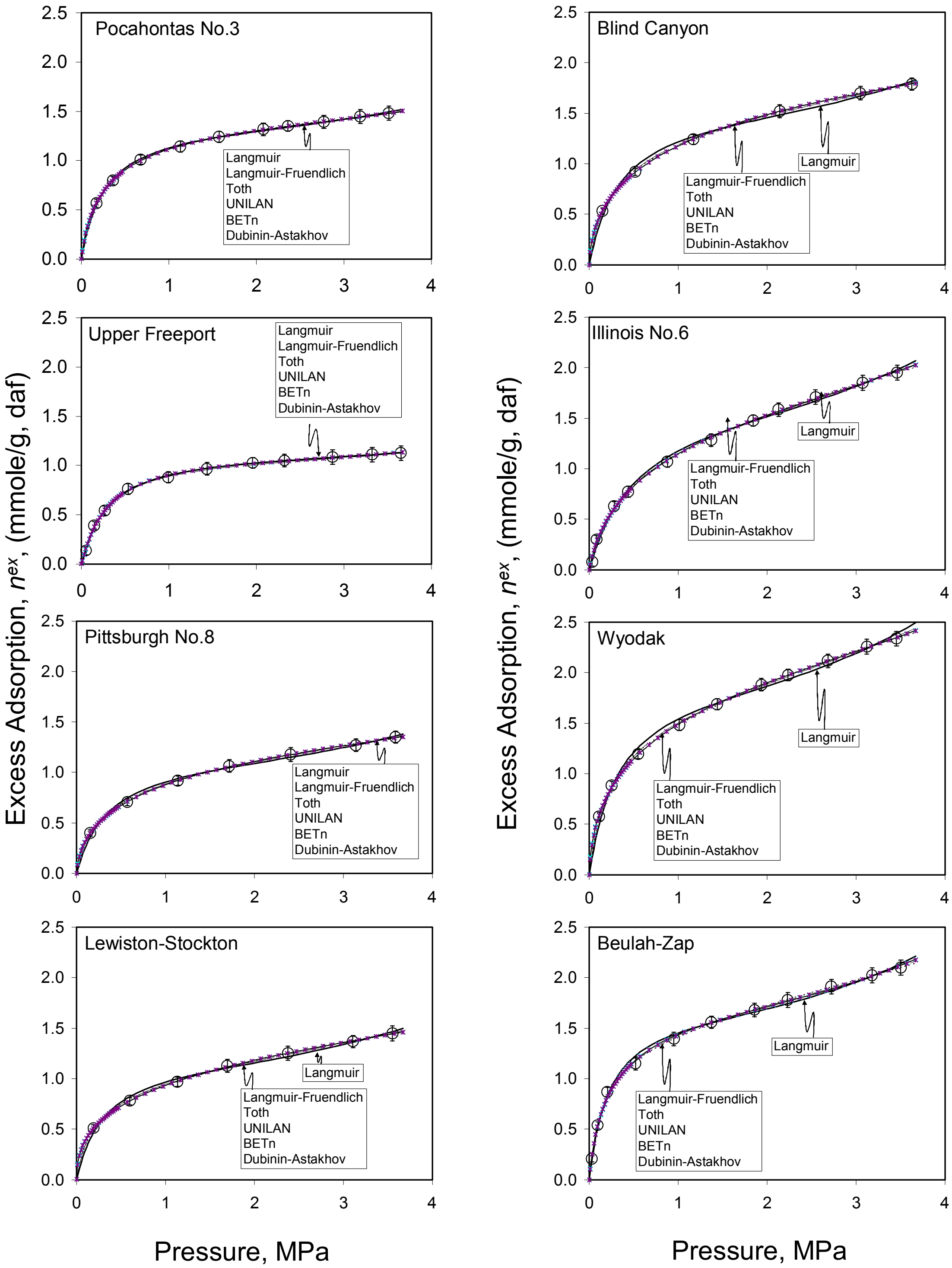

Figure 24. Best-fit curves obtained from Eq.(45) using the model equations in Table 5 for the absolute adsorption term, n^{abs}

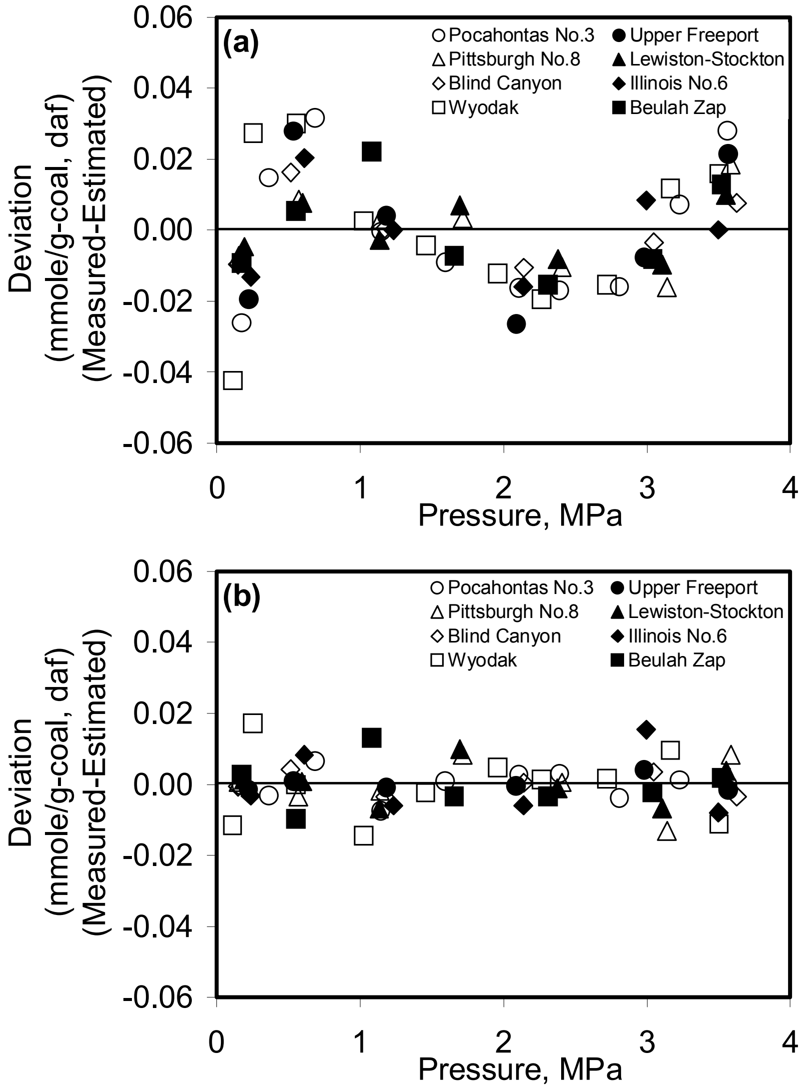

Figure 25. Deviation plots comparing (a) the conventional Dubinin-Astakhov and (b) modified Dubinin-Astakhov equations for each of the Argonne Premium coals

Table 11 shows the model parameters obtained from Eq.(45) for each of the adsorption equations shown in Table 5. The values are within reasonable limits. However, in same cases, the adsorption capacities of coals reported by the Langmuir-Freundlich, Toth, and UNILAN equations are 2 to 3 times greater than those reported by the Langmuir, modified BET, and Dubinin-Astakhov equations. This is somewhat expected since Toth(227) indicated that "although many single component adsorption isotherm can be described by both the UNILAN and Toth equations, the forms of the two equations – from the thermodynamic standpoint – are incorrect”. Therefore, the Langmuir-Freundlich, Toth, and UNILAN equations were eliminated in further interpretation of the excess adsorption isotherm data. Furthermore, because both the two-parameter Langmuir equation and the modified BET (BETn) equation report the monolayer adsorption capacity rather than the storage capacity of coals, these model equations were also eliminated in further discussions. As a result, the Dubinin-Astakhov model equation, which was derived for an adsorption with a pore filling mechanism (see section 2.2.1), was selected to represent the absolute adsorbed amount (n^{abs}).

Table 11. Best-fit parameters at 4 MPa and 22 °C obtained from Eq.(45)

	1.Langmuir	2.Langmuir-Freundlich	3.Toth	4.UNILAN	5.BETn	6.Dubinin-Astakhov
			Pocahontas No.3			
n_o	1.45	1.67	1.76	1.64	1.16	1.41
K_i	0.28	0.49	0.35	0.38	30.19	0.07
j_i	-	0.78	0.66	1.83	1.84	2.01
γ	0.049	0.036	0.034	0.035	0.024	0.041
			Upper Freeport			
n_o	1.20	1.14	1.15	1.16	1.19	1.06
K_i	0.32	0.25	0.29	0.30	18.40	0.03
j_i	-	1.10	1.13	0.00	1.02	2.61
γ	0.020	0.026	0.025	0.025	0.020	0.029
			Pittsburgh No.8			
n_o	1.24	2.44	4.64	3.23	0.88	1.40
K_i	0.37	1.75	0.57	10.55	28.84	0.20
j_i	-	0.57	0.27	5.14	3.01	1.40
γ	0.056	0.023	0.019	0.030	0.003	0.027
			Lewiston-Stockton			
n_o	1.27	5.13	8.32	3.51	0.91	1.61
K_i	0.32	4.45	0.54	14.89	34.37	0.28
j_i	--	0.43	0.10	5.77	3.34	1.16
γ	0.066	0.022	0.020	0.041	0.000	0.025
			Blind Canyon			
n_o	1.65	3.83	9.52	5.01	1.16	1.94
K_i	0.36	2.22	0.58	24.69	30.47	0.23
j_i	-	0.53	0.22	6.03	3.54	1.31
γ	0.072	0.023	0.019	0.039	-0.024	0.028
			Illinois No.6			
n_o	1.83	2.59	3.88	5.44	1.21	1.83
K_i	0.57	1.26	0.75	22.30	19.24	0.19
j_i	-	0.76	0.46	5.17	3.86	1.59
γ	0.089	0.063	0.054	0.060	-0.009	0.067
			Wyodak			
n_o	2.06	4.28	8.59	6.14	1.46	2.37
K_i	0.35	1.86	0.55	22.48	31.35	0.21
j_i	-	0.55	0.25	6.00	3.63	1.36
γ	0.113	0.059	0.054	0.074	-0.008	0.064
			Beulah Zap			
n_o	1.78	2.04	2.25	2.23	1.36	1.76
K_i	0.23	0.42	0.33	0.44	40.71	0.06
j_i	-	0.80	0.63	2.34	2.53	2.07
γ	0.105	0.088	0.082	0.077	0.041	0.093

n_o: mmole/g-coal, daf; K_1: MPa; K_2: MPa^t; K_3: $MPa^{1/t}$; K_4: MPa; K_5, K_6, and t: dimensionless; γ:MPa^{-1}

4.3.4 Modified Dubinin-Astakhov Equation for the Interpretation of the Excess Adsorption Isotherms of CO_2 on Coals Accounting for Volume Changes

The general adsorption equation, Eq.(45), takes the form, when the Dubinin-Astakhov equation, Eq.(22), where $K_6 = RT/\beta E_o$, is inserted in Eq.(45) for n^{abs} term, as

$$n^{ex} = \left(1 - \rho \big/ \rho^{a}\right) n_o e^{-\left[\frac{RT}{\beta E_o}\ln\left(P_s \big/ P\right)\right]^{j}} + \rho V_{icoal}\left(e^{\gamma P} - 1\right) \qquad (46)$$

Eq.46 will be employed hereafter in order to interpret the excess adsorption isotherm data. When Eq.46 is fit to the excess adsorption isotherm data, the parameters, such as

- *the adsorption capacity (n_o),*
- *the characteristic heat of adsorption (E_o),*
- *the Dubinin coefficient (j),* and
- *the expansion coefficient (γ)*

can be obtained from the best fit solution of the CO_2 excess adsorption isotherm data. The volume changes, the surface area, the isosteric heat of adsorption, and the average pore size of coals can also be calculated using these parameters.

- *Calculation of Volume Changes of Coals:* The volume changes of coals as a function of pressure can be calculated from the expansion coefficient using:

$$\Delta V_{coal} = V_{icoal}\left(e^{\gamma P} - 1\right) \qquad (47)$$

where percent volume change of the coal is

$$\Delta V_{coal}\,\% = 100\left(e^{\gamma P} - 1\right) \tag{48}$$

♦ *Calculation of Surface Area of Coals:* The surface areas of coals is calculated from the CO_2 adsorption capacity using Eq.(49):

$$S = n_o N \sigma \tag{49}$$

where N is Avogadro's number (6.02 10^{23} molecules/mole) and σ is the cross-sectional area of the adsorbate (0.253 nm^2 for one molecule of CO_2).(41)

♦ *Isosteric heat of Adsorption:* The characteristic heat of adsorption, E_o, can be related to the isosteric heat of adsorption, Q_{st}, Eq.(50)(228) at the fractional filling ϕ of e^{-1} using the enthalpy of vaporization ΔH_v at the boiling point (17.1548 kJ/mole for CO_2)(137).

$$Q_{st,\phi=e^{-1}} = \Delta H_v + \beta E_o \tag{50}$$

♦ *Calculation of Average Pore Size of coals from CO_2 Adsorption Isotherm:* The Dubinin-Astakhov exponent, j, and the characteristic heat of adsorption, E_o, are related to the surface heterogeneity of the adsorbent.(31,153) From these two parameters, the average pore sizes of coals can be calculated from Medek's approach:(31,153)

$$r_e = \frac{\left(k/E_o\right)^{1/3}}{\Gamma\left(\frac{3j+1}{3j}\right)} \tag{51}$$

where k (= 3.145 $kJnm^3mol^{-1}$ for CO_2) is a constant(153) and Γ is the gamma function.

♦ *Calculation of the absolute adsorbed amount of* CO_2 *on coals* (n^{abs})*:* The amount of CO_2 adsorbed at any pressure and temperature is the amount obtained using the D-A equation:

$$n^{abs} = n_o e^{-\left[\frac{RT}{\beta E_o} \ln\left(P_s/P\right)\right]^j} \tag{52}$$

4.3.5 Excess (n^{ex}) and Absolute (n^{abs}) Adsorption Isotherms of CO_2 on Coals

It has been shown that volume changes strongly influence the excess adsorption isotherms (n^{ex}) of CO_2 on coal. Here, it has been attempted to separate the major effects leading to the observed excess adsorption. As shown in Figure 26, the measured adsorption isotherms can be divided into two contributing parts. One is the actual, physical adsorption of CO_2 onto the coal (n^{abs}), and the other is the extra amount due to the volume changes. These two parts are shown as absolute adsorption and extra amount due to volume change, respectively, in Figure 26. Adding these two parts gives the excess adsorption or the experimentally estimated adsorbed amount, n^{ex}. The estimated volume change is given in the secondary y-axes in Figure 26. The volume change is almost linear with CO_2 pressure during the adsorption measurements. The volume changes are small for the high rank coals (about 10%) and larger for the low rank coals (up to 40%). At low-pressures, the extra amount due to the volume changes is small when compared with the amount actually adsorbed. At high pressures, however, the changes in moles of gas in the unaccounted-for volumes become considerably larger, especially for the low rank coals, due to the compressibility of CO_2. This is important for the interpretation of adsorption isotherms and the accurate extraction of information from them. All adsorption isotherms reported in the literature ignore the possible error related to volume changes. This may be acceptable for low pressure adsorption isotherms; however, volume changes become more important for high pressure adsorption isotherms. The equation suggested here eliminates at least part of the error associated with the unaccounted for extra volume due to the interactions between coals and CO_2.

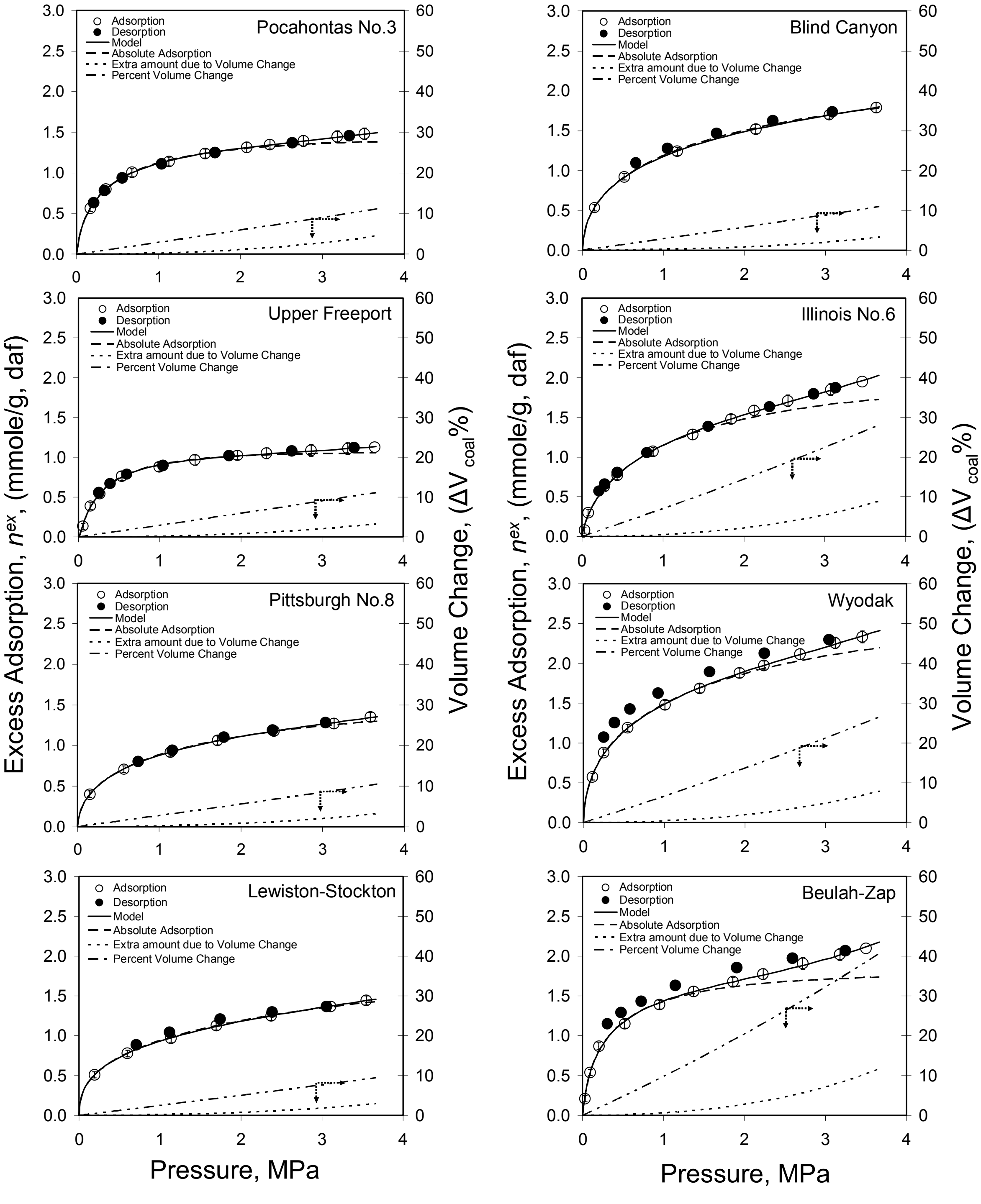

Figure 26. Fit of the adsorption isotherm data of CO_2 on Argonne Premium coals using the modified Dubinin-Astakhov equation (Eq.46) to account for volume effects

4.3.6 Comparison of the Modeling of the Excess Adsorption Isotherms with and without Including the Volume Effects

Figure 27 compares the parameter solutions of the excess adsorption isotherm data using the conventional, Eq.(10), and modified, Eq.46, equations employing the Dubinin-Astakhov equation for the n^{abs} term. As shown in Figure 27a, the adsorption capacity (n_o) of CO_2 on dried coals decreases with rank up to 86% C, and slightly increases again as rank further increases. This is consistent with the literature reported by several workers.(229,30,29) Figure 27b shows the characteristic heat of adsorption (E_o) showing a 'U-shape' with coal rank. Figure 27c shows the pore sizes of dried Argonne coals in the CO_2 atmosphere. Figure 27d shows the volume changes with coal rank calculated at about 3.8 MPa. As shown in Figure 27a, b, and c, if the conventional equation, Eq.(10), were used when the volumetric changes were not accounted, the adsorption capacity, the characteristic heat of adsorption, and the average pore size would be overestimated by 15-45%, 6-25%, and 4-13%, respectively, as a result of the volumetric changes from 10 to 40% as shown in Figure 27d. Consequently, the choice of modeling equation had a dramatic effect on the calculated values of the physical constants.

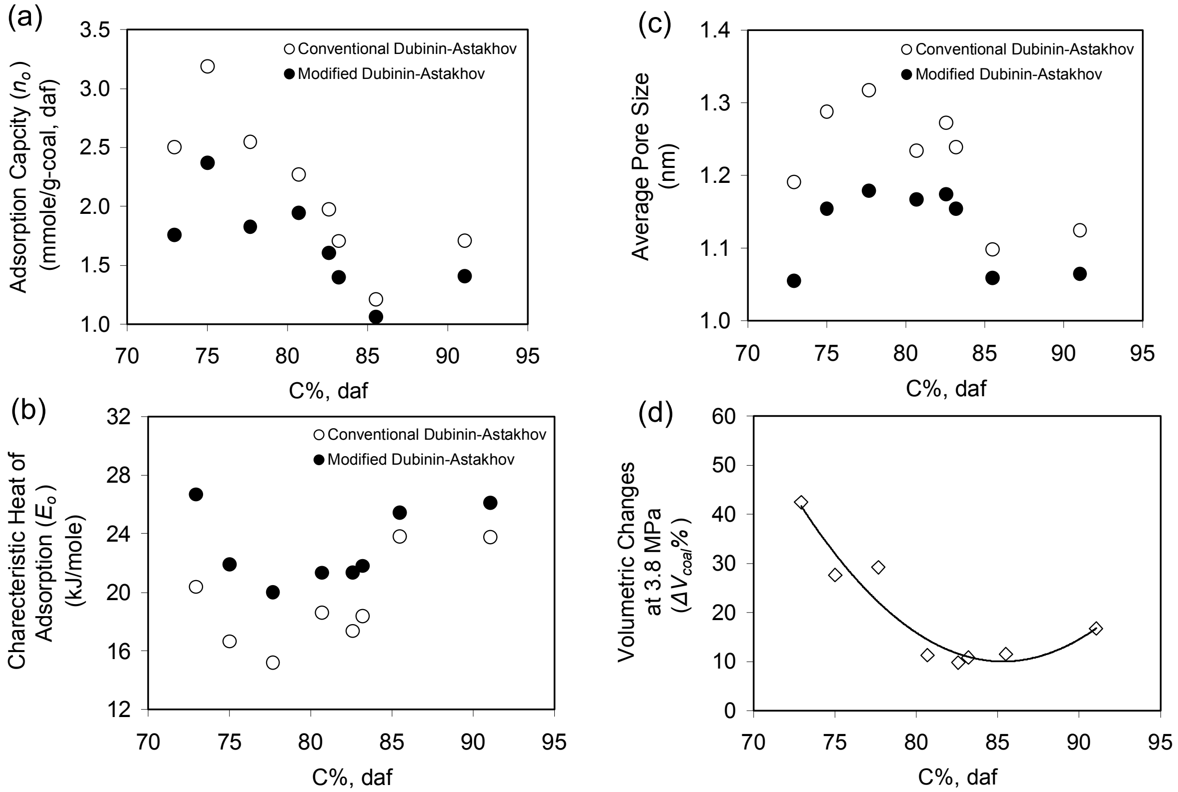

Figure 27. Comparison of the conventional and modified Dubinin-Astakhov equation for the estimation of (a) the adsorption capacity (n_o), (b) characteristic heat of adsorption (E_o), (c) average pore size, and (d) volume changes

4.3.7 Expansion Coefficient, γ, of Powdered Coals under CO_2 Atmosphere

Figure 28 compares the expansion coefficient, γ, obtained under a CO_2 atmosphere for the Argonne Premium coals as well as for other coals of various ranks as reported by Walker et al.(101). In previous one, the expansion coefficient or pore compressibility was obtained from the CO_2 adsorption isotherms using the modified Dubinin-Astakhov equation while, in the latter case, the bulk compressibility was estimated from the dimensional change as depicted in Figure

8. As shown in the figure, the pore compressibility under CO_2 atmosphere obtained from the adsorption isotherms (this work) is 10 times higher than the bulk compressibility obtained from the dimensional change (Walker's data). The trend is in good agreement with the literature data although these values are 1 to 2 orders of magnitude larger than the expansion factors estimated from dimensional changes under triaxial stress tests. For instance, Harpalani et al.(230) reported the compressibility factor of coal measured under the triaxial conditions as $1.3*10^{-4}$, $66.0*10^{-4}$, and $9.1*10^{-4}$ MPa^{-1} for the bulk, pore, assuming a 2% porosity, and matrix shrinkage compressibility, respectively.

The pore compressibility estimated under a CO_2 atmosphere is higher for the low rank coals. It decreases with coal rank up to 83 C%, and then, slightly increases as the coal rank further increases. This is a trend similar to that observed for the shrinkage of coals upon moisture loss, shown in Figure 23. The values of γ, from which the volume changes can be calculated, clearly show that there is a volumetric effect on the adsorption isotherm measurements and should be treated accordingly.

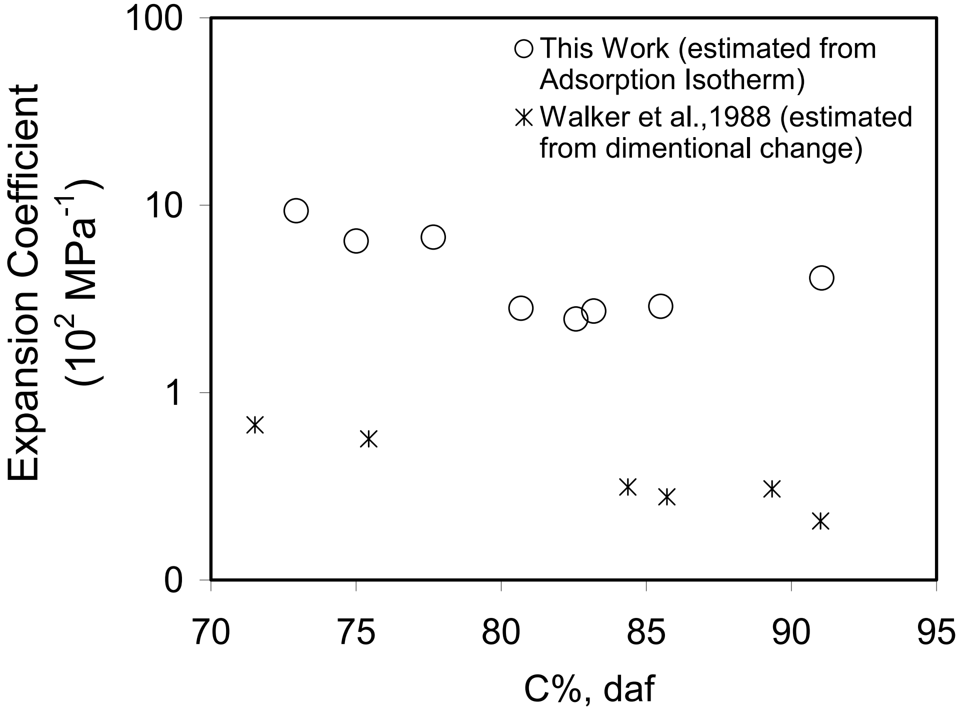

Figure 28. Comparison of the expansion coefficient or pore compressibility, γ, for coals under a CO_2 atmosphere as obtained from the adsorption isotherms (this study) and the bulk compressibility obtained from the dimensional changes reported by Walker et al.(101)

4.3.8 Storage Capacity of CO_2 on Dried Coals: Effect of Rank

Figure 29 shows the absolute adsorbed amount (n^{abs}) of CO_2 and the expected volume changes calculated from Eq.(52) and Eq.(48), respectively. As shown in Figure 29a, it was found that a 25 to 50 standard m^3-CO_2 per ton of coal could be stored in 'dried' coals under laboratory conditions. During this process, as shown in Figure 29b, up to 10% expansion in volume is expected for high-rank coals, and the expansion could be as large as 30-40% for the low rank coals at pressures up to 4 MPa. However, this capacity and volume changes may not be realized in water-saturated and constrained coal seams as will be discussed in detail in the next section.

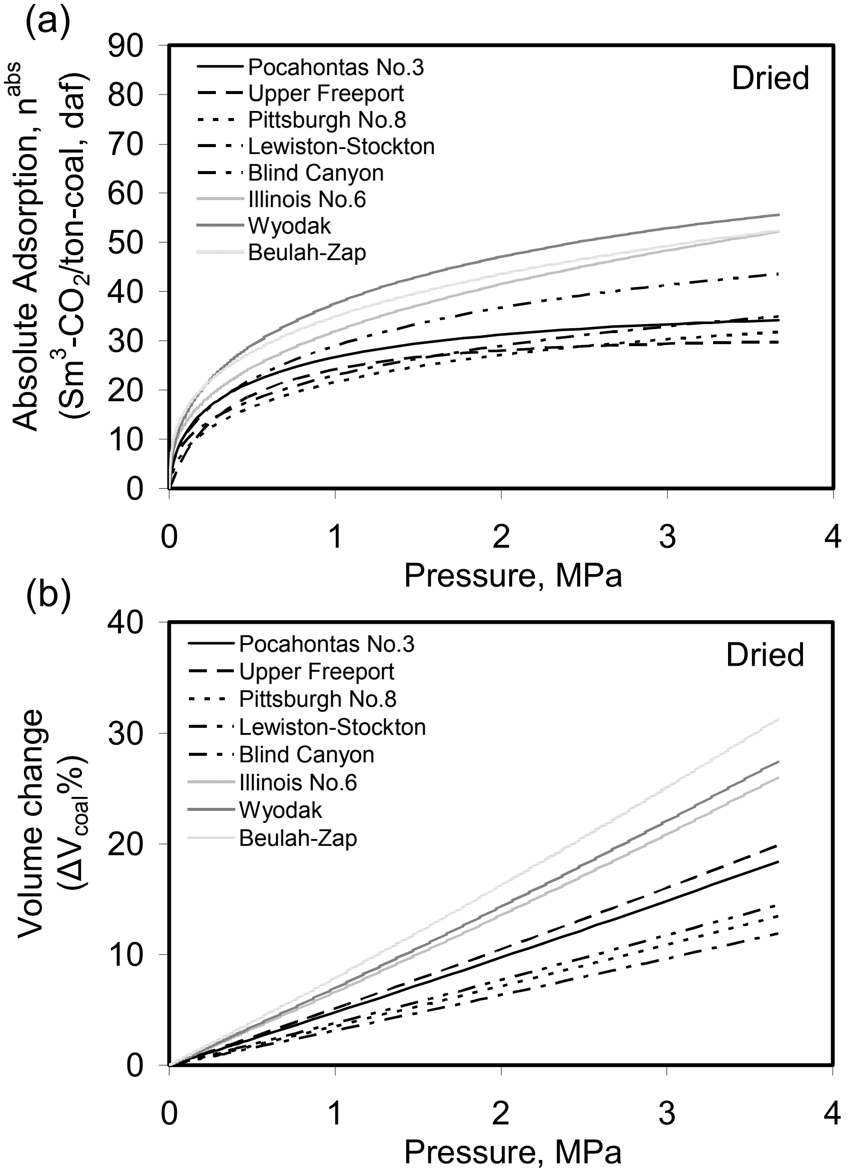

Figure 29. The absolute adsorbed CO_2 on Argonne coals and the expected volume change with pressure

4.4 EFFECT OF MOISTURE ON CO_2 ADSORPTION CAPACITY OF COALS

4.4.1 Adsorption and Desorption Isotherms of CO_2 on As-Received and Dried Argonne Coals

Figure 30 shows the excess adsorption and desorption isotherms of CO_2 on eight of the as-received and dried Argonne Premium coals. Lines are the best fit to the modified Dubinin-Astakhov equation, Eq.46. These are coals of different rank and moisture contents. As shown in Table 7, Pocahontas No.3 is the highest rank coal and contained the least moisture (0.63%). Upper Freeport, Pittsburgh No. 8, Blind Canyon, Lewiston Stockton, and Wyodak coals decrease in rank and increase in moisture content. Beulah-Zap is the lowest rank coal and contains the highest moisture content (24.51%). Drying the coals at 80 ^{o}C for 36 hrs under vacuum removed a smaller fraction of the total moisture content for the higher rank coals and a progressively larger fraction for the lower rank coals. For instance, the moisture content decreased from 0.63% to 0.54% (14% of the initial moisture was removed) for Pocahontas No.3, a high rank coal, but decreased from 20.72% to 3.40% (84% removed) for the low rank Wyodak coal. The effect of moisture removal was smaller for the higher rank coals than for the lower rank coals. The adsorption isotherm of CO_2 changed little for the high rank Pocahontas No.3 coal, but the original moisture content was small. On the other hand, significant increases in adsorption were obtained for the low rank coals.

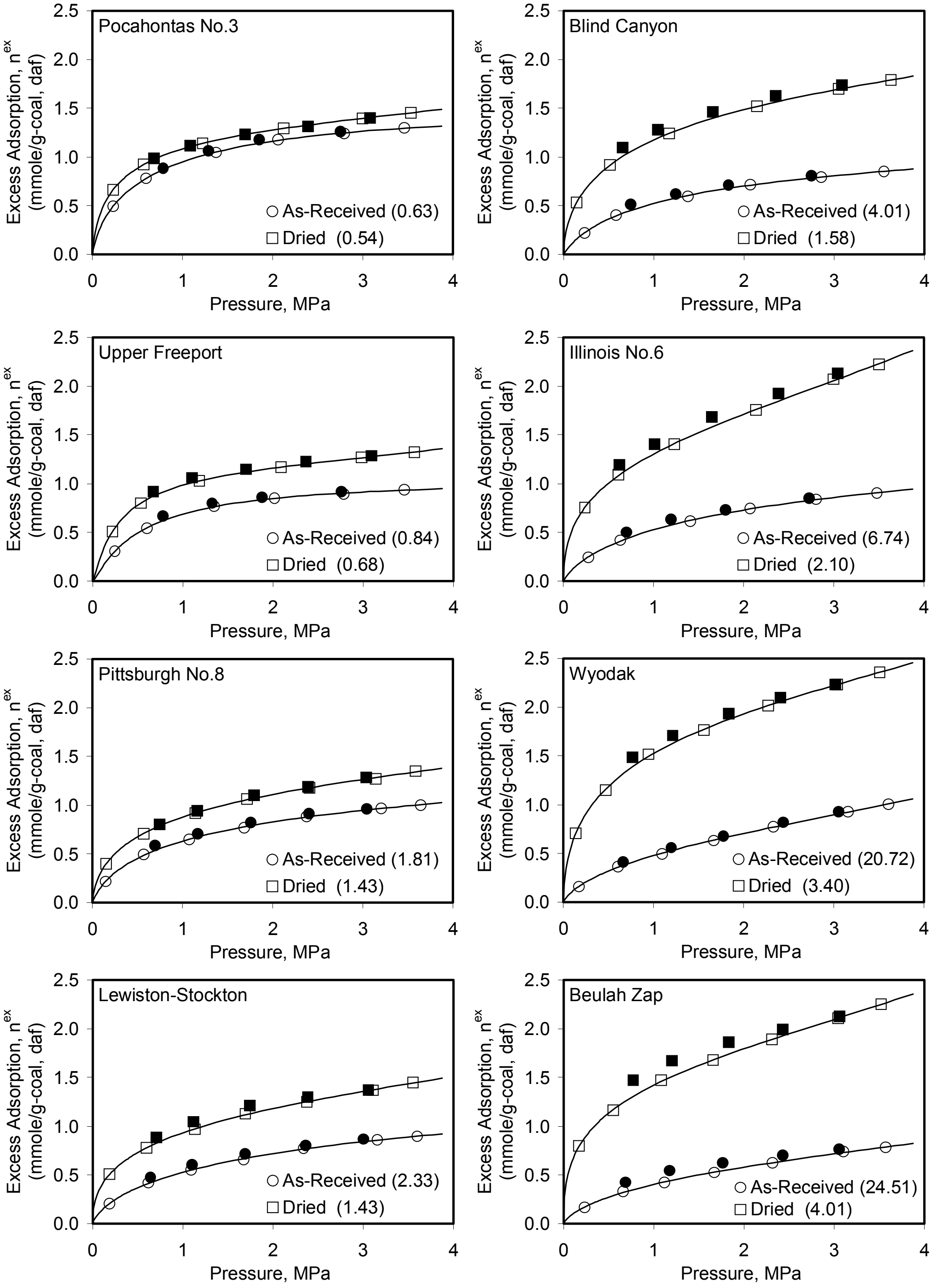

Figure 30. Excess adsorption (open symbols) and desorption (closed symbols) isotherms of CO_2 on as-received and dried Argonne Premium coals (numbers in parenthesis show the percent moisture content in coals)

As shown in Figure 30, a small hysteresis was observed between the adsorption and desorption isotherms. This hysteresis was absent or negligible for high rank and as-received coals, however, it was obvious for low rank and dried coals. The rectilinear form of the adsorption isotherm data fit the conventional adsorption equation poorly. However, the curves calculated from the best-fit solutions of the adsorption data to modified Dubinin-Astakhov equation (Eq.(46)) gave better fits for all the coals as depicted in Figure 30.

4.4.2 Variation of Physical Constants with Coal Rank and Moisture Content

By fitting the observed excess CO_2 adsorption data to modified D-A equation, Eq.46, the values of the physical constants such as adsorption capacity, characteristic heat of adsorption, Dubinin exponent, and volume effects, n_o, E_o, j and ΔV, respectively, can be obtained. Effects of rank and moisture contents of coals on the physical constants are summarized in the following sections.

4.4.2.1 Adsorption Capacity of CO_2 on As-Received and Dried Argonne Coals: Figure 31 shows the adsorption capacity of CO_2 on as-received and dried Argonne coals with different rank obtained from fitting Eq.46 to the adsorption isotherm data displayed in Figure 30. As shown in the figure, the adsorption capacity is dependent on the moisture content of coals and varies with coal rank. The adsorption capacity exhibits a minimum with carbon content for dried coals. However, the adsorption capacity increases generally with rank for as-received coals. The adsorption capacity decreases from about 2.5 mmole/g-coal to about 1.0 mmole/g-coal, dry- ash-free basis, as the rank increases up to a carbon content of coals about 86% and then increases slightly as the carbon content further increases. For as-received coals, the adsorption capacity is almost constant at about 1.0 mmole/g-coal but increased slightly to about 1.3 mmole/g-coal, dry-ash- free basis for the high-rank Pocahontas coal.

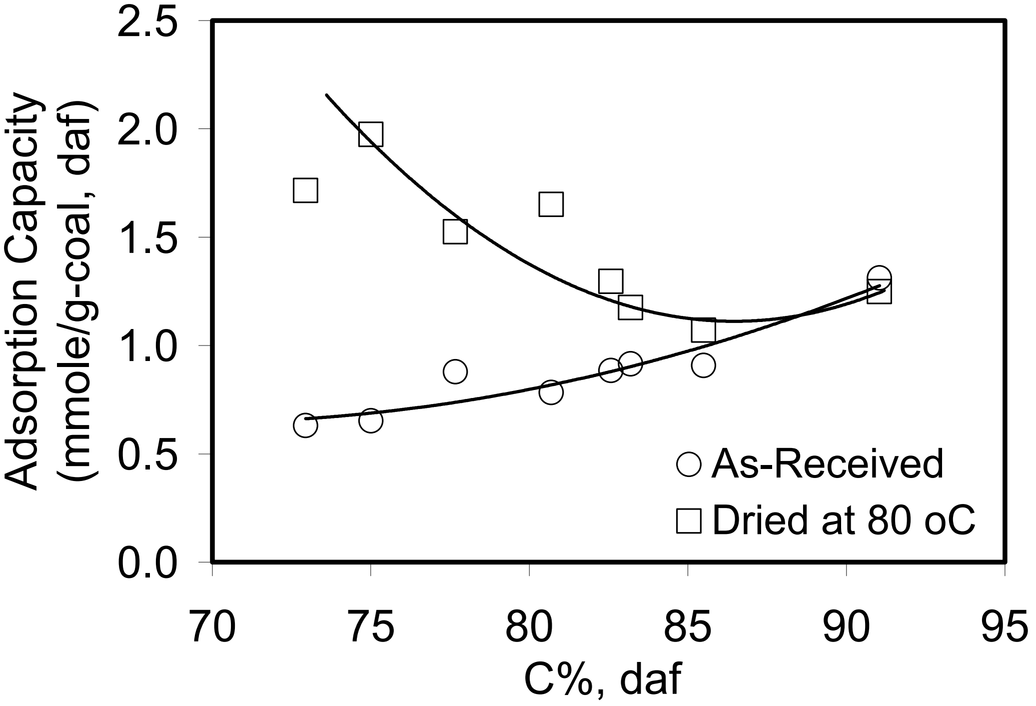

Figure 31. Adsorption capacities of as-received and dried Argonne Premium coals

4.4.2.2 Surface Areas of As-Received and Dried Argonne Coals: The surface areas of the as-received and dried Argonne coals were calculated from Eq.(49) using the CO_2 adsorption capacities which were obtained by applying the modified D-A equation (Eq.46) to the full range of high-pressure data. Figure 32 shows these calculated surface areas along with the surface areas of different ranks of coal from the literature, which were calculated from data obtained under low-pressure experimental conditions.(24,29) Because the volumetric effects are small at low pressures, the literature data obtained at low pressures give surface areas which are supposedly free of error.(156) In addition, because the swelling is small at low pressures, it is expected that the error in these surface areas would be smaller. The comparison in Figure 32 shows that the surface areas estimated from high pressure adsorption isotherms employing modified D-A equation, Eq.46, are in good agreement with the low pressure adsorption isotherm values reported by Larsen et al.(24) for the same set of dried Argonne coals. Only Illinois No.6 coal failed to give equivalent results for the dried coal whereas the agreement was excellent for the as-received coal. The disagreement for the Illinois No.6 coal is probably due to the different method of drying as described by Larsen et al.(24). Note that good agreement is obtained only if the volumetric effect is taken into account. When the volumetric effects were not accounted for in the high-pressure data, the surface areas estimated for the dried coals were about 40% higher for high rank coals and 60% to 100% higher for low rank coals.

The surface areas of the as-received coals were smaller than the surface areas of dried coals. The decrease in the surface area was especially significant for the lower rank coals, probably due to the accessibility of CO_2 to those pores which were occupied and/or blocked by the water. The surface areas of non-Argonne coals reported by Gan et al.(29) were randomly distributed around the surface areas for the dried and as-received Argonne coals. The variation of the coal surface area with rank could be due to different extents of drying. For example, Larsen et al.(24) dried the Argonne coals overnight at room temperature and 10^{-6} Torr, except for the Illinois No.6 coal. The Illinois No.6 coal was dried in an all-glass vacuum apparatus at room temperature and 10^{-5} Torr. In addition, the amount of coal sample used, may affect the degree of drying for each coal. Gan et al.(29) dried their coal samples at 130 °C for 1 hr and then degassed at 130 °C and 10^{-5} Torr for 12 h. It is clear that the degree of drying affects the adsorption capacity and the calculated surface area of coals. This indicates that the surface areas of coals reported by different labs may compare poorly due to a lack of a standard experimental procedure.

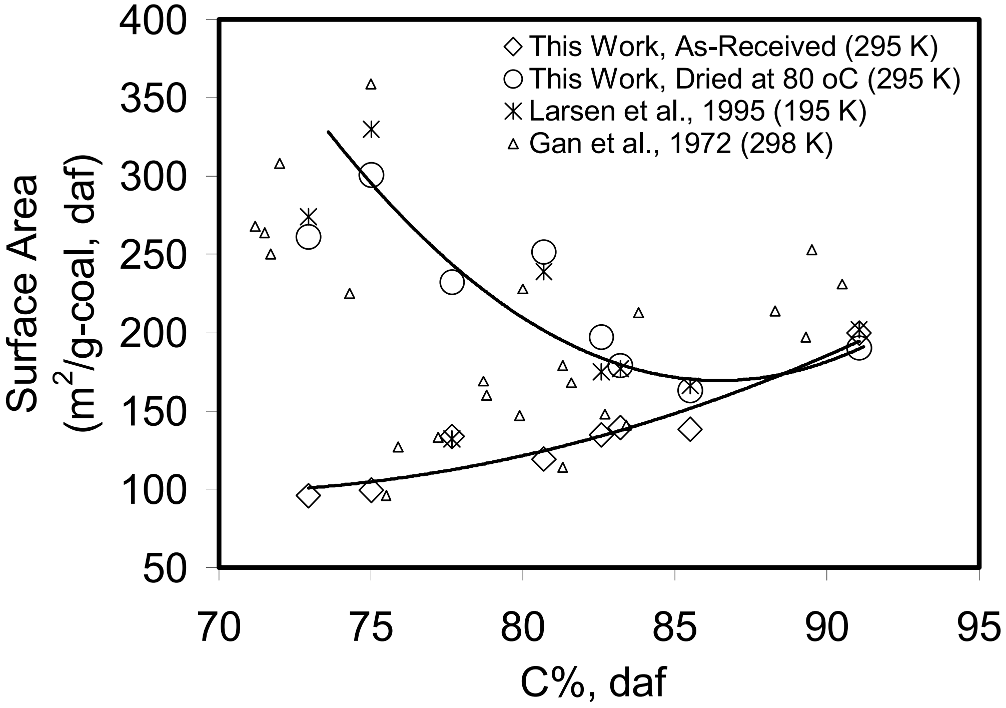

Figure 32. Surface areas of Argonne Premium coals as a function of carbon content

4.4.2.3 Isosteric heat of Adsorption: The isosteric heat of adsorption for CO_2 adsorbed on each as-received and dried Argonne coals was calculated from the characteristic heat of adsorption employing Eq.(50). As shown in Figure 33, the isosteric heat of adsorption is a 'U-shape' with carbon content for dried coals displaying a distinct minimum at about 82% carbon and a corresponding heat of adsorption of about 25.3 kJ/mole. The range of heats of adsorption for these dried coals was small, between 25.3 and 27.3 kJ/mole, regardless of the coal rank. The literature data is limited for comparison for all the Argonne coal samples studied. The agreement between the isosteric heat of adsorption obtained for the Illinois No.6 using the modified D-A equation and that reported by Glass and Larsen(231) using the inverse gas chromatography is excellent (Figure 33). The isosteric heats of adsorption for CO_2 display an almost linear dependence on rank for as-received coals. The range of heats of adsorption for these coals was also small between 23 and 25 kJ/mole, regardless of the coal rank. The range and magnitude of these isosteric heats of adsorption values suggests a physical-adsorption mechanism rather than a chemisorption mechanism.(231)

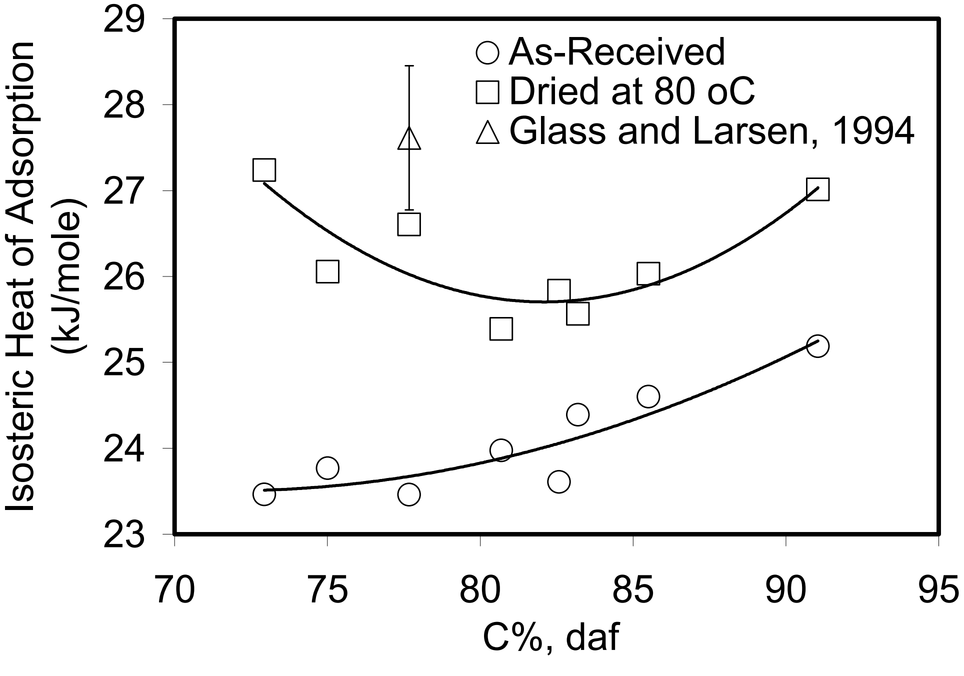

Figure 33. Isosteric heat of CO_2 adsorption on as-received and dried Argonne Premium coals

4.4.2.4 Average Pore Sizes of As-Received and Dried Argonne Coals Obtained with CO_2:

The average pore size of each coal was calculated using the Dubinin-Astakhov exponent, *j*, and the characteristic heat of adsorption, E_o, in Eq.(51). Figure 34 shows the average pore sizes of the as-received and dried Argonne coals. In this figure, the pore sizes of as-received coals shows a decreasing trend from 1.35 nm to 1.15 nm with carbon content. On the other hand, the pore sizes of the dried coals exhibits a maximum at about 82 C%, where all the pore sizes were calculated to be between 1.05 nm and 1.20 nm. This is consistent with the X-ray scattering measurements of the layered structure of the Argonne coals which indicate that the distance between layers decreases as the rank of the coal increases (see Table 2). The pore sizes estimated here are lower than the literature.(90,92) For instance, Amarasekera et al.(90) estimated the pore sizes of four brown coals, one medium-volatile subbituminous coal, one high-volatile subbituminous coal, and one low-volatile bituminous coal by CO_2 adsorption and found the pore sizes to be 1.3-1.4 nm independent of coal rank. Radovic et al.(92) reported the micropore sizes of coals estimated from the CO_2 adsorption isotherms to be between 1.58-1.91 nm. However, they did not account the volumetric effects on the shape of the adsorption isotherms, which may result in larger pore sizes being reported. The pore sizes of as-received coals are always higher than those of the dried coals, indicating that the pores were collapsing as a result of drying. This finding is in good agreement with the collapsing of pores upon removal of water from the coal structure(91).

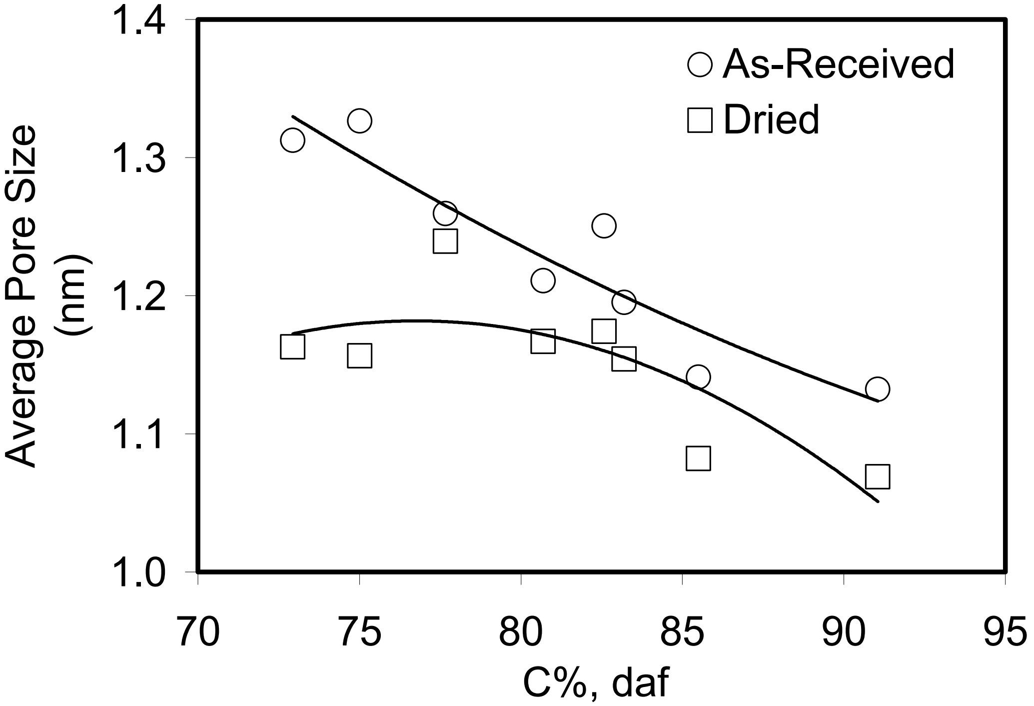

Figure 34. Average Pore sizes of Argonne Premium coals estimated from CO_2 adsorption isotherms at 22 ^{o}C

4.4.2.5 Volumetric Effects: Figure 35 shows the change in volume for dried and as-received Argonne coals, which were estimated from the adsorption isotherms of CO_2 over the 3.8 MPa range studied. The volume change for dried coals is a typical 'U-shape' with rank while it is nearly flat for the as-received coals. The volume change for dried coals is about 60% for low rank coals and about 20% for high rank coals whereas the volume change for each rank of the as-received coals is about 10%. Because the presence of the moisture occupies the adsorption sites in coal and/or block the apertures to the pores available for adsorption, CO_2 cannot access the pores in the as-received coals in the same manner as helium. Therefore, the change in volume is small for the as-received coals. The volume change for the as-received coals is smaller than the volume change for the dried coals clearly indicating that moisture can play an important role in coal swelling.

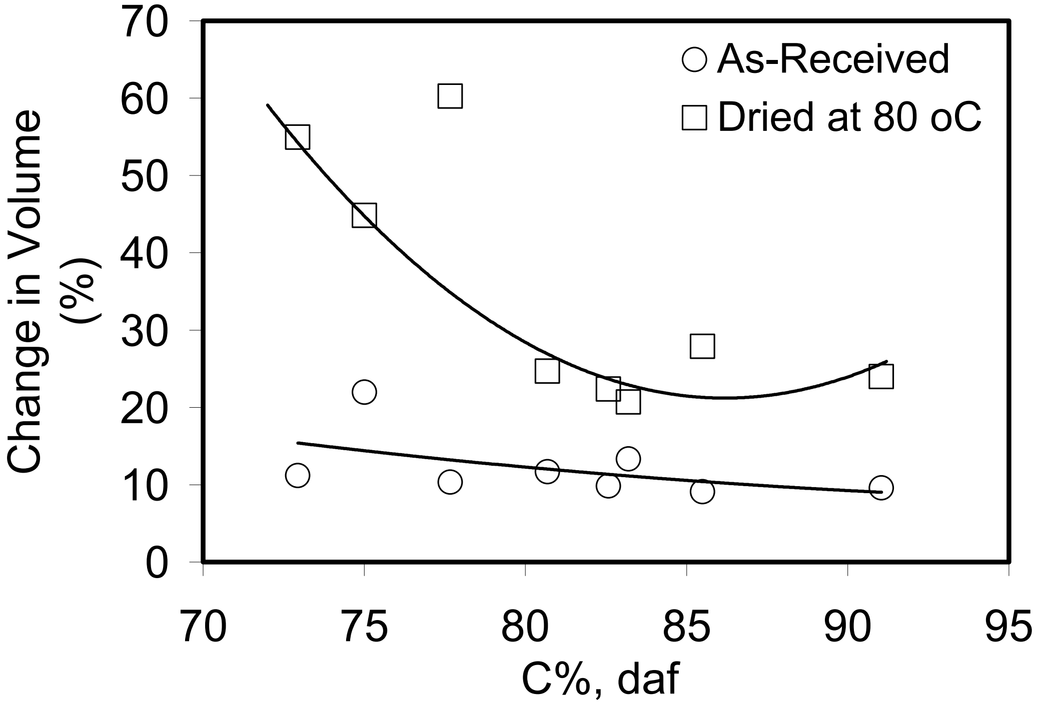

Figure 35. Estimated volume change during the adsorption measurements at 3.8 MPa

On the other hand, comparison of Figure 35 to Figure 22 shows that the trend in the volume change upon CO_2 adsorption on dried coals is similar to that seen for the volume change due to the moisture loss. This can better be seen from the relationship between the percent volume change estimated from the adsorption isotherms of CO_2 on Argonne coals and the shrinkage of these coals as a result of the moisture loss estimated from the helium expansion method as shown in Figure 36. There is an excellent relationship between the shrinkage due to moisture loss and swelling upon CO_2 adsorption of coals where estimated volume change for the Illinois No.6 was not included in the regression analysis. This implies that the shrinkage resulted from the moisture loss for the dried coals can be restored upon the CO_2 adsorption as CO_2 is also known as a swelling agent for coals. However, the volume change due to adsorption is about 21% higher than the volume change due to moisture loss. The volume effects are the origin of the rectilinear shape of the adsorption isotherm at high pressures. When these volume changes were not considered in the evaluation of the adsorption isotherm data, the estimated values of the physical constants in the absolute adsorption model equation would be overestimated.

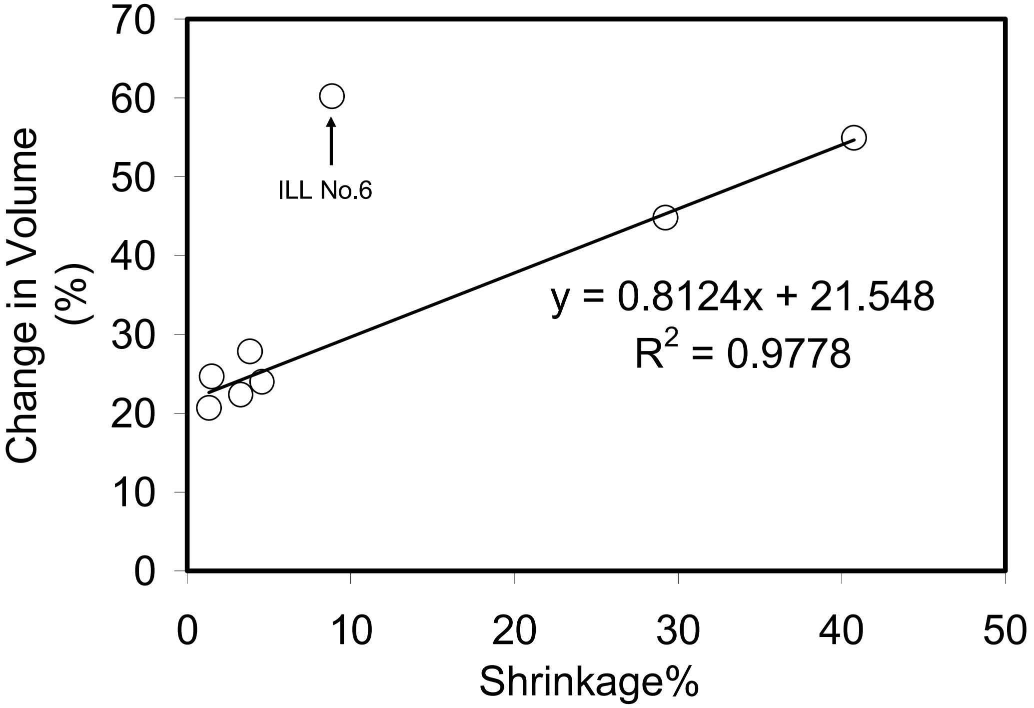

Figure 36. Comparison of the percent volume change estimated from the adsorption isotherms of CO_2 on Argonne coals to the shrinkage of these coals as a result of the moisture loss estimated from the helium expansion method (Volume change for the Illinois No.6 was not included in the regression analysis)

4.4.3 Absolute Adsorption Isotherms of CO_2 on Coals (n^{abs})

The amount of CO_2 adsorbed on Argonne coals was calculated using the Dubinin-Astakhov equation, Eq.(52), once the curve fit parameters were estimated from the best fit solution of Eq.46 for the adsorption isotherm data. Figure 37 shows the absolute adsorption isotherms of CO_2 on eight as-received and dried Argonne Premium coals. As shown in Figure 37a and b, the storage capacity of as-received coals could be as much as 20 to 40 Sm^3-CO_2 per ton of coal, and the volume change could be up to 8%, depending on the rank of the coal. On the other hand, the storage capacity increases for the dried coals. As shown in Figure 37c and d, the storage capacity could be from 25 to 60 Sm^3-CO_2 per ton of dried coals, and the expected volume change could be from 10 to 40% at pressures up to 4 MPa, again depending on the rank of the coal. The volume change is in good agreement with the literature data where the expansion of coals were reported as the dimensional change as shown in Figure 8 rather than the volumetric changes obtained from the CO_2 adsorption isotherms. However, these values were obtained at laboratory conditions where the coal samples are free to expand. At in-seam conditions, because the coal is water-saturated and constrained due to overburden pressure exerted by the overlying strata, these capacities and volume changes may not be realized.

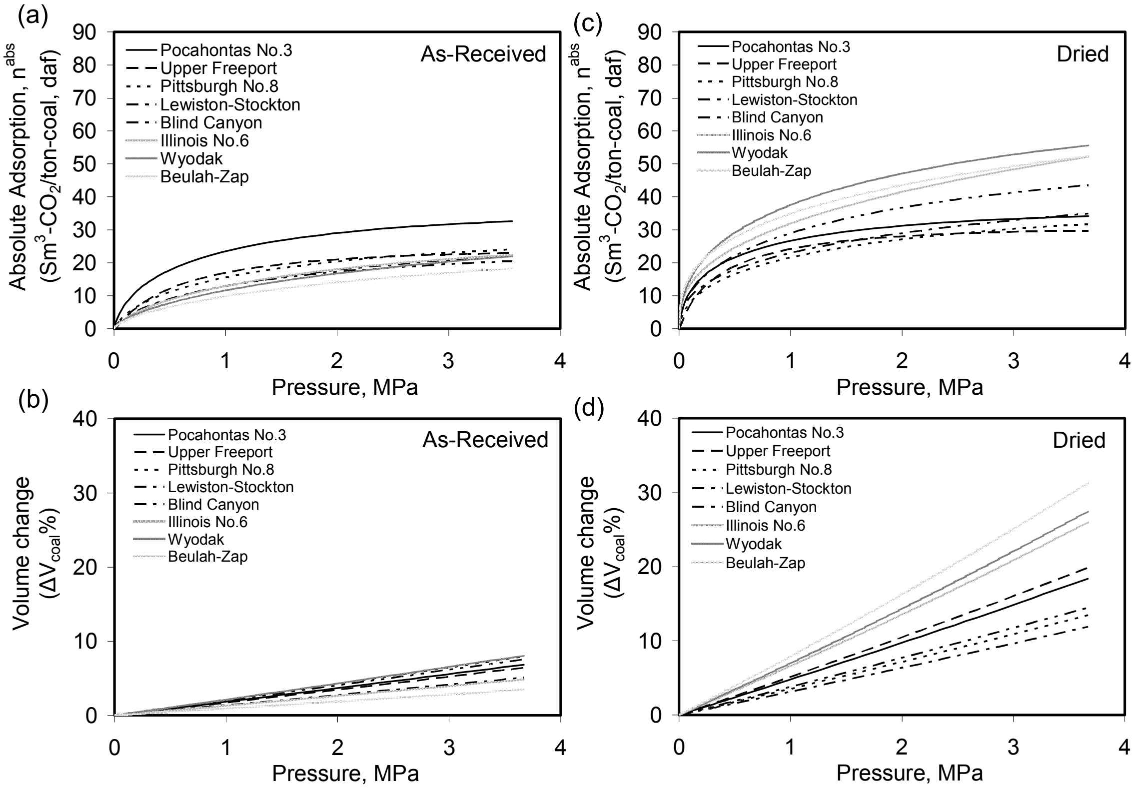

Figure 37. Calculated absolute adsorption (n^{abs}) and volumetric changes for CO_2 adsorption onto (a) as-received and (b) dried Argonne Premium coals

4.4.4 Quantifying the Effect of Moisture on the Adsorption Capacity of Coals

Figure 38 shows the adsorption isotherms of CO_2 on the Argonne Premium Pittsburgh No.8, Illinois No.6, Wyodak, and Beulah-Zap coals partially dried to different moisture contents. The lines are the best fit with the modified Dubinin-Astakhov equation, Eq.46, to the adsorption isotherm data. As shown in the figure, small amount of CO_2 is adsorbed on moist coals. The amount of CO_2 adsorbed appeared to increase as more and more moisture was removed from the as-received coals.

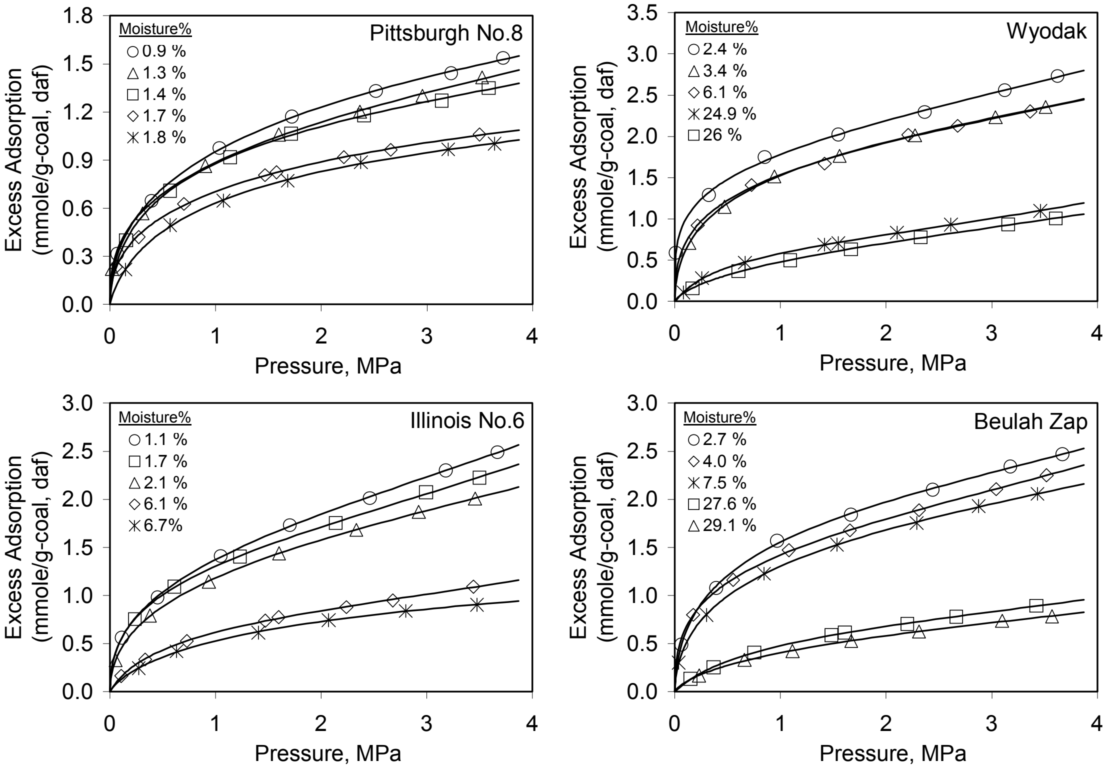

Figure 38. Effect of moisture content on the adsorption capacity of CO_2 on coals

The adsorbed CO_2 on moist coals can be represented by the Ettinger's empirical equation, Eq.(28). The linear form of Eq.(28), which has been employed for the adsorption of CH_4 on moist coals by Joubert et al.$^{(40)}$, is

$$\frac{n_d}{n_w} = A\,m + 1 \qquad \left(m \le m_c\right) \tag{53}$$

There are reasons not to employ Eq.(53) to quantify the CO_2 adsorption on moist coals. For instance, it is difficult to obtain a coal sample with free of moisture. Removing the tightly bound ‘unfreezable’ water may require harsh conditions such as drying of the coal at higher temperatures which may denature the coal structure.(232) Thus, it may not be possible to estimate the adsorbed amount for the dried coal, n_d, accurately. As discussed above, the use of adsorbed amount, n_w or n_d, may be erroneous due to the effect of volumetric changes on the shape of the excess adsorption isotherms of coals. As a result, the coefficient (A) would vary with pressure as evidenced by Joubert et al.(40). Here, we suggest using the adsorption capacity of coals obtained from the best curve fit resolution of the adsorption isotherms rather than the adsorbed amount at any pressure. Therefore, the adsorption of CO_2 on partially dried coals was estimated using the adsorption capacity (n_o) instead of the adsorbed amount (n) at any pressure. In contrast to Joubert et al.,(40) the Ettinger’s equation, Eq.(53), was modified such that

$$\frac{1}{(n_o)_w} = \frac{A}{(n_o)_d} m + \frac{1}{(n_o)_d} \qquad (m \le m_c) \tag{54}$$

where $(n_o)_w$ and $(n_o)_d$ are the adsorption capacity of moist and moisture-free coals estimated from fitting the adsorption isotherm data to the modified D-A equation, Eq.46, respectively.

Figure 39 shows the linear relationship between the inverse of the adsorption capacity of partially dried coals, $1/(n_o)_w$, *vs.* their percent moisture content, m. Thus, one can obtain the adsorption capacity of a moisture-free coal, $(n_o)_d$, from the intercept, and the coefficient, A, from the slope using the intercept value as $A = slope / Intercept$.

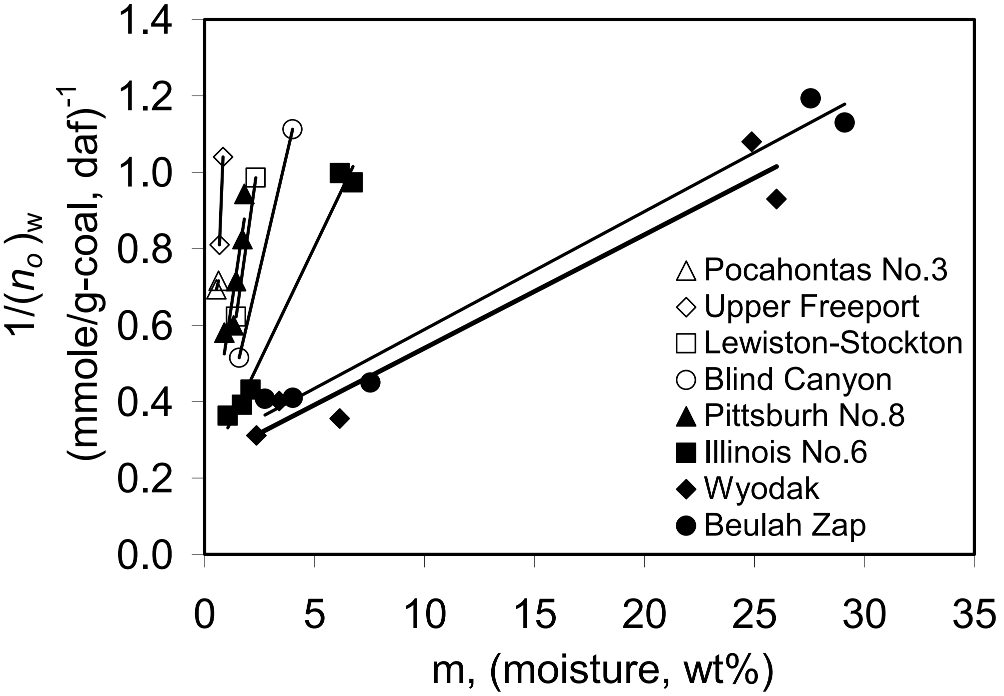

Figure 39. The linear relationship between the inverse of the adsorption capacity of partially dried coals, $1/(n_o)_w$, *vs.* moisture content of coals, m

On the other hand, the linear relationship between the CO_2 adsorption capacity of partially dried coals and their moisture content can well be represented by a linear relationship

$$(n_o)_w = (n_o)_d - \alpha\, m \qquad (m \le m_c) \tag{55}$$

where α is the slope of the linear relationship between the adsorption capacity of partially dried coals and their percent moisture content, in mmole CO_2 per g-coal, daf, per percent moisture content (wt%). As shown in Figure 40, the CO_2 adsorption capacity of partially dried coals, $(n_o)_w$, decreases linearly with moisture content, m. This is consistent with the CH_4 adsorption on moist coals as reported by several investigators.(41,39)

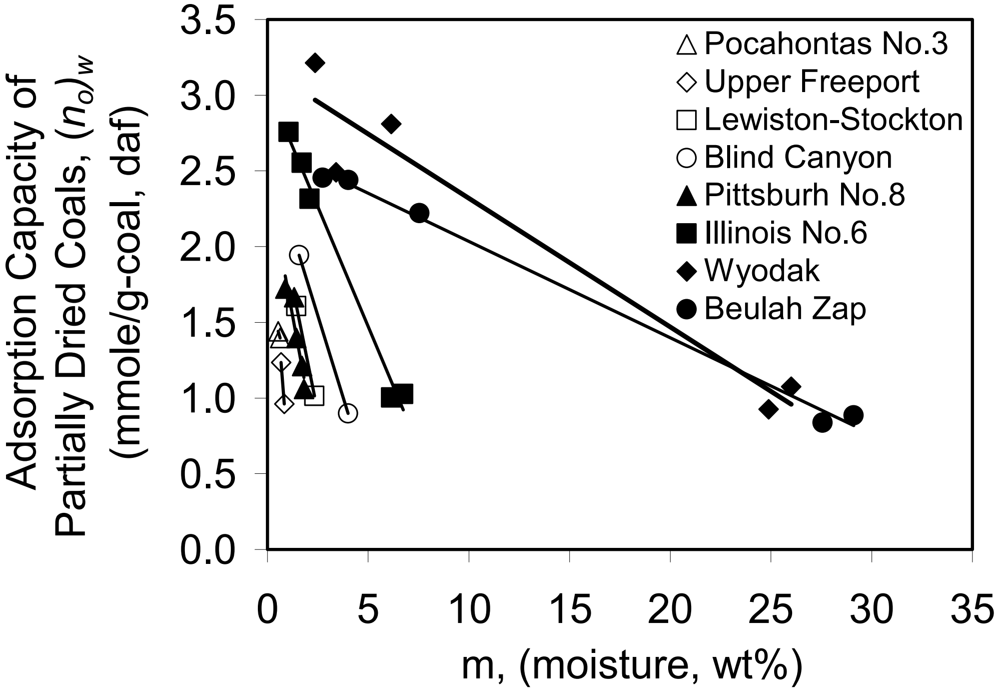

Figure 40. Effect of moisture content on the adsorption capacity of CO_2 on coals

Figure 41 shows the comparison of the coefficient, A, in moisture%$^{-1}$, and the slope, α, in mmole CO_2 per g-coal, daf, per percent moisture content (wt%), and the adsorption capacity of moisture-free coals, $(n_o)_d$, obtained from Eq.(54) and Eq.(55), respectively. As shown in Figure 41a, the coefficient values and the slope values vary with different ranks of coals. However, they show similar trend. Nevertheless, as shown in Figure 41b, the adsorption capacities of medium rank moisture-free coals obtained using Eq.(55) are generally less than those obtained using Eq.(54). The adsorption capacities of moisture-free coals obtained using Eq.(54) usually scatters and reports higher adsorption capacities whereas the trend is more consistent when the adsorption capacities of moisture-free coals were obtained employing Eq.(55). Therefore, Eq.(55) seems to be more reliable than the Ettinger et al.'s approach. Consequently, the adsorption capacity of moisture-free Argonne coals should be obtained from the linear relationship between the adsorption capacity of partially dried coals and their moisture contents (Eq.(55)). As a result, the ultimate adsorption capacity of moisture-free Argonne coals is about 2.8 mmole/g-coal, daf basis.

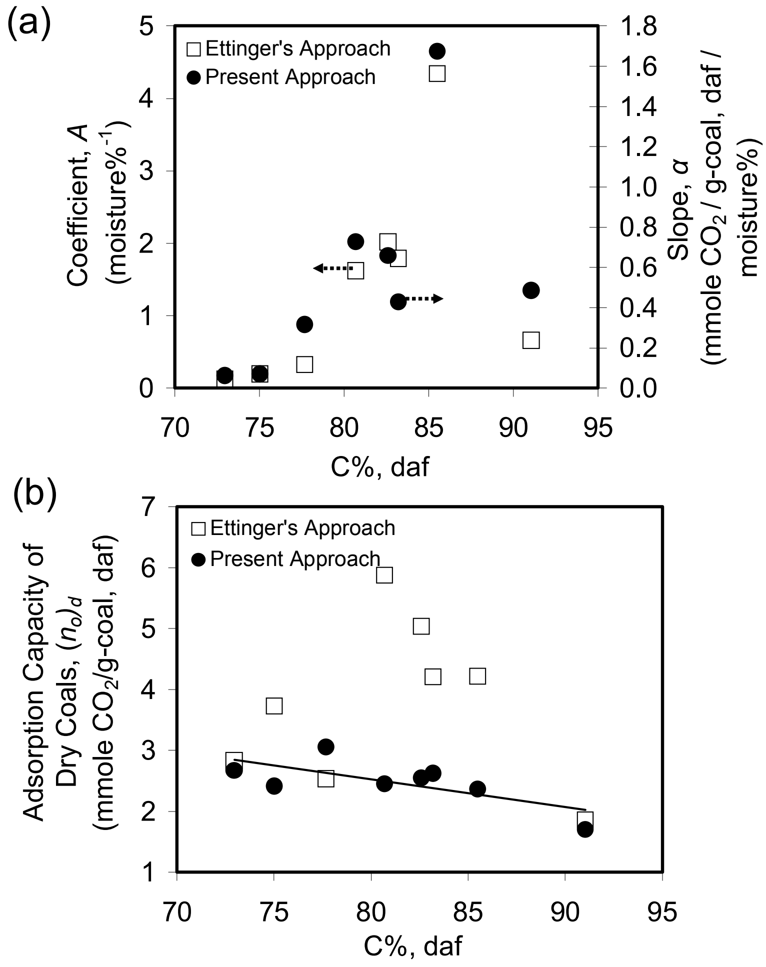

Figure 41. Comparison of the coefficient, *A*, and slope, α, and the adsorption capacities of dry coals, $(n_o)_d$, obtained from Figure 39 employing Eq.(54), suggested by Ettinger et al.$^{(41)}$, and Figure 40 employing Eq.(55)

The slopes (α) of the linear relationships between the adsorption capacity of the partially dried coals and their moisture contents in Figure 40 may provide information about the importance of water to the CO_2 adsorption. Conversion of moisture%, the g water per 100 g coal, to millimoles of water lost per g of coal gives the slope of moles of water lost per mole of CO_2 adsorbed. As shown in Figure 42, for the high rank coals, the slopes appear to be between 0.8 and 1.2 moles of water lost per mole of CO_2 adsorbed. Thus, the effect of moisture on the adsorption may be one of competition between H_2O and CO_2 for the same pore cavity or for the same binding sites in the high rank coals. However, the slopes, moles of water lost per mole of CO_2 adsorbed, become generally greater as one moves through the mid-rank to the low rank coals. The slopes of the Wyodak and Beulah Zap coals are about 8 to 9 moles of water lost per mole of CO_2 adsorbed. Thus, in the case of low rank coals, either many adsorption sites that are active for H_2O adsorption are unfavorable for CO_2 adsorption or clusters of water molecules block the pores or the CO_2 binding sites.

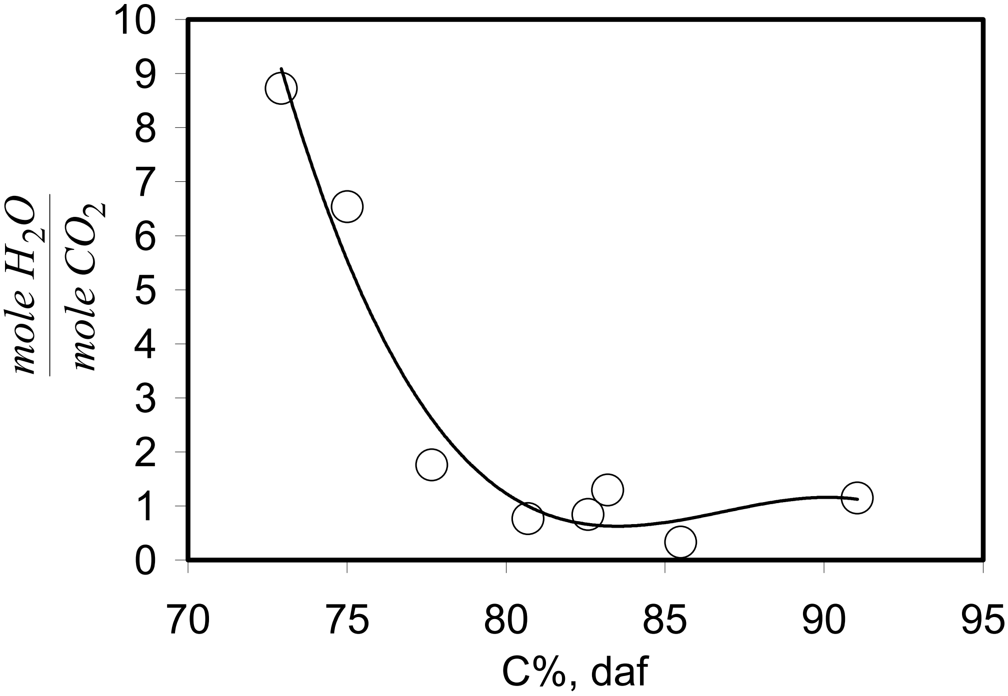

Figure 42. Moles of water lost per mole of CO_2 adsorbed with coal rank

4.4.5 Implication to the Mechanism of CO_2 Adsorption on Moist Coals

Figure 43 illustrates a possible mechanism for the CO_2 adsorption on the moist coals. In this mechanism, coal has a cross-linked layered macromolecular structure associated with both covalent and non-covalent interactions as evidenced by high-resolution transmission electron microscopy (HRTEM)(84,85) and wide-angle X-ray scattering (WAXRS)(86) studies.(233,234,85) Water is held within the coal either in free phase as bulk ‘freezable’ water or in adsorbed as tightly bound ‘unfreezable’ water.(232,235) Because the pores are filled by the water, the only external surface is exposed to the adsorbing gas. As shown in Figure 31 and Figure 40, the adsorption capacity is small for wet coals and it increases as more and more water is removed from coals. As shown in Figure 35, CO_2 cannot penetrate into the moist coals whereas, as water is removed from these pores, it can penetrate in these pores especially for the low rank coals. As shown in Figure 33, the isosteric heat of adsorption for wet coals is smaller than that for dried coals, indicating that the adsorption occurs mostly on the surface rather than within the micropores, where the surface potential for adsorption is high. As shown in Figure 34, the average pore sizes are large for moist coals whereas they shrink and collapse for the dried coals. The extend to which coal swells depends on the relative abundance of covalent cross-links and secondary forces, such as hydrogen bonding ionic interactions, van der Waals interaction in the coal, and on the disruption or re-association of these cross-links by water, CO_2, or any other swelling agents.(236) As shown in Figure 22, coals do shrink upon moisture lost.(215) However, the degree of shrinkage is larger than the volume of the water removed. As shown in Figure 42, as moisture is removed from the coal structure, the available volume is filled by CO_2 for the high rank coals since the shrinkage of high rank coal due to moisture loss is very small. On the other hand, the space available for adsorption as a result of moisture removal was small for low rank coals to be replaced with the adsorbed CO_2. This was expected because, as shown in Figure 22, the volume change (shrinkage) for the low rank coals is high. When the moisture is removed from the low rank coals, only part of the volume of the removed water is filled by CO_2, and the rest of the volume is either collapsed or blocked by water clusters for CO_2 to access the entire pores. Thus, because the preadsorbed water fills the pores and occupies the active sites for adsorption, the CO_2 cannot penetrate into those available sites for adsorption. As a result, lower adsorption capacities would be expected in wet coals.

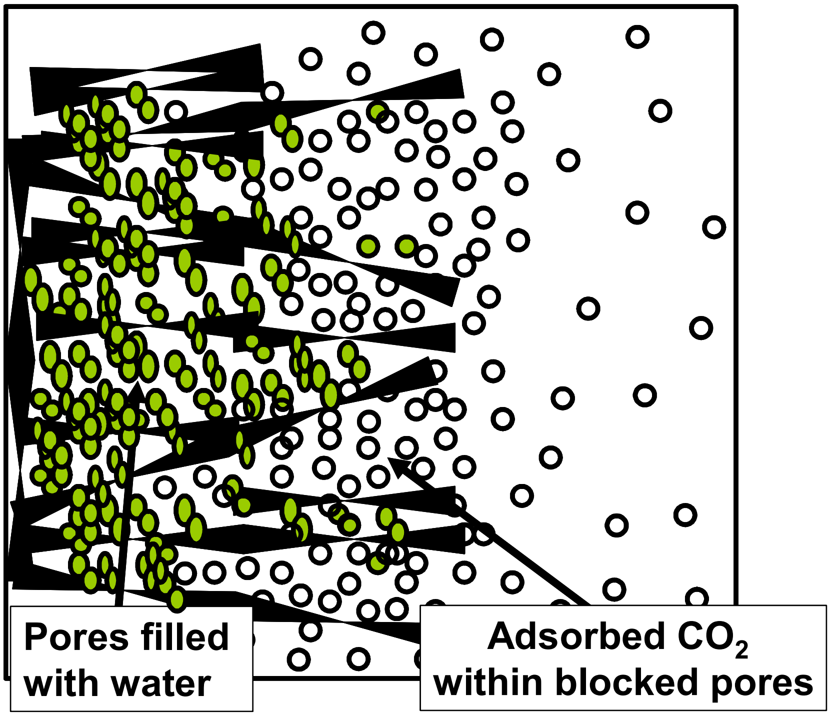

Figure 43. Proposed mechanism of gas adsorption onto a moist coal

4.4.6 Significance to the CO_2 Sequestration Modeling

Coal seams are naturally water-saturated. Although the common practice in coalbed methane (CBM) production is to withdraw the water from the coal seam to reduce the hydrostatic pressure, this only helps reduce the water in the cleat system but it is difficult to completely dry out the coal. Injection of CO_2 may displace the bulk water in the cleat system and it may partially dry out the coal matrix as evidenced from drying of powdered coal samples with supercritical CO_2 at laboratory conditions.(237) However, drying the chunks of coal in-place with supercritical CO_2 would be detrimental. In CO_2 sequestration/ECBM production, a moisture gradient along the coal seam and within the coal matrix is inevitable. Because the presence of moisture significantly decreases the CO_2 adsorption capacities of coals, CO_2 adsorption isotherms of dried coals may not provide the information needed to interpret or model CO_2 sequestration or ECBM production process. The moisture will be present in coal at all times during the sequestration. The presence of pore water will reduce the adsorption capacity of CO_2 either by blocking the path to or by occupying the adsorption sites within the coal matrix.

4.5. EFFECT OF TEMPERATURE ON ADSORPTION ISOTHERMS AND ADSORPTION CAPACITY OF CO_2 ON COALS

The excess adsorption isotherms of CO_2 on the dried Argonne Premium coals were measured by the volumetric method at 22, 30, 40, and 55 ^{o}C and pressures up to 4 MPa as shown in Figure 44. Lines are the best fit to modified Dubinin-Astakhov equation, Eq.46. The saturation pressures at these temperatures, P_s, used in the modified D-A equation, was obtained from Ref.(137) and they are given in Table 9. As shown in the figure, the excess adsorption isotherms show similar rectilinear shape at each temperature. The adsorbed excess amount (n^{ex}) decreases as the temperature increases.

The absolute adsorbed amount (n^{abs}) and the curve fit parameters, such as the adsorption capacity (n_o), the characteristic heat of adsorption (E_o), the Dubinin exponent (j), and the volume change, can be obtained from the best fit curves. The curve fit parameters and the calculated values such as the isosteric heat of adsorption and the average pore size of coals are listed in Table 12 through Table 16.

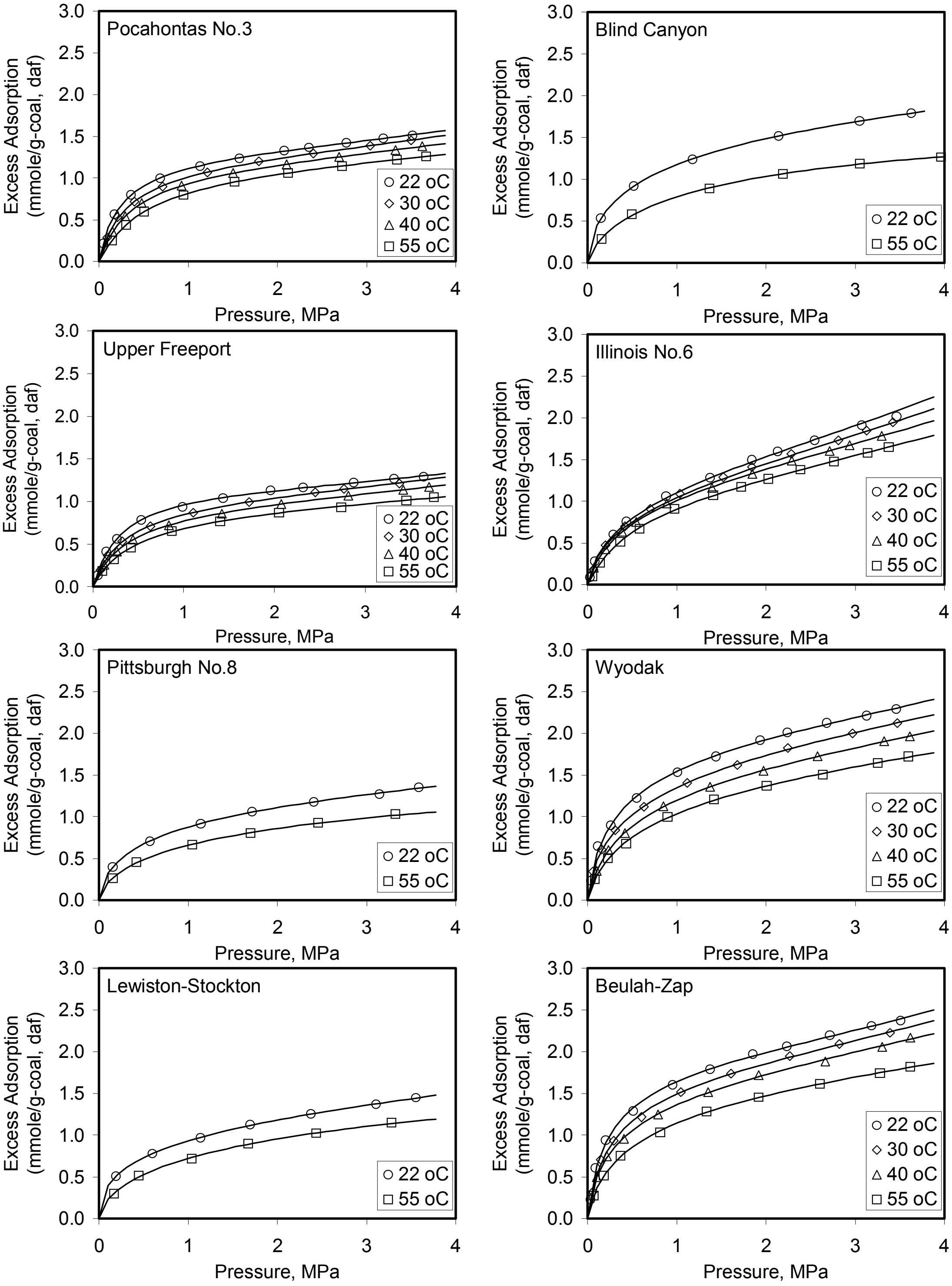

Figure 44. Adsorption isotherms of CO_2 on Argonne Premium coals at 22, 30, 40, and 55 ^{o}C and pressures upto 4 MPa

As shown in Table 12, the adsorption capacity of CO_2 on coals decreases slightly with temperature, however, the difference between the adsorption capacities is not too big with the temperature. As shown in Table 13, the characteristic heat of adsorption for the CO_2 adsorption on dried coals increases slightly with temperature, but, the change in magnitude is very small. As shown in Table 14, the Dubinin exponent does not change with temperature for dried Argonne coals although some deviations were seen at different temperatures showing that the surface heterogeneity was not affected for these dried coals at different temperatures. As shown in Table 15, the average pore size is not altered with temperature for dried Argonne coals similar to the surface heterogeneity predicted from the Dubinin exponent. And, as shown in Table 16, the volume change decreases slightly with temperature, however, it is too small, which is within the expected error range. The effect of temperature on the adsorption isotherms of coals is accounted in the Dubinin coefficient, $D=R\boldsymbol{T}/\beta E_o$. Thus, under different temperatures studied and employing the modified adsorption equation, the physical characteristics of the coals were found not to change with temperature but a slight decrease in the adsorption capacity of coals for CO_2 at increasing temperatures.

Table 12. Effect of temperature on the adsorption capacity (n_o) of CO_2 on Argonne Premium coals, (mmole/g-coal, daf)

Temperature, °C	22	30	40	55
Argonne Coals	adsorption capacity (n_o) (mmole/g-coal, daf)			
Pocahontas No.3	1.19	1.11	1.07	1.05
Upper Freeport	1.02	0.94	0.90	0.86
Pittsburgh No.8	1.17	n/a	n/a	1.49
Lewiston-Stockton	1.30	n/a	n/a	1.40
Blind-Canyon	1.65	n/a	n/a	1.37
Illinois No.6	1.31	1.07	1.13	1.09
Wyodak	1.81	1.77	1.56	1.51
Beulah-Zap	1.74	1.64	1.61	1.60

Table 13. Effect of temperature on the characteristic heat of adsorption (E_o) for CO_2 adsorption on Argonne Premium coals, (kJ/mole)

Temperature, °C	22	30	40	55
Argonne Coals	characteristic heat of adsorption (E_o) (kJ/mole)			
Pocahontas No.3	27.4	27.1	27.2	26.9
Upper Freeport	25.9	26.3	26.9	27.7
Pittsburgh No.8	24.0	n/a	n/a	20.5
Lewiston-Stockton	24.8	n/a	n/a	22.4
Blind-Canyon	23.5	n/a	n/a	23.9
Illinois No.6	22.8	25.5	26.1	26.1
Wyodak	25.7	25.0	25.4	25.9
Beulah-Zap	28.1	27.9	28.5	27.3

Table 14. Effect of temperature on the Dubinin exponent (*j*)

Temperature, ^{o}C	22	30	40	55
Argonne Coals		Dubinin exponent (*j*)		
Pocahontas No.3	2.5	2.5	2.6	2.6
Upper Freeport	2.7	2.5	2.4	2.5
Pittsburgh No.8	1.6	n/a	n/a	1.3
Lewiston-Stockton	1.3	n/a	n/a	1.5
Blind-Canyon	1.5	n/a	n/a	1.8
Illinois No.6	1.8	2.3	2.1	2.3
Wyodak	1.9	1.7	1.9	1.9
Beulah-Zap	2.2	2.2	2.0	1.9

Table 15. Effect of temperature on the average pore sizes of coals estimated from the CO_2 adsorption isotherms, (Å)

Temperature, ^{o}C	22	30	40	55
Argonne Coals		average pore size (Å)		
Pocahontas No.3	10.4	10.4	10.4	10.4
Upper Freeport	10.5	10.5	10.4	10.3
Pittsburgh No.8	11.1	n/a	n/a	11.8
Lewiston-Stockton	11.1	n/a	n/a	11.4
Blind-Canyon	11.2	n/a	n/a	11.0
Illinois No.6	11.2	10.6	10.6	10.6
Wyodak	10.7	10.9	10.8	10.7
Beulah-Zap	10.3	10.4	10.3	10.5

Table 16. Effect of temperature on the percent volume change ($\Delta V_{coal}\%$) for CO_2 adsorption on Argonne Premium coals

Temperature, °C	22	30	40	55
Argonne Coals	percent volume change ($\Delta V_{coal}\%$)			
Pocahontas No.3	16.6	18.2	17.3	14.7
Upper Freeport	14.2	16.4	15.5	12.9
Pittsburgh No.8	12.8	n/a	n/a	2.1
Lewiston-Stockton	14.2	n/a	n/a	8.6
Blind-Canyon	14.0	n/a	n/a	7.2
Illinois No.6	38.0	46.5	42.1	39.2
Wyodak	28.2	26.3	27.7	23.2
Beulah-Zap	32.0	33.0	31.3	22.2

4.6. EFFECT OF pH ON ADSORPTION ISOTHERMS AND ADSORPTION CAPACITY OF CO_2 ON COALS

4.6.1 pH Treatment/Leaching of Coals

Six of the eight Argonne premium coals: Pocahontas No.3, Upper Freeport, Pittsburgh No.8, Lewiston-Stockton, Blind Canyon, and Illinois No.6 (Table 7) were treated with dilute acid (H_2SO_4) and dilute base (NaOH) solutions as described in the experimental section. Attempts to similarly treat the Wyodak and Beulah-Zap coals were unsuccessful because the base treatment resulted in a suspension which could be separated neither *via* filtration through a 45 µm filter nor centrifugation. Therefore, Wyodak and Beulah-zap coals were excluded from further evaluation. Table 17 shows the ash content of the pH treated coals.

The goal of these experiments was to determine what effect surface charge might have on the adsorption capacity of different coals. In a sequestration environment, the surface charge of the coal would be determined by the liquid phase in contact with it. In this study, pH values of 2, 7, and 10 were chosen as representative of the central and extreme values that might be encountered in a sequestration environment. To differentiate between the effects of mineral dissolution and surface charge, all samples were initially treated with weak acid solution prior to the final pH adjustment. As can be seen, the magnitude of the ash removal was usually highest at the end of the initial acid and base treatments, and it was lower for the subsequent pH adjustments. For example, the ash content of Pocahontas No.3 coal decreased from 4.77% to 3.92 % after the initial acid and base treatments. The subsequent pH adjustments reduced the ash content to 3.82 % and 3.71 % for the neutralization and final acid treatment steps, respectively. Similarly, the ash content for the Pittsburgh No.8 was reduced from 9.25 % to 8.86 %, 8.59 %, and 8.42 % after the initial acid and base treatment, neutralization, and final acid treatment steps, respectively. However, the ash content for the Illinois No.6 coal was reduced more evenly from 15.48 % to 14.55 %, 13.30%, and 12.75 % after the initial acid and base treatment, neutralization, and final acid treatment steps, respectively. Overall, very little ash was removed from any coal during the pH treatment using dilute acid and base solutions at room temperature and most of the ash content was retained in the coal samples. Although, the magnitude of the ash removal was largest after the initial acid and base treatments, subsequent pH treatments did extract additional inorganics. Thus, considering the isoelectric pH for coals (pH~3.8),(161) the pH treated coal samples were prepared as negatively charged and positively charged at the end of their final basic and neutral pH treatments, and the acidic treatment, respectively, with small mineral matter removal.

Table 17. Ash Content of Leached Coals

Coals	Ash Content (%, moisture free basis)			
	Non-Treated	Base Washed	Neutralized	Acid Washed
Pocahontas No.3	4.77	3.92	3.82	3.71
Upper Freeport	13.18	12.87	12.69	12.43
Pittsburgh No.8	9.25	8.86	8.59	8.42
Lewiston-Stockton	19.84	18.90	18.79	18.47
Blind Canyon	4.71	4.11	3.75	3.27
Illinois No.6	15.48	14.55	13.30	12.75

The filtrates of the pH-treated coal samples were analyzed for their metal contents. Table 18 shows the analytical results obtained on the filtrates collected from the initial acid treatment, base treatment, neutralization, and final acid treatment of the coals. The initial acid treatment removed mostly calcium (Ca), magnesium (Mg), and iron (Fe). Of the calcium reported in the coal,(207) 60-90% was removed during the initial acid washing and 80-100% of it was removed by the combination of washes. Calcite dissolution is the most likely the source of calcium under acidic conditions.

$$CaCO_3 + H^+ \rightarrow Ca^{+2} + HCO_3^- \tag{56}$$

Filtrates from the base washing contained mostly potassium (5-40% of the K within the coals). Subsequent neutralization with H_2SO_4 consumed little acid. The filtrates contained predominately K, Ca, and Mg. The final acidification removed mostly Fe and some additional Ca, K, and Mg. The only samples to show iron extraction upon the initial acidification were the

Pocahontas and Blind Canyon coals. The presence of acid extractable iron in these samples supports to the tentatively reported presence of siderite in these samples.(207) In some cases, iron was not removed during the initial acidification, but was removed during the final acidification subsequent to the base treatment. In these cases, pyrite may have been removed according to reactions (57) and (58).(159) The hematite formed in reaction (57) is insoluble in base but soluble in acid as shown in reaction (58).

$$30NaOH + 8FeS_2 \rightarrow 4Fe_2O_3 + 14Na_2S + Na_2S_2O_3 + 15H_2O \tag{57}$$

$$Fe_2O_3 + 3H_2SO_4 \rightarrow Fe_2(SO_4)_3 + 3H_2O \tag{58}$$

Other metals (Mn, P, Sr, Ba, and Mg), when present, are removed in only small amounts (5-10%). Aluminum silicate clays are only slightly reactive toward acidic and basic solutions at low temperatures. However, it should be cautioned that the lack of solubility of a certain mineral under these conditions may not be fully indicative of the dissolution that may occur over prolonged periods. In this study, equilibration was considered complete when the pH remained constant over three hours. In an actual sequestration scenario, contact time will be on the order of decades. The equilibrium concentrations and the composition of the mineral phases that will ultimately be present are probably predicted better using geochemical models.

Table 18. Metals removed from coals (mg/g-coal)

	Pocahontas No.3				Upper Freeport			
	Initial Acid Washing	Base Washing	Neutralization	Acid Washing	Initial Acid Washing	Base Washing	Neutralization	Acid Washing
Al	0.025	0.001	0.000	0.022	0.030	-0.001	0.000	0.053
Ba	0.000	0.001	0.001	0.001	0.000	0.000	0.000	0.001
Ca	3.453	0.097	0.127	0.059	2.297	0.007	0.537	0.292
Fe	0.911	0.000	0.000	0.346	0.130	-0.002	0.000	2.094
K	0.070	0.090	0.052	0.098	0.031	0.077	0.216	0.173
Mg	0.202	0.002	0.017	0.019	0.043	0.000	0.005	0.007
Mn	0.012	0.000	0.000	0.001	0.017	0.000	0.000	0.003
Na	N/A				N/A			
P	0.003	0.000	0.000	0.003	0.005	0.000	0.000	0.005
S	N/A				N/A			
Si	-0.007	-0.009	-0.013	-0.035	0.029	0.001	0.017	0.131
Ti	0.000	0.000	0.000	0.000	0.000	0.000	0.000	0.000
Sr	0.034	0.002	0.003	0.002	0.008	0.000	0.002	0.002
	Pittsburgh No.8				Lewiston-Stockton			
Al	0.021	0.000	0.000	0.020	0.032	0.045	0.002	0.034
Ba	0.001	0.000	0.000	0.002	0.000	0.000	0.000	0.001
Ca	1.511	0.049	0.055	0.136	0.209	-0.001	0.005	0.066
Fe	0.060	-0.002	0.000	0.832	0.359	0.008	0.000	0.132
K	0.072	0.339	0.450	0.264	0.074	0.018	0.089	0.354
Mg	0.036	0.000	0.002	0.005	0.064	0.002	0.000	0.017
Mn	0.009	0.000	0.000	0.001	0.005	0.000	0.000	0.001
Na	N/A				N/A			
P	0.054	0.000	0.000	0.002	0.001	0.002	0.000	0.004
S	N/A				N/A			
Si	0.018	0.036	0.021	0.071	0.039	0.035	-0.010	-0.004
Ti	0.000	0.000	0.000	0.000	0.000	0.000	0.000	0.000
Sr	0.012	0.001	0.001	0.003	0.005	0.000	0.000	0.003
	Blind Canyon				Illinois No.6			
Al	0.440	0.000	0.000	0.190	0.056	-0.001	0.000	0.016
Ba	0.000	0.000	0.001	0.000	0.000	0.000	0.000	0.001
Ca	2.193	0.120	1.114	0.437	2.460	2.111	2.969	0.675
Fe	0.658	-0.002	0.000	0.246	0.233	-0.001	0.000	0.690
K	0.180	0.111	0.153	0.239	0.064	0.020	0.099	0.103
Mg	0.221	0.001	0.009	0.013	0.066	0.003	0.006	0.005
Mn	0.003	0.000	0.000	0.001	0.055	0.000	0.003	0.007
Na	N/A				N/A			
P	0.001	0.000	0.000	0.002	0.013	0.000	0.000	0.003
S	N/A				N/A			
Si	0.137	0.150	0.119	0.150	0.036	0.001	-0.011	0.024
Ti	0.000	0.000	0.000	0.000	0.000	0.000	0.000	0.000
Sr	0.029	0.002	0.005	0.004	0.006	0.002	0.002	0.001

pH is often an important parameter in natural systems,(238) and it will change during sequestration process. Because of the formation of carbonic acid, the pH within the sequestration media will drop to around 2 at high CO_2 pressures, favoring the dissolution of calcite. This may be beneficial if mineral dissolution provides better access to the organic matrix, but would be detrimental if dissolution of cap-rock resulted.

4.6.2 Adsorption Isotherms of CO_2 on Leached Coals

Figure 45 compares the CO_2 excess adsorption isotherms of the pH treated Argonne Premium coals to the original untreated sample. The isotherms were measured at 22 ^{o}C and pressures up to 4 MPa. The lines represent the best-fit values using the modified Dubinin-Astakhov equation, Eq.46. The error calculated for the experimental apparatus was less than 3% (Appendix D). As shown in Figure 45 the adsorption isotherms of CO_2 on pH treated coals have rectilinear shapes similar to those of the untreated coals. The excess adsorbed amounts of CO_2 on the untreated and pH treated coals are close. For the base treated coals, the excess adsorption is smaller than the untreated and acid-treated coals, especially for the lower rank coals. For the acid-treated coals, the excess adsorption is higher than the untreated and base-treated coals. For the neutralized coals, the excess adsorption is between the acid- and base-treated coals and usually follows the isotherms of the untreated coals.

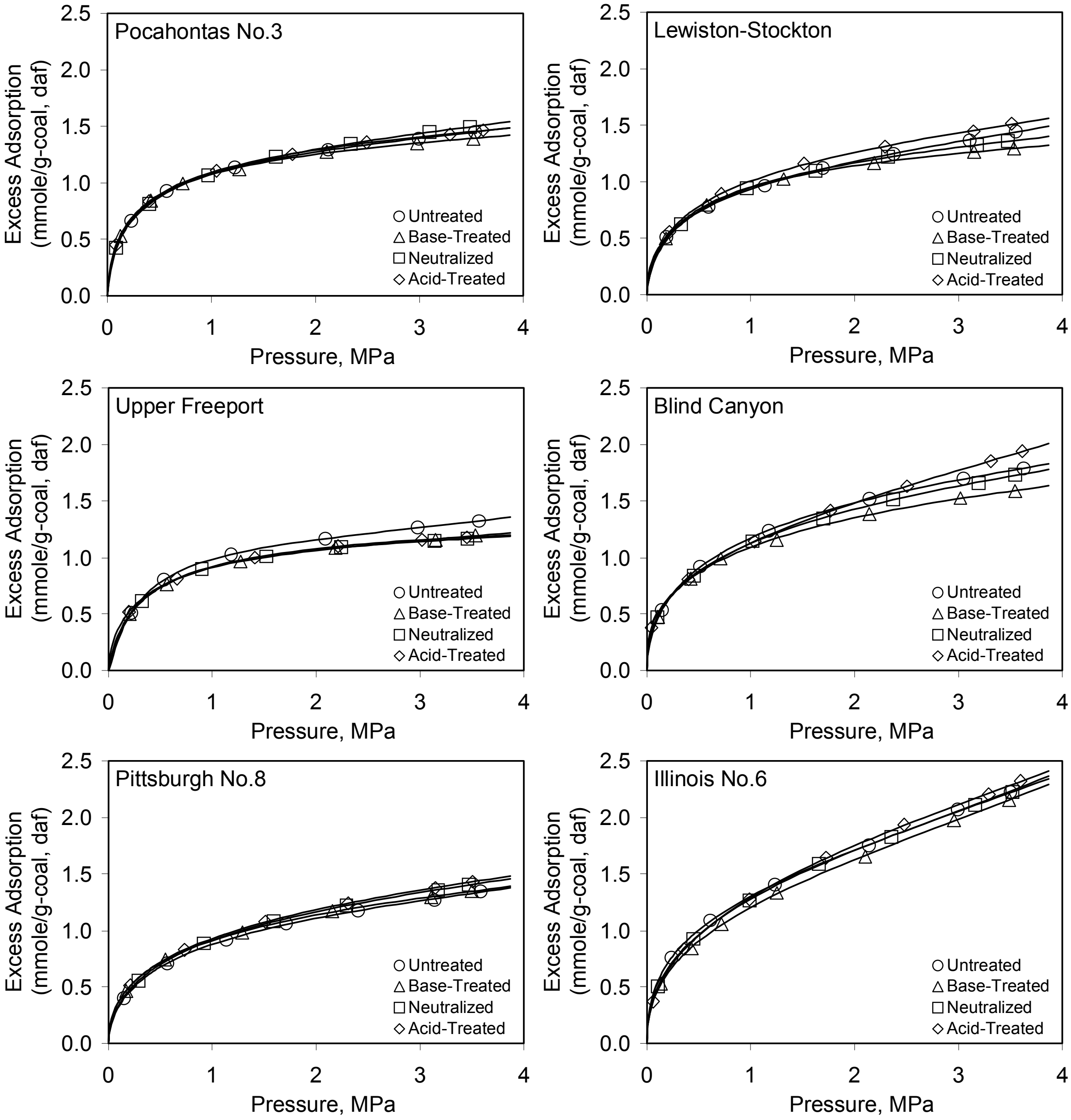

Figure 45. Adsorption isotherms of leached and non-leached Argonne Premium coals

4.6.3 Effect of pH on the Physical Parameters

4.6.3.1 CO_2 Adsorption Capacity of the Leached Argonne Coals: The absolute adsorption capacities were obtained by fitting the excess adsorption isotherm data to Eq.46. Figure 46 compares the adsorption capacity of CO_2 on the pH treated and untreated coals. The absolute adsorption capacities usually increase with increasing ash removal. As shown in the figure, the adsorption capacity of CO_2 on base treated coals is generally lower compared to the untreated coal samples. The adsorption capacity of CO_2 on the neutralized coals is more or less the same as the untreated coals whereas it is greater for the acid treated coals. Because the removal of mineral matter increases the aperture size of pores and creates extra pore space for adsorption,(174) the removal of the mineral matter from coals is expected to increase the adsorption capacity. In general, this is true for the pH-treated coals. As shown in Figure 46, the adsorption capacity increases as more and more ash is removed. However, as can be seen in the figure, although the mineral matter removal during the initial acid and base treatments is larger than that removed during the subsequent neutralization and acidification, the adsorption capacity of the base treated coals was still lower than that of the untreated coals. The neutralized coals have more or less the same adsorption capacity as the untreated coals even though more mineral matter was removed. The acid treated coals always have higher CO_2 adsorption capacities and higher ash removals.

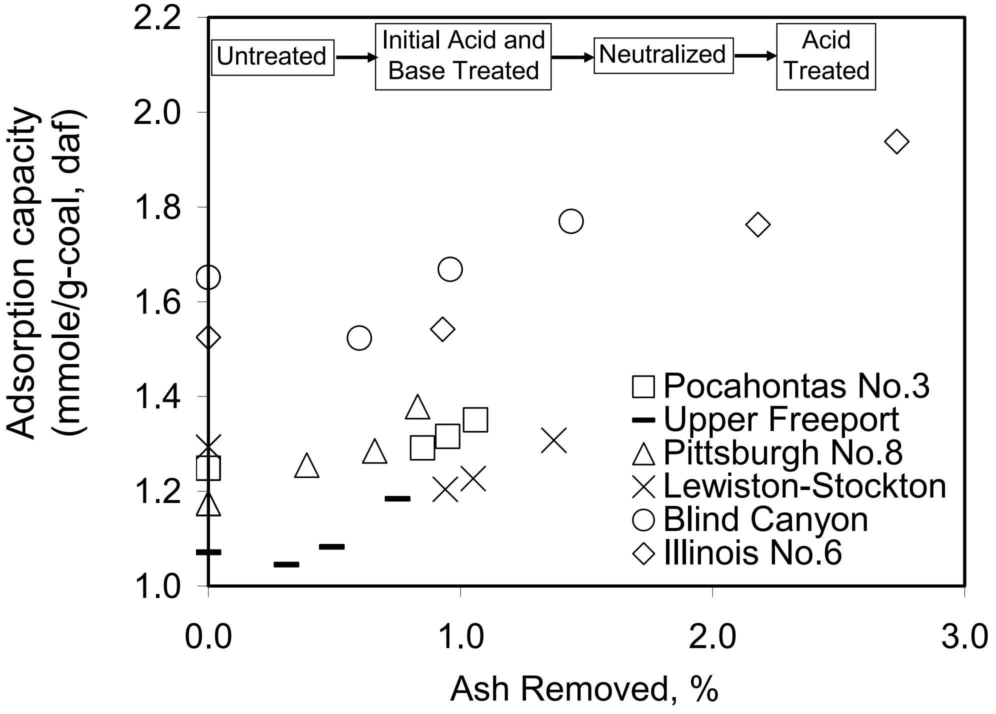

Figure 46. Adsorption capacity of CO_2 on leached Argonne Coals

The relatively lower adsorption capacity of the base treated coals, albeit their reduced ash contents, may be explained by the effect of surface charge and its effect on the 3-D structure of coals. At pH greater than the isoelectric point (about 3.8 for coals), most of the coal surface is negatively charged. The removal of the Ca and Mg from the coal structure during the acid and base treatments as well as during the neutralization steps may convert the carboxylic groups in their ionic forms. At pH of 2, most of the coal surface is positively charged. The removal of the Ca and Mg from the coal structure at the end of acidic treatment may convert the carboxylic groups in their protonated forms rather than in their salts. The negatively charged surface would possess stronger surface interactions, which make the coal structure more rigid. Consequently, the 3-D structure of the coal may have been affected by the negatively or positively charged surfaces of the coal.

4.6.3.2 Isosteric Heat of Adsorption: Figure 47 shows the isosteric heat of adsorption of CO_2 on the pH treated and untreated coals. As shown in the figure, the isosteric heat of adsorption is generally higher for the base treated coals compared to the acid treated, neutralized, and untreated coals. The isosteric heat of adsorption is generally similar for the neutralized and untreated coals whereas the isosteric heat of adsorption is generally lower for the acid treated coals. The literature data related to the isosteric heat of adsorption of pH treated coals is limited. Here, the agreement between the isosteric heat of adsorption obtained for the Illinois No.6 using the modified D-A equation and that reported by Glass and Larsen(231) using the inverse gas chromatography is excellent. The range and magnitude of all of the values suggests a physical-adsorption mechanism rather than a chemisorption mechanism.

It is recognized that the heat of adsorption is related to the degree of interaction between the adsorbed CO_2 and the chemical groups on the surfaces of the coal as well as the pore size of the coal.(231,31) Therefore, the higher isosteric heat of adsorption for the base treated coals may be due to the stronger interaction of CO_2 with the negatively charged surface groups. Or, as will be shown next, the higher isosteric heat of adsorption may be due to the narrower pore sizes resulting from the pH treatment. A wider pore diameter results in a low isosteric heat of adsorption, and a narrower pore size results in a higher isosteric heat of adsorption due to the surface potential in the pore.(27)

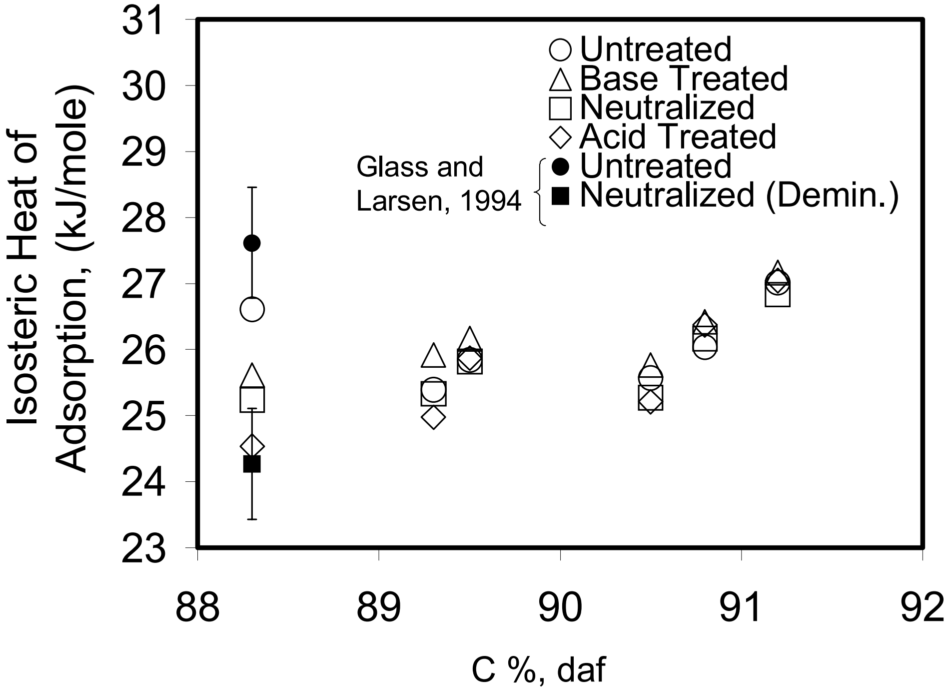

Figure 47. Isosteric heat of CO_2 adsorption on leached Argonne Premium coals

4.6.3.3 Average Pore Sizes of the Leached Argonne Coals Reported by CO_2: The average pore sizes of pH-treated coals were calculated from Eq.(51). Figure 48 shows the average pore size of the pH-treated and untreated coals. As shown in the figure, the average pore size for the base treated coals is generally lower compared to the acid treated, neutralized, and untreated coals. The pore sizes are generally similar for the neutralized and untreated coals. Whereas, the average pore size for the acid treated coal is generally higher compared to the others. The data suggest that removal of ash from coals creates extra pore space in pH treated coals, which, as discussed earlier, affects both the adsorption capacity and the isosteric heat of adsorption of CO_2 on coals.

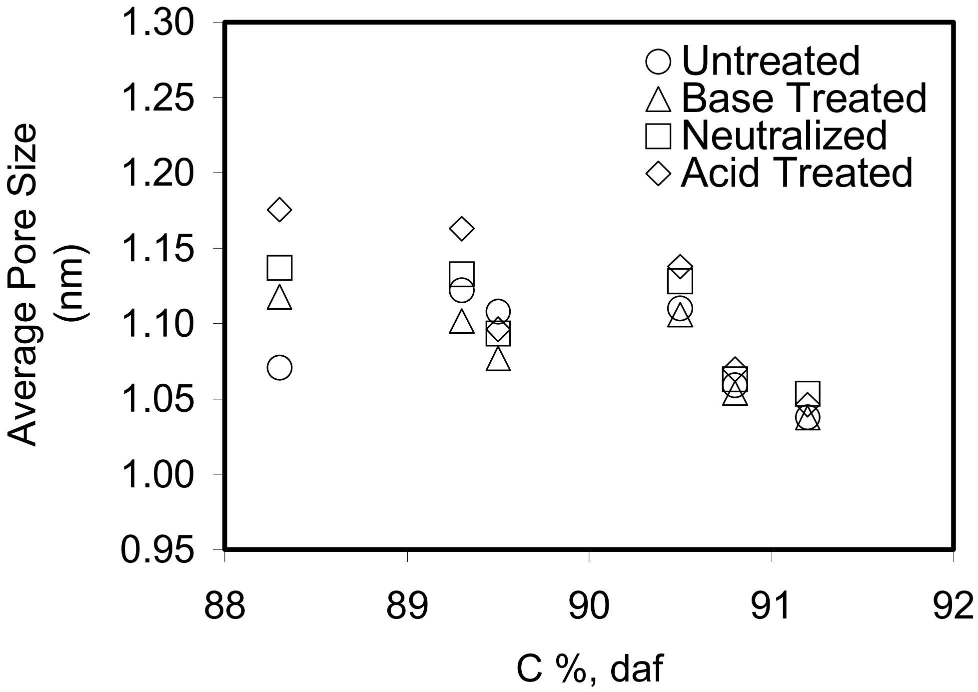

Figure 48. Average Pore sizes of leached coals estimated from CO_2 adsorption isotherms

4.6.3.4 Volumetric Effects: Figure 49 shows the estimated overall effect of the volumetric changes on the adsorption isotherm measurement over the pressure range used. The magnitude of the volume effects for the pH treated coals is less than the volume effects obtained for the untreated coals. The smaller volume change indicates a more rigid 3-D structure. The treatment of coals with acidic and basic solutions extracts the Ca and Mg, and accordingly the pores may become large enough that there is no limitation to the access of either helium or CO_2 to the pores.

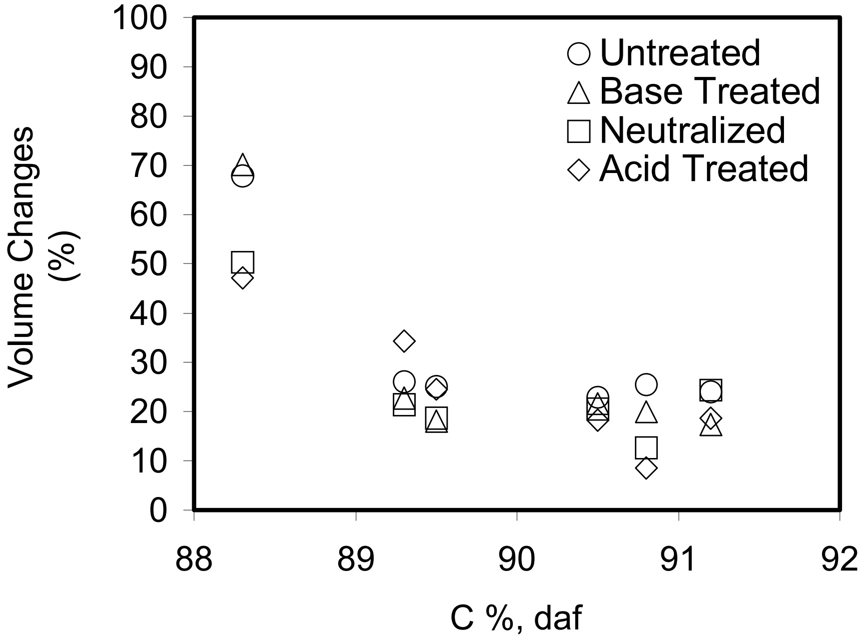

Figure 49. Estimated volume change during the adsorption measurements at 4 MPa

4.6.3.5 Importance of pH to the CO_2 Sequestration: Even if initially dry, the coal seam will certainly become wet as a result of drilling operations, fracturing of the coal bed and over-lying strata, and the deposition of a combustion gas which may contain residual water of combustion. Thus, an aqueous phase will be present and will vary in composition according to its source and the nature of the coal bed and the surrounding minerals with which it is in contact. In natural systems, pH is often an important parameter(238) and it will change during sequestration. Because of the formation of carbonic acid, the pH within the sequestration media will drop up to around 2 at high CO_2 pressures, favoring the dissolution of calcite. This may be beneficial if mineral dissolution provides better access to the organic matrix and increase the permeability within the cleat system. But, it would be detrimental if dissolution of cap-rock resulted.

4.7. SUPERCRITICAL CO_2 ADSORPTION ON COALS

CO_2 is in the gaseous state at room temperature and atmospheric pressure, but it becomes a supercritical 'fluid' at temperatures and pressures greater than its critical temperature and pressure. The critical temperature and pressure for CO_2 are 31.1 ^{o}C and 7.38 MPa, respectively. Considering the geothermal gradient of about 0.029 ^{o}C/m,(239) and a hydrostatic gradient of about 0.01 MPa/m,(240) CO_2 will be a gas at depths less than about 1000m, and supercritical in deeper coal formations. Therefore, CO_2 can be a compressed gas, a liquid, or a supercritical fluid depending on the *in-situ* conditions of the coal seam. Here, we studied the adsorption and desorption of CO_2 on the Argonne Premium coals at temperature of 55 ^{o}C and pressures up to 15 MPa. At 55 ^{o}C and pressures greater than 7.38 MPa used in this study, CO_2 was a supercritical fluid.

Figure 50 shows the adsorption and desorption isotherms of CO_2 on each coal. The error bars show the expected error as estimated from the error analysis (Appendix D) for the manometric gas adsorption apparatus used. The lines represent the best fit of the adsorption isotherm data to Eq.46. As shown in Figure 50, the adsorption isotherms showed almost Langmuir-like to rectilinear shape behavior at pressures up to 10 MPa. At pressures greater than 10 MPa, the excess adsorbed amount increased dramatically. As can be seen in the figure, good fits were obtained employing the modified D-A equation, Eq.46. Following the adsorption, the excess desorption data of CO_2 from each coal was obtained. There was significant hysteresis between the excess adsorption and desorption isotherms for all ranks of coal. During the initial desorption steps, the excess amount increased as if more adsorption took place, and then, decreased in a fashion paralleling the excess adsorption isotherms.

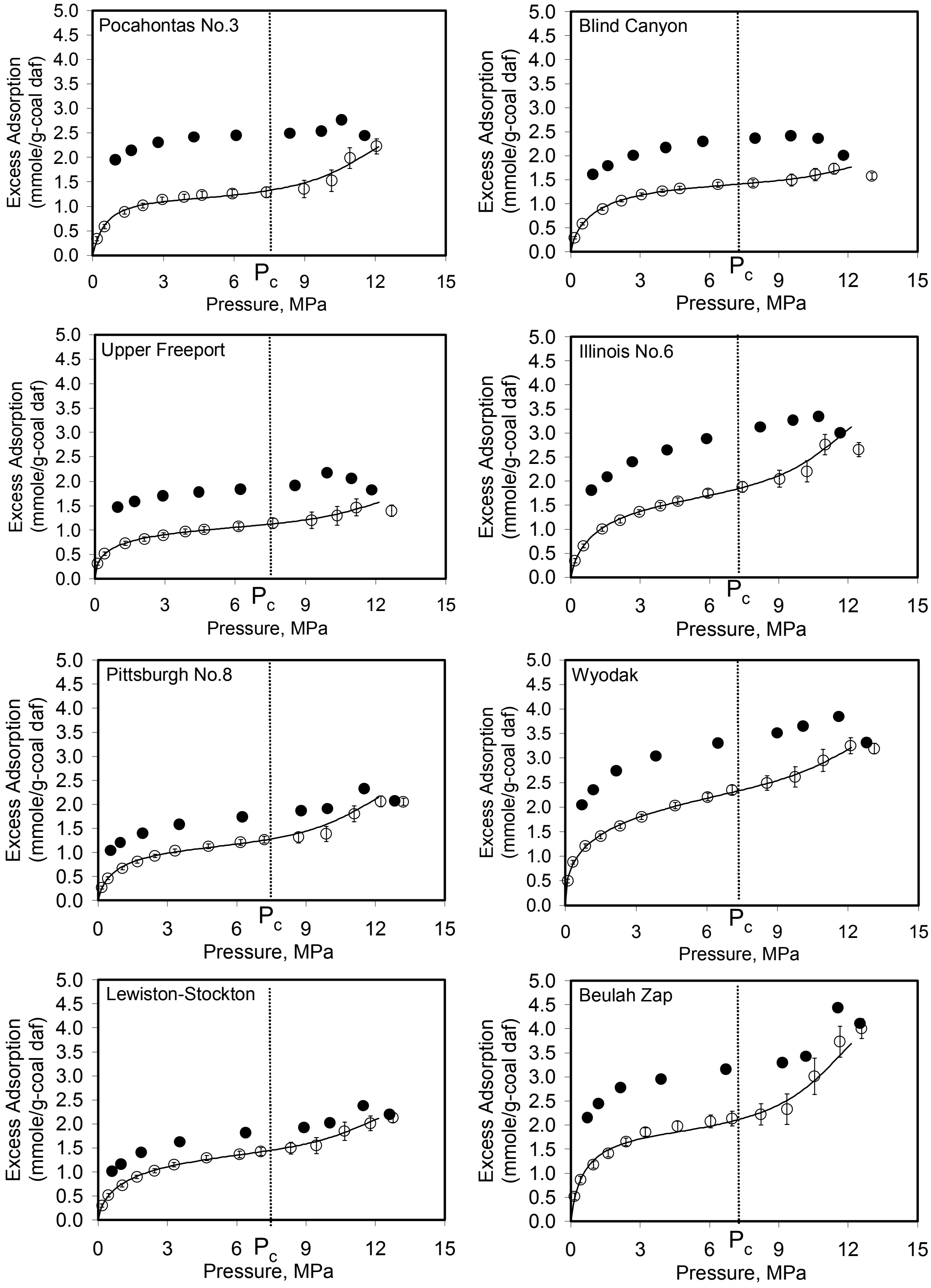

Figure 50. High-pressure adsorption (○) and desorption (●) isotherms of CO_2 on Argonne Premium coals at 55 °C

Unusual adsorption isotherms of CO_2 on coals have been reported in the available literature as shown in Figure 51.(54,55,56) The excess and absolute adsorption isotherms up to 9 MPa are almost Langmuir-like. However, these isotherms at pressures greater than 9 MPa show an unusual behavior. While Zhou's(55) and Hall et al.'s(54) data show trends similar to those in the present study, the data of Krooss et al. (56) are different. In the Kroos study, the absolute adsorption decreased to negative values at pressures between 9 and 10 MPa and increased back to positive values at pressure greater than 10 MPa. Obviously, negative 'absolute adsorption' has no physical meaning.

The high pressures adsorption isotherms appear different from the conventional low pressure adsorption isotherms.(241) For instance, for a rigid solid the measured adsorbed amount generally increases monotonically with pressure at low-pressures, and then, decreases as the pressure further increases, exhibiting a maximum. The adsorption of CO_2 on activated carbon is an example.(178,133) On the other hand, as shown in Figure 51, the adsorption isotherms of, not only CO_2,(32) but also H_2O,(179) CH_3OH,(179) and organic vapors(35,33) on coals and other non-rigid solids such as polymers show a monotonically increasing trend, exhibiting an almost rectilinear shape. Desorption isotherms of these adsorbates typically show a hysteresis.(35,156) The hysteresis between the adsorption and desorption isotherms is related to the material swelling.(156,242)

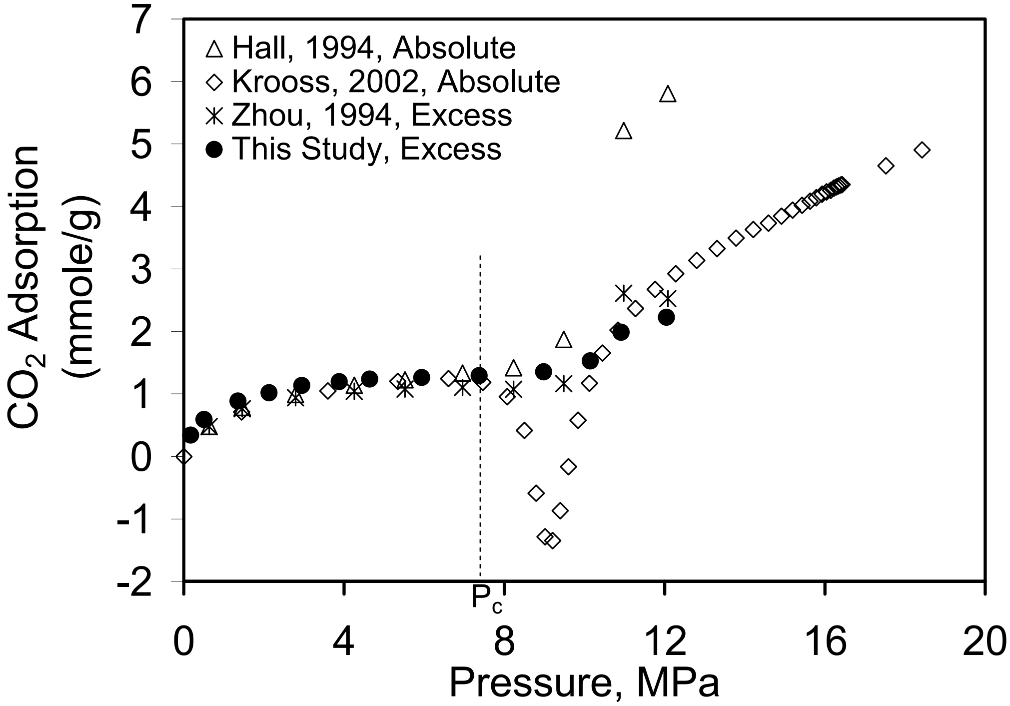

Figure 51. Comparison of the adsorption isotherm of CO_2 on coals at high pressures

In order to address the unusual behavior of CO_2 adsorption on coal at pressures greater than 9 MPa, an error analysis was performed. The details of the error analysis can be found in Appendix D. The error analysis was applied to the operating variables, including the initial and final pressures in the reference and sample cells (± 0.005442 MPa); the volume of the reference cell (± 0.2 %); the void volume in the sample cell (± 0.2 %); the weight of the coal sample (± 0.5%); and the temperature (± 0.1 ^{o}K). The values in the parentheses show the possible variation due to the experimental uncertainties in the measurements. Figure 52 shows the expected error for the excess adsorption isotherm of CO_2 on the Pocahontas coal. As shown in the figure, the expected error associated with the adsorption isotherm data at each step is relatively small at low pressures up to 6 MPa. However, as the pressure increases, the expected error becomes larger.

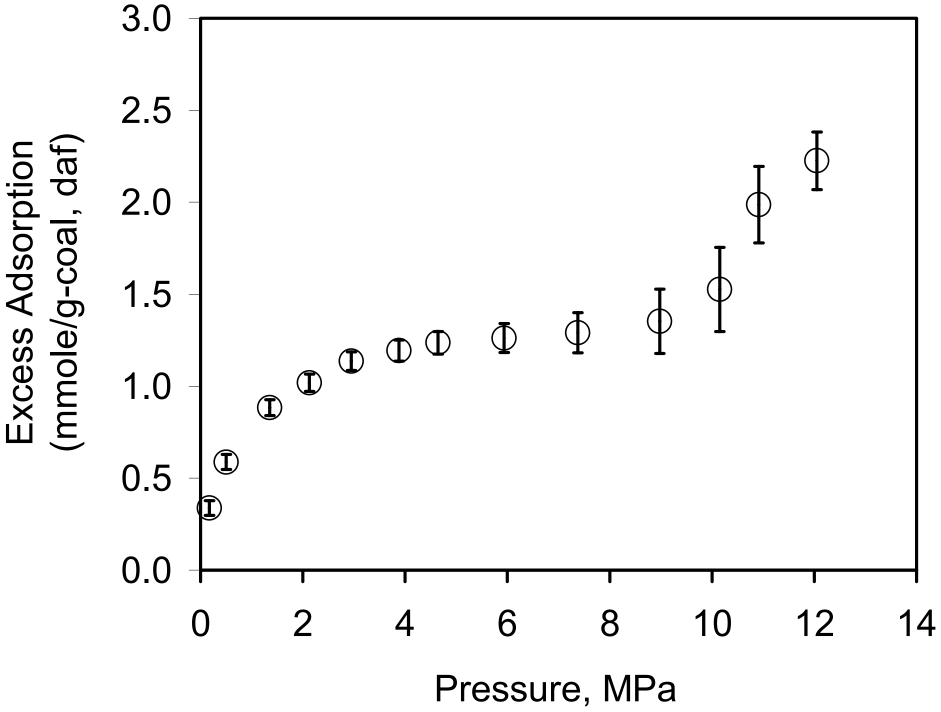

Figure 52. Expected error in the estimation of the adsorption isotherms of CO_2 on Argonne Premium Pocahontas No.3 coal

The sudden increase in the excess adsorption at pressures greater than 9 MPa could be due either to volume changes or to the experimental uncertainties. In the former case, larger volume changes may be realized due to coal swelling or to the supercritical CO_2 extraction of low-molecular-weight compounds from the coal. It is well-known that CO_2 dissolves in water.(243) The solubility of CO_2 increases with pressure and decreases with temperature and water salinity.(244) Increasing CO_2 pressure results in decrease in the pH in the moisture containing coals, which may dissolve the mineral matter. As shown in Section 4.6, dissolution of mineral matter will increase the access of gases to those pores initially blocked by the mineral matter and increase the adsorption capacity of the coal. In addition, supercritical CO_2 is a powerful solvent and extractor.(245) When supercritical CO_2 is contacted with coal, it is expected that the small molecules, such as water, small molecular weight hydrocarbons, and volatile matter, trapped within macromolecular network of the coal may be extracted.(246,237) Here, the unusual behavior of CO_2 adsorption in supercritical region is assumed to be due mostly to the volume change which was, in part, accounted for by the modified D-A equation.

4.7.1 Physical Constants Obtained from Supercritical CO_2 Adsorption on Argonne Coals

By fitting the observed excess supercritical CO_2 adsorption data to the modified D-A equation, Eq.46, the values of the physical constants including the adsorption capacity, characteristic heat of adsorption, Dubinin exponent, and expansion coefficient, n_o, E_o, j and γ, respectively, were obtained. To determine the effect of increasing pressure, these values were estimated for increasingly larger pressure ranges, using only the first few data points of the excess adsorption isotherm initially at about 2 MPa, progressively using more of the data points for the subsequent values, and finally using the full range of data at about 12.317 MPa, which is the theoretical saturation pressure for CO_2 at 55 ^oC (see Table 9). The physical parameters obtained over the various pressure ranges are summarized in the following sections.

4.7.1.1 Adsorption Capacity of Supercritical CO_2 on Dried Argonne Coals: Figure 53 shows the adsorption capacity of CO_2 on dried Argonne coals as obtained by fitting the excess adsorption isotherm data over increasing pressure ranges to Eq.46. As shown in the figure, the general trend for the adsorption capacity is to increase as pressure increases up to 10 MPa. At pressures greater than 10 MPa, the adsorption capacity decreases slightly. The adsorption capacity of the Beulah Zap coal showed a different maximum at 5 MPa, after which the capacity decreased as the pressure increased further. As will be discussed later, the increase in the adsorption capacity can be related to pore volume increase as a result of the swelling of coal during the CO_2 adsorption.

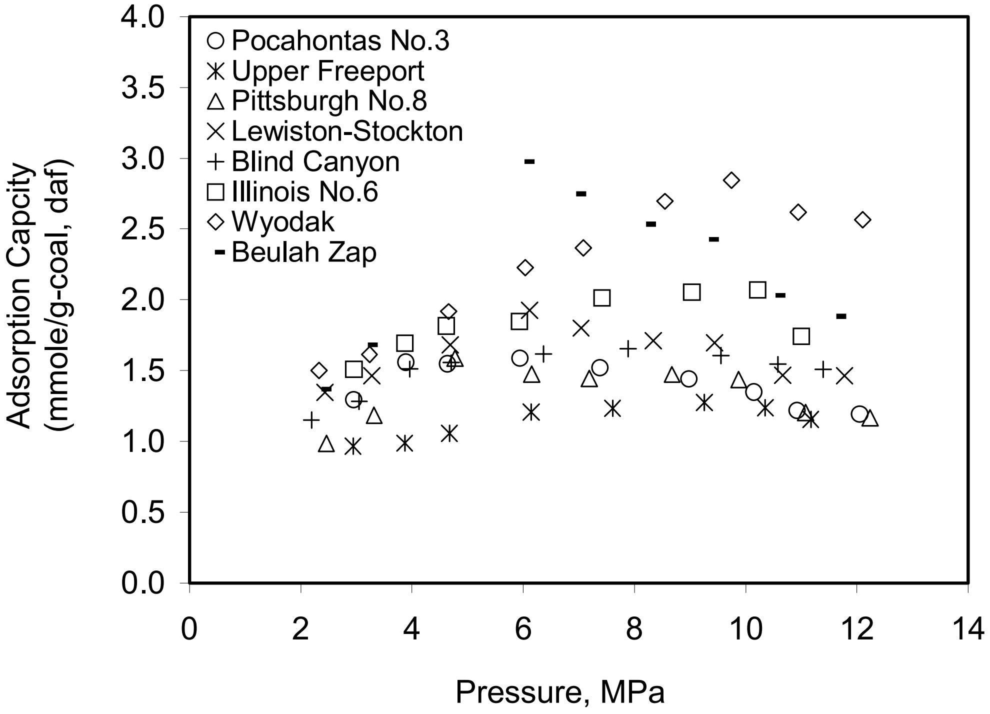

Figure 53. Adsorption capacities of dried Argonne Premium coals at 55 ^{o}C and over increasing pressure ranges

4.7.1.2 Isosteric Heat of Adsorption: Figure 54 shows the isosteric heat of adsorption for CO_2 adsorbed on each dried Argonne coal and its response to increasing pressure. As shown in the figure, the isosteric heat goes through a minimum as pressure increases. The decrease in isosteric heat of adsorption can be related to the increasing in the pore sizes. As the pore size increases, the isosteric heat of adsorption becomes smaller because of a weakening of the surface potential exerted by the opposite walls of the coal matrix. The effect of increasing CO_2 pressure on the isosteric heat of adsorption is small, about 2 kJ/mole, for coals of all ranks.

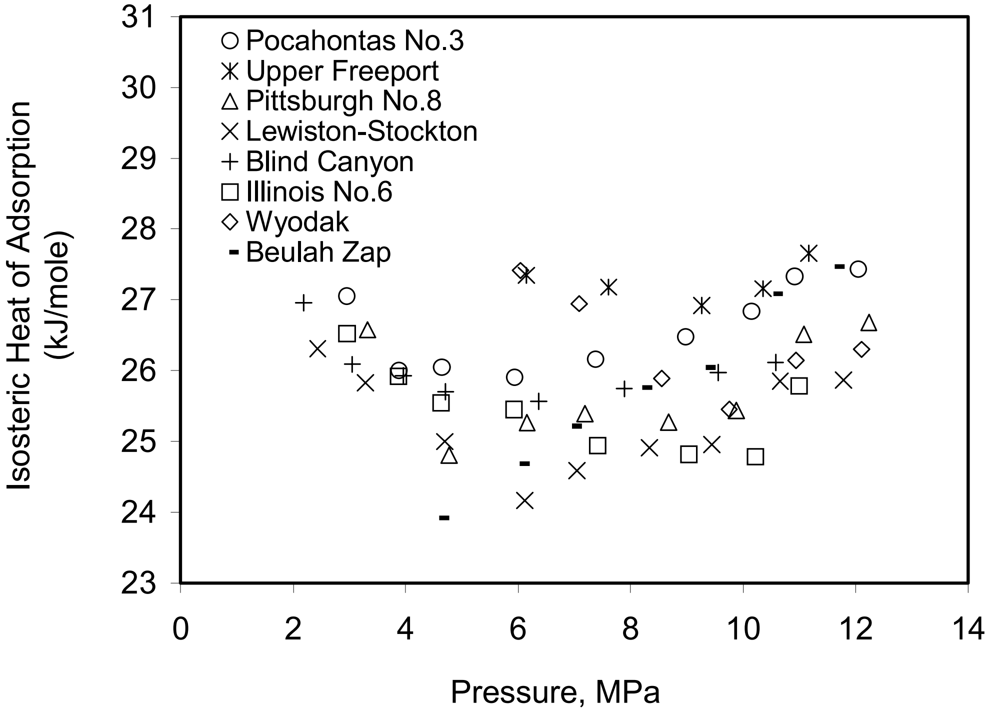

Figure 54. Isosteric heat of CO_2 adsorption on dried Argonne Premium coals with increasing pressure

4.7.1.3 Average Pore Sizes of Dried Argonne Coals Obtained from Supercritical CO_2 Adsorption Isotherms: The average pore size can be calculated using the Dubinin-Astakhov exponent, j, and the characteristic heat of adsorption, E_o, in Eq.(51). Figure 55 shows the average pore sizes of dried Argonne coals calculated for increasing pressure ranges. As shown in the figure, the average pore sizes of dried coals goes through a maximum as pressure increases. This is somewhat expected because of the coal swelling that was discussed in the previous sections. For instance, the coal pores were shown to collapse as a result of the drying that occurred before the adsorption isotherm measurements were conducted. According to the figure, upon CO_2 adsorption, these pores re-open as coal continues to swell under higher CO_2 pressures. As the pressure approaches 6-10 MPa, the coal becomes saturated with the adsorbed CO_2. As the pressure increases further, the average pore sizes become smaller due in part to filling of those pores with the adsorbed CO_2 and/or to the change in the effective stress.

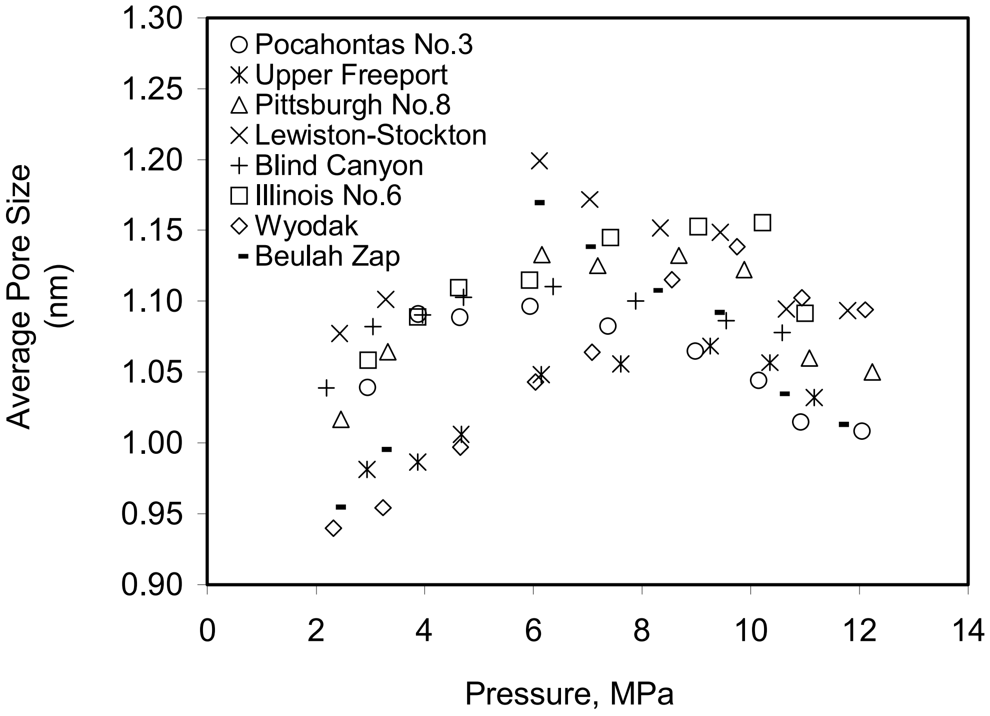

Figure 55. Average Pore sizes of Argonne Premium coals with increasing pressure estimated from supercritical CO_2 adsorption isotherms

4.7.1.4 Expansion Coefficient and the Volume Change for the Dried Argonne Coals: The expansion coefficients for the dried Argonne coals were also estimated from the excess adsorption isotherms. Figure 56 shows these values with increasing pressures. As can be seen from the figure, the expansion coefficient for all coal ranks is greatest at low pressures. This indicates that the volumetric change is significant at low pressures when CO_2 is introduced to the dry coal samples as the volume of the coal sample changes rapidly as a result of the recovery of the original volume of the coals which was shrunken as a result of drying.

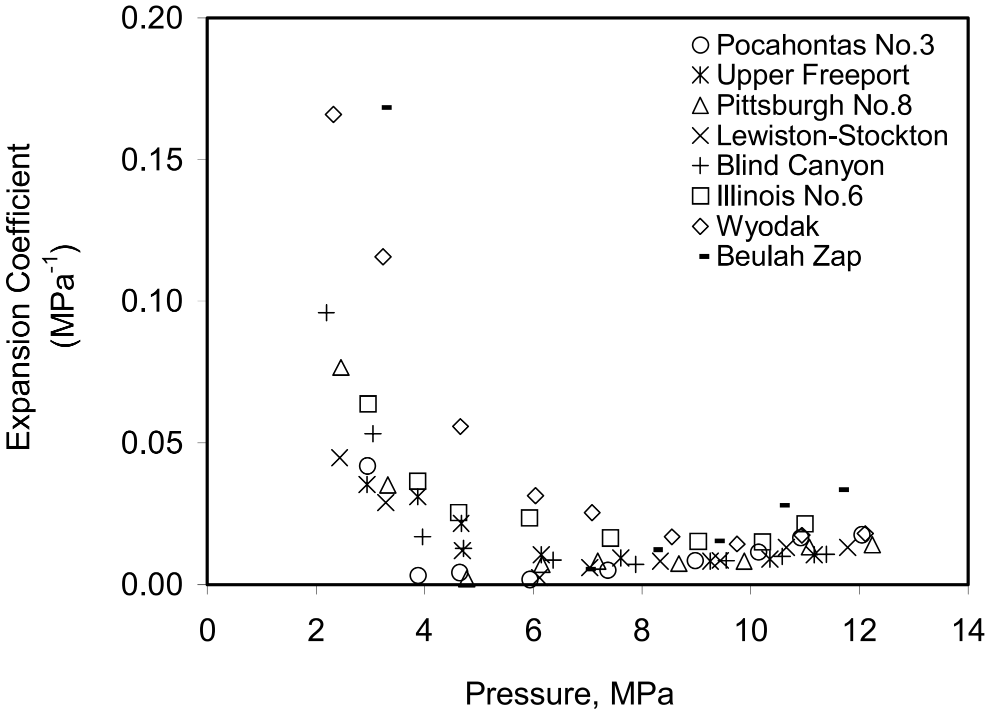

Figure 56. Expansion coefficient for coals with increasing pressures estimated from supercritical CO_2 adsorption isotherms

The volume change for the Argonne coals with the increasing pressures follows a trend similar to the expansion coefficients as shown in Figure 57. The volume change for the coals is initially higher at low pressures, about 10% to 20% for high rank coals and 35% to 60 % for low rank lignite coals. The volume change goes through a minimum as pressure increases. This volume change may be due in part to the volumetric changes caused by the dissolution of CO_2 in the coal matrix; the sieving effect due to differences in molecular sizes between He and CO_2, and expansion and contraction of the coal matrix. As shown in Figure 55, the average pore sizes increase as pressure increases indicating that the coals swell in CO_2 as pressure increases. As the coals swell, the accessible pore volume increases, which leads to decreased the observed volume change values.

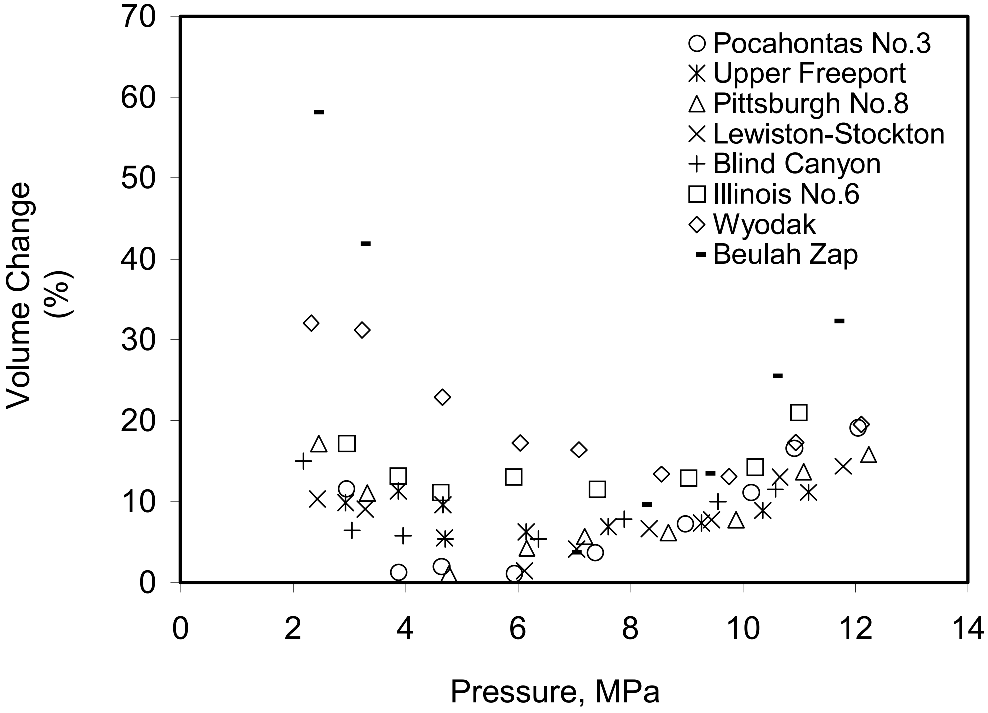

Figure 57. Volume change with increasing pressure calculated from expansion coefficient

As can be seen from the fitting parameters, the adsorption on non-rigid solids is a dynamic process. The adsorption equation used to interpret the adsorption isotherm should account for the nature of the adsorption process as well as the dynamic changes that occur during the adsorption. These concurrent events are to be expected when a sorbate adsorbs on a non-rigid adsorbent, i.e. CO_2 adsorption on coal. The modified D-A equation was derived to explicitly account for the volumetric effects that are present in the excess adsorption isotherms. In addition, constants used in the D-A equation to represent the absolute amount, including the adsorption capacity (n_o), the characteristic heat of adsorption (E_o), and the Dubinin exponent (j), may not be constant for non-rigid solids. In such a dynamic adsorption environment, these parameters can be affected by the adsorption process. In the future, an equation representing the dynamic nature of the adsorption isotherm for non-rigid solids should be developed.

4.8 MODELING OF CO_2 SEQUESTRATION IN COAL SEAMS

In order to relate the physical parameters obtained in this study and elsewhere to the CO_2 injection process, the transport of gases and water through the coal seam was modeled.

4.8.1 Modeling of Fluid Flow in Coal Seams

Coals are naturally fractured porous solids. They are confined between a cap rock and floor strata, which are known to be impermeable to fluids. Most coal beds of importance to CO_2 sequestration are saturated with water and may contain coalbed methane (CBM). The seam pressure is near the hydrostatic pressure which increases with depth of the formation. It has been suggested that the methane is adsorbed within the coal matrix and water resides in the cleat system.(247) Because about 90% of the gas storage occurs within the coal matrix, any water occupying the coal matrix decreases the adsorption capacity and inhibits diffusion within the coal matrix. Therefore, the first step in coal seam sequestration as it will be practiced in gassy seams will be to drain the water and recover adsorbed methane.

4.8.1.1 Flow Geometry: The coal seams can be represented by either rectangular or cylindrical geometries for the modeling purposes. Because the thickness of the coal seam is much smaller than the drainage radius, (e.g. ~3 m vs. ~500 m), the cylindrical geometry was chosen in this study to represent the fluid flow in coal seams assuming that the cleat porosity and coal seam properties are evenly distributed along the reservoir. Figure 59 illustrates the layout of a coal seam containing a well with a radius of r_w and its drainage radius, r_e,. In order to model the fluid flow within a coal seam, a differential volume element was considered at a distance of r from the well with a thickness of dr.

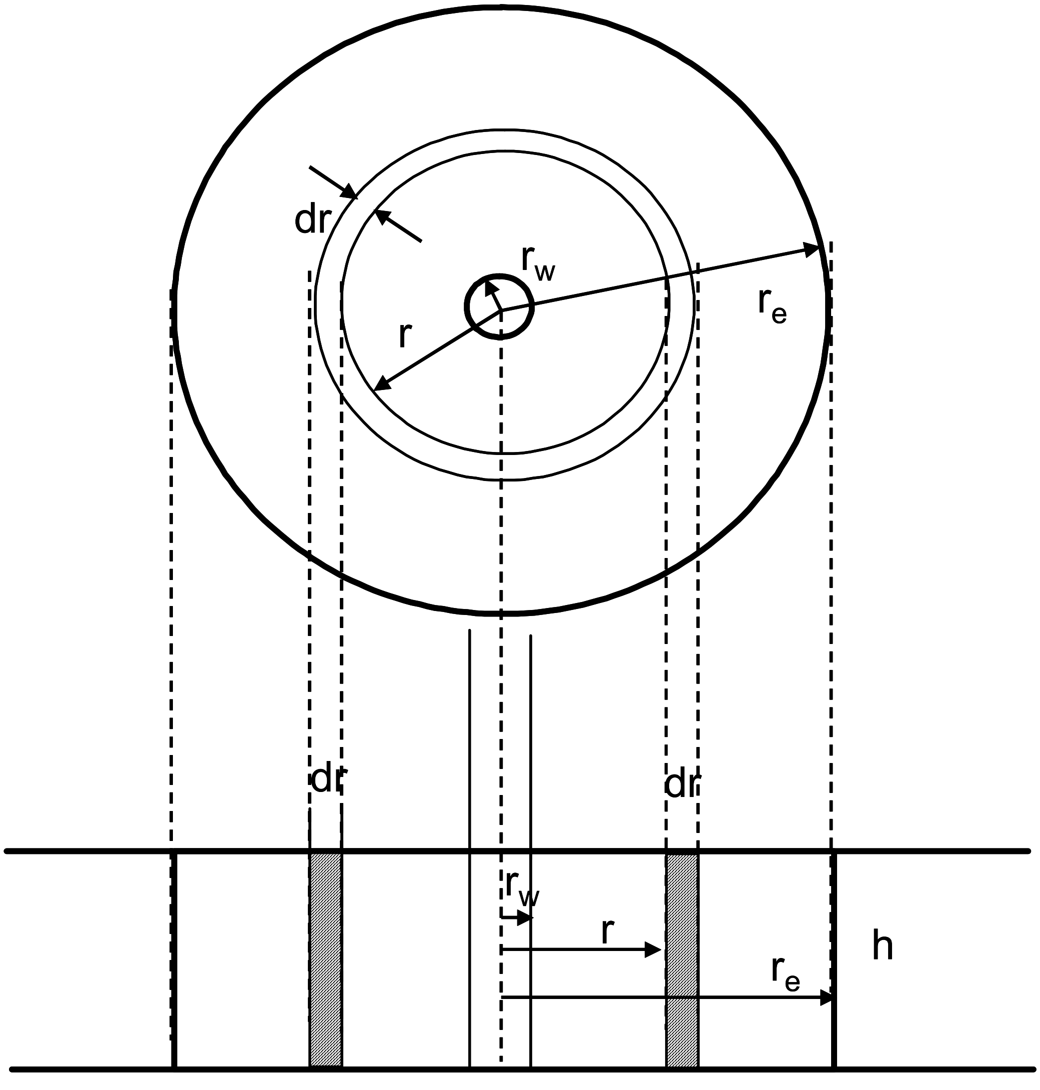

Figure 58. The layout for a coal seam

4.8.1.2 Assumptions: The following assumptions were considered in the modeling:

1. The reservoir is horizontal and its thickness is constant.
2. The porous medium is a continuum and its physical properties on the entire system can be represented by a control volume element.
3. The system is isothermal.
4. The flow in a coal seam is a two-phase flow including a water phase and a gas phase.
5. The free gas behaves as a real gas.
6. The fluid flow in the cleat porosity is a laminar flow due to larger pore sizes (from 0.01 μm to millimeters) and governed by the Darcy's law while the flow in the coal matrix is a diffusional flow due to smaller pores (from 4 Å to 20 Å) and governed by Fick's Law. Thus, the flow in coal matrix is much slower than the flow in cleat porosity due to diffusion vs. convection.

4.8.1.3 Derivation of the Continuity Equation: A differential equation can be developed to model a two-phase fluid flow in a coal seam by conducting a mass balance on a differential volume element as illustrated in Figure 59. A general mass balance can be written around the volume element over the time interval Δt, in word form, is:

$$[in] - [out] \pm [generation/consumption] = [accumulation] \qquad (59)$$

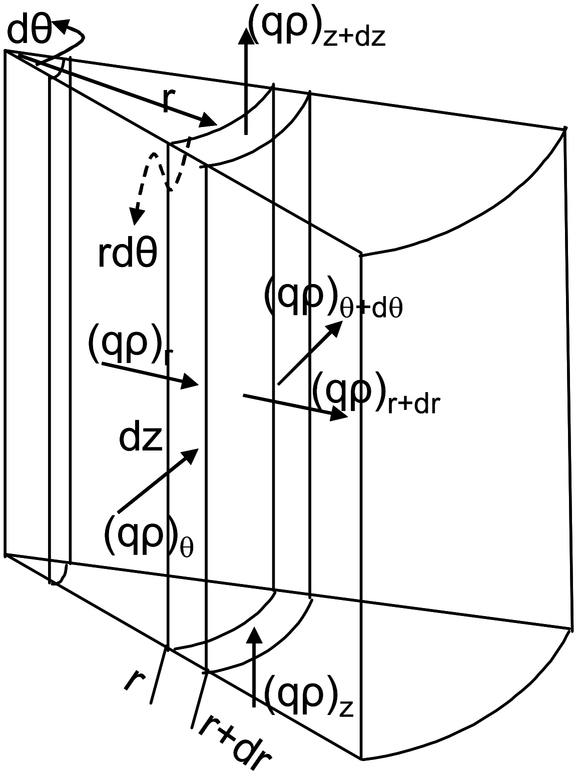

Figure 59. Representation of material balance for a fluid on a differential volume element in cylindrical coordinates

The mass flux for each phase entering the control volume during the period of Δt is

$$m_{fr} = \left(\rho_f v_{fr} r d\theta dz\right)_r \tag{60}$$

$$m_{f\theta} = \left(\rho_f v_{f\theta} dr dz\right)_\theta \tag{61}$$

$$m_{fz} = \left(\rho_f v_{fz} r d\theta dr\right)_z \tag{62}$$

Definition of each symbol can be found in the nomenclature.

The mass flux for each phase leaving the control volume during the period of Δt is

$$m_{fr+dr} = \left(\rho_f v_{fr} r d\theta dz\right)_r + \frac{\partial}{\partial r}\left(\rho_f v_{fr} r d\theta dz\right)_r dr \tag{63}$$

$$m_{f\theta+d\theta} = \left(\rho_f v_{f\theta} drdz\right)_\theta + \frac{\partial}{\partial \theta}\left(\rho_f v_{f\theta} drdz\right)_\theta d\theta \tag{64}$$

$$m_{fz+dz} = \left(\rho_f v_{fz} r d\theta dr\right)_z + \frac{\partial}{\partial z}\left(\rho_f v_{fz} r d\theta dr\right)_z dz \tag{65}$$

Substitution of Eqs (60)-(65) into Eq.(59) yields

$$\begin{aligned}
&\left(\rho_f v_{fr} r d\theta dz\right)_r - \left[\left(\rho_f v_{fr} r d\theta dz\right)_r + \frac{\partial}{\partial r}\left(\rho_f v_{fr} r d\theta dz\right)_r dr\right] \\
&+ \left(\rho_f v_{f\theta} drdz\right)_\theta - \left[\left(\rho_f v_{f\theta} drdz\right)_\theta + \frac{\partial}{\partial \theta}\left(\rho_f v_{f\theta} drdz\right)_\theta d\theta\right] \\
&+ \left(\rho_f v_{fz} r d\theta dr\right)_z - \left[\left(\rho_f v_{fz} r d\theta dr\right)_z + \frac{\partial}{\partial z}\left(\rho_f v_{fz} r d\theta dr\right)_z dz\right] \\
&\pm q_{fa} = \frac{\partial}{\partial t}\left(\phi r d\theta drdz \rho_f S_f\right)
\end{aligned} \tag{66}$$

Dividing Eq.(66) by the differential volume, $V_b = rd\theta drdz$, yields

$$-\frac{1}{r}\frac{\partial}{\partial r}\left(r\rho_f v_{fr}\right) - \frac{1}{r}\frac{\partial}{\partial \theta}\left(\rho_f v_{f\theta}\right) - \frac{\partial}{\partial z}\left(\rho_f v_{fz}\right) \pm \frac{q_{fa}}{V_b} = \frac{\partial}{\partial t}\left(\phi \rho_f S_f\right) \tag{67}$$

Eq.(67) is known as the continuity equation(189,180,181,182,183) for fluid flow in cylindrical coordinates.

4.8.1.4 Flow in Cleats: Figure 60 illustrates the cross-section of a coal seam perpendicular to the fluid flow. The image at the left corner of the figure shows the cleats and the coal matrix and the illustration at the right corner represents the fluid flow through the cleat porosity. The instant equilibrium at the surface and the diffusion through the coal matrix were also depicted. Naturally, the transport in cleat system is much faster than the transport in coal matrix, i.e. convection vs. diffusion. Therefore, the transport of fluids through a coal seam can be considered to be a two-stage process. One is the transport in cleats and the other is the transport within the coal matrix.

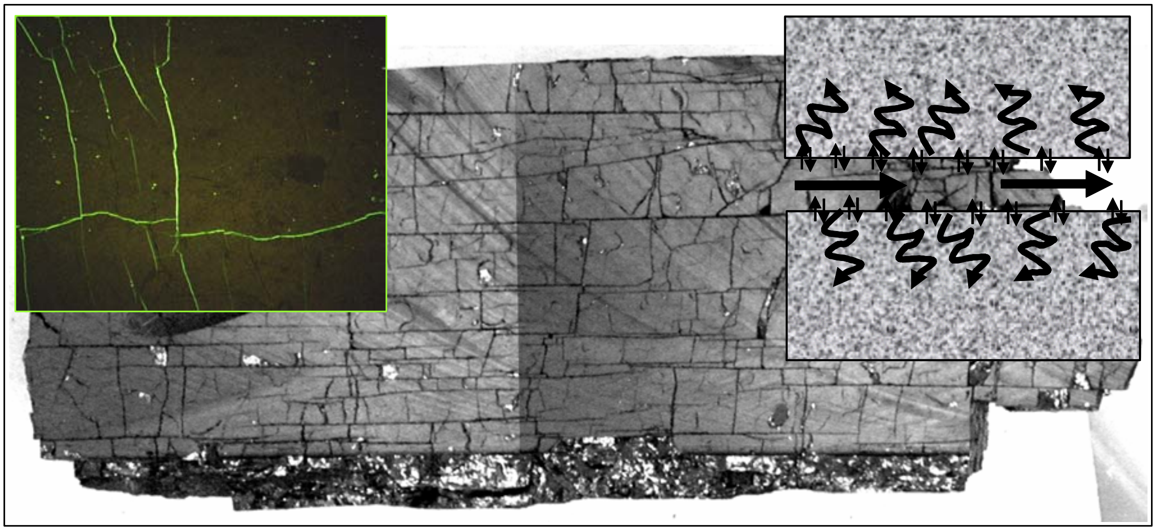

Figure 60. Cross section of a coal seam for fluid flow. Left corner: the image for cleats and the coal matrix. Right corner: representation of fluid flow within the cleats, instant equilibrium at the surface of the coal matrix and diffusion through the coal matrix

The mass of each phase entering and leaving the elemental volume in macrospores can be given by the general form of the continuity equation, Eq.(67). However, the fluid flow in θ-direction in the cylindrical coordinates can be ignored due to the symmetry. Also, the fluid flow in z-direction can also be ignored because the thickness of the coal seam is much less than the external radius of the coal seam. Therefore, the flow of fluids in coal seam could be represented as one-dimensional flow through the radial direction in the cylindrical coordinates.

$$-\frac{1}{r}\frac{\partial}{\partial r}\left(r\rho_f v_{fr}\right)-\frac{1}{r}\cancel{\frac{\partial}{\partial\theta}\left(\rho_f v_{f\theta}\right)}-\cancel{\frac{\partial}{\partial z}\left(\rho_f v_{fz}\right)}\pm\frac{q_{fa}}{V_b}=\frac{\partial}{\partial t}\left(\phi\rho_f S_f\right) \tag{68}$$

The flow stream in cleats includes the simultaneous flow of gas, dissolved gas in water, water, and water in gas phase. The water in gas phase at in-seam conditions is much smaller and can be ignored in the derivations. Although the dissolved gas in water is small comparing to the free gas phase in the cleat porosity, it is included in the model equations. Eq.(68) can be modified for the flow of gas, the dissolved gas in the water, and the water in the cleat porosity can be described as follows.

For gas phase

$$-\frac{1}{r}\frac{\partial}{\partial r}\left[r\left(\rho_g v_g + r_{sw}\rho_w v_w\right)\right]\pm q_q = \frac{\partial}{\partial t}\left(\phi\rho_g S_g + r_{sw}\phi\rho_w S_w\right) \tag{69}$$

For water phase

$$-\frac{1}{r}\frac{\partial}{\partial r}\left(r\rho_w v_w\right)\pm q_w = \frac{\partial}{\partial t}\left(\phi\rho_w S_w\right) \tag{70}$$

where r_{sw} is the ratio of the dissolved gas in the water phase in kg/ kg-water, and q_g and q_w are the mass cross-flow rate between the coal matrix and the cleat porosity in kg/day/m^3.

The density of the gas phase can be obtained from the real gas equation accounting the compressibility factor for the gas

$$\rho_g = \frac{MP_g}{zRT} \tag{71}$$

The appropriate equation for a slightly compressible fluid of water can be derived by the definition of compressibility under isothermal conditions as

$$\rho_w = \frac{\rho_{wsc}}{B_w} \tag{72}$$

Substituting Eq.(71) and Eq.(72) into Eq.(69) and Eq.(70), and dividing by constants *M/RT* and ρ_{wsc}, respectively, yields

for gas phase

$$-\frac{1}{r}\frac{\partial}{\partial r}\left[r\left(\frac{P_g}{z}\nu_g + r_{sw}\frac{RT}{M}\frac{\rho_w}{B_w}\nu_w\right)\right] \pm \frac{RT}{M}q_q = \frac{\partial}{\partial t}\left(\phi S_g\frac{P_g}{z} + r_{sw}\frac{RT\rho_{wsc}}{MB_w}\phi S_w\right) \tag{73}$$

for water phase

$$-\frac{1}{r}\frac{\partial}{\partial r}\left(r\frac{1}{B_w}\nu_w\right) \pm \frac{1}{\rho_{wsc}}q_w = \frac{\partial}{\partial t}\left(\frac{\phi S_w}{B_w}\right) \tag{74}$$

The transport of water is assumed to obey the Darcy's Law, then, the superficial velocity for water in Eq.(74) is

$$\nu_w = -\frac{\alpha k k_{rw}}{\mu_w}\frac{\partial P_w}{\partial r} \tag{75}$$

The transport of compressible gas is assumed to be under the influence of two fields, the potential field and the concentration field.(201) Velocity through the potential field is laminar flow process and can be described by Darcy's Law:

$$v_g^D = -\frac{\alpha\alpha_1 k k_{rg}}{\mu_g}\frac{\partial P_g}{\partial r} \tag{76}$$

The velocity through the concentration gradient field is a diffusion (i.e. Knudsen diffusion) process and can be described by Fick's Law of diffusion:

$$v_g^F = -\frac{M D_a}{\rho_g}\frac{\partial C_a}{\partial r} \tag{77}$$

where

$$C_a = \frac{\rho_g}{M} S_g \tag{78}$$

From the definition of the gas density, Eq.(71), and concentration, Eq.(78), Eq.(77) becomes

$$v_g^F = -D_a \frac{z}{P_g}\frac{\partial}{\partial r}\left(\frac{P_g}{z} S_g\right) \tag{79}$$

These two velocities created by the two fields are additive(201)

$$v_g = v_g^D + v_g^F \tag{80}$$

Hence, the velocity of the compressible gas phase is

$$v_g = -\frac{\alpha\alpha_1 k k_{rg}}{\mu_g}\frac{\partial P_g}{\partial r} - D_a \frac{z}{P_g}\frac{\partial}{\partial r}\left(\frac{P_g}{z} S_g\right) \tag{81}$$

The nonideality of the gas phase can be accounted by assigning the volume formation factor for gas, which is defined as the volume of the gas in the reservoir condition divided by its volume at the surface conditions, at the standard pressure, P_{sc}, and standard temperature, T_{sc}.

$$B_g = \frac{\left(\frac{zRT}{P}\right)}{\left(\frac{zRT}{P}\right)_{sc}} = \frac{zT}{P}\left(\frac{P_{sc}}{T_{sc}}\right) \tag{82}$$

Substituting Eq.(81) and (82) into Eq.(73) for the gas phase and Eq.(75) into Eq.(74) for the water phase and dividing by (TP_{sc}/T_{sc}), the material balance equations for each gas and water phases in the cleat porosity become:

for the gas phase

$$-\frac{1}{r}\frac{\partial}{\partial r}\left\{r\left[\frac{\alpha\alpha_1 kk_{rg}}{\mu_g B_g}\frac{\partial P_g}{\partial r}+D_a\frac{\partial}{\partial r}\left(\frac{S_g}{B_g}\right)+R_{sw}\frac{\alpha kk_{rw}}{\mu_w B_w}\frac{\partial P_w}{\partial r}\right]\right\}\pm q_{ai} = \frac{\partial}{\partial t}\left(\frac{\phi S_g}{B_g}+R_{sw}\frac{\phi S_w}{\alpha_1 B_w}\right) \qquad (83)$$

for the water phase

$$-\frac{1}{r}\frac{\partial}{\partial r}\left(r\frac{\alpha kk_{rw}}{\mu_w B_w}\frac{\partial P_w}{\partial r}\right)\pm q_{wi} = \frac{\partial}{\partial t}\left(\frac{\phi S_w}{\alpha_1 B_w}\right) \qquad (84)$$

where R_{sw} is now in Sm^3/Sm^3, and q_{ai} and q_{wi} are in $Sm^3/day/m^3$.

In the presence of CO_2 injection, the gas phase will compose of at least two components, CO_2 and CH_4. In this case, the material balance equations for each gas and water phases become:

for CO_2 in the gas phase

$$-\frac{1}{r}\frac{\partial}{\partial r}\left\{r\left[\frac{y_1\alpha\alpha_1 kk_{rg}}{\mu_g B_g}\frac{\partial P_g}{\partial r}+y_1 D_a\frac{\partial}{\partial r}\left(\frac{S_g}{B_g}\right)+R_{sw1}\frac{\alpha kk_{rw}}{\mu_w B_w}\frac{\partial P_w}{\partial r}\right]\right\}\pm\left(q_{ai}\right)_1 = \frac{\partial}{\partial t}\left(\frac{y_1\phi S_g}{B_g}+R_{sw1}\frac{\phi S_w}{\alpha_1 B_w}\right) \qquad (85)$$

for CH4 in the gas phase

$$
\begin{aligned}
&-\frac{1}{r}\frac{\partial}{\partial r}\left\{r\left[\frac{y_2\alpha\alpha_1 kk_{rg}}{\mu_g B_g}\frac{\partial P_g}{\partial r}+y_2 D_a\frac{\partial}{\partial r}\left(\frac{S_g}{B_g}\right)+R_{sw2}\frac{\alpha kk_{rw}}{\mu_w B_w}\frac{\partial P_w}{\partial r}\right]\right\}\pm\left(q_{ai}\right)_2 \\
&=\frac{\partial}{\partial t}\left(\frac{y_2\phi S_g}{B_g}+R_{sw2}\frac{\phi S_w}{\alpha_1 B_w}\right)
\end{aligned}
\qquad (86)
$$

and, for the water phase

$$
-\frac{1}{r}\frac{\partial}{\partial r}\left(r\frac{\alpha kk_{rw}}{\mu_w B_w}\frac{\partial P_w}{\partial r}\right)\pm q_{wi}=\frac{\partial}{\partial t}\left(\frac{\phi S_w}{\alpha_1 B_w}\right) \qquad (87)
$$

The following relationships for the two-phase flow through the porous media exist:

Capillary pressure

$$
P_{cgw}=P_g-P_w \qquad (88)
$$

Saturation

$$
S_g+S_w=1.0 \qquad (89)
$$

Gas composition

$$
y_1+y_2=1.0 \qquad (90)
$$

By substituting Eqs.(88) and (89) into Eq.(87), and Eq.(90) into Eq.(86), the final forms of the governing equations for each gas and water phases in the cleat porosity become:

for CO_2 in the gas phase

$$-\frac{1}{r}\frac{\partial}{\partial r}\left\{r\left[\frac{y_1\alpha\alpha_1 kk_{rg}}{\mu_g B_g}\frac{\partial P_g}{\partial r}+y_1 D_a\frac{\partial}{\partial r}\left(\frac{S_g}{B_g}\right)+R_{sw1}\frac{\alpha kk_{rw}}{\mu_w B_w}\frac{\partial\left(P_g-P_{cgw}\right)}{\partial r}\right]\right\}\pm\left(q_{ai}\right)_1 = \frac{\partial}{\partial t}\left(\frac{y_1\phi S_g}{B_g}+R_{sw_1}\frac{\phi\left(1-S_g\right)}{\alpha_1 B_w}\right) \tag{91}$$

for CH_4 in the gas phase

$$-\frac{1}{r}\frac{\partial}{\partial r}\left\{r\left[\frac{\left(1-y_1\right)\alpha\alpha_1 kk_{rg}}{\mu_g B_g}\frac{\partial P_g}{\partial r}+\left(1-y_1\right)D_a\frac{\partial}{\partial r}\left(\frac{S_g}{B_g}\right)+R_{sw2}\frac{\alpha kk_{rw}}{\mu_w B_w}\frac{\partial\left(P_g-P_{cgw}\right)}{\partial r}\right]\right. = \frac{\partial}{\partial t}\left(\frac{\left(1-y_1\right)\phi S_g}{B_g}+R_{sw_2}\frac{\phi\left(1-S_g\right)}{\alpha_1 B_w}\right) \tag{92}$$

for the water phase

$$-\frac{1}{r}\frac{\partial}{\partial r}\left(r\frac{\alpha kk_{rw}}{\mu_w B_w}\frac{\partial\left(P_g-P_{cgw}\right)}{\partial r}\right)\pm q_{wi} = \frac{\partial}{\partial t}\left(\frac{\phi\left(1-S_g\right)}{\alpha_1 B_w}\right) \tag{93}$$

The initial and the boundary conditions for the governing equations, Eqs.(91)-(93), are given in section 4.8.3.

4.8.1.5 Flow in Coal Matrix: The fluid flow in the coal matrix is a diffusional flow due to smaller pore sizes ranges from 4 Å to 20 Å compared to the molecular sizes of gas and water of about 4 Å. The transport through the coal matrix can be modeled as equilibrium or non-equilibrium sorption models. The equilibrium models assume that the adsorption and desorption processes are so rapid that the kinetics of the process is negligible. In this case, the source term in Eqs.(91)-(93) is

$$\frac{\partial C_{ie}}{\partial t} = -q_{ai} \tag{94}$$

where the concentration or the adsorbed amount can be described by one of the adsorption equations, i.e. the extended Langmuir equation(135) for the mixture of gases

$$C_{ie} = \frac{C_{io} b_i y_i P_g}{1 + \sum_i b_i y_i P_g} \tag{95}$$

Then, the source term can be given as

$$\frac{\partial C_{ie}}{\partial t} = -q_{ai} = \frac{\partial C_{ie}}{\partial P_g} \frac{\partial P_g}{\partial t} \tag{96}$$

In non-equilibrium models, because the flow in the cleat porosity is much faster than the flow in the coal matrix, i.e. convection vs. diffusion, the adsorption and desorption processes will be time dependent. In this case, the surface of the coal matrix in the cleat porosity reaches equilibrium with the adsorbing/desorbing gases in the cleat porosity instantly. Therefore, the diffusion occurs in the coal matrix due to the concentration difference. As a result, the diffusion into and out of the coal matrix is retarded or delayed while changes in the pressure and gas concentrations occur faster in the cleats. This phenomenon is depicted with the illustration in the right corner of Figure 60.

The adsorption and desorption of gases within the coal matrix and the delay in entering and disappearing of these components in the cleat porosity can be obtained by conducting a mass balance on a differential element in the coal matrix. After closely investigating the cross-section of the coal seam as shown in Figure 60, it can be seen that the coal matrix is divided into rectangular, cylindrical, and rhombic types of shapes surrounded by the cleat porosity. In other words, each coal matrix is separated from each other by the cleats. Because the face cleats are longer than the butt cleats, the coal matrix was considered to be a cylindrical shape parallel to the face cleats as shown in Figure 61. Note that similar (r, θ, z) notations will be used to represent the coal matrix with the reservoir; however, their values would be different.

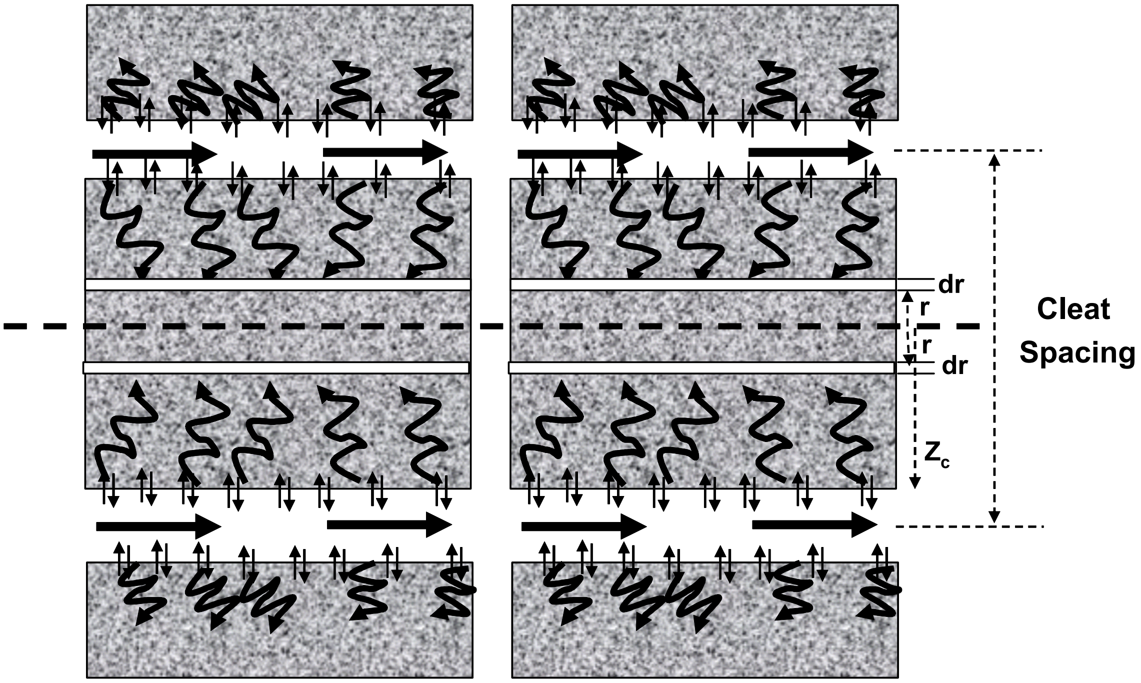

Figure 61. Cross-section of the coal matrix: Flow occurs by convection in cleats and by diffusion in coal matrix. Instantaneous equilibrium establishes at the surface of the coal matrix.

A mass balance can be conducted on a differential volume element in the coal matrix. The mass flux for each component entering the control volume during the period of *Δt* is

$$m_{ir} = \left(-MD_i r d\theta dz \frac{\partial C_i}{\partial r} \right)_r \tag{97}$$

$$m_{i\theta} = \left(-MD_i dr dz \frac{\partial C_i}{\partial \theta} \right)_\theta \tag{98}$$

$$m_{iz} = \left(-MD_i r d\theta dr \frac{\partial C_i}{\partial z} \right)_z \tag{99}$$

The mass flux for each component leaving the control volume during the period of *Δt* is

$$m_{ir+dr} = \left(-MD_i r d\theta dz \frac{\partial C_i}{\partial r} \right)_r + \frac{\partial}{\partial r}\left(-MD_i r d\theta dz \frac{\partial C_i}{\partial r} \right)_r dr \tag{100}$$

$$m_{i\theta+d\theta} = \left(-MD_i dr dz \frac{\partial C_i}{\partial \theta} \right)_\theta + \frac{\partial}{\partial \theta}\left(-MD_i dr dz \frac{\partial C_i}{\partial \theta} \right)_\theta d\theta \tag{101}$$

$$m_{iz+dz} = \left(-MD_i r d\theta dr \frac{\partial C_i}{\partial z} \right)_z + \frac{\partial}{\partial z}\left(-MD_i r d\theta dr \frac{\partial C_i}{\partial z} \right)_z dz \tag{102}$$

Substitution of Eqs (97)-(102) into Eq.(59) yields

$$\begin{aligned}
&\left(-MD_i r d\theta dz \frac{\partial C_i}{\partial r} \right)_r - \left[\left(-MD_i r d\theta dz \frac{\partial C_i}{\partial r} \right)_r + \frac{\partial}{\partial r}\left(-MD_i r d\theta dz \frac{\partial C_i}{\partial r} \right)_r dr \right] \\
&+ \left(-MD_i dr dz \frac{\partial C_i}{\partial \theta} \right)_\theta - \left[\left(-MD_i dr dz \frac{\partial C_i}{\partial \theta} \right)_\theta + \frac{\partial}{\partial \theta}\left(-MD_i dr dz \frac{\partial C_i}{\partial \theta} \right)_\theta d\theta \right] \\
&+ \left(-MD_i r d\theta dr \frac{\partial C_i}{\partial z} \right)_z - \left[\left(-MD_i r d\theta dr \frac{\partial C_i}{\partial z} \right)_z + \frac{\partial}{\partial z}\left(-MD_i r d\theta dr \frac{\partial C_i}{\partial z} \right)_z dz \right] \\
&= \frac{\partial}{\partial t}\left(r d\theta dr dz M C_i \right)
\end{aligned} \tag{103}$$

Simplifying Eq.(66) and dividing by the differential volume, $V_b = r d\theta dr dz$, yields

$$-\frac{1}{r}\frac{\partial}{\partial r}\left(-rD_i \frac{\partial C_i}{\partial r} \right)_r - \frac{1}{r}\frac{\partial}{\partial \theta}\left(-D_i \frac{\partial C_i}{\partial \theta} \right)_\theta - \frac{\partial}{\partial z}\left(-D_i \frac{\partial C_i}{\partial z} \right)_z = \frac{\partial C_i}{\partial t} \tag{104}$$

Because the face cleats are longer than the butt cleats, the diffusion in z-direction would be much smaller than the diffusion in r-direction, and therefore, the diffusion in z-direction can be neglected. The diffusion in θ-direction can also be neglected due to the symmetry.

$$-\frac{1}{r}\frac{\partial}{\partial r}\left(-rD_i\frac{\partial C_i}{\partial r}\right)_r-\cancel{\frac{1}{r}\frac{\partial}{\partial \theta}\left(-D_i\frac{\partial C_i}{\partial \theta}\right)_\theta}-\cancel{\frac{\partial}{\partial z}\left(-D_i\frac{\partial C_i}{\partial z}\right)_z}=\frac{\partial C_i}{\partial t} \qquad (105)$$

Therefore, the transport of gases into and out of the coal matrix can be calculated by solving Eq.(106) by employing the initial and the boundary conditions.

$$\frac{\partial}{\partial r}\left(rD_i\frac{\partial C_i}{\partial r}\right)=\frac{\partial C_i}{\partial t} \qquad (106)$$

The initial condition for Eq.(106) is that the initial adsorbed gas concentration, which is supposed to be in equilibrium with the free gas phase at the initial pressure of P_{go}, can be calculated from the Extended Langmuir equation, Eq.(95)

$$at \qquad t=0 \qquad all \quad r \qquad C_i=C_{io}=\frac{C_{io}b_iy_iP_{go}}{1+\sum_i b_iy_iP_{go}} \qquad (107)$$

The first boundary condition is that, at the surface of the coal matrix, the adsorbed gas phase is in equilibrium with the gas at the pressure of P_g in the cleats

$$at \qquad t>0 \qquad r=Z_c \qquad C_i=C_{ie}=\frac{C_{io}b_iy_iP_g}{1+\sum_i b_iy_iP_g} \qquad (108)$$

Here, Z_c is the half of the cleat spacing and C_{ie} is the amount of gas which is in equilibrium with the free gas.

At the center of the coal matrix, the mass flux is equal to zero due to the symmetry

$$at \qquad t > 0 \qquad r = 0 \qquad \frac{\partial C_i}{\partial r} = 0 \tag{109}$$

Solving Eq.(106) using the boundary conditions yields the concentration profile within the coal matrix, which is a function of the space and time.

The appearance and disappearance of each gas species in the cleat porosity, in other words, adsorption and desorption of each species on the coal matrix, can be calculated form the mass flux at the surface using the concentration profile as

$$(q_{ai})_i = -\frac{A}{V} D_i \frac{RT_{sc}}{P_{sc}} \left. \frac{\partial C_i}{\partial r} \right|_{r=Z_c} \tag{110}$$

Here, the $(q_{ai})_i$ is the source term as appeared in the governing equations, Eqs.(91)-(93), A is the area to the diffusional flow, which is perpendicular to the direction of the diffusional flow through the coal matrix, and V is the volume of the differential element within the coal matrix, and $(\partial C_i/\partial r)|_{Zc}$ at the surface of the coal matrix is the mass flux. It should be noted that the A/V ratio corresponds to inverse of the half of the cleat spacing, $1/(Z_c/2)$.

Therefore, the governing differential equations representing the simultaneous flow of gas and water phases in a coal seam have been coupled with a non-equilibrium source term.

4.8.1.6 Dependence of Coefficients in the Governing Equations on Pressure and Solubility: In most instances, actual in-seam data are not available. In these circumstances, a correlation is used to compute the property in question. Parameters such as porosity, absolute permeability, relative permeability, viscosity, formation volume factor, capillary pressure, and compressibility factor are pressure and saturation dependent, and these relationships are given in Appendix D.

4.8.2 Solution of the Governing Equations

The governing equations, Eq.(91)-(93) and Eq.(110), can be solved analytically for only certain simplified conditions. Instead, because these equations are quite complex and non-linear, a numerical solution should be implemented. The Athena Visual Workbench Software Package® is a computational tool that allows programmers to solve complex systems of equations.(248) The package uses the finite-difference approximation to transform the governing partial differential equations describing the flow of gas and water in a coal seam into algebraic finite-difference equations. The advantages of using Athena are that it is faster and saves time. It can solve the nonlinear systems of equations once they are organized as input variables. The disadvantages using Athena are that Athena can solve only one-dimensional unsteady state equations and the wells at the external boundary may not be defined. Cylindrical coordinates were used in the solution. The numerical solution for the governing equations was implemented by superimposing a finite-difference grid over the idealized coal seam. The finite-difference solution then produces the values of pressure and saturation at discrete points in the coal seam and calculates the flow rates and cumulative productions for the gas and water during the CBM production or CO_2 injection process. The computer code to solve the governing equations for gas and water flow in fractured coal seams is given in Appendix E.

4.8.3 Calculation of the Flow Rates at the Wells

The derivation of the flow rate at the well is straight forward for the incompressible water phase. Assuming a steady-state flow at the well, the superficial velocity for water and the Darcy's law can be written as

$$v_w = \frac{Q_w B_w}{2\pi r h} = -\frac{\alpha k k_{rw}}{\mu_w}\frac{\partial P}{\partial r} \tag{111}$$

Separating the variables

$$\frac{Q_w}{2\pi h \alpha}\int_{r_w}^{r_e}\frac{dr}{r} = -\int_{P_{well}}^{P_e}\frac{k k_{rw}}{\mu_w B_w}dP \tag{112}$$

Since the physical constants for the incompressible fluids change very little with pressure, Eq.(112) can be easily integrated. Thus, the rate of water flow can be expressed as

$$Q_w = -\frac{2\pi h \alpha k k_{rw}}{\mu_w B_w \ln\left(\frac{r_e}{r_w}\right)}\left(P_e - P_{well}\right) \tag{113}$$

The derivation of the gas flow rate at the well needs special attention. Because the gas phase is compressible, it expands as the pressure drops; the velocity becomes greater at the downstream end than at the upstream end, and consequently the pressure gradient increases toward the downstream end. Expressing the gas flow rate in the standard cubic meter per day and substituting the definition of the gas formation volume factor, Eq.(82), the superficial velocity for gas phase can be written as

$$v_g = \frac{Q_g B_g}{2\pi r h} = \frac{Q_g}{2\pi r h}\frac{zT}{P}\left(\frac{p_{sc}}{Tsc}\right) = -\frac{\alpha\alpha_1 k k_{rg}}{\mu_g}\frac{\partial P}{\partial r} \tag{114}$$

Separating the variables

$$\frac{Q_g}{2\pi h \alpha\alpha_1} T\left(\frac{P_{sc}}{T_{sc}}\right)\int_{r_w}^{r_e}\frac{dr}{r} = -\int_{P_{well}}^{P_e}\frac{kk_{rg}}{z\mu_w}PdP \tag{115}$$

The physical constants for the case of the gas phase such as compressibility factor, *z*, and the gas phase viscosity, μ_g, are dependent on the pressure and may not be taken out of the integral. However, the product of compressibility factor and the gas viscosity, $z\mu_g$, was shown to be nearly constant at pressures less than 13.6 MPa whereas $P/z\mu_g$ is nearly constant at pressures greater than 13.6 MPa.(249) Therefore, $z\mu_g$ can be withdrawn from the integrals as if they were invariant with pressure provided that their average values should be used. In this case, integration of Eq.(115), the gas flow rate can be expressed as

$$\bar{Q}_g = -\frac{2\pi h\alpha\alpha_1 kk_{rg}}{\bar{z}\,\bar{\mu}_g T\left(\frac{P_{sc}}{T_{sc}}\right)\mathbf{ln}\left(\frac{r_e}{r_w}\right)}\left(\frac{P_e^2 - P_{well}^2}{2}\right) \tag{116}$$

On the other hand, Eq.(116) can be reorganized with respect to average pressure such that

$$\begin{aligned}\bar{Q}_g &= -\frac{2\pi h\alpha\alpha_1 kk_{rg}}{\bar{z}\,\bar{\mu}_g T\left(\frac{P_{sc}}{T_{sc}}\right)\mathbf{ln}\left(\frac{r_e}{r_w}\right)}\left(P_e - P_{well}\right)\frac{\left(P_e + P_{well}\right)}{2} \\ &= -\frac{2\pi h\alpha\alpha_1 kk_{rg}}{\bar{\mu}_g\frac{\bar{z}T}{\bar{P}}\left(\frac{P_{sc}}{T_{sc}}\right)\mathbf{ln}\left(\frac{r_e}{r_w}\right)}\left(P_e - P_{well}\right)\end{aligned} \tag{117}$$

Therefore, the average gas flow rate can be calculated as

$$\bar{Q}_g = -\frac{2\pi h \alpha \alpha_1 k k_{rg}}{\bar{\mu}_g \bar{B}_g \ln\left(\frac{r_e}{r_w}\right)}\left(P_e - P_{well}\right) \tag{118}$$

Eq.(118) is similar to Eq.(113), except that the physical values are calculated at the average pressure.

4.8.4 Modeling of Dewatering and Degasification of a Coal Seam

In order to solve the governing non-linear differential equations for the water and methane production from a coal seam, the initial and boundary conditions must be specified. Because the water and adsorbed methane need to be withdrawn from the coal seam before the CO_2 is injected, it was considered that using multiple wells will assist the dewatering/degasification of the coal seam in shorter times as shown in Figure 62. The distance between each well is more or less the same so that one well and its boundaries can be specified in the model.

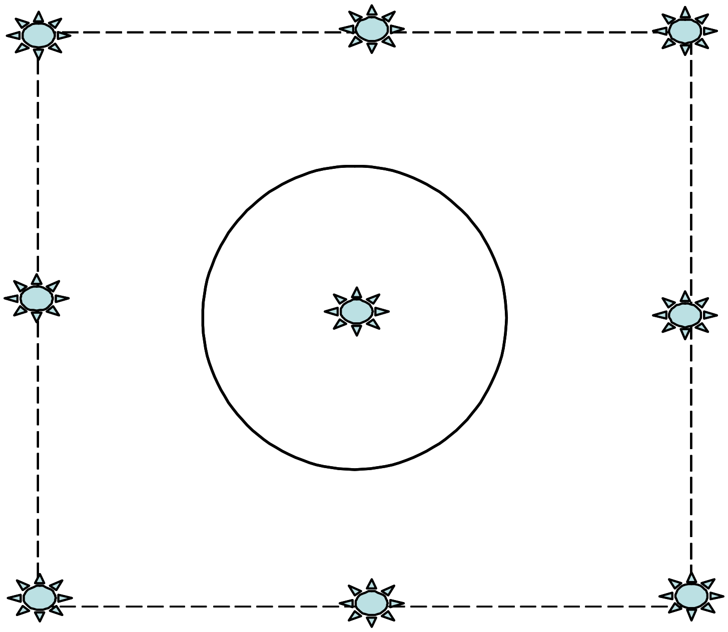

Figure 62. Model coal seam dewatering/degasification set-up

The initial condition for pressure can be approximated by the local pressure gradient and depth of the coal seam whereas the initial condition for the gas saturation is set to zero as a default value.

$$P_{go} = P_{atm} + gd \tag{119}$$

$$S_{go}=0.0 \tag{120}$$

The initial micropore gas concentration is therefore

$$C_{io}^{o} = \frac{C_{io} b_i y_i P_{go}}{1 + \sum_i b_i y_i P_{go}} \tag{121}$$

The internal boundary condition at the well can be given as either a pressure constrained well or a rate constrained well. For the pressure constrained well, the bottomhole pressure is specified. For rate constrained well, either gas production rate, water production rate, or total production rate can be specified. Similarly, the external boundary condition can be defined as either a constant pressure (constant flow rate) boundary condition or a no-flow outer boundary condition. For instance, for the pressure constrained well, the inner boundary condition at the well is

$$P_g = P_{well} \tag{122}$$

$$\nabla S_g = 0.0 \tag{123}$$

The outer boundary condition can be assumed to be a no-flow outer boundary due to the symmetrically located wells

$$\nabla P_g = 0.0 \tag{124}$$

$$\nabla S_g = 0.0 \tag{125}$$

When the pressure is specified at the well, the production rate for gas, water, and total production rate can be calculated from the Dupuit equation.(250)

$$\bar{Q}_g = -\frac{2\pi h \alpha \alpha_1 k k_{rg}}{\bar{\mu}_g \bar{B}_g \ln\left(\frac{r_e}{r_w}\right)}\left(P_e - P_{well}\right) \tag{126}$$

$$Q_w = -\frac{2\pi h \alpha k k_{rw}}{\mu_w B_w \ln\left(\frac{r_e}{r_w}\right)}\left(P_e - P_{well}\right) \tag{127}$$

$$Q_T = \frac{2\pi h\alpha k}{\ln\left(\frac{r_e}{r_w}\right)}\left(\frac{k_{rg}}{\bar{\mu}_g\,\bar{B}_g} + \frac{\alpha_1 k_{rw}}{\mu_w B_w}\right)\left(P_e - P_{well}\right) \tag{128}$$

When the production rate, i.e. the total production rate, is specified, the bottomhole pressure can be calculated from

$$P_{well} = P_e - \frac{Q_T \ln\left(\frac{r_e}{r_w}\right)}{2\pi h\alpha k\left(\frac{k_{rg}}{\bar{\mu}_g\,\bar{B}_g} + \frac{\alpha_1 k_{rw}}{\mu_w B_w}\right)} \tag{129}$$

4.8.5 Validation of the Two-Phase Fluid Flow Model

The compositional two-phase fluid flow model developed in this study was tested against a two-phase model developed by Sung.(251,252) The Sung's model has also been used by others to test their models.(184,253) While the present model uses cylindrical coordinates for the solution of the governing equations, the Sung's model employs the Rectangular coordinates. Both models were run using the reservoir system described in Table 19, Figure 63, and Figure 64. The present model was compared with the Sung's model in four sets of data of simulation runs. In the first runs, the pressure was specified at the production well while the source term was excluded in the simulation. In the second runs, the constant total flow rate was specified at the production well and the source term was excluded. In the third runs, the pressure was specified at the production well including the source term. And, in the fourth runs, the constant total flow rate was specified at the production well while including the source term.

Table 19. Physical parameters used in the model

```
----------------------------------------------------------------------
FORMATION PROPERTIES
----------------------------------------------------------------------
  RESERVOIR AREA..............................=      0.54       (KM)2
  AVERAGE RESERVOIR DEPTH.....................=    975.36           M
  FORMATION THICKNESS.........................=      3.05           M
  EFFECTIVE POROSITY..........................=      2.00           %
  ABSOLUTE PERMEABILITY.......................=      2.00          MD
  FORMATION COMPRESSIBILITY...................=  0.15E-03       1/MPA
  COAL DENSITY................................=      1.36      GR/CM3
  FORMATION TEMPERATURE.......................=     68.10          OC
  INITIAL FORMATION PRESSURE..................=     15.17         MPA
  INITIAL WATER SATURATION....................=      0.95    FRACTION

INITIAL GAS AND WATER IN PLACE
----------------------------------------------------------------------
   CO2 IN ADSORBED PHASE......................=      0.00   SM3*10**6
   CH4 IN ADSORBED PHASE......................=     29.34   SM3*10**6
   COMPOSITION FOR CO2 IN BULK GAS PHASE......=      0.00    FRACTION
   COMPOSITION FOR CH4 IN BULK GAS PHASE......=      1.00    FRACTION
   CO2 IN BULK GAS PHASE......................=      0.00   SM3*10**3
   CH4 IN BULK GAS PHASE......................=    827.52   SM3*10**3
   TOTAL CO2-IN-PLACE.........................=      0.00   SM3*10**6
   TOTAL CH4-IN-PLACE.........................=     30.16   SM3*10**6
   TOTAL H2O-IN-PLACE.........................=     30.95   SM3*10**3

WELLBORE PROPERTIES
----------------------------------------------------------------------
  WELL RADIUS.................................=      8.89          CM
  WELLBORE PRESSURE...........................=      0.17         MPA
  SKIN FACTOR.................................=      0.00

ADSORPTION ISOTHERMS
----------------------------------------------------------------------
  ADSORPTION CAPACITY FOR CO2.................=      5.47     SM3/TON
  ADSORPTION CAPACITY FOR CH4.................=      0.61     SM3/TON
  LANGMUIR PRESSURE FOR CO2...................=      0.10         MPA
  LANGMUIR PRESSURE FOR CH4...................=      1.15         MPA

TRANSPORT PARAMETERS
----------------------------------------------------------------------
  CLEAT SPACING...............................=      1.31          CM
  MICROPORE DIFFUSION COEFFICIENT.............=  0.19E-06      M2/DAY
  SORPTION TIME CONSTANT......................=    231.46         DAY
  CRITICAL WATER CONTENT (SWC)................=      0.25    FRACTION
  CRITICAL GAS CONTENT (SGC)..................=      0.00    FRACTION
  RELATIVE PERMEABILITY TO WATER AT SGC.......=      1.00          MD
  RELATIVE PERMEABILITY TO GAS AT SWC.........=      1.00          MD
----------------------------------------------------------------------
```

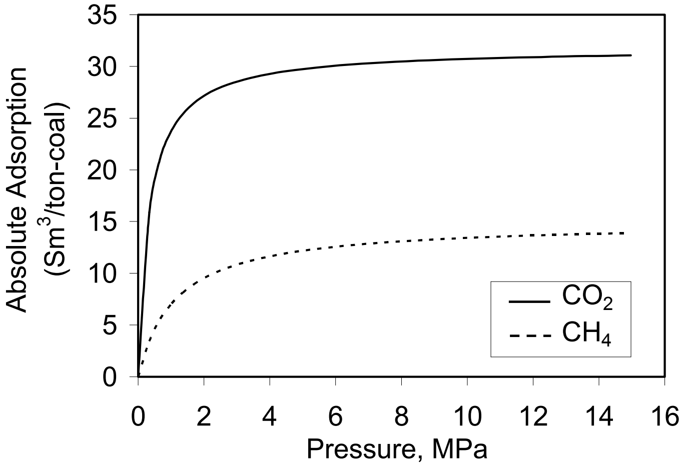

Figure 63. Adsorption Capacity of Coal used in the present model

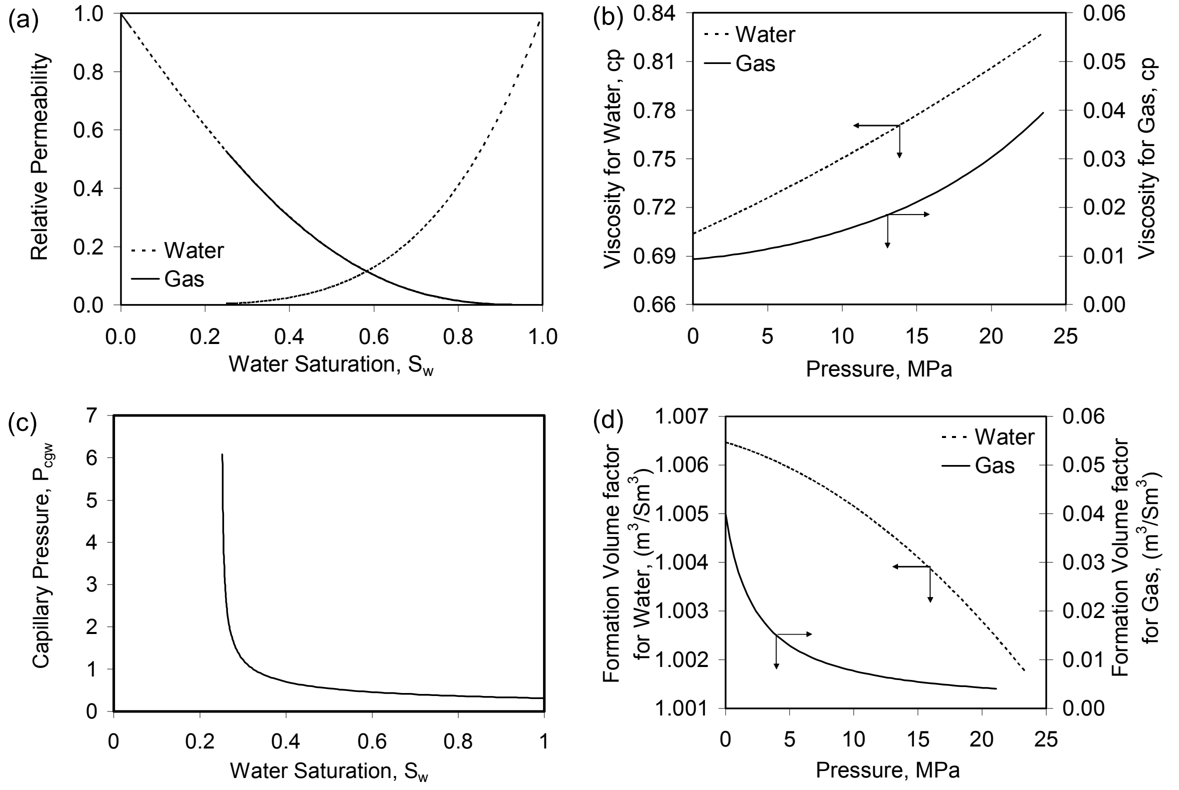

Figure 64. The Parameters for gas and water phases used in the models (a) relative permeability (b) Viscosity (c) Capillary pressure, and (d) Formation volume factor

In the first runs, the pressure was specified at the production well while the source term was excluded. In this case, the coal seam is filled with 95% of water and 5% of gas and both phases are pumped out from the coal seam while setting the bottomhole pressure to near the atmospheric pressure (0.17 MPa). Figure 65 shows the production rates and the cumulative productions of gas and water. As shown in the figure, the two models produce similar results. The present model predicts slightly higher gas and water production rates at the initial production period (Figure 65a and b). The gas and water production rates decline with time. The cumulative gas and water productions are slightly higher at the initial production period (Figure 65c and d), but, at about 20 years of production, both models predict similar cumulative gas and water productions. The small deviation between the two models may come from the use of different coordinate systems (Cylindrical vs. Rectangular) for the solution of the governing differential equations. Overall, the agreement between the two models is better than expected.

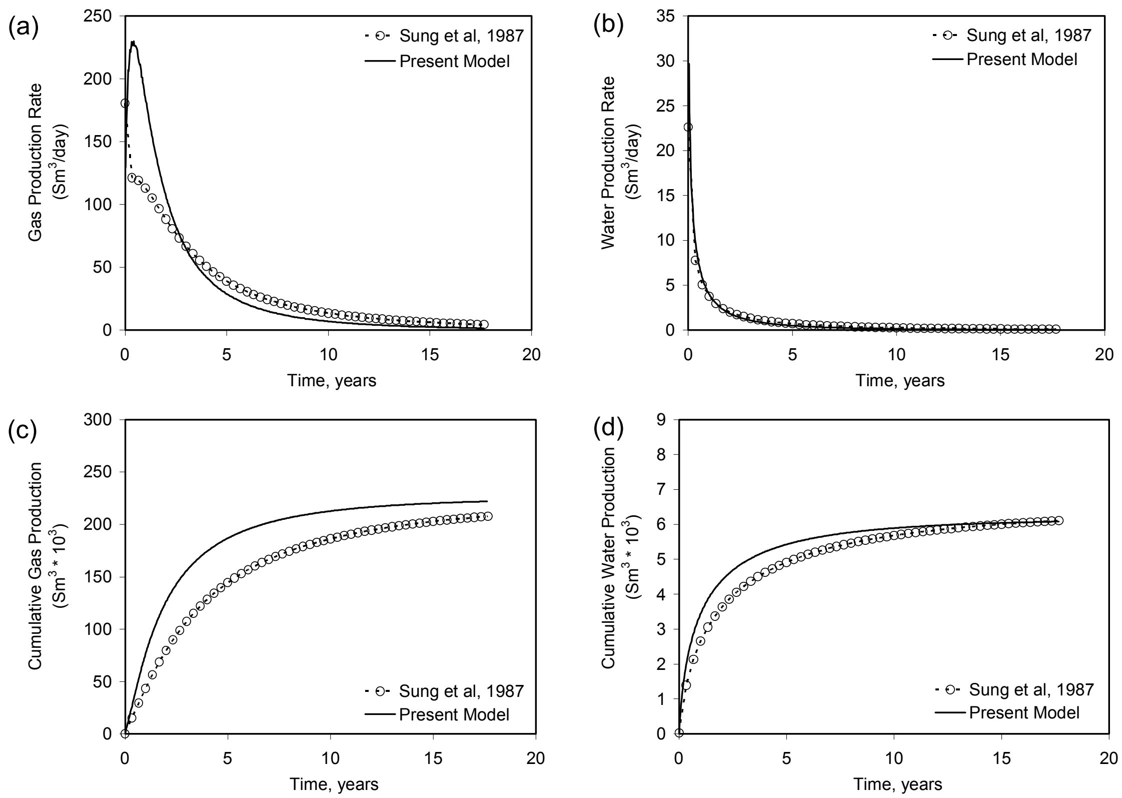

Figure 65. Comparison of results produced from the present model and the model developed by Sung$^{(251)}$ for the case of constant pressure constraint at the well. (a) Gas production rate (b) Water production rate (c) Cumulative production rate for gas (d) Cumulative production rate for water

In the second runs, the constant total flow rate was specified at the production well and the source term was excluded. Again, the coal seam is filled with 95% of water and 5% of gas and both phases are pumped out from the coal seam with a constant flow rate. Figure 66 shows the production rates and the cumulative productions of gas and water phases while Figure 67 compares the bottomhole pressure. As shown in Figure 66, the Sung's model predicts the production for about 6 years. After 6 years, the simulation stops since the bottomhole pressure reaches the abandonment pressure of the atmospheric pressure and the system does not support the constraint of the constant flow rate. In the present model, the production continues until about 11 years with a steady pace, then, the production rates declined. The bottomhole pressure predicted with the present model is about 1 to 2 MPa higher than the Sung's model (Figure 67). Comparing the cumulative production of gas and water with the constant pressure constrained well predictions (Figure 65), it can bee seen that the agreement between the total gas and water production predicted by the present model is better than expected. On the other hand, the cumulative gas and water production predicted by Sung's model is lower than those estimated by the present model. The difference in the bottomhole pressures and the deviations observed for the production rate and the cumulative production of gas and water phases, estimated from the present model, may be due to the use of different coordinate systems to solve the governing equation.

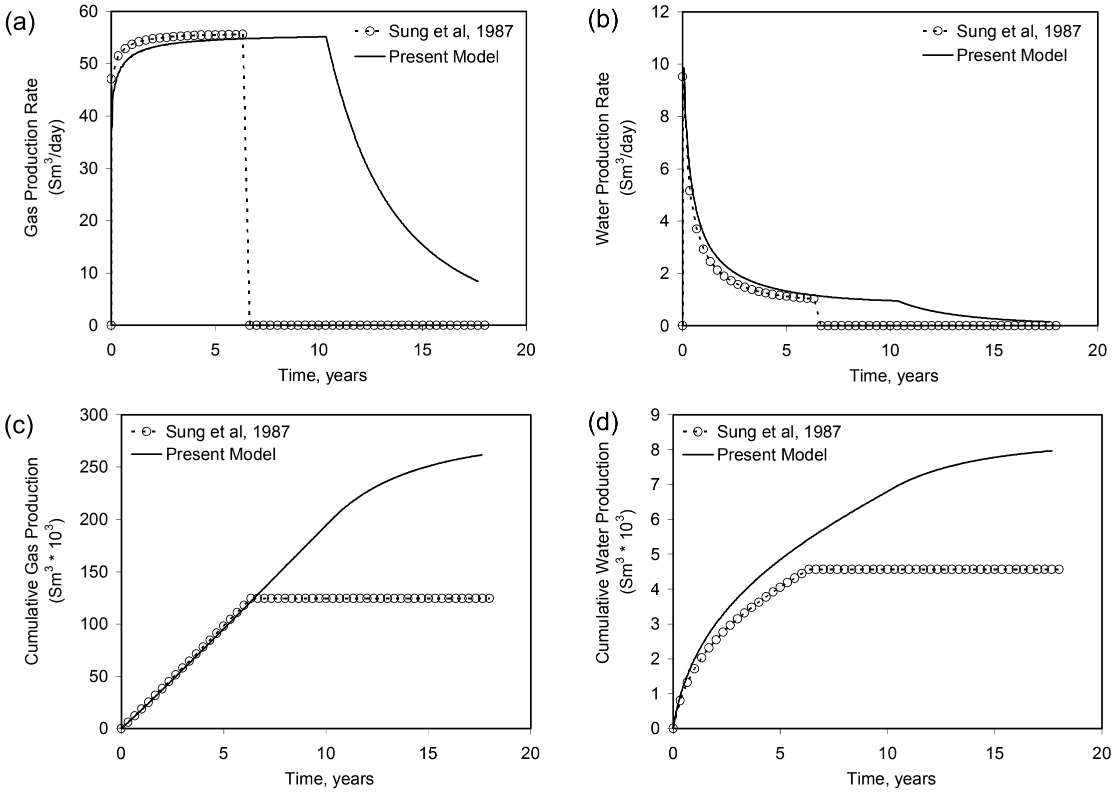

Figure 66. Validation runs for the case of constant total flow rate at the well. (a) Gas production rate (b) Water production rate (c) Cumulative production rate for gas (d) Cumulative production rate for water

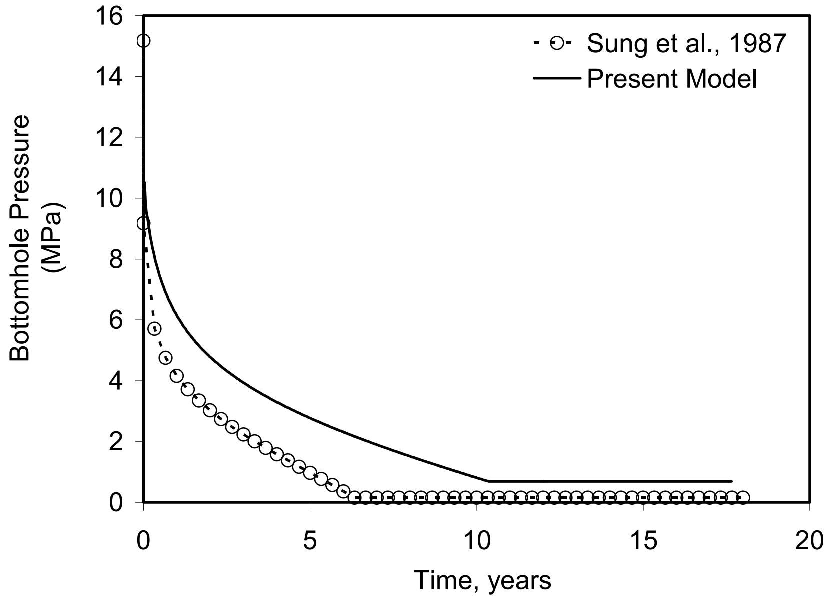

Figure 67. Bottomhole pressure for the case of constant total flow rate at the well

In the third runs, the pressure was specified at the production well, but this time, the source term is included. Figure 68 compares the production rates and the cumulative production of gas and water phases. As shown in Figure 68a, the production rate of the gas phase predicted by the present model is about 50% higher than that of predicted by the Sung's model. On the other hand, the agreement is excellent after the production period of 7 years. It has been shown that the unsteady-state sorption/desorption models predict higher production rates comparing to the quasysteady-state sorption/desorption models. For instance, Kolesar et al.(247) compared the unsteady- and quasysteady- state sorption models and indicated that, at the start of the simulation, the production rate predicted by the unsteady-state model is approximately 50% higher than the rate predicted by the quasysteady-state model. The early rate difference reduced to less than 25% after 10 days of production, and as the time went, the two models converged at a slower rate such that after 100 and 1000 days of production, the rates varied by less than 20% and 10%, respectively. Here, the difference between the gas production rates predicted by the present model and the Sung's model may come from the treatment of the source term in the governing differential equations as the unsteady-state in the case of the present model and the quasysteady-state as in the case of the Sung's model in addition to the choice of the coordinate system used by the two models. On the other hand, the agreement between the two models for the water production rate and the cumulative production of gas and water is better than expected.

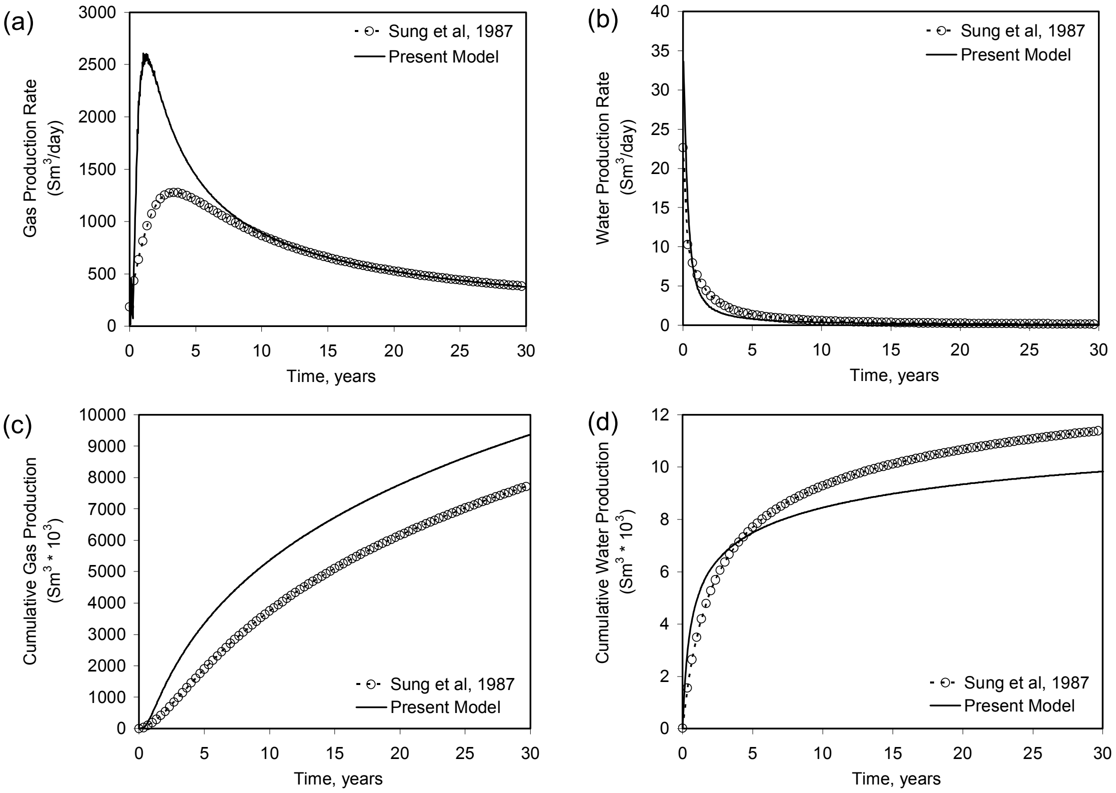

Figure 68. Validation of the present model with the model developed by Sung(251) for the case of constant pressure at the well while the source term was excluded. (a) Gas production rate (b) Water production rate (c) Cumulative production rate for gas (d) Cumulative production rate for water

In the fourth set of runs, the constant total flow rate was specified at the production well and the source term was included. Figure 69 and Figure 70 show the comparison of the results for the production rates, cumulative production of gas and water phases, and the bottomhole pressures, respectively. As shown in Figure 69, the agreement is excellent. The gas and water production rates and the cumulative gas production predicted by the two models agree well. The cumulative water production and the bottomhole pressure predicted by the present model showed little deviation comparing to the Sung's model. The deviation may come from the use of different coordinate systems and the choice of unsteady- or quasysteady- state representation of the micropore transport model. The predicted results may be best compared by the actual seam data when available. These numerical simulation exercises indicate that the compositional two-phase model developed in this study is more efficient as being faster and better optimized than that of the Sung's two-phase model. Therefore, the present model was considered to be used to relate the parameters involving the gas and water transport in a coal seam to the CO_2 sequestration and the ECBM production processes.

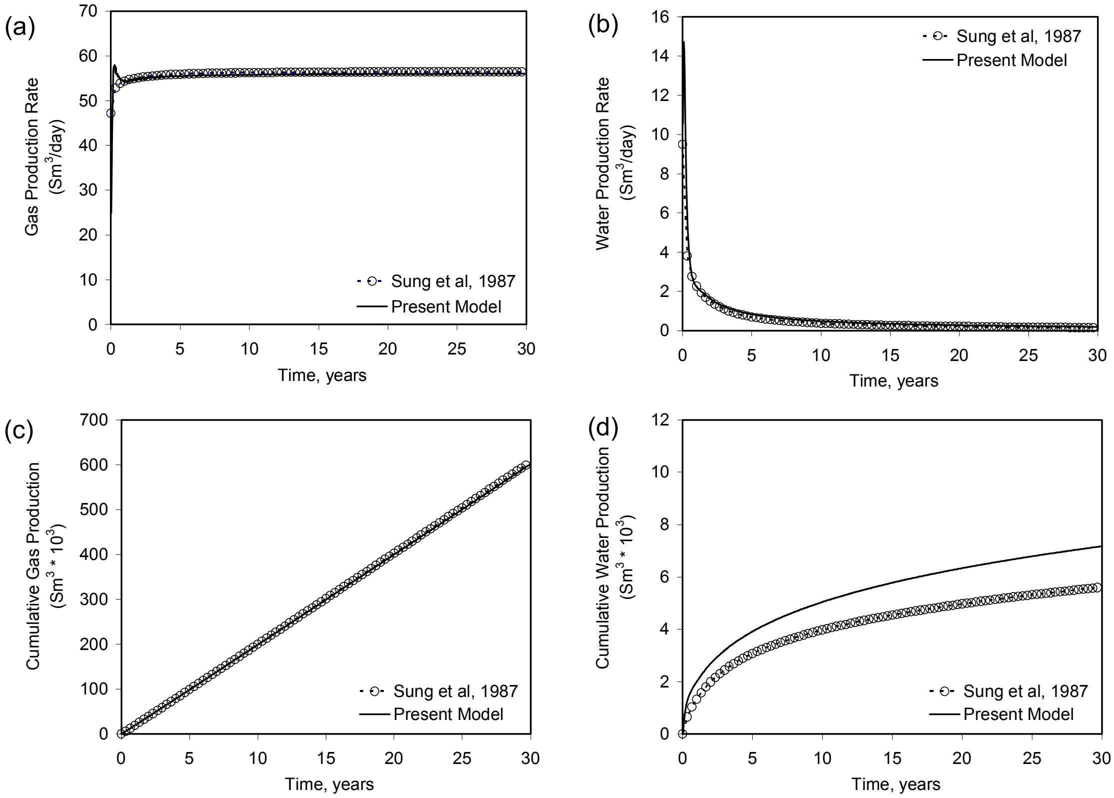

Figure 69. Validation of the present model with the model developed by Sung(251) for the case of constant pressure at the well while the source term was included. (a) Gas production rate (b) Water production rate (c) Cumulative production rate for gas (d) Cumulative production rate for water

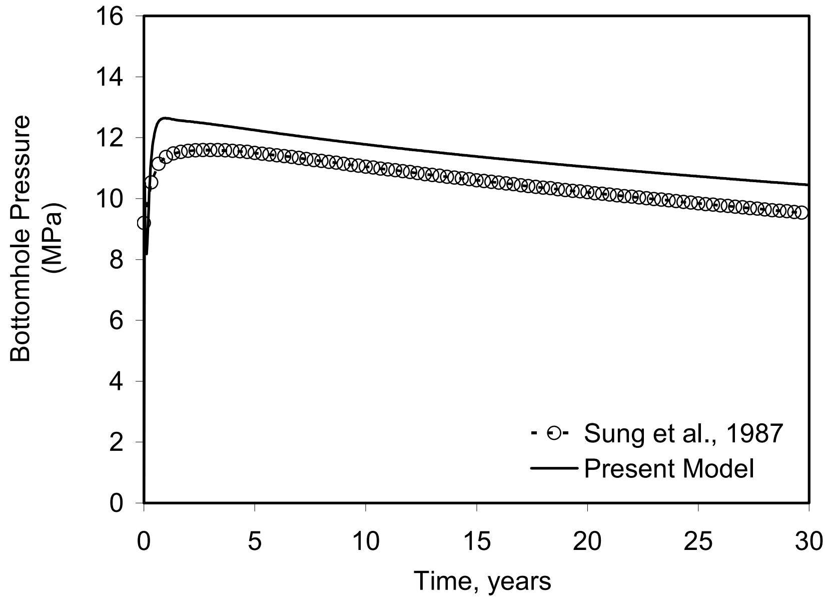

Figure 70. Bottomhole pressure for the case of constant total flow rate including the source term

4.8.6 Dewatering and Degasification of a Coal Seam

A series of computer runs were performed to illustrate the methane and water production from a coal seam. As mentioned earlier, the production rate or the bottomhole pressure can be specified at the production well. The selected values for the production rate could be any values, which could be low or high for the dewatering and degasification of a coal seam. Similarly, the selected values for the bottomhole pressure could be from near the atmospheric pressure up to the initial in-seam pressure. In order to investigate which value or values would be better for the internal boundary conditions at the production well, a set of computer runs were conducted.

Figure 71 shows the effect of bottomhole pressure selected for the internal boundary condition on the gas and water production rate and the cumulative productions. These data suggest that, typically, there are three stages in coal dewatering/degasification process.(254) At stage I, which corresponds to the first year in Figure, a huge amount of water is produced at the initial drainage because water initially occupies the cleat porosity in the reservoir, which controls the flow to the production well. At this stage, the relative permeability for water is high. As the water production continues, the hydrostatic pressure decreases, which result in the adsorbed methane to desorb and enter into the cleat porosity. The gas production rate is low and it increases as the water continues to be removed from the cleat system. The relative permeability to water decreases while the relative permeability to the gas increases. As can be seen in the figure, at the end of about 2 years, most of the water is pumped-off and the gas production rate reached at its maximum. At stage II, which corresponds to the second and third year in Figure 71, the gas production reaches at its maximum while the water production rate is considerably reduced. At this stage, the reservoir flow condition is almost stabilized until the beginning of the third stage. At stage III, which corresponds to the third year and thereafter in Figure 71, the gas production rate starts to decline. At this stage, the water production is low or negligible. Also, at this stage, both of the relative permeabilities to gas and water change very little.

As shown in Figure 71a and c, the gas production rate and the cumulative gas production are the highest when the bottomhole pressure is specified at its lowest level, i.e. near the atmospheric pressure. When the bottomhole pressure specification is increased, the production rate and the cumulative production decrease as well. Similar results were obtained for the water production rate and cumulative water production. As can be seen in Figure 71b and d, the water production rate decreased as the specified bottomhole pressure is higher. Here, the water production rate in Figure 71b was given for the first 5 years to better display the data. However, the cumulative water produced did not change significantly unless the specified bottomhole pressure is near the initial pressure at the in-seam condition. The intension here is to withdraw the gas and water from the coal seam as quickly as possible to be able to inject the CO_2 at the earliest time possible. Therefore, the bottomhole pressure should be selected as low as possible.

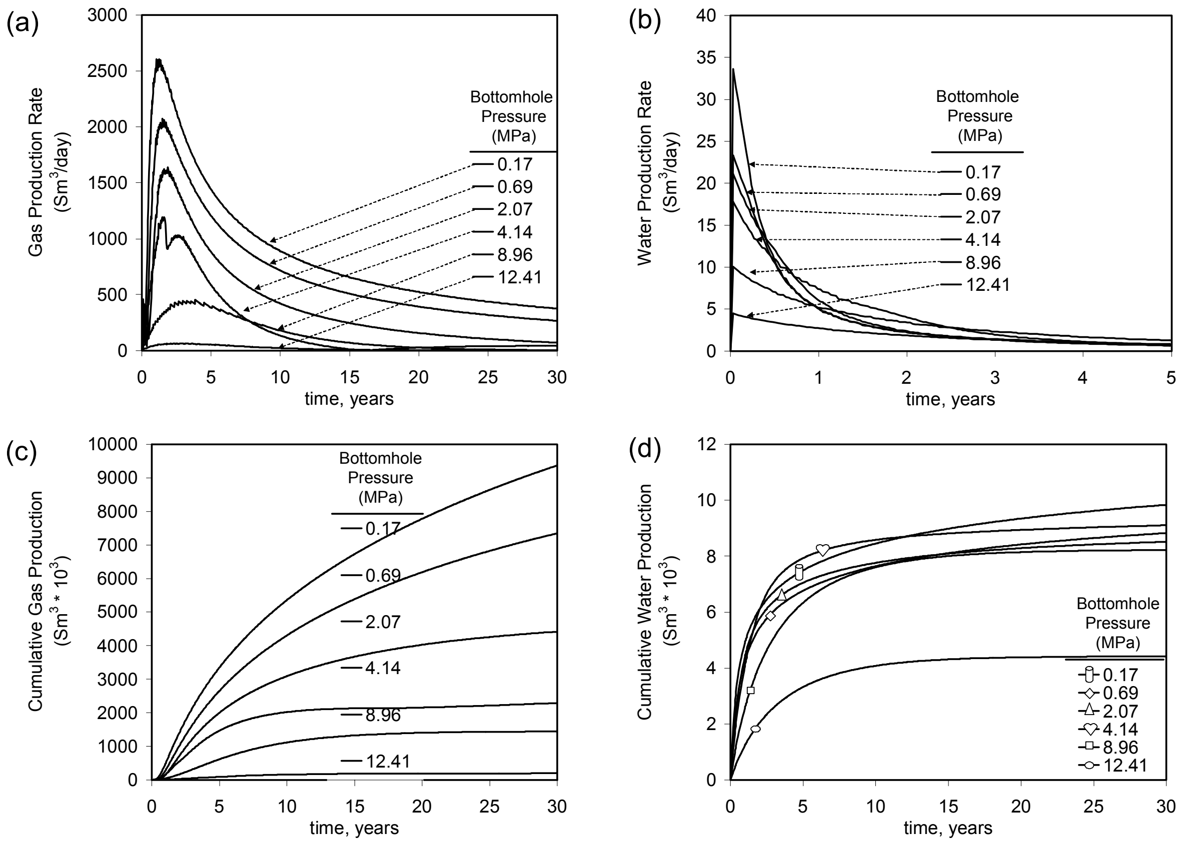

Figure 71. Effect of bottomhole pressure specification at the internal boundary on the gas and water production rates and the cumulative productions (a) Gas production rate (b) Water production rate (c) Cumulative production rate for gas (d) Cumulative production rate for water

The constant flow rate specification could also be made as the internal boundary condition at the production well. Figure 72 shows the effect of constant total flow rate specification at the internal boundary condition on the production rate and the cumulative production for the gas and water phases. In addition, the bottomhole pressures were also compared for the different production rate specifications as shown in Figure 73. As shown in Figure 72a and c, the greater the specified total production rate, the greater the gas production rate and the cumulative gas production could be obtained. However, as shown in Figure 72b and d, the effect of total production rate specification at the well was not significant on the production rate and the cumulative production for the water phase. The production rate and cumulative production of water phase increased slightly when the total flow rate at the well increased.

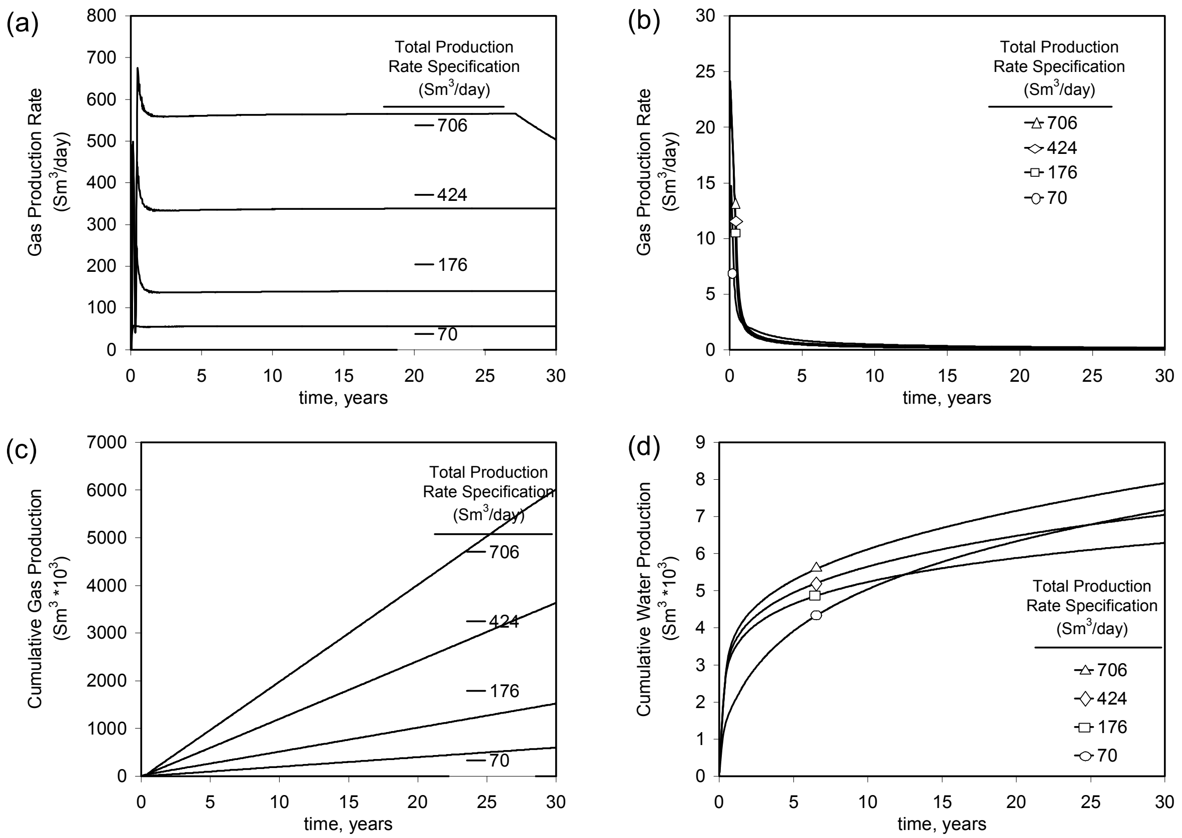

Figure 72. Effect of constant total flow rate specification at the internal boundary on the production rate and the cumulative production for the gas and water phases (a) Gas production rate (b) Water production rate (c) Cumulative production rate for gas (d) Cumulative production rate for water

The bottomhole pressure was nearly the initial in-seam pressure for the low production rate specification of 70 Sm^3/day as shown in Figure 73. As the total production rate at the well increased, the bottomhole pressure became smaller. After about 27 years of production, the bottomhole pressure was calculated to be near the atmospheric pressure for the production rate of 706 Sm^3/day. The low in-seam pressure could be advantageous because the higher injection rate of CO_2 could be achieved if the pressure difference is bigger between the injection point and the coal seam. These simulation results indicate that the production rate should be specified as large as possible to achieve faster degasification and dewatering of the coal seam as well as lower in-seam pressures. Therefore, if the constant production rate is to be specified at the production well, the highest production rates should be implemented. Or, because an aggressive degasification and dewatering of a coal seam will reduce the time to start the CO_2 injection, for the practical purposes, the near atmospheric bottomhole pressure, i.e. 0.17 MPa as used in this study, could be specified at the production well.

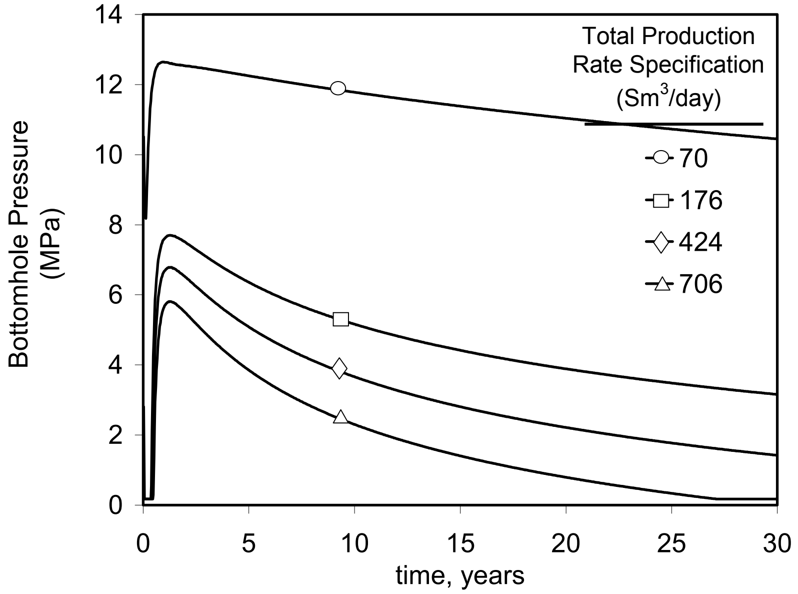

Figure 73. Bottomhole pressure for the case of constant total flow rate (the source term was included)

The length of the dewatering and degasification process is controlled by the physical properties of the coal seam and project development parameters. For instance, fracturing the coal seam and a closely spaced well configuration could significantly reduce the time for the dewatering and degasification processes of a coal seam. For instance, Figure 74 shows the pressure distribution along the coal seam and in the vicinity of the production well during the dewatering and degasification process. Here, the pressure at the well was specified to be near atmospheric (0.17 MPa) for an aggressive dewatering and degasification of the coal seam and to achieve maximum production rates. As can be seen, the pressure decline is more noticeable at the vicinity of the production well. Because the cleat porosity was occupied by the water and the production of water reduces the hydrostatic pressure, the pressure reduces along the coal seam over time. As a result of the pressure decline, the adsorbed methane starts to desorb and fill the cleat porosity. This is, as expected, increases the gas saturation in the cleat system as shown in Figure 75. As can be seen from the figure, the saturation near the well is higher than the rest of the coal seam. This is in good agreement with the pressure profile, as can be seen in Figure 74, the pressure near the well is at its lowest levels and bigger at the rest of the coal seam. However, the gas saturation could only be increased up to 70% near the well and 40% far from the well over a 30 year period. At this time, the pressure could decrease up to 1.56 MPa. At this pressure, according to the adsorption isotherm shown in Figure 63, most of the stored gas is still left behind which could reduce the storage capacity of coal for CO_2.

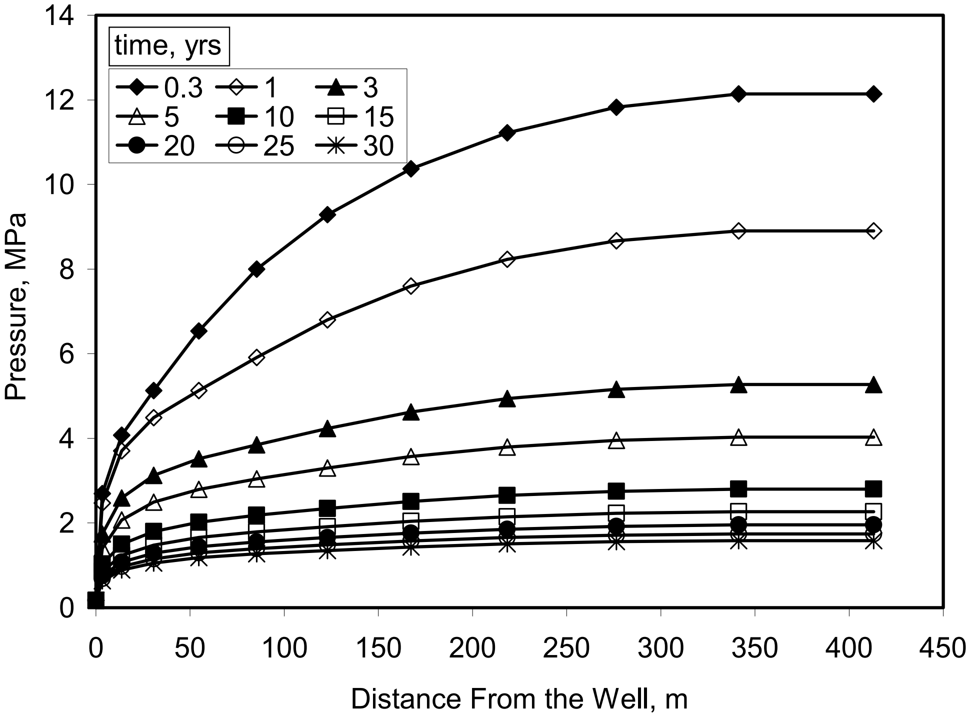

Figure 74. Pressure distribution during the dewatering and degasification of a coal seam

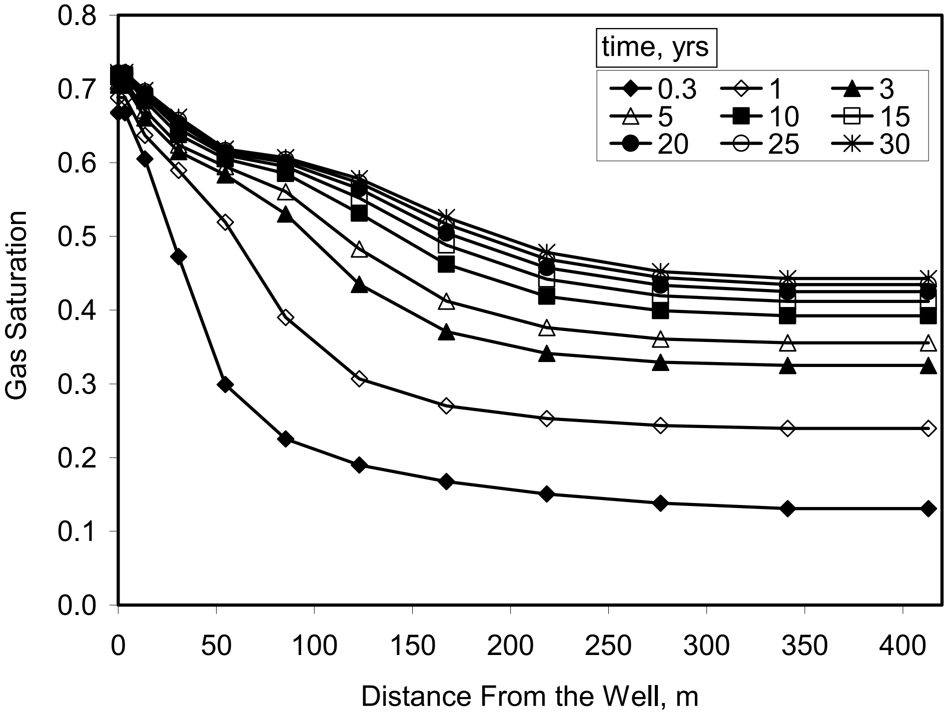

Figure 75. Gas saturation within the coal seam during the degasification process

At the specified reservoir conditions defined in Table 19, it seams that the pressure could only be reduced to about 1.56 MPa and the gas saturation increased up to 50% at the end of 30 years of degasification process. On the other hand, in 5 years of production, the gas saturation could reach up to 40% and the pressure could be reduced up to 4 MPa. This is due to the continuous desorption of adsorbed methane especially at lower pressures. Delaying the injection process for 30 years may not be practical for the degasification and dewatering of a coal seam before starting the CO_2 injection. However, the length of the degasification process can significantly be reduced, for instance, when well spacing is optimized. Therefore, a set of computer runs were conducted to investigate the effect of the drainage area on the production rates and the duration of the degasification and dewatering process as shown in Figure 76. Here, the near atmospheric pressure was specified at the production well to achieve maximum production rates. As can be seen in the figure, the gas and water production rates as well as the cumulative gas and water production are higher as the drainage area increased. However, as can be seen in Figure 76a, the peak gas production rate could be reached in a shorter time when the drainage area is smaller. The well spacing is therefore an important parameter for the efficiency of the production as well as the injection processes.

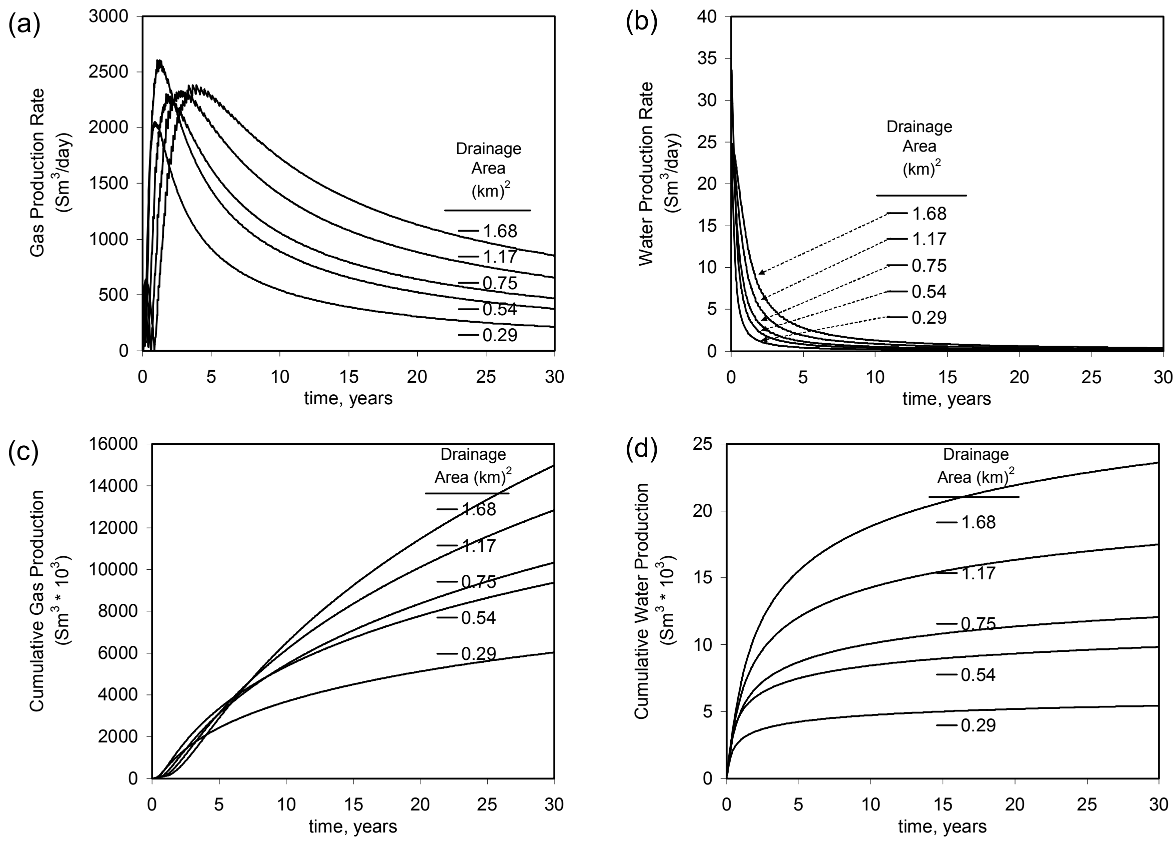

Figure 76. Effect of well spacing on the duration of the degasification and dewatering of a coal seam (a) Gas production rate (b) Water production rate (c) Cumulative production rate for gas (d) Cumulative production rate for water

4.8.7 Modeling of CO_2 Sequestration in the Previously Dewatered and Degasified Coal Seam

The previously defined layout (Figure 62) for the dewatering and degasification of a coal seam was rearranged for the CO_2 injection process as shown in Figure 77. In this configuration, the production well at the center will now be used for the CO_2 injection while its surrounding wells will continue the degasification and dewatering process. The default reservoir parameters used in these simulations are listed in Table 20. Here, the reservoir size was taken to be 826 m, which is the double size of the field that was studied for the degasification and dewatering process. The initial gas saturation and in-seam pressure were taken to be 0.4 and 3.4 MPa, respectively, considering a 5 years of dewatering and degasification as discussed in the previous section. The CO_2 was planned to be injected at the injection well where the pressure, the mole fraction of CO_2, and the gas saturation were set to be 15.2 MPa, 1.0, and 1.0, respectively. The production wells were set to continue pump out the gas and water from the coal seam at about 0.17 MPa which is near the atmospheric pressure. Because Athena Workbench Software Package is not capable of representing the production wells, the external boundary conditions were taken to be the same everywhere which was assumed to be the same with the boundary conditions at one of the production wells. Therefore, the flow rates at the production well could not be reported. Instead, the CO_2 injection rates, the cumulative injected CO_2, the CO_2 composition, the pressure, and gas saturation profiles along the coal seam were reported. The external boundary was set to shut-in in the model runs when the mole fraction of CO_2 reaches to the value of 0.5. Thereafter, the model runs were continued until the in-seam pressure reaches closer to the in-situ pressure.

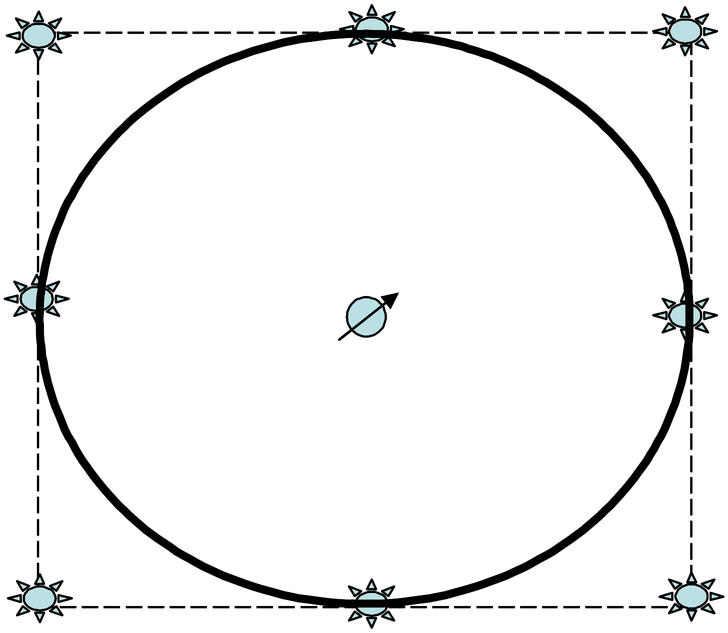

Figure 77. Layout for the CO_2 injection in a coal seam

Table 20. Default (base case) parameters for CO_2 injection in a coal seam

```
----------------------------------------------------------------------
 FORMATION PROPERTIES
 ----------------------------------------------------------------------
   RESERVOIR AREA..............................=      2.14       (KM)2
   AVERAGE RESERVOIR DEPTH.....................=    975.36           M
   FORMATION THICKNESS.........................=      3.05           M
   EFFECTIVE POROSITY..........................=      2.00           %
   ABSOLUTE PERMEABILITY.......................=      2.00          MD
   FORMATION COMPRESSIBILITY...................=  0.15E-03       1/MPA
   COAL DENSITY................................=      1.36      GR/CM3
   FORMATION TEMPERATURE.......................=     68.10          OC
   INITIAL FORMATION PRESSURE..................=      3.45         MPA
   INITIAL WATER SATURATION....................=      0.60    FRACTION

 INITIAL GAS AND WATER IN PLACE
 ----------------------------------------------------------------------
    CO2 IN ADSORBED PHASE......................=      0.00   SM3*10**6
    CH4 IN ADSORBED PHASE......................=     94.59   SM3*10**6
    COMPOSITION FOR CO2 IN BULK GAS PHASE......=      0.00    FRACTION
    COMPOSITION FOR CH4 IN BULK GAS PHASE......=      1.00    FRACTION
    CO2 IN BULK GAS PHASE......................=      0.00   SM3*10**3
    CH4 IN BULK GAS PHASE......................=      6.75   SM3*10**6
    TOTAL CO2-IN-PLACE.........................=      0.00   SM3*10**6
    TOTAL CH4-IN-PLACE.........................=    101.34   SM3*10**6
    TOTAL H2O-IN-PLACE.........................=     78.23   SM3*10**3

 WELLBORE PROPERTIES
 ----------------------------------------------------------------------
   WELL RADIUS.................................=      8.89          CM
   WELLBORE PRESSURE...........................=     15.17         MPA
   SKIN FACTOR.................................=      0.00

 ADSORPTION ISOTHERMS
 ----------------------------------------------------------------------
   ADSORPTION CAPACITY FOR CO2.................=      3.55     SM3/TON
   ADSORPTION CAPACITY FOR CH4.................=      0.61     SM3/TON
   LANGMUIR PRESSURE FOR CO2...................=      0.10         MPA
   LANGMUIR PRESSURE FOR CH4...................=      1.15         MPA

 TRANSPORT PARAMETERS
 ----------------------------------------------------------------------
   CLEAT SPACING...............................=      1.31          CM
   MICROPORE DIFFUSION COEFFICIENT.............=  0.19E-06      M2/DAY
   SORPTION TIME CONSTANT......................=    231.46         DAY
   CRITICAL WATER CONTENT (SWC)................=      0.00    FRACTION
   CRITICAL GAS CONTENT (SGC)..................=      0.00    FRACTION
   RELATIVE PERMEABILITY TO WATER AT SGC.......=      1.00          MD
   RELATIVE PERMEABILITY TO GAS AT SWC.........=      1.00          MD
 ----------------------------------------------------------------------
```

The first computer run was performed to illustrate the CO_2 injection into a fractured formation without the source term. Figure 78 shows the CO_2 injection rate, the cumulative injected CO_2, the mole fraction of CO_2 in gas phase in the fractures, the pressure distribution, and the gas saturation along the formation over the injection time. As can be seen in Figure 78a, the injection rate is about $12*10^3$ Sm^3/day and a sharp decrease in the injection rate was seen at early times of injection. The injection rate stabilized after two months of injection. After 9 months of injection, the injected Co2 reached to the external boundary where the production wells were shut-in. After this time, the injection rate was seen to decrease. A total of $4.5*10^6$ Sm^3 of CO_2 could be injected within the fractured formation without adsorption. As can be seen in Figure 78b, the injected CO_2 flows through the fractured formation with an advancing front. In about 9 months, the CO_2 front reaches to the production well. As can be seen in Figure 78c, a linear pressure profiles were established between the injection and the production wells. When the production wells were shut-in and the injection continued, the pressure in the seam increased until it reaches closer to the initial in-situ pressure. The gas saturation, as shown in Figure 78d, increased as the injection continued up to a certain distance. The saturation at the production well was also slightly increased. The saturation profiles suggest that the fractured media became fully dry near the injection well. However, the saturation was not affected away from the injection well and just replaced the methane filled in the cleat porosity in the fractured reservoir.

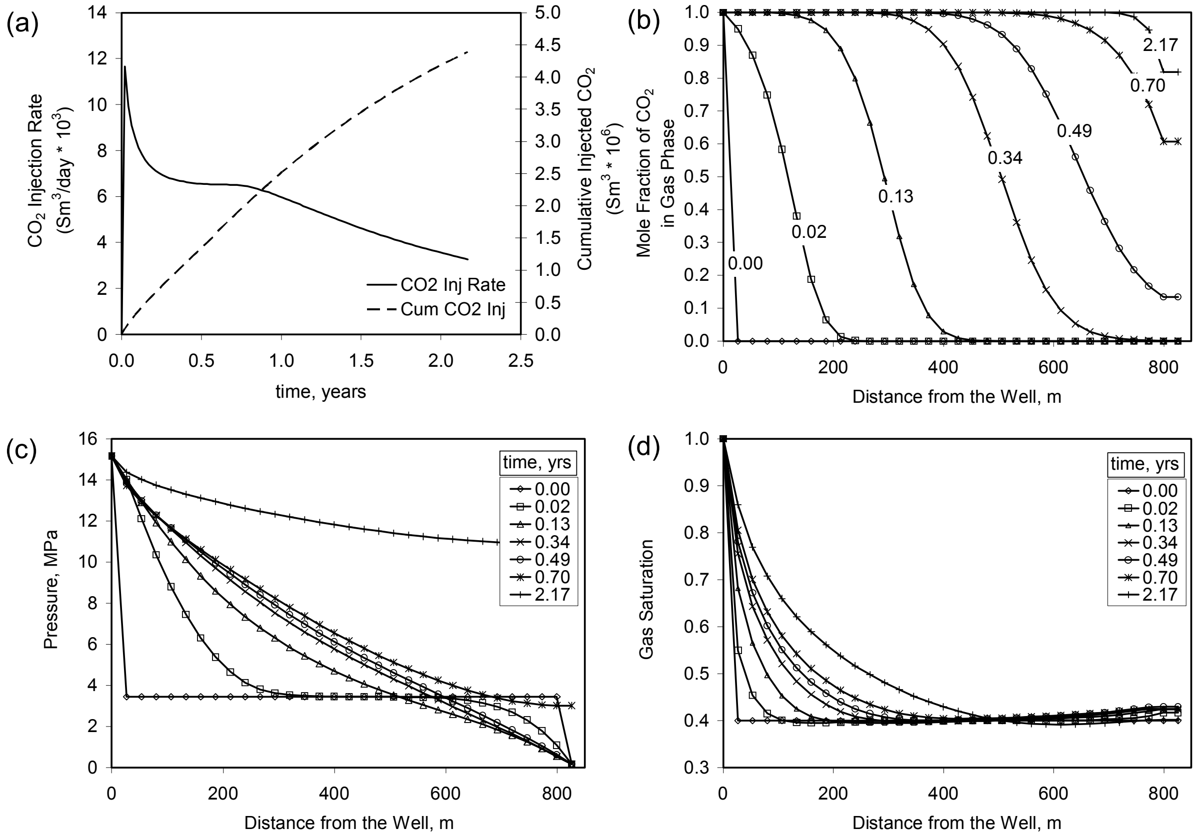

Figure 78. CO_2 injection in a coal seam without the source term (a) CO_2 injection rate and the cumulative injected CO_2, (b) mole fraction of CO_2 in the gas phase (c) pressure (d) gas saturation

The second computer run was conducted on a CO_2 injection process using the default system. At this time, the adsorption and desorption, or the source term, was included. Figure 79 shows the CO_2 injection rate, the cumulative injected CO_2, the mole fraction of the CO_2 in the gas phase, the pressure, and the gas saturation along the coal seam over time. As shown in Figure 79a, a $12*10^3$ Sm^3/day of CO_2 could be injected into the specified coal seam, where the injection rate decreases slightly to about $9*10^3$ Sm^3/day initially and then recovers over time reaching a steady injection rates in about 10 years. The injection rate becomes almost steady until the CO_2 front reaches to the production well at which the production wells were shut-in. This is consistent with the actual field data from San Juan basin, where the CO_2 injection rate was first reduced and then slightly recovered over 3 to 5 years. After the external boundary was shut-in, the injection rate started to decrease sharply until the injection process is complete. Figure 79b shows the mole fraction of CO_2 in the gas phase along the coal seam. As can be seen, the injected CO_2 flows through the coal seam towards the production well with a moving front. The mole fraction of CO_2 behind the moving front is about unity whereas there is no CO_2 after the moving front. The mole fraction decreases sharply at the moving front. The CO_2 breakthrough was seen at about 30 years for the present configuration. Figure 79c shows the pressure profiles during the CO_2 injection. As can be seen from the figure, almost linear pressure profiles were established between the injection and the production wells until the CO_2 breakthrough was observed. After the production wells were shut-in, the pressure was steadily build-up and reached closer to the initial in-situ pressures after 43 years. Figure 79d shows the gas saturation profiles within the coal seam. As can be seen from the figure, the gas saturation is about 1.0 near the injection well and decreases along the coal seam. As shown in the figure, the gas saturation decreases sharply near the moving front (see Figure 79b) indicating that the CO_2 replaces the water and pushes it toward the production well. For the present system, the injected CO_2 reaches the production well in about 30 years, where the coal is saturated by the injected CO_2. After the CO_2 front reaches the production well, the additional CO_2 injection fills up the cleat porosity by building up the pressure in the cleat system towards the completion of the injection process.

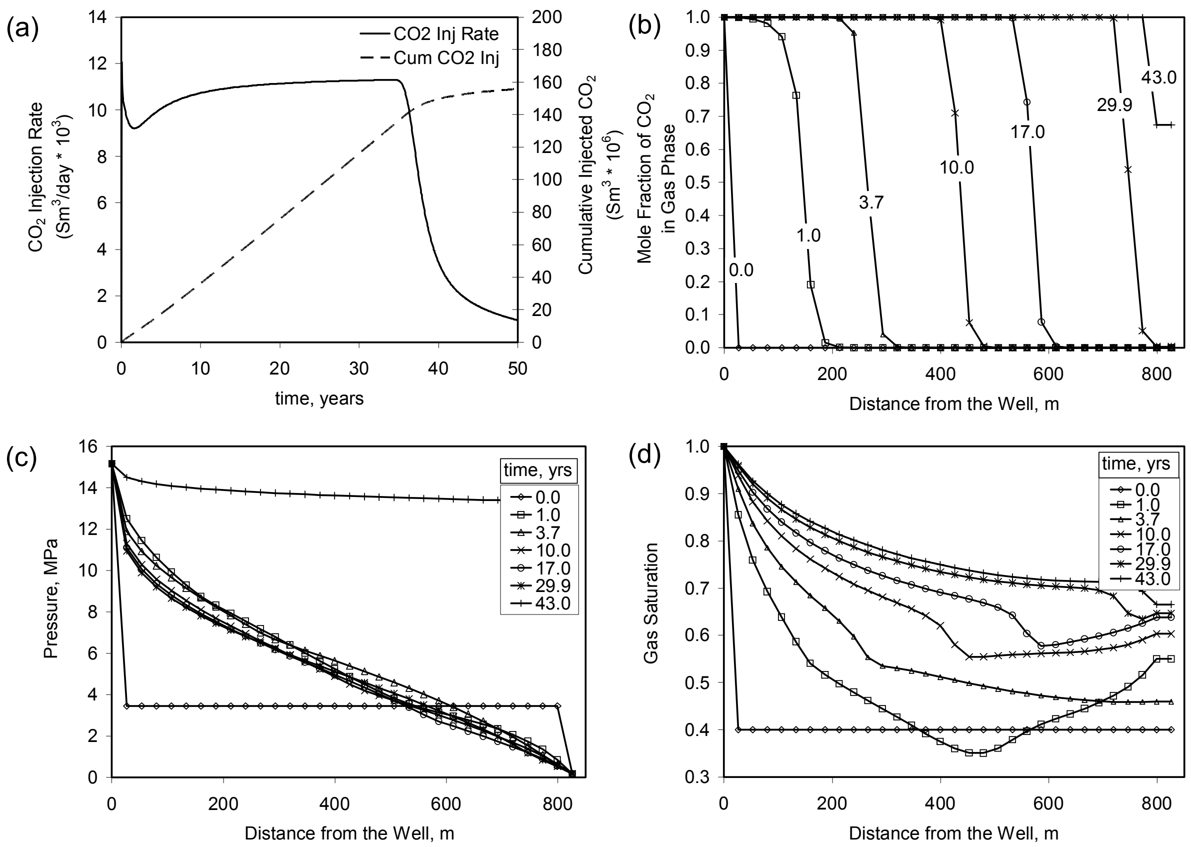

Figure 79. CO_2 injection in coal seam including the source term (a) CO_2 injection rate and the cumulative injected CO_2, (b) mole fraction of CO_2 in the gas phase (c) pressure (d) gas saturation

4.8.8 Effect of Coal Seam Properties on CO_2 Sequestration: Parametric Studies

A parametric study was conducted to investigate the effects of the intrinsic coal-seam properties as well as the thermodynamic and physical relationships that exist between these properties on CO_2 sequestration in coal seams. The default parameters (base case) shown in Table 20 were used in the model by altering only one parameter at a time for the subsequent runs for comparison. In fact, an actual coal seam sequestration process could have been modeled as a case study where the actual coal seam parameters are used and the results could be compared with the field data. However, this is not the case here due to lack of field data; instead, it was aimed to analyze the effect of the important parameters on the CO_2 sequestration process in a coal seam.

4.8.8.1 Effect of Coal Thickness on CO_2 Sequestration: The model was run for the default parameters listed in Table 20 while replacing the coal thickness values for the subsequent runs. Figure 80 shows the effect of coal seam thickness on CO_2 injection rate and the cumulative injected CO_2. As can be seen, the CO_2 injection rate increases as the coal thickness increases. In addition, the cumulative stored CO_2 is also increased with the coal thickness. The CO_2 breakthrough does not change. A higher coal seam thickness is therefore important for the amount of CO_2 that can be sequestered in coal seams at higher injection rates.

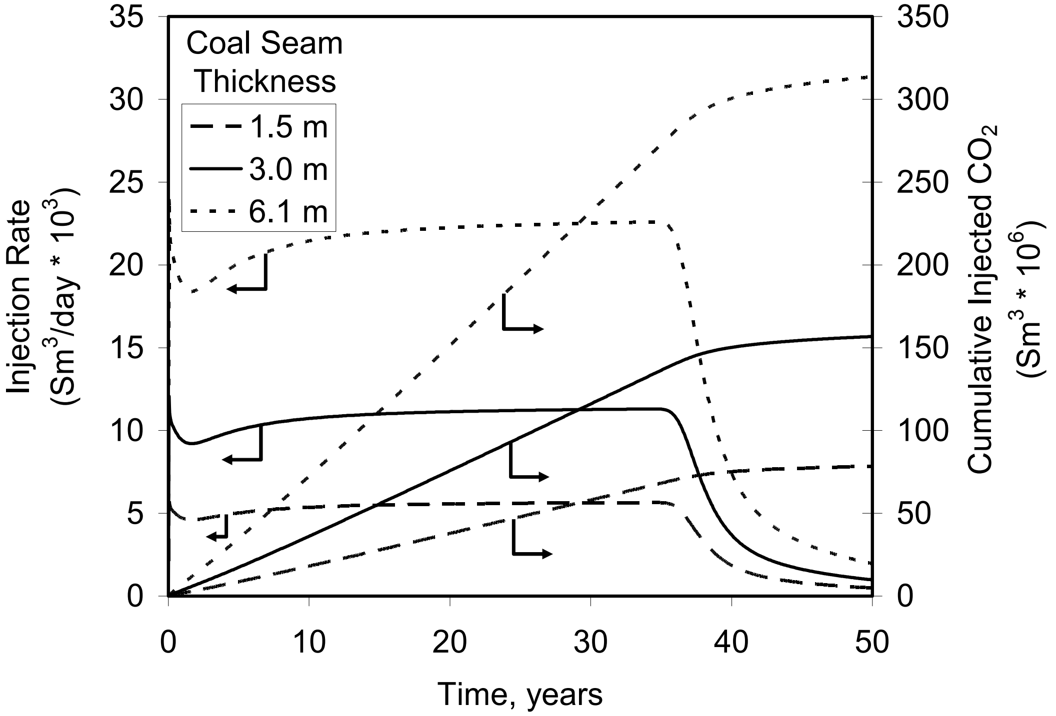

Figure 80. Effect of coal seam thickness on the CO_2 sequestration

4.8.8.2 Effect of Permeability on CO_2 Sequestration: The permeability is a property of a porous medium, which is related to how fast the coal seam can conduct the fluids. Therefore, permeability is one of the most important parameters in coal seam sequestration. Because the CO_2 sequestration would most probably be applied to the deep, unmineable coal seams, the permeability values for such coal seams is expected to be lower. Therefore, the permeability values were selected to be 0.5, 2.0, and 5.0 md, respectively. As can be seen in Figure 81, there is a huge effect of the permeability on the CO_2 injection rate. The injection rate is higher in those coal seams possessing higher permeability values whereas the injection rate is smaller for those possessing lower permeability values. In addition, as shown in the figure, the breakthrough for those coal seams possessing higher permeability values results in shorter length of time for the

CO_2 breakthrough whereas longer length of time is required for the breakthrough for the low permeable coal seams. Therefore, the low permeable coal seams require low injection rate and longer periods of injection.

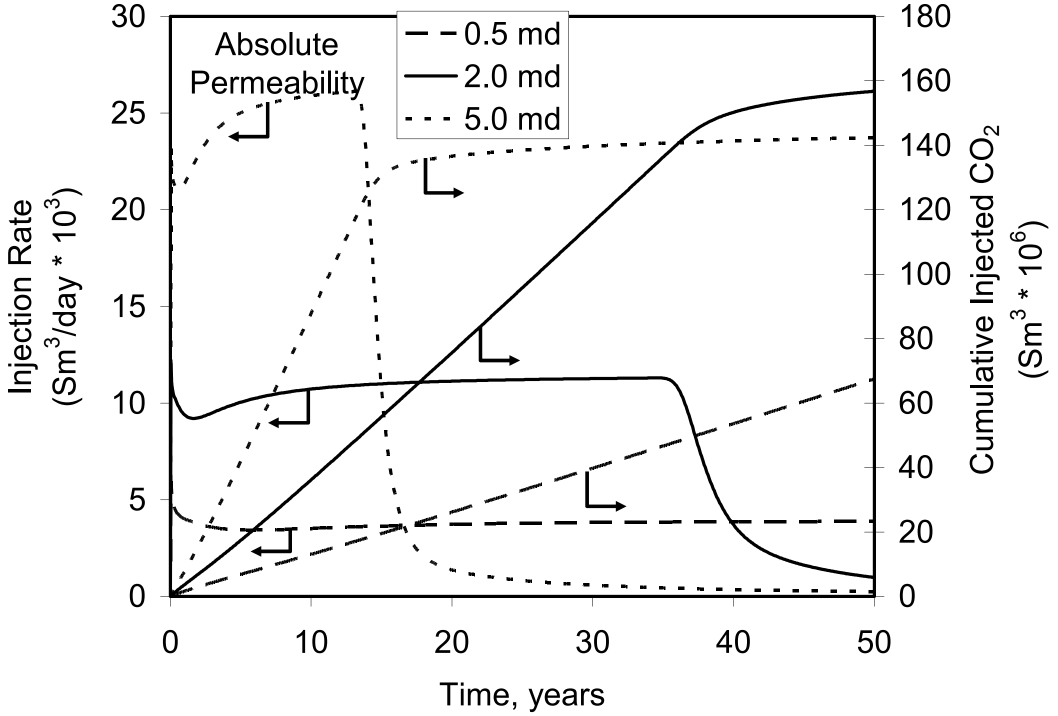

Figure 81. Effect of permeability on the CO_2 sequestration

4.8.8.3 Effect of Compressibility of Coal on CO_2 Sequestration: Compressibility of a coal seam is related to the volumetric changes of the coal matrix under the influence of the effective stress as well as the swelling-shrinkage properties of the coal. The compressibility of coal can also be related to the permeability because any change in expansion or contraction in coal will affect the cleat opening, and therefore, the cleat porosity within the coal seam. As shown in Figure 82, a low compressibility of $1.45*10^{-4}$ to $1.45*10^{-3}$ MPa^{-1} seems to affect the injection process little, however, higher coal compressibility values, say $1.45*10^{-2}$ MPa^{-1} or lower, are shown to decrease the injection rate and increase the length of time for the breakthrough. The effect of compressibility on the coal matrix along with the matrix shrinkage/swelling due to the desorption/adsorption processes can also be accounted, i.e. by using Eq.(143). Because the reservoir studied here was for an ideal case, only the compressibility of coal was accounted due to the change in the confining stress.

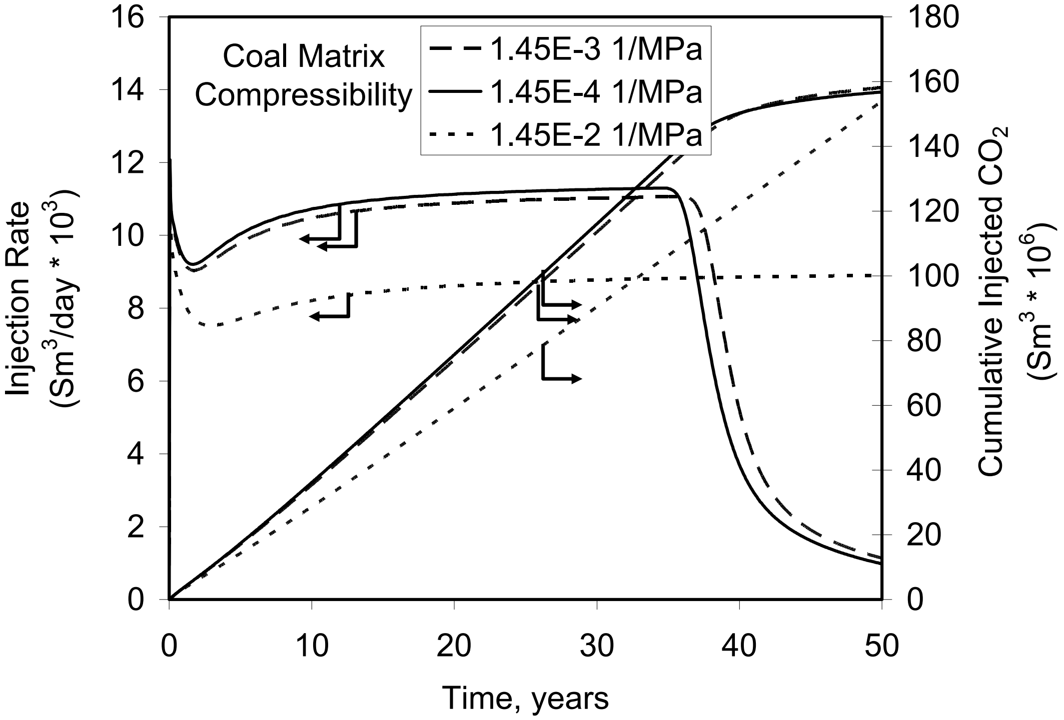

Figure 82. Effect of coal compressibility on the CO_2 sequestration

4.8.8.4 Effect of Cleat Porosity on CO_2 Sequestration: Cleat porosity is the space between the coal matrixes serving as both the conduit for the fluid flow and the space for gas storage. As shown in Figure 83, higher injection rates can be achieved for the coal seams possessing higher cleat porosity. The breakthrough was seen in shorter times in such coal seams. However, the cumulative injected CO_2 was shown to be smaller. While the cleat porosity providing extra volume for gas storage, the volume for the coal matrix became smaller. As shown in the figure, the storage capacity for the injected CO_2 is lower for the coal seam with larger cleat porosity.

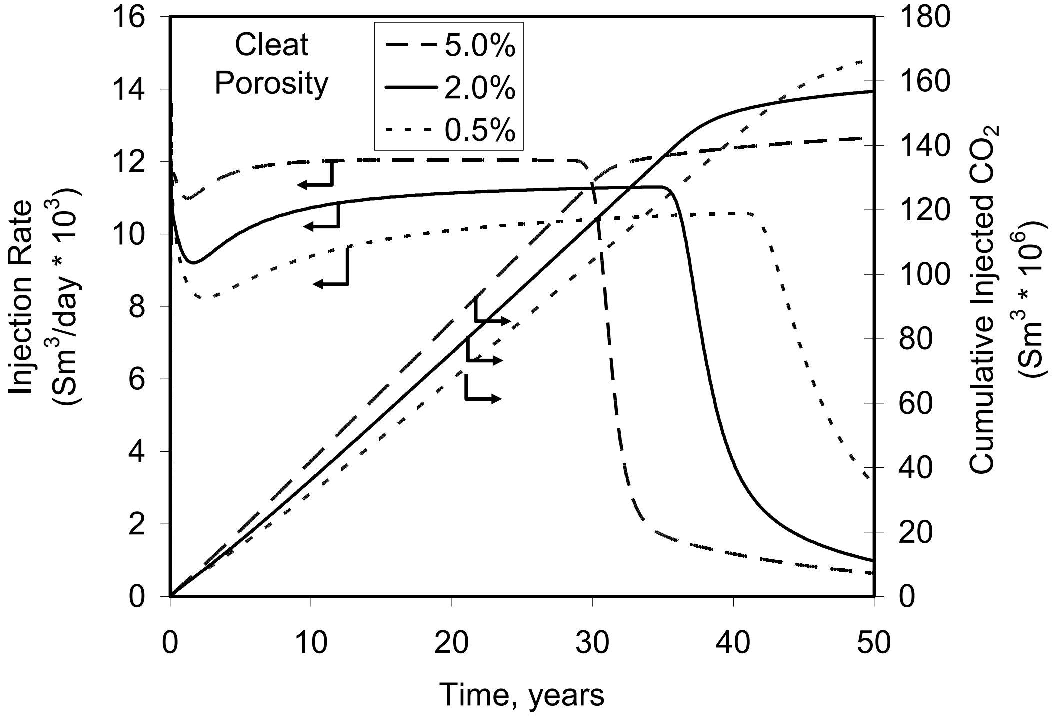

Figure 83. Effect of cleat porosity on the CO_2 sequestration

4.8.8.5 Effect of Cleat Spacing or Sorption Time Constant on CO_2 Sequestration: Cleat spacing is a characteristic dimension of the coal matrix in a coal seam. The cleat spacing, *s (m)*, and the matrix diffusion coefficient, D_i *(m^2/day)*, are related to sorption time constant, τ *(day)*, which determines the rate at which gas is released from the micropores to the cleat system or *visa versa* by the following equations for a cubical matrix element:(189)

$$\tau = \frac{\left(s/2\right)^2}{D_i} \tag{130}$$

The sorption time constant was calculated to be 1.35, 134.5, and 231.5 days for the cleat spacing of 0.1, 1.0, and 1.31 cm, respectively. Figure 84 shows the effect of the cleat spacing or the sorption time constant on the CO_2 injection process. As can be seen from the figure, neither the injection rate nor the cumulative injected CO_2 were affected by the cleat spacing until the period of the breakthrough. This indicates that the flow within the porous reservoir is so slow enough that the sorption/desorption process can support the appearance disappearance of gases in the cleat system. For the larger cleat spacing, the length for the breakthrough is slightly shorter; however, it is not much significant.

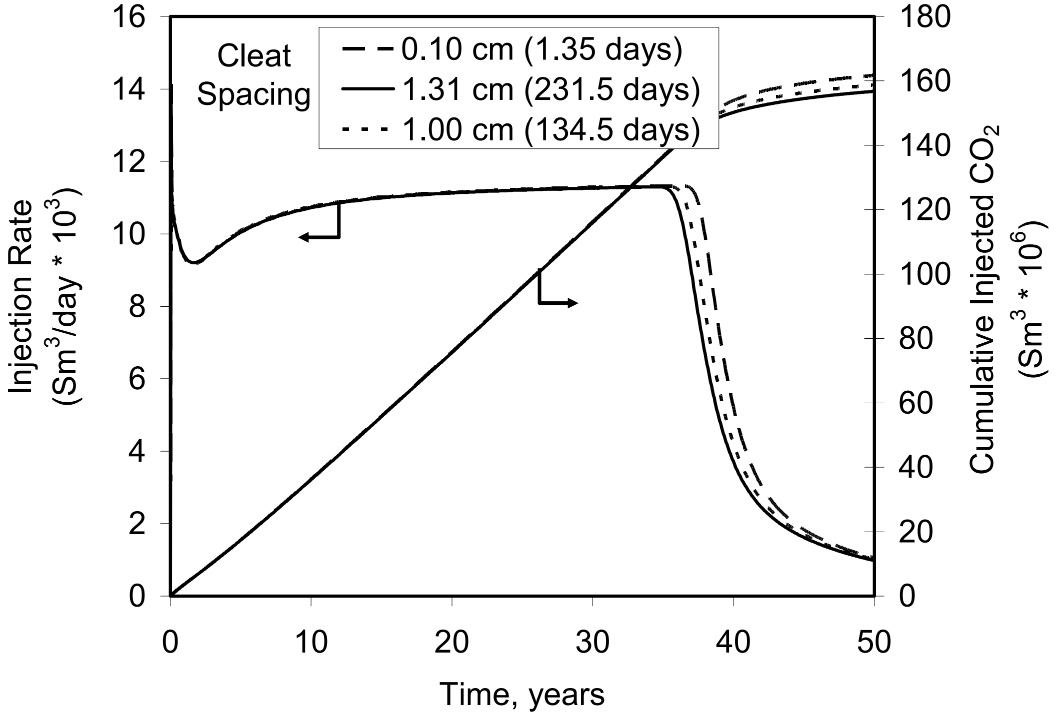

Figure 84. Effect of cleat spacing or sorption time constant on CO_2 sequestration

4.8.8.6 Effect of Adsorption Capacity on CO_2 Sequestration: Adsorption capacity may vary from seam to seam depending on the chemical and physical nature of the coal seams and the additional occupants within the coal matrix as discussed in the previous sections. For instance, the microporosity within the coal matrix is essential for the storage of gases by adsorption. Coalbed methane is one of the adsorbed components in microporosity in the coal matrix which was shown to be left behind at the end of the degasification and dewatering process (see section 4.8.6). Another most important component is the moisture. The fact that the adsorbing gases compete with moisture for the adsorption sites and/or the pore volumes in the coal matrix at the laboratory conditions is well known.(40) At the in-seam conditions, the injected CO_2 has to compete with the moisture which already occupied the available pore space. Therefore, the adsorption capacity of a coal seam may vary depending on the availability of the microporosity in the bulk coal. Here, the model runs were conducted using three different adsorption capacities as shown in Figure 85. For the coal seams having less adsorption capacity, the injection rate was smaller and the breakthrough was shorter. As the adsorption capacity of a coal seam is higher, the injection rate would be higher, the duration of the injection process would be longer, and the cumulative injected CO_2 would be higher. The slight increase in the injection rate, for instance, experienced in the San Juan Basin(206) could be related to the increase in the adsorption capacity of coal over the injection period since the injected CO_2 could dissolve the mineral matter within the coal matrix and increases the storage capacity of the coal.

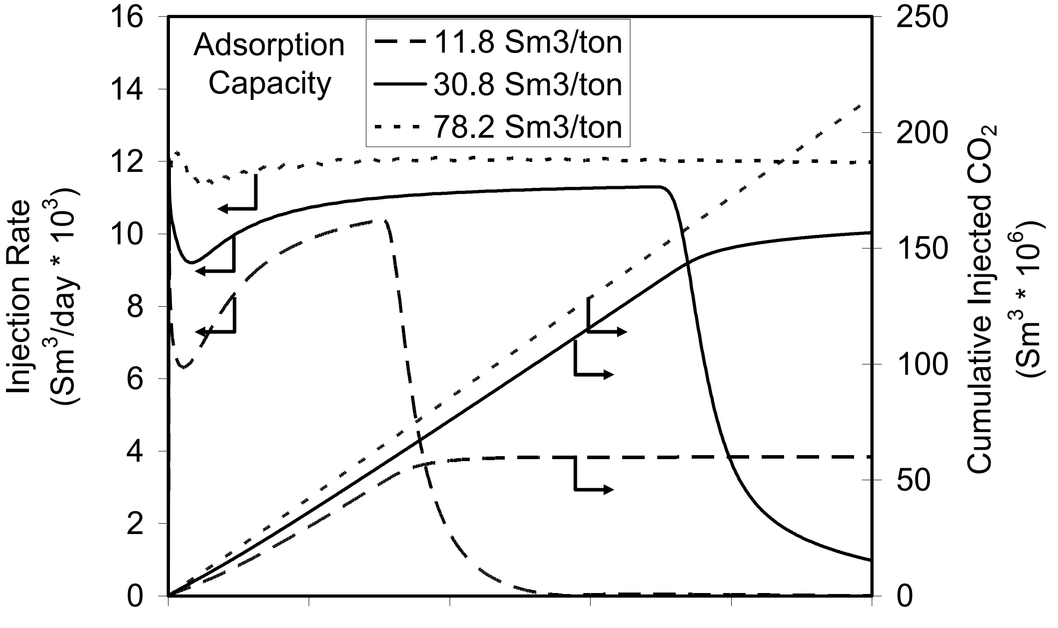

Figure 85. Effect of adsorption capacity of coal on the CO_2 sequestration

5.0 CONCLUDING REMARKS

An experimental and theoretical study has been conducted to obtain the adsorption capacity of coals and parameters that affect the coal-CO_2 interactions. An experimental setup was constructed to measure the adsorption and desorption isotherms of CO_2 on eight Argonne Premium coals, including Pocahontas No.3, Upper Freeport, Pittsburgh No.8, Lewiston-Stockton, Blind Canyon, Illinois No.6, Wyodak, and Beulah-Zap coals. From these experimental results, the following concluding remarks could be made:

- Upon drying, the coals, especially low rank coals, were found to shrink. A 2% to 5 % shrinkage was observed for the high rank coals as a result of moisture lost, and up to 40% shrinkage was observed for the low rank coals. The volume change of the coals upon moisture loss was found to be greater than the volume of removed water to indicate the collapsing of the pores in coal.
- The shapes of the adsorption isotherms of CO_2 on coals were found to be more-or-less rectilinear. Hysteresis were seen between adsorption and desorption isotherms and typically the hysteresis were larger as the coal rank decreased. The volumetric changes were thought to be the reason for the hysteresis and the rectilinear shape of the adsorption isotherms.

- The excess adsorption isotherms of CO_2 on coals were found to fit to the conventional model equations poorly. This was related mostly to the volumetric changes during the adsorption isotherm measurements. Thus, an improved adsorption isotherm model was derived, which explicitly took account for the volume changes. It was shown that when the volumetric changes were not accounted for in the high-pressure CO_2 adsorption isotherm data for coals, the estimated surface areas and the adsorption capacity would be over-estimated amounting from about 15% to 40%.
- Employing the modified Dubinin-Astakhov equation, high temperatures were shown to decrease the adsorbed amount and the adsorption capacity of coals while there were no major changes on their coal's physical characteristics.
- The presence of moisture was found to significantly decrease the CO_2 adsorption capacities of coals due to either blocking the path to or by occupying the adsorption sites within the coal matrix.
- Acidic pHs was shown to dissolve the mineral matter in coal especially calcite. The adsorption capacity of acid-treated coals was found to be higher than those untreated and base-treated coals. The increase in the adsorption capacity was related to the removal of the ash content of coals.
- The unusual shape of the high-pressure adsorption isotherms of CO_2 on coals was shown to be the result of both the volumetric changes due to the extracted volatile matter by the supercritical CO_2 and the experimental uncertainties especially at pressures higher than 9 MPa.

- The injection process is highly affected by the coal seam properties especially permeability, adsorption capacity, cleat spacing, and the presence of both water and CBM in the coal seams.

The CO_2 adsorption capacity for powdered and partially dried Argonne coals was estimated to be about 10-30 Sm^3/ton-coal, dry, ash free basis. These capacities were expected to be well below for the actual coal seams, especially when the coal seams are saturated with water. However, these capacities would suggest that the coal seams could be a good sink for the CO_2 sequestration considering the tons of coals underlying underground to be unmineable. The coal which is unmineable in today's conditions would be mineable in the future; however, these issues should be considered in planning the available candidate coal seams. On the other hand, the sequestration of CO_2 in coal seams can be profitable. For example, the production of methane from coal seams may offset the sequestration costs, and in mostl cases, it is profitable. While sequestering the CO_2 in coal seams, the coalbed methane could be produced, which makes this option more advantageous.

6.0 FUTURE WORK

The excess adsorption isotherms of CO_2 on Argonne coals were measured and their CO_2 sorption capacities were estimated. These measurements were performed on the partially dried powder coals. Although the adsorption capacity for powdered coals can give insights about what the maximum storage capacities could be achieved in a candidate coal seam, these capacities reported for the powdered coals would be different at the actual coal seam conditions. The future work would be to estimate the sorption capacity of coals using core coal sample albeit it takes longer times for equilibration, in the order of months, which were not applicable for a graduate students' program of study. However, it could be more useful if the adsorption capacities of the coals are estimated using core coal samples while accounding for the volumetric effects during the adsorption isotherm measurements.

It was shown that the adsorption on non-rigid solids is a dynamic process. The model equations in the literature to represent the adsorbed amount assume that the surface sites for the adsorption as well as constant adsorption energies are constant, and thus, do not account this dynamic nature of the adsorption process. The future work would be to investigate a more sophisticated adsorption equation which represents the dynamic nature of the adsorption in systems such as CO_2 adsorption on coals and adsorption of organic vapors on polymers.

A mathematical model was developed for the CO_2 sequestration and CBM production in coal seams. The model is simple, fast, and handy. It can run using any PC installed with Athena Visual Workbench® software program. However, this model could not be tested using a real field data. The future work would be to analyze the real field data by applying the developed model and any parameter related to the coal reservoir can be estimated and/or optimized.

APPENDIX A

COMPRESSIBILITY FACTORS FOR HELIUM (He) AND CARBON DIOXIDE (CO$_2$)

A1.1 COMPRESSIBILITY FACTOR FOR HELIUM

Compressibility factor for helium was calculated from the virial type equation of state, Eq.A1-1, given by Angus et al..

$$\begin{aligned}\frac{P}{\rho RT} &= 1 + w\sum_{i=0}^{8} n_{1i}\tau^{(i-2)/2} + w^2\sum_{i=0}^{7} n_{2i}\tau^{i/2} + w^3\sum_{i=0}^{3} n_{3i}\tau^{(2i+1)/2} \\ &\quad + w^4\sum_{i=0}^{5} n_{4i}\tau^{(i+2)/4} + w^5\sum_{i=0}^{1} n_{5i}\tau^{i+1} + w^2 e^{\gamma w^2}\left[\sum_{i=0}^{2} n_{6i}\tau^{i+1} + w^2\sum_{i=0}^{2} n_{7i}\tau^{i+1}\right]\end{aligned} \tag{A1-1}$$

where, $w=\rho/\rho_c$; $\tau = T_c/T$, $\rho_c = 0.017399$ mol/cm^3, and $T_c = 5.03$ ^{o}K.

Coefficients of the Angus Equation of state for high temperatures (T > 20 ^{o}K) were given in Table 21.

The compressibility factor for helium was calculated from the Angus Equation of State using an iteration method by simply computing in QBASIC.

Table 21. Coefficients n_{ji} and γ of the Angus-EOS for helium

j *i*	1	2	3	4	5	6	7
0	-0.000 045 987	-0.132 911 108 09	0.055 334 373 97	-0.114 221 631 9	4.033 948 879 53	0.088 527 896 71	0.306 305 701 36
1	-0.004 431 786 27	2.601 050 533 91	0.926 486 049 27	0.132 468 957 54	-19.687 712 414 6	0.230 895 686 65	-0.055 294 329 1
2	0.202 738 009 94	-19.463 282 274 4	0.239 789 555 9	2.340 382 213 34	0	-1.868 427 752 5	0.299 638 181 52
3	0.568 152 317 41	45.838 130 005 2	-0.193 125 134 91	-7.117 159 675 49	0	0	0
4	-1.777 640 932 89	-59.397 087 203 2	0	10.649 918 944 7	0	0	0
5	-1.404 484 713 03	80.404 427 546 5	0	-7.816 990 440 91	0	0	0
6	2.532 155 695 38	-44.672 751 923 3	0	0	0	0	0
7	-1.448 530 868 75	10.375 561 866 2	0	0	0	0	0
8	0.257 224 547 01	0	0	0	0	0	0

$\gamma = -15.1357$

A1.1.2 Results: Compressibility Factor for Helium

The compressibility factor for helium was calculated by computing the Angus Equation of State, Eq.A1-1 in QBASIC at various temperature and pressures. The compressibility values are listed in Table 22 and also shown in Figure 86.

Table 22. Compressibility factor for helium at various temperatures and pressures

P (psia)	**15 ^{o}C (288.15 K)**	**22 ^{o}C (295.15 K)**	**25 ^{o}C (298.15 K)**	**30 ^{o}C (303.15 K)**	**40 ^{o}C (313.15 oC)**	**55 ^{o}C (328.15 K)**
10	1.000345	1.000336	1.000332	1.000326	1.000315	1.000299
30	1.001034	1.001007	1.000996	1.000978	1.000943	1.000895
60	1.002064	1.002011	1.001988	1.001952	1.001883	1.001788
100	1.003432	1.003343	1.003306	1.003246	1.003132	1.002973
150	1.005131	1.004999	1.004944	1.004854	1.004684	1.004448
200	1.00682	1.006644	1.006572	1.006453	1.006228	1.005915
300	1.010167	1.009907	1.009799	1.009624	1.00929	1.008826
420	1.014129	1.013771	1.013623	1.013382	1.012921	1.012281
550	1.018358	1.017898	1.017707	1.017397	1.016803	1.015977
700	1.023159	1.022586	1.022347	1.02196	1.021218	1.020184
900	1.029438	1.028719	1.02842	1.027934	1.027003	1.025702
1200	1.038614	1.037689	1.037304	1.036678	1.035477	1.033796

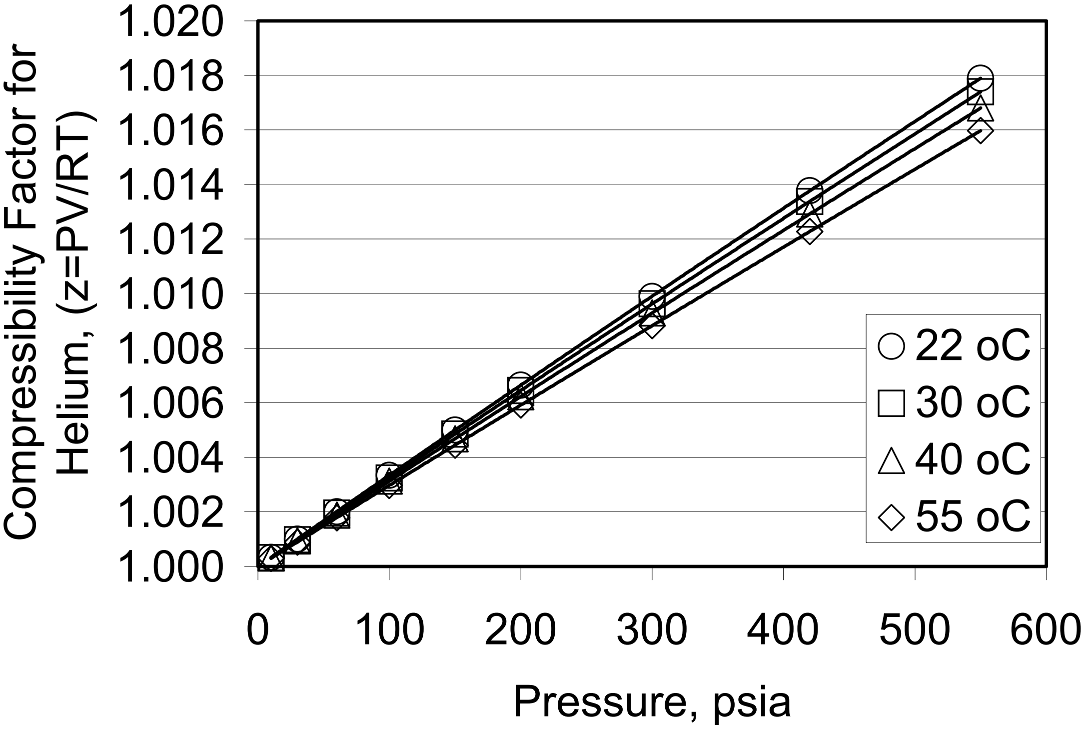

Figure 86. Compressibility factor for helium calculated from the Angus-EOS at various temperature and pressures

A1.2 COMPRESSIBILITY FACTOR FOR CARBON DIOXIDE (CO_2)

Compressibility factor for carbon dioxide was calculated from Peng-Robinson Equation of State (PR-EOS) given by Peng et al., 1976,(255) Angus Equation of State given by Angus et al., 1976,(256) and Span and Wagner Equation of State given by Span and Wagner, 1996.(210) The PR-EOS was derived theoretically whereas the later two were obtained from the curve fit to experimental data. In this section, the compressibility factor for CO_2 was calculated from PR-EOS, Angus-EOS, and Span and Wagner-EOS and compared them for the best to represent the CO_2 data.

A1.2.1 Compressibility Factor for CO_2 calculated from the PR-EOS

The Peng-Robinson EOS can be written as

$$P = \frac{RT}{v-b} - \frac{a(T)}{v(v+b)+b(v-b)} \tag{A1-2}$$

This equation can be reduced in terms of the compressibility factor, z.

$$z^3 - (1-B)z^2 + (A - 3B^2 - 2B)z - (AB - B^2 - B^3) = 0 \tag{A1-3}$$

where,

$$A = \frac{aP}{R^2T^2} \tag{A1-4}$$

$$B = \frac{bP}{RT} \tag{A1-5}$$

$$z = \frac{Pv}{RT} \qquad \text{(A1-6)}$$

At any temperature, a and b can be written as:

$$a(T) = a(T_c)\,\alpha(T_r, \omega) \qquad \text{(A1-7)}$$

(A1-7)

$$b(T) = b(T_c) \qquad \text{(A1-8)}$$

(A1-8)

where,

$$a(T_c) = 0.45724\frac{R^2T_c^2}{P_c} \qquad \text{(A1-9)}$$

$$b(T_c) = 0.07780\frac{RT_c}{P_c} \qquad \text{(A1-10)}$$

and

$$\alpha(T_r, \omega) = 1 + \left(1 - T_r^{1/2}\right)\left(0.37464 + 1.54226\omega - 0.26992\omega^2\right) \qquad \text{(A1-11)}$$

A1.2.1.1 Calculation of the Compressibility Factor for CO_2: Analytical Solution of Cubic Equation: Cubic equation (Eq.A1-3) of compressibility factor can be solved analytically. For instance, for the cubic equation:

$$x^3 + a_1x^2 + a_2x + a_3 = 0 \qquad \text{(A1-12)}$$

$$Q = \frac{a_1^2 - 3a_2}{9} \qquad \text{(A1-13)}$$

$$R = \frac{2a_1^3 - 9a_1a_2 + 27a_3}{54} \qquad \text{(A1-14)}$$

if $R^2 - Q^3 > 0$, then the cubic equation has only one root given by:

$$x_1 = -\operatorname{sgn}(R)\left[\left(\sqrt{R^2 - Q^3} + |R|\right)^{1/3} + \frac{Q}{\left(\sqrt{R^2 - Q^3} + |R|\right)^{1/3}}\right] - \frac{a_1}{3} \tag{A1-15}$$

if $R^2 - Q^3 \geq 0$, then the cubic equation has three real roots and can be calculated by computing

$$\theta = \arccos\left(\frac{R}{\sqrt{Q^3}}\right) \tag{A1-16}$$

The three roots are given by:

$$x_1 = -2\sqrt{Q}\,\mathbf{cos}\left(\frac{\theta}{3}\right) - \frac{a_1}{3} \tag{A1-17}$$

$$x_2 = -2\sqrt{Q}\,\mathbf{cos}\left(\frac{\theta + 2\pi}{3}\right) - \frac{a_1}{3} \tag{A1-18}$$

$$x_3 = -2\sqrt{Q}\,\mathbf{cos}\left(\frac{\theta + 4\pi}{3}\right) - \frac{a_1}{3} \tag{A1-19}$$

Thermodynamic constants for carbon dioxide are as follows:(210)

T_c = 304.2 ^{o}K

P_c = 73.8 bar

V_c = $94*10^{-6}$ m^3/mol

z_c = 0.274

w = 0.225

The compressibility factors for CO_2 calculated from Peng-Robinson Equation of State are shown in Table 23.

A1.2.1.2. Results: Compressibility Factor for CO_2 from Peng Robinson-EOS

Table 23. Compressibility Factors for CO_2 calculated from the PR-EOS

	Temperature			
P, psia	**22 °C**	**30 °C**	**40 °C**	**55 °C**
14.70	0.9943	0.9947	0.9952	0.9959
30	0.9883	0.9892	0.9902	0.9916
65	0.9744	0.9765	0.9787	0.9817
100	0.9603	0.9635	0.9671	0.9717
200	0.9189	0.9257	0.9332	0.9429
300	0.8752	0.8861	0.8982	0.9133
400	0.8286	0.8445	0.8617	0.8831
500	0.7784	0.8004	0.8237	0.8520
600	0.7230	0.7530	0.7836	0.8200
700	0.6597	0.7010	0.7411	0.7870
800		0.6422	0.6955	0.7528
900		0.5717	0.6455	0.7173
1000		0.4718	0.5894	0.6803
1100		0.2250	0.5232	0.6416
1200		0.2233	0.4390	0.6012
1300		0.2290	0.3430	0.5593
1400		0.2371	0.3052	0.5169
1500		0.2463	0.2970	0.4766
1600		0.2560	0.2976	0.4428
1700		0.2661	0.3020	0.4190
1800		0.2763	0.3082	0.4047
1900		0.2867	0.3156	0.3974
2000		0.2971	0.3237	0.3949
2100		0.3076	0.3323	0.3955
2200		0.3181	0.3412	0.3982
2300		0.3286	0.3503	0.4024
2400		0.3390	0.3596	0.4077
2500		0.3495	0.3690	0.4137
2600		0.3599	0.3785	0.4204
2700		0.3703	0.3880	0.4274
2800		0.3807	0.3976	0.4348
2900		0.3910	0.4072	0.4425
3000		0.4013	0.4169	0.4504

A1.2.2 Compressibility Factor for CO_2 calculated from the Angus-EOS

Compressibility factor for CO_2 was calculated from the virial type equation of state, Eq.A1-20, given by Angus et al. in 1976.

$$\frac{P}{\rho RT} = 1 + w\sum_{j=0}^{6}\sum_{i=0}^{9} n_{ji}\left(\tau - 1\right)^{j}\left(w - 1\right)^{i} \qquad \text{(A1-20)}$$

where, $w=\rho/\rho_c$; $\tau = T_c/T$, $\rho_c = 0.01063$ mol/cm^3, and $T_c = 304.2$ ^{o}K.

Coefficients of the equation of state given by Angus et al. are shown in Table 24

The compressibility factor for CO_2 are as shown in Table 25 calculated from the Angus Equation of State using iteration method by simply computing in QBASIC.

Table 24. Coefficients n_{ji} of the Angus-EOS for CO_2

j i	0	1	2	3	4	5	6
0	-0.725 854 437x100	-0.168332974x101	0.259587221x100	0.376945574x100	-0.670755370x100	-0.871456126x100	
1	0.447 869183x100	0.126050691x101	0.596957049x101	0.154645885x102	0.194449475x102	0.864880497x101	
2	-0.172011999x100	-0.183458178x101	-0.461487677x101	-0.382121926x101	0.360171349x101	0.492265552x101	
3	0.446304911x10-2	-0.176300541x101	-0.111436705x102	-0.278215446x102	-0.271685720x102	-0.642177872x101	
4	0.255491571x100	0.237414246x101	0.750925141x101	0.661133318x101	-0.242663210x101	-0.257944032x101	
5	0.594667298x10-1	0.116974683x101	0.743706410x101	0.150646731x102	0.957496845x101	0	
6	-0.147960010x100	-0.169233071x101	-0.468219937x101	-0.313517448x101	0	0	
7	0.136710441x10-1	-0.100492330x100	-0.163653806x101	-0.187082988x101	0	0	
8	0.392284575x10-1	0.441503812x100	0.886741970x100	0	0	0	
9	-0.119872097x10-1	-0.846051949x10-1	0.464564370x10-1	0	0	0	

A1.2.2.2 Results: Compressibility Factor for CO_2 from the Angus-EOS

Table 25. Compressibility Factors for CO_2 calculated from the Angus-EOS

	Temperature			
P, psia	**22 °C**	**30 °C**	**40 °C**	**55 °C**
10	0.9964	0.9967	0.9970	0.9975
30	0.9892	0.9901	0.9911	0.9924
60	0.9782	0.9801	0.9821	0.9847
100	0.9634	0.9665	0.9700	0.9744
150	0.9443	0.9492	0.9546	0.9614
200	0.9248	0.9315	0.9389	0.9482
300	0.8837	0.8947	0.9065	0.9211
420	0.8304	0.8475	0.8655	0.8874
550	0.7653	0.7914	0.8180	0.8492
700	0.6741	0.7173	0.7578	0.8026
750				0.7863
800	0.5932			
900	0.4405	0.5864	0.6635	0.7348
1000		0.4791	0.6062	
1050				
1200			0.4424	0.6160
1430				0.5051
1450			0.2684	
1550			0.2693	
1650				0.4061
1950				0.3640
2150				0.3682

A1.2.3 Compressibility Factor for CO_2 calculated from the Span and Wagner-EOS

The EOS for the compressibility factor of CO_2 was given as

$$\frac{P}{\rho RT} = 1 + \delta\phi_\delta^r \tag{A1-21}$$

where

$$\begin{aligned}\phi_\delta^r = {} & \sum_{i=1}^{7} n_i d_i \delta^{d_i-1}\tau^{t_i} + \sum_{i=8}^{34} n_i e^{-\delta^{c_i}}\left[\delta^{d_i-1}\tau^{t_i}\left(d_i - c_i\delta^{c_i}\right)\right] + \sum_{i=35}^{39} n_i \tau^{d_i}\tau^{t_i} e^{-\alpha_i(\delta-\varepsilon_i)^2-\beta_i(\tau-\gamma_i)^2}\left[\frac{d_i}{\delta} - 2\alpha_i\left(\delta-\varepsilon_i\right)\right] \\ & + \sum_{i=40}^{42} n_i\left[\Delta^{b_i}\left(\Psi + \delta\frac{\partial\Psi}{\partial\delta}\right) + \frac{\partial\Delta^{b_i}}{\partial\delta}\delta\Psi\right]\end{aligned} \tag{A1-22}$$

where δ=*ρ/ρ*$_c$; *τ* = *T*$_c$*/T*, *ρ*$_c$ = 0.01063mol/cm^3, and *T*$_c$ = 304.2 ^{o}K

and,

$$\Delta = \theta^2 + B_i\left[(\delta-1)^2\right]^{a_i} \tag{A1-23}$$

$$\theta = (1-\delta) + A_i\left[(\delta-1)^2\right]^{1/(2\beta_i)} \tag{A1-24}$$

$$\Psi = e^{-C_i(\delta-1)^2 - D_i(\tau-1)^2} \tag{A1-25}$$

$$\frac{\partial\Psi}{\partial\delta} = -2C_i(\delta-1)\Psi \tag{A1-26}$$

$$\frac{\partial\Delta^{b_i}}{\partial\delta} = b_i\Delta^{b_i-1}\frac{\partial\Delta}{\partial\delta} \tag{A1-27}$$

$$\frac{\partial\Delta}{\partial\delta} = (\delta-1)\left\{A_i\theta\frac{2}{\beta_i}\left[(\delta-1)^2\right]^{1/(2\beta_i)-1} + 2B_i a_i\left[(\delta-1)^2\right]^{a_i-1}\right\} \tag{A1-28}$$

The compressibility factor for CO_2 was calculated from the Span and Wagner-Equation of State by simply computing in QBASIC as show in Section A1.2.3.1. The compressibility factors for CO_2 calculated using the Span and Wagner-EOS are shown in Table 26.

A1.2.3.1 Calculation of the Compressibility Factor for CO_2 from the Span and Wagner-EOS: Computing in QBASIC

```
REM Compressibility Factor for Carbon Dioxide (CO2)

REM by Span and Wagner, 1996

REM Critical Constants for CO2
   PRINT "TEMPERATURE", "PRESSURE", "COMPRESSIBILITY"
   PRINT "oC", "psia", "z"
   PRINT "-------------", "------------", "------------------"
2 MW = 44.009
   REM "g/mole"
   Tc = 304.1282
   REM "oK"
   Pc = 73.825
   REM "bar"
   roc = 467.6
   REM "kg/m3"

   ro = 200

   R = .1889241
REM "kJ/(kgK)"

REM convert "kJ/(kgK)" to "barm3/(kgK)"

   R = R / 100
DIM n(42)
DIM d(42)
DIM T(42)
DIM c(42)
DIM alfa(42)
DIM beta(42)
DIM gama(42)
DIM e(42)
DIM CA(42)
DIM CB(42)
DIM CC(42)
DIM CD(42)
DIM b(42)
DIM a(42)

n(1) = .38856823203161#
n(2) = 2.938547594274#
n(3) = -5.5867188534934#
n(4) = -.7675319959247699#
n(5) = .31729005580416#
n(6) = .54803315897767#
n(7) = .12279411220335#
n(8) = 2.165896154322#
n(9) = 1.5841735109724#
n(10) = -.23132705405503#

n(11) = .058116916431436#
n(12) = -.55369137205382#
n(13) = .48946615909422#
n(14) = -.024275739843501#
n(15) = .062494790501678#
n(16) = -.12175860225246#
n(17) = -.37055685270086#
n(18) = -.016775879700426#
n(19) = -.11960736637987#
n(20) = -.045619362508778#
```

```
  n(21) = .035612789270346#
  n(22) = -.0074427727132052#
  n(23) = -.0017395704902432#
  n(24) = -.021810121289527#
  n(25) = .024332166559237#
  n(26) = -.037440133423463#
  n(27) = .14338715756878#
  n(28) = -.13491969083286#
  n(29) = -.02315122505348#
  n(30) = .012363125492901#

n(31) = .002105832197294#
  n(32) = -3.3958519026368D-04
  n(33) = .0055993651771592#
  n(34) = -3.0335118055646D-04
  n(35) = -213.6548868832#
  n(36) = 26641.569149272#
  n(37) = -24027.212204557#
  n(38) = -283.41603423999#
  n(39) = 212.47284400179#
  n(40) = -.66642276540751#

n(41) = .72608632349897#
  n(42) = .055068668612842#

d(1) = 1
  d(2) = 1
  d(3) = 1
  d(4) = 1
  d(5) = 2
  d(6) = 2
  d(7) = 3
  d(8) = 1
  d(9) = 2
  d(10) = 4

  d(11) = 5
  d(12) = 5
  d(13) = 5
  d(14) = 6
  d(15) = 6
  d(16) = 6
  d(17) = 1
  d(18) = 1
  d(19) = 4
  d(20) = 4

d(21) = 4
  d(22) = 7
  d(23) = 8
  d(24) = 2
  d(25) = 3
  d(26) = 3
  d(27) = 5
  d(28) = 5
  d(29) = 6
  d(30) = 7
  d(31) = 8
  d(32) = 10
  d(33) = 4
  d(34) = 8
  d(35) = 2
  d(36) = 2
  d(37) = 2
  d(38) = 3
  d(39) = 3
  a(40) = 3.5
  a(41) = 3.5
  a(42) = 3

  T(1) = 0
  T(2) = .75
  T(3) = 1
  T(4) = 2
  T(5) = .75
  T(6) = 2
  T(7) = .75
  T(8) = 1.5
  T(9) = 1.5
  T(10) = 2.5
  T(11) = 0
  T(12) = 1.5
  T(13) = 2
  T(14) = 0
  T(15) = 1
  T(16) = 2
  T(17) = 3
  T(18) = 6
```

T(20) = 6
T(21) = 8
T(22) = 6
T(23) = 0
T(24) = 7
T(25) = 12
T(26) = 16
T(27) = 22
T(28) = 24
T(29) = 16
T(30) = 24
T(31) = 8
T(32) = 2
T(33) = 28
T(34) = 14
T(35) = 1
T(36) = 0
T(37) = 1
T(38) = 3
T(39) = 3
b(40) = .875
b(41) = .925
b(42) = .875
c(8) = 1
c(9) = 1
c(10) = 1
c(11) = 1
c(12) = 1
c(13) = 1
c(14) = 1
c(15) = 1
c(16) = 1
c(17) = 2

c(18) = 2
c(19) = 2
c(20) = 2
c(21) = 2
c(22) = 2
c(23) = 2
c(24) = 3
c(25) = 3
c(26) = 3
c(27) = 4
c(28) = 4
c(29) = 4
c(30) = 4
c(31) = 4
c(32) = 4
c(33) = 5
c(34) = 6
alfa(35) = 25
alfa(36) = 25
alfa(37) = 25
alfa(38) = 15
alfa(39) = 20
beta(40) = .3
beta(41) = .3
beta(42) = .3
beta(35) = 325
beta(36) = 300
beta(37) = 300
beta(38) = 275
beta(39) = 275
CA(40) = .7
CA(41) = .7
CA(42) = .7

T(19) = 3
gama(35) = 1.16
gama(36) = 1.19
gama(37) = 1.19
gama(38) = 1.25
gama(39) = 1.22

CB(40) = .3
CB(41) = .3
CB(42) = 1

e(35) = 1
e(36) = 1
e(37) = 1
e(38) = 1
e(39) = 1

CC(40) = 10
CC(41) = 10
CC(42) = 12.5

CD(40) = 275
CD(41) = 275
CD(42) = 275

H = 0

```
REM INPUT "T (oC) =", Temp
   Temp = 55
 REM convert "oC" to "oK"

   Temp = Temp + 273.15

 INPUT "P (psia) =", P
   REM convert "psia" to "bar"
   P = P / 14.5038
5  term7 = 0
   term34 = 0
   term39 = 0
   term42 = 0

   resd = 0

   tao = ro / roc
   tt = Tc / Temp
   FOR i = 1 TO 7
   term7 = term7 + n(i) * d(i) * (tao ^ (d(i) - 1)) * (tt ^ T(i))
   NEXT i

   FOR i = 8 TO 34
   term34 = term34 + n(i) * (EXP(-tao ^ c(i))) * (((tao ^ (d(i) - 1)) * (tt ^ T(i)) * (d(i) - c(i) * tao ^
c(i))))
   NEXT i
   FOR i = 35 TO 39
   term39 = term39 + n(i) * (tao ^ d(i)) * (tt ^ T(i)) * (EXP((-alfa(i) * (tao - e(i)) ^ 2) - (beta(i) * (tt -
gama(i)) ^ 2))) * (d(i) / tao - 2 * alfa(i) * (tao - e(i)))
   NEXT i

   FOR i = 40 TO 42
   phi = (1 - tt) + CA(i) * ((tao - 1) ^ 2) ^ (1 / (2 * beta(i)))
   kisi = EXP(-CC(i) * (tao - 1) ^ 2 - CD(i) * (tt - 1) ^ 2)
   kisider = -2 * CC(i) * (tao - 1) * kisi
   delta = phi ^ 2 + CB(i) * ((tao - 1) ^ 2) ^ a(i)
   deltader = (tao - 1) * (CA(i) * phi * (2 / beta(i)) * ((tao - 1) ^ 2) ^ (1 / (2 * beta(i)) - 1) + 2 * CB(i) *
a(i) * ((tao - 1) ^ 2) ^ (a(i) - 1))
   deltaderbi = b(i) * (delta ^ (b(i) - 1)) * deltader
   term42 = term42 + n(i) * ((delta ^ b(i)) * (kisi + tao * kisider) + deltaderbi * tao * kisi)
   NEXT i
   resd = term7 + term34 + term39 + term42
```

```
   ro1 = P / (R * Temp * (1 + tao * resd))

   H = H + 1

   IF H = 1000 GOTO 150

   diff = ABS(ro1 - ro)
   IF diff <= .00001 THEN GOTO 100

   ro = ro1

   GOTO 5

100 z = P / (ro1 * R * Temp)

   P = P * 14.5038
   Temp = Temp - 273.15

   PRINT Temp, P, z, ro1

150 INPUT "NEXT 1/0 ? =", M
   IF M = 0 GOTO 200
   IF M = 1 GOTO 2

200 STOP
   END
```

A1.2.3.2 Results: Compressibility Factor for CO_2 from the Span and Wagner-EOS

Table 26. Compressibility Factors for CO_2 calculated from the Span and Wagner-EOS

	Temperature			
P, psia	**22 ^{o}C**	**30 ^{o}C**	**40 ^{o}C**	**55 ^{o}C**
15	0.9947	0.9951	0.9956	0.9963
30	0.9893	0.9902	0.9912	0.9925
60	0.9785	0.9803	0.9824	0.9849
90	0.9674	0.9703	0.9734	0.9773
120	0.9562	0.9601	0.9643	0.9696
150	0.9448	0.9497	0.9551	0.9619
200	0.9253	0.9321	0.9395	0.9488
230	0.9133	0.9213	0.9300	0.9408
260	0.9011	0.9104	0.9203	0.9327
290	0.8886	0.8992	0.9106	0.9246
320	0.8758	0.8878	0.9006	0.9164
350	0.8628	0.8762		0.9081
380	0.8494	0.8644	0.8803	0.8997
410	0.8356	0.8523	0.8699	0.8912
440	0.8215	0.8400	0.8593	0.8826
470	0.8070	0.8273	0.8485	0.8739
500	0.7919	0.8144	0.8376	0.8651
530	0.7764	0.8011	0.8264	0.8562
560	0.7603	0.7875	0.8150	0.8472
590	0.7436	0.7734	0.8034	0.8381
620	0.7260	0.7590		0.8288
650	0.7077	0.7440	0.7793	0.8194
680	0.6883	0.7285	0.7669	0.8099
710	0.6676	0.7124		0.8003
740	0.6454	0.6956	0.7411	0.7905
800		0.6594	0.7137	0.7704
830		0.6397	0.6994	0.7601
860	0.5262	0.6186		0.7497
920		0.5708	0.6533	0.7283
980		0.5095	0.6192	0.7060
1040		0.3983		
1070			0.5606	0.6710
1280			0.3418	0.5801
1310			0.3092	0.5659
1340			0.2894	0.5514
1430			0.2700	
1610			0.2729	0.4218
1640			0.2748	
2060				0.3658
2300				0.3775

A1.3 COMPARISON OF EQUATION OF STATES FOR THE COMPRESSIBILITY FACTOR OF CO_2

The three equation of states, Peng-Robinson (PR-EOS), Angus (Angus-EOS), and Span and Wagner (Span and Wagner-EOS), were compared as shown in Figure 87. The compressibility factor for CO_2 obtained from PR-EOS deviates from the compressibility factors obtained from Angus-EOS and Span and Wagner-EOS considerably. On the other hand, the compressibility factor for CO_2 obtained from Angus-EOS and Span and Wagner-EOS coincides each other showing a good agreement.

As a conclusion, either the Angus-EOS or the Span and Wagner-EOS can be used in calculations in order to estimate the adsorption-desorption isotherms of CO_2 on coals. On the other hand, the PR-EOS can not be used in calculations. Any literature data on the adsorption and desorption isotherms of CO_2 calculated using the PR-EOS is therefore not accurate.

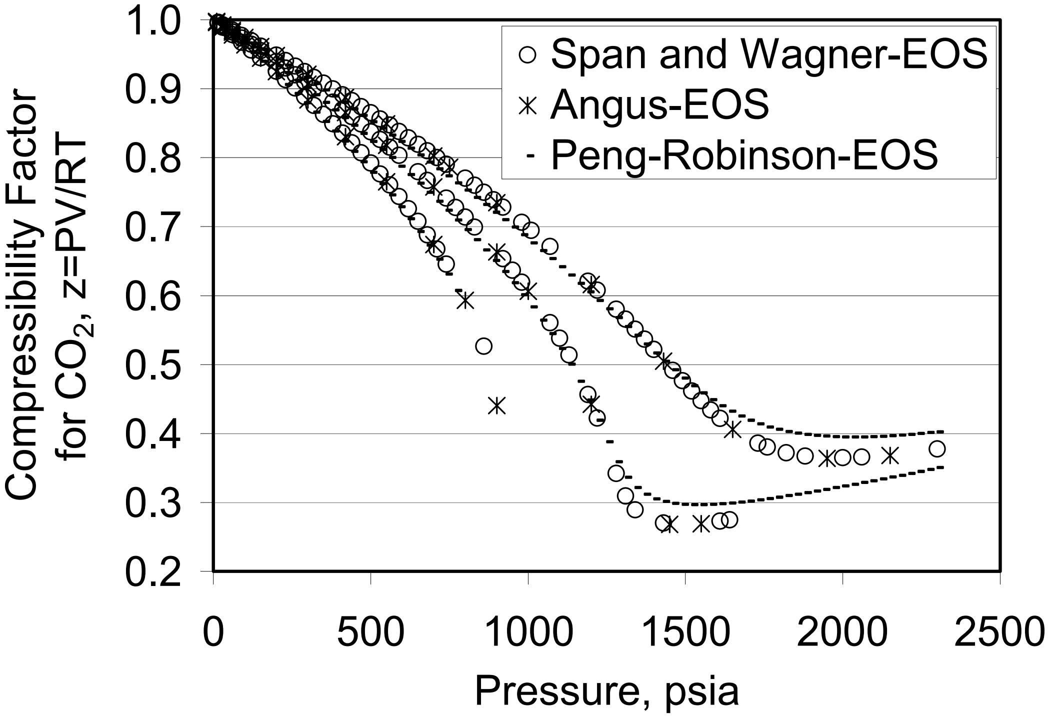

Figure 87. Comparison of the compressibility factor of CO_2 obtained from the PR-EOS, the Angus-EOS, and the Span and Wagner-EOS

APPENDIX B

MEASUREMENTS OF THE CO_2 ADSORPTION ISOTHERMS ON COALS USING THE EXPERIMENTAL APPARATUS

B1.1 DESIGN AND CONSTRUCTION OF THE HIGH-PRESSURE MANOMETRIC GAS ADSORPTION APPARATUS

In order to estimate the sorption capacity of CO_2 on coals, a high-pressure manometric gas adsorption apparatus was designed and constructed. A schematic diagram of the high-pressure manometric gas adsorption apparatus is shown in Figure 16. A brief description of the components of the high-pressure manometric gas adsorption apparatus is given in Table 8.

B1.2 LEAK TEST

A leak test was conducted by introducing helium to the system at the desired maximum pressure of adsorption study. If not otherwise stated, this pressure was up to 800 psia for adsorption study at 22 ^{o}C and 3000 psia for adsorption study at 55 ^{o}C. The pressure was recorded overnight at constant temperature. Any leak occurred was detected from the decline in the pressure recordings. The location of the leak, if any, was then detected by SNOOP® and shortly fixed.

B1.3 CALIBRATION OF PRESSURE TRANSDUCERS

The pressure transducers were calibrated against the standard up to 3000 psia at 22, 30, 40, and 55 °C, respectively. The calibration rechecked several times and corrected if any deviation occurred. The offsets and the slopes for each pressure transducers were adjusted with respect to standard pressure readings. Therefore, any error due to the quoted full-scale accuracy (0.25%FS) of the pressure transducers was reduced or totally eliminated by calibrating the pressure transducers against the standard up to 3000 psia.

B1.4 ESTIMATION OF THE EMPTY VOLUMES OF THE REFERENCE AND SAMPLE CELLS

The empty volumes of the sample and reference cells were determined by a series of helium expansions from reference cell to the sample cell when the sample cell was empty and it was filled with glass-beads with a known reference volume. The expansions were carried out in several steps to pressures up to 500 psia. The following procedure was used to estimate the volumes of the reference and sample cells:

(1) Initially, the reservoir and sample cells contained n_{R1} moles of gas at a pressure of P_{R1} and n_{S1} moles of gas at a pressure of P_{S1}, respectively.

(2) The reservoir cell was charged with n moles of fresh gas. At this point, the moles of gas in the reservoir cell became $(n_{R1}+n)$ at a pressure of P_{R2}.

(3) A portion of the gas, Δn_R moles, was transferred from the reservoir to the sample cell and both cells were allowed to equilibrate. At equilibrium, the reservoir and the sample cells contained $(n_{R1}+n-\Delta n_R)$ moles of gas at a pressure of P_{R3} and $(n_{S1}+\Delta n_S)$ moles of gas in the gas phase at the pressure of P_{S3}, respectively.

Since there is no adsorption in empty cells, Δn_S is equal to Δn_R, which corresponds to

$$\left(n_{R_1}+n\right)-\left(n_{R_1}+n-\Delta n_R\right)=\left(n_{S_1}+\Delta n_S\right)-n_{S_1} \tag{B1}$$

Here, the mole of gas can be calculated from the real gas law accounting the compressibility factor, z

$$n=\frac{PV}{zRT} \tag{B2}$$

Eq.B1 can be written in measurable quantities such as,

$$\frac{P_{R_2}}{z_{R_2}}\frac{V_R}{RT}-\frac{P_{R_3}}{z_{R_3}}\frac{V_R}{RT}=\frac{P_{S_3}}{z_{S_3}}\frac{V_S}{RT}-\frac{P_{S_1}}{z_{S_1}}\frac{V_S}{RT} \tag{B3}$$

Therefore, the ratio of volume of the reference cell to the volume of the sample cell becomes

$$\frac{V_R}{V_S}=\frac{\left(\dfrac{P_{S_3}}{z_{S_3}}-\dfrac{P_{S_1}}{z_{S_1}}\right)}{\left(\dfrac{P_{R_2}}{z_{R_2}}-\dfrac{P_{R_3}}{z_{R_3}}\right)}=a \tag{B4}$$

The gas expansion procedure was also repeated when the sample cell was filled with a known volume of solid. In this case, the solid used was glass-beads with a diameter of 0.5 cm.

The volume of the glass beads were estimated by a liquid pycnometry using water as the liquid. Since glass-beads are known to be non-porous and the adsorption of helium on the glass beads is none or negligible, the glass-beads were found to be a good choice to calibrate the reference and sample cell volumes.

When the sample cell was loaded with glass-beads, the ratio of volume of reference cell to the volume of the void volume in the sample cell is obtained from the mass balance as

$$\frac{V_R}{\left(V_S - V_{gb}\right)} = \frac{\left(\frac{P_{S_3}}{z_{S_3}} - \frac{P_{S_1}}{z_{S_1}}\right)}{\left(\frac{P_{R_2}}{z_{R_2}} - \frac{P_{R_3}}{z_{R_3}}\right)} = b \tag{B5}$$

The gas expansion procedure was repeated for several times with increasing or decreasing pressures. Both *a* and *b* values were estimated from Eq.B4 and Eq.B5, respectively, for each helium expansion steps. Then, the volume of sample cell and the volume of the reference cell were calculated from Eq.B6 and Eq.B7, respectively.

For the empty volume of the sample cell:

$$V_S = \left(\frac{b}{b-a}\right) V_{gb} \tag{B6}$$

For the empty volume of the reference cell:

$$V_R = aV_S = \left(\frac{ab}{b-a}\right) V_{gb} \tag{B7}$$

B2.0 CONSTRUCTION OF THE ADSORPTION AND DESORPTION ISOTHERMS

B2.1 PLACEMENT OF THE COAL SAMPLES INTO THE SAMPLE CELLS

The pre-weighted coal samples were placed into the sample cells in a glow bag under helium atmosphere. The frit included in the sample cell was used to prevent the coal to be carried out from the sample cell during injection and venting of the gas. Before starting the gas expansion procedure, the system was leak tested.

B2.2 ESTIMATION OF VOID VOLUME IN THE SAMPLE CELL

Before the adsorbing gas (i.e. CO_2) was introduced into the sample cell, the void volume within the sample cell was estimated by helium expansion method. The void volume is the available volume to the gas-phase in the sample cell, which is not occupied by the volume of the skeleton volume of the solid adsorbent. It was assumed that helium has the smallest molecular size so that it can report the possible available void volume in the sample cell and it is a non-adsorbing gas (although there are debates in the literature about such assumptions, which has also discussed in this thesis). A series of helium expansion from reference cell into sample cell were performed in order to determine the void volume of sample cell. The procedure and the calculation method are similar to the procedure described in Section 3.2.3 for the estimation of empty volume of the reference and sample cells. The only difference bow is that the coal sample was replaced by the glass beads. When the sample cell was loaded with the coal sample, the ratio of volume of reference cell to the void volume in the sample cell can be obtained from the mass balance without adsorption as

$$\frac{V_R}{V_o} = \frac{V_R}{\left(V_S - V_{coal}\right)} = \frac{\left(\frac{P_{S_3}}{z_{S_3}} - \frac{P_{S_1}}{z_{S_1}}\right)}{\left(\frac{P_{R_2}}{z_{R_2}} - \frac{P_{R_3}}{z_{R_3}}\right)} = c \tag{B8}$$

The gas expansion procedure was repeated for several times with increasing or decreasing pressures. For each gas expansion steps, the ratio of the volume of the reference cell to the void volume in the sample cell, c, was estimated. Since the volume of reference cell is known, the void volume of sample cell was calculated from Eq.B9. Furthermore, the volume, and thus, the density of the coal sample can also be estimated.

For the void volume of the sample cell:

$$V_o = \frac{V_R}{c} \tag{B9}$$

B2.3 ESTIMATION OF THE ADSORPTION AND DESORPTION ISOTHERMS

The adsorption and desorption isotherms were easily estimated once the empty volume of the reference and sample cells were known; the sample cell was leak tested; and the void volume available to the gas in the sample cell was estimated. The following procedure was employed for the estimation of the adsorption and desorption isotherms:

1. Initially, the reservoir and sample cells contained n_{R1} moles of gas at a pressure of P_{R1} and n_{S1} moles of gas at a pressure of P_{S1}, respectively.

2. The reservoir cell was charged with *n* moles of adsorbing gas, i.e. CO_2. At this point, the moles of gas in the reservoir cell became $(n_{R1}+n)$ at a pressure of P_{R2}.
3. A portion of the gas, Δn_R moles, was transferred from the reservoir to the sample cell and both cells were allowed to equilibrate. During this period both temperature and pressure were monitored to ensure both thermal and thermodynamic equilibrium. At equilibrium, the reservoir and the sample cells contained $(n_{R1}+n-\Delta n_R)$ moles of gas at a pressure of P_{R3} and $(n_{S1}+\Delta n_S)$ moles of gas in the gas phase at the pressure of P_{S3}, respectively.

If no adsorption were to occur, Δn_S would equal to Δn_R. Normally, however, the moles of gas transferred from the reference cell did not equal the moles of gas found in the sample cell. The missing gas was accounted to be the adsorbed CO_2 on the coal.

Following the procedure above, the amount of adsorbed gas can be calculated from the mass balance as

$$\Delta n^{ex} = [\Delta n_R] - [\Delta n_S] \tag{B10}$$

which corresponds to?

$$\Delta n^{ex} = [(n_{R_1} + n) - (n_{R_1} + n - \Delta n_R)] - [(n_{S_1} + \Delta n_S) - (n_{S_1})] \tag{B11}$$

In measurable quantities, the measured adsorbed amount per gram of adsorbent (*w*) can be obtained as

$$\Delta n^{ex} = \frac{1}{w}\left[\left(\frac{P_{R_2}}{z_{R_2}} - \frac{P_{R_3}}{z_{R_3}}\right)\frac{V_R}{RT} - \left(\frac{P_{S_3}}{z_{S_3}} - \frac{P_{S_1}}{z_{S_1}}\right)\frac{V_0}{RT}\right] \tag{B12}$$

In order to construct an adsorption isotherm, the above procedure was repeated for incrementally increasing pressures of CO_2. The measured total amount of the adsorbed gas at the end of the i^{th} step was determined from

$$n^{ex} = \Delta n_1^{ex} + \Delta n_2^{ex} + \Delta n_3^{ex} + \textbf{....} + \Delta n_i^{ex} \tag{B13}$$

B3.0 EXPERIMENTAL RESULTS

B3.1 EXPANSION OF GAS FROM THE REFERENCE CELL INTO THE SAMPLE CELL

In Volumetric (manometric) measurement method, the adsorption and desorption isotherms of gases can be constructed by measuring pressures and temperatures in the reference and sample cells. Because the volume of the reference cell is constant and the void volume of the sample cell is taken to be the volume estimated by the helium expansion prior to the adsorption measurement, the adsorbed amount can be calculated from a simple mass balance between reference and sample cells at each gas expansion steps.

Figure 88 shows one of the gas expansion procedures to construct the adsorption isotherms of CO_2 on coal. Initially, both reference and sample cells were isolated from each other through an on/off valve. In this process, the reference cell was first filled with fresh gas at pressure P_{R2} while the pressure in sample cell is P_{S1}. After all the thermal and thermodynamic equilibrium was established, the gas in the reference cell was expanded into the sample cell for 2 to 5 seconds and both cells were isolated again. At equilibrium, the pressures in the reference and sample cells became P_{R3} and P_{S3}, respectively. Since both cells were placed in the same constant temperature water bath, temperatures in both cells were the temperature of the water bath. This procedure was repeated several times by injection fresh gas in the reference cell and, after thermal and thermodynamic equilibrium, expanding it into the sample cell to complete the adsorption isotherms.

For desorption isotherm, the process was reverse of the construction of the adsorption isotherm. Shortly, once the construction of the adsorption isotherm was complete, a portion of the gas in the reference cell was evacuated into the atmosphere. After thermal equilibrium was reached, the gas in the sample cell was expanded into the reference cell. A sufficient time was allowed for sample and reference cells to reach thermal and thermodynamic equilibrium in the constant temperature water bath. The evacuation of a portion of gas from the reference cell and expansion of gas from sample cell into the reference cell was repeated several times until the desired pressure was reached.

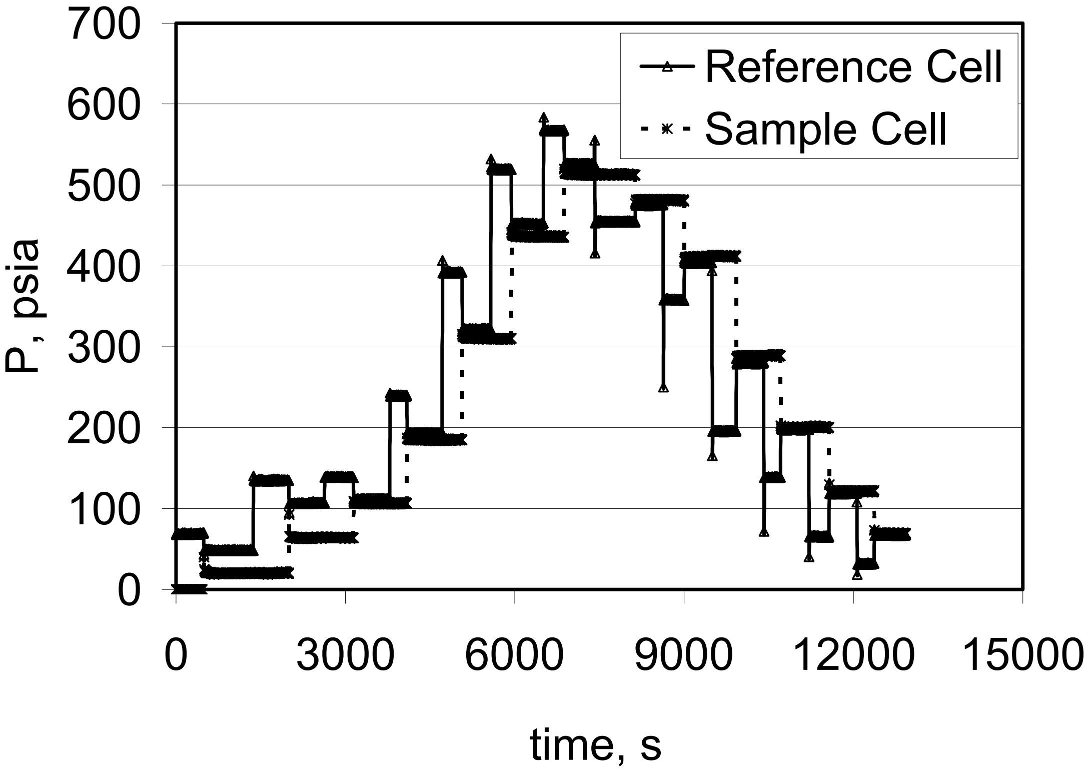

Figure 88. Typical gas expansion procedure

B3.2 THERMAL AND THERMODYNAMIC EQUILIBRIUM

Construction of the adsorption and desorption isotherms require the expansion of gas from one cell into the other. Figure 89a shows the gas expansion procedure for one of the adsorption isotherm construction procedure. As shown in Figure 89a, some of the gas was expanded into the sample cell by opening the valve that isolates both cells from each other. Once the valve was open, both pressures in the reference cell and sample cell became equal, but once the valve was shut down, the pressure in the reference cell stayed steady, but the pressure in the sample cell decreased sharply first due to adsorption of gas onto the coal sample and slightly until the adsorption was complete. During the adsorption and desorption process, the temperature was increased or decreased (depending on the injection or evacuation process) as a result of the Joule-Thompson effect. As shown in Figure 89b, the temperature first increased when a fresh gas was injected into the reference cell. During the gas expansion, the temperature was decreased in the reference cell while it was increased in sample cell. However, at equilibrium, both temperatures were reached the temperature of the water bath. For the overall, reaching thermal and thermodynamic equilibrium was short. 5 minutes was satisfactory for reaching the thermal equilibrium. Because the coal samples were used to be micron size (150 μm), a 30 min was satisfactory for reaching the thermodynamic equilibrium.

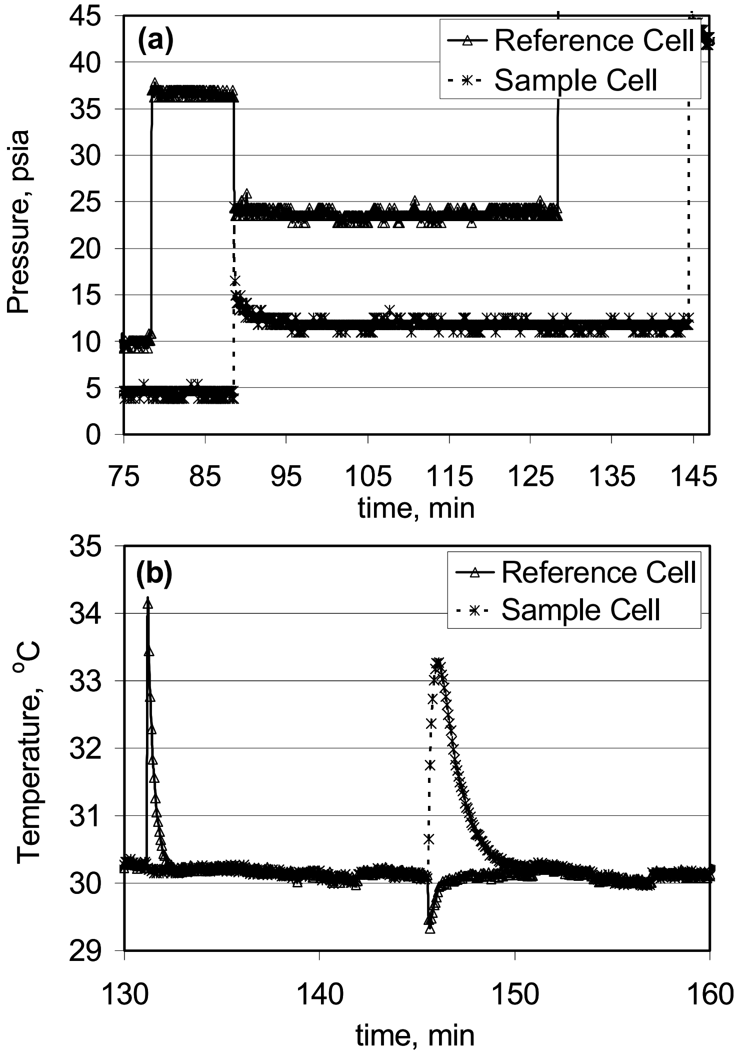

Figure 89. Thermal and pressure equilibrium during the gas expansion process

B3.3 ESTIMATION OF THE EMPTY VOLUMES OF REFERENCE AND SAMPLE CELLS

The volumes of the empty reference and sample cells were obtained by allowing the gas, helium, to expand from the reference cell into the sample cell or vice versa, in a fashion similar to the technique used for the construction of the adsorption and desorption isotherms. This procedure was performed with both the empty sample cell was and with the sample cell filled with glass beads of a known volume for calibration. At the end of each measurement, the ratio of the volume of the reference cell to the empty volume of the sample cell (V_R/V_S) and the ratio of the volume of the reference cell to the void volume of the sample cell (V_R/V_S-V_{gb}) were obtained and plotted as shown in Figure 90. For both cases, the deviation of the ratios was less than ± 0.003, which corresponds to an error of about ± 0.01 cm^3 and ± 0.02 cm^3 for sample and reference cells, respectively. Therefore, the estimated error in the calculation of the reference and sample cell volumes is less than 0.2%.

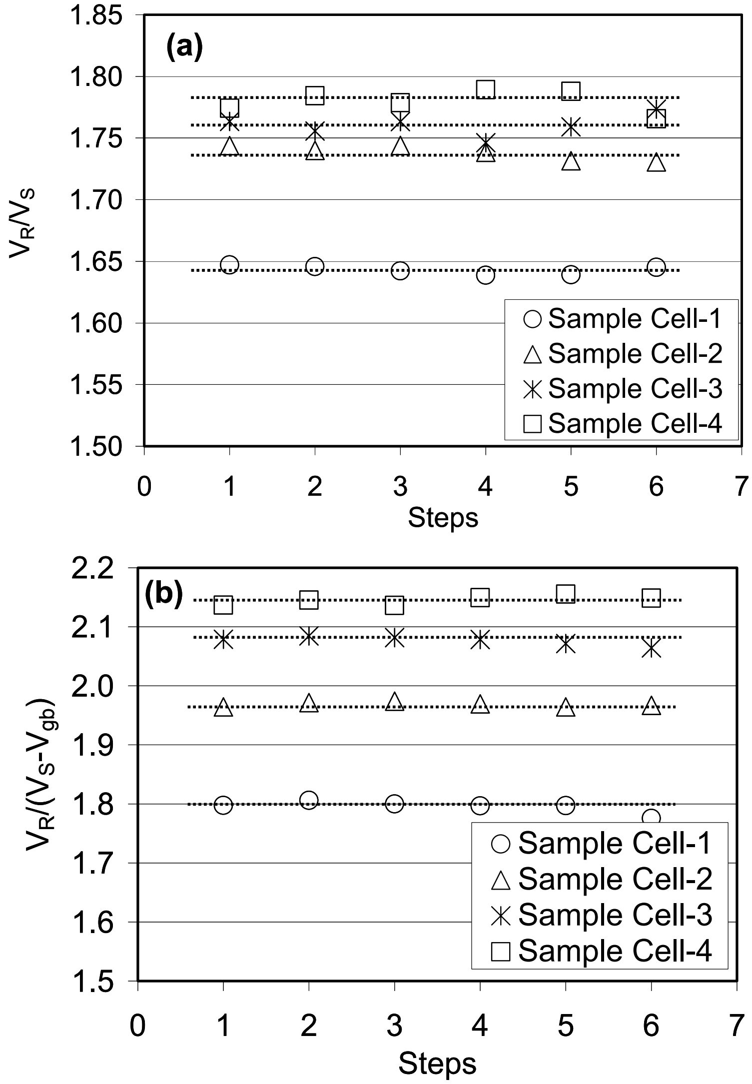

Figure 90. Estimation of the empty volumes of the reference and sample cells

B3.4 CONSTRUCTION OF THE ADSORPTION AND DESORPTION ISOTHERMS

Once the coal samples were placed into the sample cells, their volume, or the void volume in the sample cell, which is available to the gas phase and which is not occupied by the volume of the solid adsorbent should be estimated. This was performed by a gas expansion procedure. Helium is the generally used gas for this purpose.

B3.4.1 Estimation of the Void Volume of the Sample Cells

Similar to the estimation of the empty volumes of the reference and sample cells, the void volume in the sample cell was estimated by the helium expansion method. The ratio of the volume of the reference cell to the volume of the void volume was calculated from the pressure measurement at the end of each gas expansion step as shown in Figure 91. The deviation similarly was less than +/- 0.003. Because the volume of the reference cell was calculated before, the void volume, and thus, the volume of the coal sample was easily calculated.

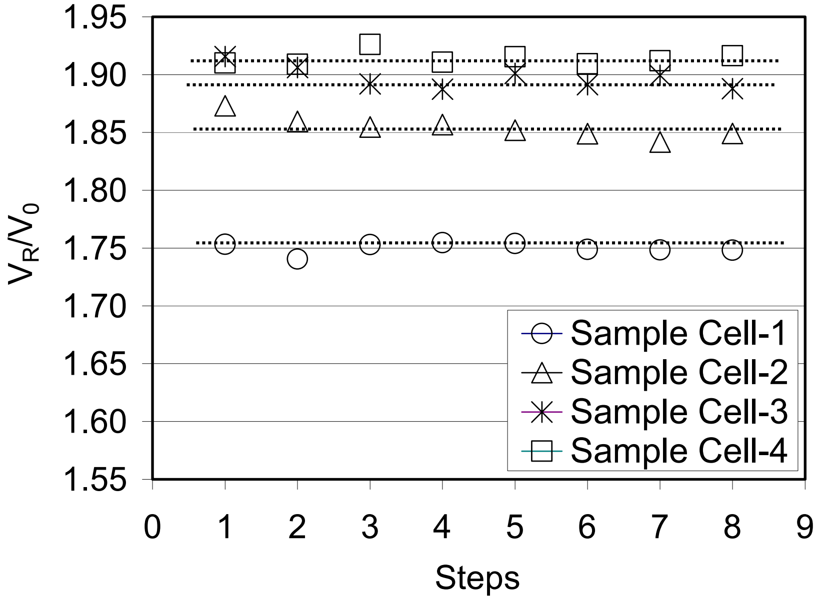

Figure 91. Estimation of the void volume of the sample cell, from which the volume of the sample is calculated

B3.4.2 Construction of the Adsorption and Desorption Isotherms

The adsorption and desorption isotherms were obtained from the amount of gas adsorbed at the end of each expansion procedure. Figure 92 shows the adsorption desorption isotherms of CO_2 on the Argonne Premium Pittsburgh No.8 coal at 22 ^{o}C and the adsorbed amount at each gas expansion procedure. The adsorption isotherms were constructed by adding these values at each step.

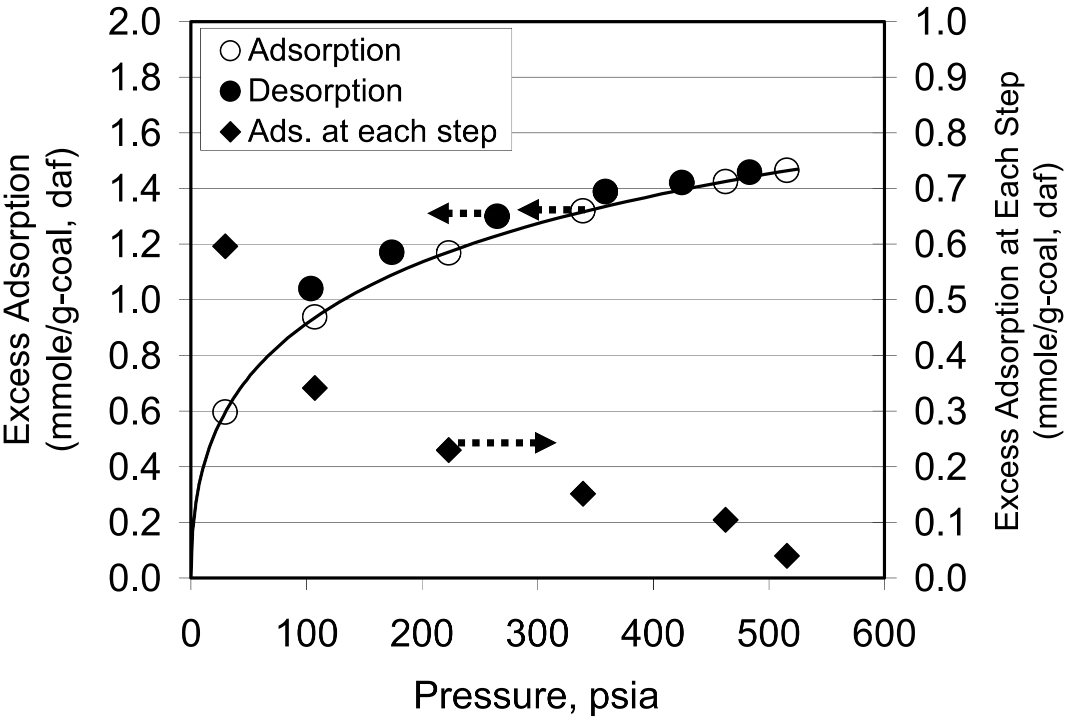

Figure 92. Construction of the adsorption and desorption isotherms of CO_2 on Argonne Premium Pittsburgh No.8 Coal

B3.5 Reproducibility

In order to determine the reproducibility of the adsorption isotherm data, samples of Argonne Premium Illinois No.6 coal, ranging from 0.2 to 1.3 g, were placed in four different sample cells. As shown in Figure 93, the reproducibility of the adsorption isotherms of CO_2 on the four different Illinois No.3 coal samples is excellent. Furthermore, the adsorption isotherms of CO_2 on Upper Freeport coal obtained for different runs on different days showed also similar results. The reproducibility was excellent.

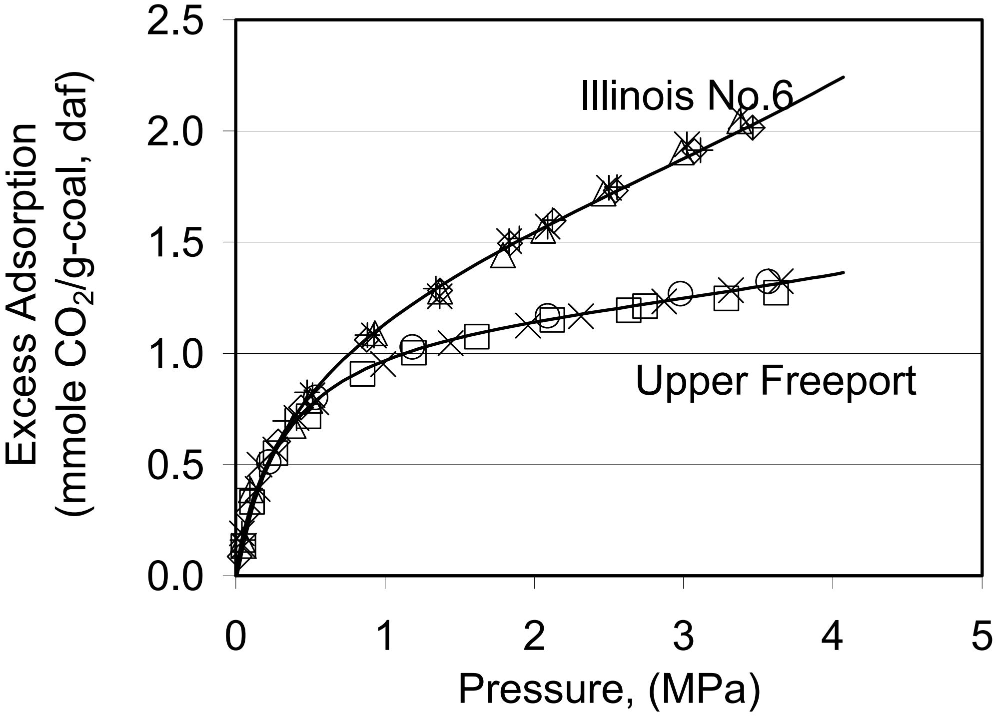

Figure 93. Repeatability of the adsorption measurement using the manometric adsorption apparatus shown in Figure 16

APPENDIX C

ERROR ANALYSIS OF THE ADSORPTION ISOTHERMS AS DETERMINED BY THE VOLUMETRIC METHOD

C1.1 ERROR ANALYSIS OF THE ADSORPTION ISOTHERMS AS DETERMINED BY THE VOLUMETRIC METHOD

The accuracy and precision of the information obtained from the adsorption isotherms will depend on the error associated with each measured variables, as well as on the validity of the adsorption model.

The limit of error of some function, $F = f(x_1, x_2, x_3, \ldots\ldots, x_n)$, can be calculated from the limit of error of each variable(257,140) such as:

$$dF = \left|\frac{\partial F}{\partial x_1}\right|\Delta x_1 + \left|\frac{\partial F}{\partial x_2}\right|\Delta x_2 + \cdots + \left|\frac{\partial F}{\partial x_n}\right|\Delta x_n \tag{131}$$

The objective function for a gas expansion step is given as in Eq.(36). The independent variables for the excess adsorption, therefore, are the initial and final pressures in the reference and sample cells, the empty and void volume of the reference and sample cells, the sample weight, and temperature.

$$\Delta n^{ex} = f\left(P_{R_i}, P_{R_f}, V_R, P_{Sf}, P_{S_i}, V_o, w, T\right) \tag{132}$$

Also, the compressibility factor is another variable, whose value is depended on the temperature and pressure.

$$z = f(P, T) \tag{133}$$

In order to estimate the error at each step, Eq.(36) is differentiated with respect to each independent variable.

$$\frac{\partial \Delta n_j^{ex}}{\partial P_{R_i}} = \frac{V_R}{wRT}\left[\frac{z_{R_i} - \left(\frac{\partial z_{R_i}}{\partial P_{R_i}}\right)_T P_{R_i}}{{z_{R_i}}^2}\right] \tag{134}$$

$$\frac{\partial \Delta n_j^{ex}}{\partial P_{R_f}} = \frac{V_R}{wRT}\left[\frac{z_{R_f} - \left(\frac{\partial z_{R_f}}{\partial P_{R_f}}\right)_T P_{R_f}}{{z_{R_f}}^2}\right] \tag{135}$$

$$\frac{\partial \Delta n_j^{ex}}{\partial V_R} = \frac{1}{wRT}\left(\frac{P_{R_i}}{z_{R_i}} - \frac{P_{R_f}}{z_{R_f}}\right) \tag{136}$$

$$\frac{\partial \Delta n_j^{ex}}{\partial P_{S_f}} = -\frac{V_o}{wRT}\left[\frac{z_{S_f} - \left(\frac{\partial z_{S_f}}{\partial P_{S_f}}\right)_T P_{S_f}}{{z_{S_f}}^2}\right] \tag{137}$$

$$\frac{\partial \Delta n_j^{ex}}{\partial P_{S_i}} = \frac{V_o}{wRT}\left[\frac{z_{S_i} - \left(\frac{\partial z_{S_i}}{\partial P_{S_i}}\right)_T P_{S_i}}{{z_{S_i}}^2}\right] \tag{138}$$

$$\frac{\partial \Delta n_j^{ex}}{\partial V_o} = \frac{1}{wRT}\left(\frac{P_{S_f}}{z_{S_f}} - \frac{P_{S_i}}{z_{S_i}}\right) \tag{139}$$

$$\frac{\partial \Delta n_j^{ex}}{\partial w} = -\left[\left(\frac{P_{R_i}}{z_{R_i}} - \frac{P_{R_f}}{z_{R_f}}\right)\frac{V_R}{RT} - \left(\frac{P_{S_f}}{z_{S_f}} - \frac{P_{S_i}}{z_{S_i}}\right)\frac{V_o}{RT}\right]\frac{1}{w^2} \tag{140}$$

$$\frac{\partial \Delta n_j^{ex}}{\partial T} = -\left\{\begin{array}{l} \left(\frac{P_{R_i}\left[z_{R_i} + T\left(\frac{\partial z_{R_i}}{\partial T}\right)_{P_{R_i}}\right]}{{z_{R_i}}^2} - \frac{P_{R_f}\left[z_{R_f} + T\left(\frac{\partial z_{R_f}}{\partial T}\right)_{P_{R_f}}\right]}{{z_{R_f}}^2}\right)\frac{V_R}{wRT^2} - \\ \frac{P_{S_f}\left[z_{S_f} + T\left(\frac{\partial z_{S_f}}{\partial T}\right)_{P_{S_f}}\right]}{{z_{S_f}}^2}\left(-\frac{P_{S_i}\left[z_{S_i} + T\left(\frac{\partial z_{S_i}}{\partial T}\right)_{P_{S_i}}\right]}{{z_{S_i}}^2}\right)\frac{V_o}{wRT^2} \end{array}\right\} \tag{141}$$

These relationships can now be used to determine the contribution of each variable to the total error.

The following is a numerical example to show how to calculate the expected error. Because the experimental pressure data were collected in 'psia' unit, the calculations for the error analysis were performed according to this unit. The adsorption isotherm of CO_2 on Pocahontas No.3 coal was selected as the example.

Table 27 shows the parameters for the experimental setup and the limit of error for each variable.

The compressibility factor and its derivatives with respect to pressure and temperature were obtained from the equation of state given by Span and Wagner$^{(210)}$. Figure 94 shows the values of these derivatives for CO_2 at 55 °C.

Table 27. The parameters for experimental apparatus and the limits of error, Δx_n, for each experimental variable

	Parameters		Variable, x_n	Limit of Error, Δx_n
Reference Cell	Volume of Reference Cell V_R	11.87 cm^3	Initial Pressure, psi Final Pressure, psi Volume of the Reference Cell, cm^3	0.8 0.8 0.024
Sample Cell	Void Volume in Sample Cell V_o	7.30 cm^3	Initial Pressure, psi Final Pressure, psi Volume of the Reference Cell, cm^3	0.8 0.8 0.013
	Sample Weight, w	1.02 g	Sample Weight, g	0.005
	Temperature, T	328 °K	Temperature, °K	0.1

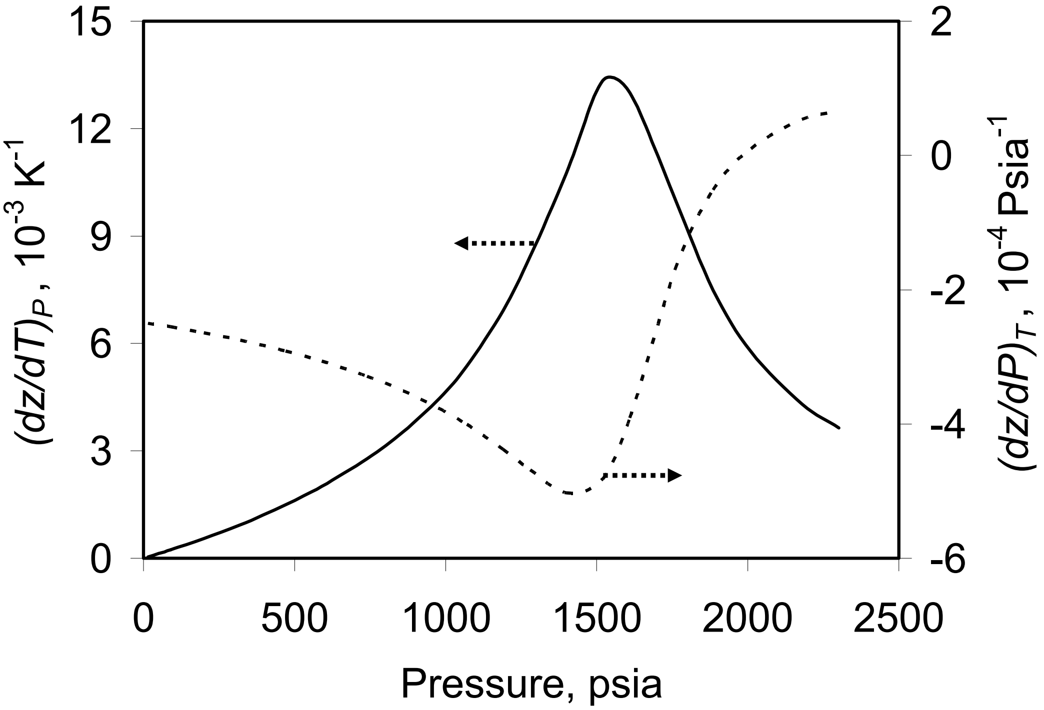

Figure 94. The derivatives of the compressibility factor for CO_2 with respect to pressure and temperature at 55 °C.

Table 28 shows the experimental values for pressures in reference and sample cells obtained during the expansion procedure from the reference cell into the sample at each step. The compressibility factor and the derivatives corresponding to each pressure reading were also included in the table.

Table 28. Experimental pressure values obtained for the adsorption isotherm of CO_2 at 55 ^oC and the compressibility factor along with the derivatives of the compressibility factor with respect to pressure and temperature

	Experimental Data		Compressibility Factor, z		$\left(\frac{\partial z}{\partial P}\right)_T$, psi^{-1}		$\left(\frac{\partial z}{\partial T}\right)_P$, K^{-1}	
	Reference Cell	Sample Cell	Reference Cell	Sample Cell	Reference Cell	Sample Cell	Reference Cell	Sample Cell
Pi	76.164	1.735	0.981	1.000	-0.00025	-0.00025	0.00022	0.00001
Pf	51.948	25.951	0.987	0.994	-0.00025	-0.00025	0.00015	0.00008
Pi	135.896		0.966		-0.00026		0.00037	
Pf	101.994	74.375	0.974	0.981	-0.00026	-0.00025	0.00029	0.00021
Pi	286.842		0.925		-0.00027		0.00081	
Pf	213.394	198.690	0.945	0.949	-0.00027	-0.00026	0.00058	0.00054
Pi	400.656		0.894		-0.00028		0.00121	
Pf	337.695	313.311	0.912	0.918	-0.00028	-0.00027	0.00098	0.00090
Pi	521.735		0.859		-0.00030		0.00171	
Pf	457.160	433.582	0.878	0.884	-0.00029	-0.00029	0.00144	0.00134
Pi	663.802		0.815		-0.00032		0.00238	
Pf	593.576	570.804	0.837	0.844	-0.00031	-0.00030	0.00204	0.00193
Pi	758.251		0.784		-0.00033		0.00288	
Pf	700.933	682.204	0.803	0.809	-0.00032	-0.00032	0.00257	0.00247
Pi	1000.402		0.698		-0.00038		0.00465	
Pf	913.225	872.701	0.731	0.745	-0.00036	-0.00035	0.00390	0.00360
Pi	1226.410		0.605		-0.00045		0.00750	
Pf	1139.240	1084.177	0.643	0.665	-0.00042	-0.00041	0.00622	0.00553
Pi	1464.532		0.489		-0.00051		0.01213	
Pf	1378.977	1319.884	0.532	0.561	-0.00050	-0.00048	0.01032	0.00915
Pi	1668.760		0.402		-0.00030		0.01621	
Pf	1592.883	1491.809	0.429	0.475	-0.00050	-0.00052	0.01486	0.01273
Pi	1780.153		0.377		-0.00014		0.00954	
Pf	1703.462	1604.808	0.392	0.424	-0.00025	-0.00040	0.01128	0.01304
Pi	2143.390		0.369		0.00005		0.00451	
Pf	1938.363	1771.096	0.365	0.378	-0.00002	-0.00015	0.00662	0.00975

Using the limit of error for each variable, *Δx$_n$*, the contribution of each variables to the total expected error was calculated. Table shows these values.

Table 29. Limit of error for each variable, *Δx$_n$*, and the contribution of each variables to the total expected error

Equilibrium Pressure	ΔP_{R_i}	ΔP_{R_f}	ΔP_{S_f}	ΔP_{S_i}	ΔV_R	ΔV_o	Δw	ΔT
psi	0.8 psi	0.8 psi	0.8 psi	0.8 psi	0.024 cm^3	0.013 cm^3	0.005 g	0.1 ^{o}K
	$\left\|\frac{\partial \Delta n_j^{ex}}{\partial P_{R_i}}\right\|\Delta P_{R_i}$	$\left\|\frac{\partial \Delta n_j^{ex}}{\partial P_{R_f}}\right\|\Delta P_{R_f}$	$\left\|\frac{\partial \Delta n_j^{ex}}{\partial P_{S_f}}\right\|\Delta P_{S_f}$	$\left\|\frac{\partial \Delta n_j^{ex}}{\partial P_{S_i}}\right\|\Delta P_{S_i}$	$\left\|\frac{\partial \Delta n_j^{ex}}{\partial V_R}\right\|\Delta V_R$	$\left\|\frac{\partial \Delta n_j^{ex}}{\partial V_o}\right\|\Delta V_o$	$\left\|\frac{\partial \Delta n_j^{ex}}{\partial w}\right\|\Delta w$	$\left\|\frac{\partial \Delta n_j^{ex}}{\partial T}\right\|\Delta T$
25.951	0.024	0.024	0.013	0.013	0.001	0.001	0.002	0.000
74.375	0.025	0.025	0.014	0.013	0.002	0.002	0.001	0.000
198.69	0.028	0.026	0.015	0.014	0.005	0.004	0.001	0.000
313.311	0.030	0.028	0.016	0.015	0.005	0.004	0.001	0.000
433.582	0.032	0.031	0.017	0.016	0.005	0.005	0.001	0.000
570.804	0.036	0.034	0.019	0.017	0.006	0.006	0.000	0.001
682.204	0.040	0.038	0.020	0.019	0.006	0.005	0.000	0.001
872.701	0.052	0.047	0.025	0.020	0.011	0.011	0.000	0.003
1084.177	0.074	0.064	0.033	0.025	0.015	0.015	0.000	0.011
1319.884	0.122	0.101	0.050	0.033	0.024	0.024	0.000	0.030
1491.809	0.131	0.158	0.072	0.050	0.026	0.026	0.000	0.039
1604.808	0.105	0.124	0.077	0.072	0.022	0.021	0.002	0.069
1771.096	0.045	0.071	0.060	0.077	0.030	0.029	0.001	0.081

Therefore, the total expected error was calculated as the sum of the errors from each parameter. Table 30 shows the equilibrium pressure, the excess adsorbed amount, the expected total error, and percentage of error.

Table 30. Adsorption isotherm data for CO_2 on the Pocahontas No.3 coal with the total calculated error on an absolute and percentage basis

Equilibrium Pressure	Excess Adsorption (n^{ex})	Error	Error
psia	(mmole/g-coal, daf)	$\lambda\left(\Delta n_j^{ex}\right)$	%
74.375	0.588	0.082	13.9
198.690	0.884	0.093	10.5
313.311	1.018	0.098	9.6
433.582	1.137	0.107	9.4
570.804	1.193	0.119	10.0
682.204	1.236	0.128	10.4
872.701	1.261	0.169	13.4
1084.177	1.290	0.237	18.3
1319.884	1.353	0.383	28.3
1491.809	1.526	0.501	32.8
1604.808	1.987	0.493	24.8
1771.096	2.225	0.392	17.6

APPENDIX D

DEPENDENCE OF COEFFICIENTS IN THE GOVERNING EQUATIONS ON PRESSURE AND SATURATION

D1.1 DEPENDENCE OF COEFFICIENTS IN THE GOVERNING EQUATIONS ON PRESSURE AND SATURATION

The pressure and saturation dependent coefficients are given as follows:

1. Cleat Porosity:

Cleat porosity (ϕ) is defined as the ratio of void space to the bulk volume of the coal seam. The porosity can be given as the total porosity including the micropores and macropores or the effective porosity which contributes to the flow of fluids. The effective porosity is the cleat porosity used in the calculations, which is a function of pressure.

$$\phi = \phi_o - \phi_o C_p \left(P_{ob} - P_g \right) \qquad (142)$$

The effective porosity is also defined as the contribution of both the pore volume compressibility and the matrix swelling and shrinkage compressibility as

$$\phi = \phi_o - \phi_o C_p (P_o - P) - (1 - \phi_o) C_m \left(\frac{\Delta P_o}{\Delta C_o} \right) (C - C_o) \tag{143}$$

Eq.(143) is suggested by Sawyer(258) and it has been used in ARI's CBM simulator, COMET.

2. Absolute Permeability:

Because gas and water flows occur within the interconnected cleat network, the permeability characteristics of coals are function of cleat properties, i.e. cleat spacing, cleat width, etc.. It has been shown that the absolute permeability (k) is a function of the effective stress which is defined as the total stress minus the seam fluid pressure and swelling and shrinkage properties of the coal.(259,260) The effective stress tends to close the cleats and to reduce the permeability within the coal. Therefore, the absolute permeability is related to the cleat porosity and defined as

$$k = k_o \left(\frac{\phi}{\phi_o} \right)^3 \tag{144}$$

3. Relative Permeability to Gas and Water:

Under the two-phase flow conditions, the relative permeability relationship between the gas and water phases control the relative flow of gas and water in the coal formation. However, accurate experimental data are not easily obtained for relative permeability. The laboratory estimation of the relative permeabilities usually misrepresent the actual in-seam relative permeabilities such that the small core samples do not represent the seam fracture network accurately and the gravity separation of gas and water in the coal seam improves the effective permeability of gas over that measured in a small core.(261) Therefore, the first approximation is to develop correlations used in the simulators, and then optimize the relative permeability curves wit respect to the actual production data. Here, the relative permeabilities are calculated using the most commonly used Corey's relationships.(262)

Relative permeability to gas (k_{rg})

$$k_{rg} = k_{rgc}\left(1 - S_{wn}^{2}\right)\left(1 - S_{wn}\right)^{2} \tag{145}$$

Relative permeability to water (k_{rw})

$$k_{rw} = k_{rwc} S_{wn}^{4} \tag{146}$$

where

$$S_{wn} = \frac{1 - S_{wirr} - S_{g}}{1 - S_{girr} - S_{wirr}} \tag{147}$$

4. Capillary pressure between gas and water phases:

Capillary pressure (P_c) may be defined as the pressure difference across a curved interface between two immiscible fluids. The capillary pressure may also be defined in terms of the pore radius and the interfacial tension between the immiscible fluids.

$$P_c = \frac{2\sigma \cos\theta}{r} \tag{148}$$

Where θ is the contact angle measured through the wetting fluid that the surface makes at the contact with the pore wall. On the other hand, the capillary pressure (P_{cgw}) between gas and water phases can be given by the Corey's relationship as a function of water saturation:

$$P_{cgw} = \frac{1}{\left[13.448\left(S_w - Swirr\right)\right]^{0.5}} \tag{149}$$

5. Viscosity of water and gas phases:

Viscosity of gas depends on the temperature, pressure, and the composition. The viscosity of water increases with decreasing temperature and in general with increasing pressure and salinity. The effect of dissolved gases is believed to cause a minor reduction in viscosity. Here, the McCaine correlation was used for the viscosity of the water phase.(249)

Water viscosity (μ_w)

$$\mu_w = AT^B\left(0.9994 + 4.0295 * 10^{-5} P + 3.1062 * 10^{-9} P^2\right) \tag{150}$$

where

$$A = 109.574 - 8.40564S + 0.313314S^2 + 8.72213 * 10^{-3} S^3 \tag{151}$$

$$\begin{aligned} B = &-1.12166 + 2.63951 * 10^{-2} S - 6.79461 * 10^{-4} S^2 \\ &- 5.47119 * 10^{-5} S^3 + 1.55586 * 10^{-6} S^4 \end{aligned} \tag{152}$$

where P, psia, T, ^{o}F, S is salinity, % by weight solid

The viscosity for gas phase can be represented by the correlation developed initially by Lee et al.(249) that gives an accurate estimate of gas viscosities.

Gas viscosity (μ_g)

$$\mu_g = 10^{-4} K \,\mathbf{exp}\left(X\rho^Y\right) \tag{153}$$

where

$$\rho = 1.4935 * 10^{-3} \frac{PM}{zT} \tag{154}$$

$$K = \frac{(9.4 + 0.02M)T^{1.5}}{209 + 19M + T} \tag{155}$$

$$X = 3.5 + \frac{986}{T} + 0.01M \tag{156}$$

$$Y = 2.4 - 0.2X \tag{157}$$

where P, psia, T, °R, and ρ, g/cc

6. Formation Volume Factor:

Formation Volume Factor for Gas (B_g) is related to the volume of gas in the reservoir to the its volume on the surface, i.e. at standard conditions, P_{sc} and T_{sc}. Assuming the compressibility factor (z) for gas at standard conditions is 1.0, the formation volume factor for gas at reservoir pressure and reservoir temperature is given as

$$B_g = \frac{P_{sc}}{T_{sc}} \frac{zT}{P} \tag{158}$$

The formation volume factor for water (B_w) is given by the following correlation initially developed by McCain$^{(263)}$

$$B_w = (1+\Delta V_{wt})(1+\Delta V_{wp}) \tag{159}$$

where

$$\Delta V_{wt} = -1.0001*10^{-2} + 1.33391*10^{-4}T + 5.50654*10^{-7}T^2 \tag{160}$$

$$\begin{aligned}\Delta V_{wp} &= -1.95301*10^{-9}PT - 1.72834*10^{-13}P^2T \\ &\quad - 3.58922*10^{-7}P - 2.25341*10^{-10}P^2\end{aligned} \tag{161}$$

where Temperature is in ^{o}F, Pressure is in Psia, and B_w is in bbl/STB

7. Compressibility Factor for Gases

The compressibility factor (z) is used to account the gas non-idealities. Here, the Hall-Yarborough equations,$^{(264)}$ developed using the Starling-Carnahan Equation of State, are employed to calculate the compressibility factor for both CH_4 and CO_2.

$$z = \frac{0.06125P_r\ \tau\ e^{-1.2\,(1-\tau)^2}}{\delta} \tag{162}$$

where P_r is the reduced pressure

$$P_r = \frac{P}{P_c} \tag{163}$$

τ is the reciprocal of the reduced temperature

$$\tau = \frac{T_c}{T} \tag{164}$$

And δ is the reduced density which is obtained from the solution of the equation

$$\begin{aligned} & -0.06125 P_r \; \tau \; e^{-1.2(1-\tau)^2} + \frac{\delta + \delta^2 + \delta^3 - \delta^4}{(1-\delta)^3} \\ & -\left(14.76\tau - 9.76\tau^2 + 4.58\tau^3\right)\delta^2 + \left(90.7\tau - 242.2\tau^2 + 42.4\tau^3\right)\delta^{(2.18+2.82\tau)} = 0 \end{aligned} \tag{165}$$

APPENDIX E

SORCE CODE IN FORTRAN 77 FOR THE MODELING OF FLUID FLOW IN COAL SEAMS

E1.1 COMPUTER CODE FOR THE MODELING FLUID FLOW IN COAL SEAMS

Below is the computer code for the modeling of fluid flow in coal seam in Fortran 77. In order to run the code, the used must define the solver which can be found in Athena Workbench®.(248)

```
      Program MAIN
      Implicit Real*8(A-H,O-Z)
      Integer NCP
      Integer NPE
      Parameter (NCP=2,NPE=NCP+2)
      Parameter (NCMAX=10,Zero=0.0D0,One=1.0D0,Pi=3.141592653589793D0)
      Parameter (LEQ=16,LRW=65000000,LIW=50000)
      Parameter (LPAR=0,LPTS=1.0E+03,LGRID=30)
      Parameter (LBREAK=0)
      Parameter (LMOD=0, KMOD=1)
      Parameter (MGRID=LGRID+2,MPTS=LPTS+2)
!
!:Variable Declaration Section
!
      Dimension U(LEQ,LGRID+2),UPRIME(LEQ,LGRID+2)
      Dimension RWORK(LRW),IWORK(LIW),RPAR(0:LPAR),IPAR(0:LPAR)
      Dimension Info(50),Tout(LPTS+2),Xgrid(LGRID+2),Xbreak(LBREAK+2)
      Dimension TSTOP(0:LMOD),USTOP(0:KMOD)
      Real*8 R,ALFA,PSC,TSC,DEPTH,DZ,CP,CM,ROC,POROI,KABSI,CLSP,PW,PGRAD,TGRAD,OBGR
     *       AD,TRES,POB,VL1,PL1,PC1,TC1,CONV1,CONV2,CONV3,CONV4,VL2,PL2,PC2,TC2,PM
```

```
     *      AX,VMAX,V,H,KRGC,KRWC,QG1,QW1,QG2,QW2,SG2,ROSC,CW,KRCW,KRCG,SWIRR,SGIR
     *      R,RW,RE,SKIN,TEMP,PGI,S,LOGR,PWELL,SWELL,PCGW,PORO,KABS,SWN,KRG,KRW,DV
     *      T,DVP,BG,BW,DA,BOB,MW,MW1,MW2,Z,ZZ,Z1,Z2,DZDPG,RO,KK1,XK1,YK1,VISG,VIS
     *      W,A,B,SG1,QGSP,QWSP,QTSP,A11,A12,A13,A21,A22,A23,VL3,VL3IRR,PO,CBET,PC
     *      ,TC,VIRR,TAO,DI,AA1,AA2,AA3,Y11,AB1,BB1,BB2,BB3,BB4,BB5,BB6,BB7,BB8,CO
     *      EFF1,COEFF2,DPGDR,DVP1,DBW,DPORO,DBG,CG,CG1,CG2,ALFA1,FLOWGP,FLOWWP,SG
     *      P,DSGDR,VL10,VL20,VL30,PGQ,ADSA,K1,K2,FLOWGI,FLOWWI,SGI,PG1,XG1,DPOROD
     *
PG,DKABSDPORO,DSWNDSG,DSWNDSW,DKRGDSWN,DKRWDSWN,EU,DZFAC,DZFAC1,DZFAC2
     *      ,D2ZDPG2,D2ZDPG21,D2ZDPG22,D2ZDPG2T,DPCGWDSW,DPCGW2DSW2,DBWDPW,DBGDPG,
     *
DVISGDROG,DROGDPG,DVISWDPW,DRSWDPG,D2BGDPG2,ADSCO2,ADSCH4,BULKCO2,BULK
     *      CH4,CO2IN,CH4IN,H2OIN,EKO01,EKO02,EKO03,EKO04,EKO05,EKO06,EKO07,EKO08,
     *      EKO09,EKO10,EKO11,EKO12,EKO13,EKO14,EKO15,EKO16,EKO17,EKO18,EKO19,EKO2
     *      0,EKO21,EKO22,EKO23,EKO24,EKO25,EKO26,EKO27,EKO28,EKO29,EKO30,DAE01,DA
     *      E02,DAE03,DAE04,DAE05,DAE06,DAE07,DAE08,DAE09,DAE10,DAE11,DAE12,DAE13,
     *      DAE14,DAE15,DAE16,DAE17,DAE18,DAE19,DAE20,RSWE01,RSWE02,RSWE03,RSWE04,
     *      RSWE05,RSWE06,RSWE07,RSWE08,RSWE09,RSWE10,RSWE11,RSWE12,RSWE13,RSWE14,
     *      RSWE15,RSWE16,RSWE17,RSWE18,RSWE19,RSWE20,RSWE21,RSWE22,RSWE23,RSWE24,
     *      RSWE25,RSWE26,RSWE27,RSWE28,RSWE29,RSWE30,RSWE31,RSWE32,RSWE33,RSWE34,
     *      RSWE35,RSWE36,C11,C12,C13,C14,C15,C16,C17,C21,C22,C23,C24,C25,C26,C27,
     *      C31,C32,C33,C34,C35,C36,C37,FM1,FM2,FM3,FM4,CE11,CE12,CE13,CE21,CE22,C
     *      E23,CE31,CE32,CE33,CE41,CE42,CE43,CE51,CE52,CE53,RSW1,RSW2,DRSW1DPG,DR
     *
SW2DPG,QGDARCY,QWDARCY,QWDARCY1,QGDARCY1L,QWDARCY2,QGDA1,QGDA2,QGDA11,
     *      QGDA12,QGDA21,QGDA22,QGDA1R,QGDA2R,QGDA11R,QGDA12R,QGDA21R,QGDA22R,QGR
     *      SW1,QGRSW2,QGRSW11,QGRSW12,QGRSW21,QGRSW22,QGRSW1R,QGRSW2R,QGRSW11R,QG
     *      RSW12R,QGRSW21R,QGRSW22R,QGDARCY1,QWDARCY11,QWDARCY21,QGDA111,QGDA121,
     *      QGDA211,QGDA221,QGRSW111,QGRSW121,QGRSW211,QGRSW221,QGDARCY1R,QWDARCY1
     *      1R,QWDARCY21R,QGDA111R,QGDA121R,QGDA211R,QGDA221R,QGRSW111R,QGRSW121R,
     *      QGRSW211R,QGRSW221R,ALI,ALI1,ALI11,ALI2,ALI22,ALI3,ALI4,XR1,XR2,XRN,MO
     *      ISTURE,ASH,MULTIPLIER,WI1,WI2,QSP,CC,QWELL,PGL,SGL,PGR,PG,SG,Y1,ZAMAN(
     *      1002),QGIN(1002),QWIN(1002),QGPRO(1002),QWPRO(1002),ADSRT1(1002),ADSRT
     *      2(1002),ADSRT3(1002),PWELL1(1002),QGCUM(1002),QWCUM(1002),ADSRATE1,ADS
     *      RATE2,ADSRATE3,QG1ATWELL,RR,PWW,UP(3,4),UPX(3,4),UPXX(3,4),ZOC(10),WOC
     *      (10),AOC(10,10),BOC(10,10)
      Integer GASCOMP,FLAG1,J1,J5,ITER1,Iloop,BC,IWELL,QB,II,NSUB,ISYM
!
!:External Declarations, Common Blocks and Data Statements
!
      External FPSUBP,EPSUBP,GPSUBP,DPSUBP
      Common/USRI00P/ IOFSET
      Common/WEIGHTS/ PROOT(NCMAX),WQ(NCMAX),AX(NCMAX,NCMAX),BXX(NCMAX,NCMAX)
      Common/USRR01P/
R,ALFA,PSC,TSC,DEPTH,DZ,CP,CM,ROC,POROI,KABSI,CLSP,PW,PGRAD,TGRAD,OBGR
     *            AD,TRES,POB,VL1,PL1,PC1,TC1,CONV1,CONV2,CONV3,CONV4,VL2,PL2,PC2,TC2,PM
     *
AX,VMAX,V,H,KRGC,KRWC,QG1,QW1,QG2,QW2,SG2,ROSC,CW,KRCW,KRCG,SWIRR,SGIR
     *            R,RW,RE,SKIN,TEMP,PGI,S,LOGR,PWELL,SWELL,PCGW,PORO,KABS,SWN,KRG,KRW,DV
     *            T,DVP,BG,BW,DA,BOB,MW,MW1,MW2,Z,ZZ,Z1,Z2,DZDPG,RO,KK1,XK1,YK1,VISG,VIS
     *            W,A,B,SG1,QGSP,QWSP,QTSP,A11,A12,A13,A21,A22,A23,VL3,VL3IRR,PO,CBET,PC
     *            ,TC,VIRR,TAO,DI,AA1,AA2,AA3,Y11,AB1,BB1,BB2,BB3,BB4,BB5,BB6,BB7,BB8,CO
     *            EFF1,COEFF2,DPGDR,DVP1,DBW,DPORO,DBG,CG,CG1,CG2,ALFA1,FLOWGP,FLOWWP,SG
     *            P,DSGDR,VL10,VL20,VL30,PGQ,ADSA,K1,K2,FLOWGI,FLOWWI,SGI,PG1,XG1,DPOROD
     *
PG,DKABSDPORO,DSWNDSG,DSWNDSW,DKRGDSWN,DKRWDSWN,EU,DZFAC,DZFAC1,DZFAC2
```

```
     *
,D2ZDPG2,D2ZDPG21,D2ZDPG22,D2ZDPG2T,DPCGWDSW,DPCGW2DSW2,DBWDPW,DBGDPG,
     *
DVISGDROG,DROGDPG,DVISWDPW,DRSWDPG,D2BGDPG2,ADSCO2,ADSCH4,BULKCO2,BULK
     *          CH4,CO2IN,CH4IN,H2OIN,EKO01,EKO02,EKO03,EKO04,EKO05,EKO06,EKO07,EKO08,
     *          EKO09,EKO10,EKO11,EKO12,EKO13,EKO14,EKO15,EKO16,EKO17,EKO18,EKO19,EKO2
     *          0,EKO21,EKO22,EKO23,EKO24,EKO25,EKO26,EKO27,EKO28,EKO29,EKO30,DAE01,DA
     *          E02,DAE03,DAE04,DAE05,DAE06,DAE07,DAE08,DAE09,DAE10,DAE11,DAE12,DAE13,
     *          DAE14,DAE15,DAE16,DAE17,DAE18,DAE19,DAE20,RSWE01,RSWE02,RSWE03,RSWE04,
     *          RSWE05,RSWE06,RSWE07,RSWE08,RSWE09,RSWE10,RSWE11,RSWE12,RSWE13,RSWE14,
     *          RSWE15,RSWE16,RSWE17,RSWE18,RSWE19,RSWE20,RSWE21,RSWE22,RSWE23,RSWE24,
     *          RSWE25,RSWE26,RSWE27,RSWE28,RSWE29,RSWE30,RSWE31,RSWE32,RSWE33,RSWE34,
     *          RSWE35,RSWE36,C11,C12,C13,C14,C15,C16,C17,C21,C22,C23,C24,C25,C26,C27,
     *          C31,C32,C33,C34,C35,C36,C37,FM1,FM2,FM3,FM4,CE11,CE12,CE13,CE21,CE22,C
     *          E23,CE31,CE32,CE33,CE41,CE42,CE43,CE51,CE52,CE53,RSW1,RSW2,DRSW1DPG,DR
     *
SW2DPG,QGDARCY,QWDARCY,QWDARCY1,QGDARCY1L,QWDARCY2,QGDA1,QGDA2,QGDA11,
     *
QGDA12,QGDA21,QGDA22,QGDA1R,QGDA2R,QGDA11R,QGDA12R,QGDA21R,QGDA22R,QGR
     *
SW1,QGRSW2,QGRSW11,QGRSW12,QGRSW21,QGRSW22,QGRSW1R,QGRSW2R,QGRSW11R,QG
     *
RSW12R,QGRSW21R,QGRSW22R,QGDARCY1,QWDARCY11,QWDARCY21,QGDA111,QGDA121,
     *
QGDA211,QGDA221,QGRSW111,QGRSW121,QGRSW211,QGRSW221,QGDARCY1R,QWDARCY1
     *
1R,QWDARCY21R,QGDA111R,QGDA121R,QGDA211R,QGDA221R,QGRSW111R,QGRSW121R,
     *          QGRSW211R,QGRSW221R,ALI,ALI1,ALI11,ALI2,ALI22,ALI3,ALI4,XR1,XR2,XRN,MO
     *          ISTURE,ASH,MULTIPLIER,WI1,WI2,QSP,CC,QWELL,PGL,SGL,PGR,PG,SG,Y1,ZAMAN
     *          ,QGIN ,QWIN ,QGPRO ,QWPRO ,ADSRT1 ,ADSRT2 ,ADSRT3 ,PWELL1 ,QGCUM ,QWCU
     *          M ,ADSRATE1,ADSRATE2,ADSRATE3,QG1ATWELL,RR,PWW,UP ,UPX ,UPXX ,ZOC ,WOC
     *          ,AOC ,BOC
      Common/USRI01P/ GASCOMP,FLAG1,J1,J5,ITER1,Iloop,BC,IWELL,QB,II,NSUB,ISYM
!
!:Perfom Dimensional Initialization
!
      Neq = LEQ
      Npar = LPAR
      NMOD = LMOD
      UMOD = KMOD
      NPTS = LPTS+2
      Ngrid = LGRID+2
      Nbreak = LBREAK + 2
      If(NPTS.LE.1)NPTS=2
!
!:Prepare Error Messages File
!
      LUN = 6
      LUNERR = 60
      Open(UNIT=LUN,FILE='CO2-ECBM-COMPOSNL.RES',STATUS='UNKNOWN')
      Rewind(UNIT=LUN)
      Open(UNIT=LUNERR,FILE='CO2-ECBM-COMPOSNL.DBG',STATUS='UNKNOWN')
      Rewind(UNIT=LUNERR)
!
!:User Defined Problem Parameters
!
```

```
FM1=1.0
FM2=1.0
FM3=0.0
FM4=1.0
PSC=14.7
TSC=60
R=10.73
ALFA=1.127E-03
ALFA1=5.615
DEPTH=3200.0
DZ=10
POROI=0.02
ROC=1.36
CLSP=(1.3114)/2.54/12
CP=1.0E-06
CM=0.0
MOISTURE=5.0
ASH=5.0
RW=0.2917
RE=2710.0/2.0
SKIN=0.0
CC=0.0
PC1=1100
TC1=64.4
MW1=44.01
PC2=673.1
TC2=-116.7
MW2=16
RWSC=62.4
CW=0.0000
VL1=1.3
PL1=33.0
VL2=0.612
PL2=167.5
VL3=6.0
VL3IRR=1.0
K1=1.0/PL1
K2=1.0/PL2
CONV1=ROC*1.0E6/(1.0E3*35.3147*453.6)
CONV2=1/RWSC/ALFA1
VL1=VL1*CONV1*MW1
VL2=VL2*CONV1*MW2
VL3=VL3*CONV2
VL3IRR=VL3IRR*CONV2
KABSI=2.0
DI=2.0E-6
DA=(0.219)*93.0
KRCW=1.0
KRCG=1.0
SWIRR=1.0E-10
SGIRR=1.0E-10
TAO=((CLSP/2)**2)/DI
CONV3=R*(460+TSC)/PSC
A11=FM4*(CONV3/MW1)*1.0/TAO
A12=FM4*(CONV3/MW2)*1.0/TAO
A13=FM4*(CONV2)*1.0/TAO
```

```
      A21=1.0/TAO
      A22=1.0/TAO
      A23=1.0/TAO
      PGRAD=0.45
      TGRAD=0.0293
      OBGRAD=0.802
      TRES=TSC+DEPTH*TGRAD
      PRES=PSC+DEPTH*PGRAD
      POB=PSC+DEPTH*OBGRAD
      TEMP=TRES
      S=0.0
      NSUB=3
      ISYM=0
      ICOORDINATE=1
      IWEIT=0
      Call UsrABWasym(ICOORDINATE,IWEIT,NCP,IERROR,ZOC,WOC,AOC,BOC)
      PGI=500.0
      SGI=4.0E-1
      Y11=1.0E-20
      VL10=VL1*K1*Y11*PGI/(1.0+K1*Y11*PGI+K2*(1.0-Y11)*PGI)
      VL20=VL2*K2*(1.0-Y11)*PGI/(1.0+K1*Y11*PGI+K2*(1.0-Y11)*PGI)
      VL30=VL3
      IWELL=1
      QB=2
      If(IWELL.EQ.1)Then
      PWELL=2200.0
      ElseIf(IWELL.EQ.2)Then
      BOB=PGI
      EndIf
      QGSP=2.0E3
      QWSP=2.0E3
      QTSP=5.0E3
      MULTIPLIER=0.9
      ITER1=0
      FLAG1=0
!
!:Calling Arguments for PDAPLUS: Partial Differential Equations
!
      IOFSET = 0
      Icord = 1
      Tini = 0
      TEND = 1.8E+04
      dT = (TEND - Tini)/Float(NPTS-1)
      Do J=1,NPTS
       Tout(J)=Tini+dT*Float(J-1)
      End Do
      Ieform = 0
      IWORK(1) = min(2*Neq-1+Neq*0, Neq*Ngrid-1)
      IWORK(2) = min(2*Neq-1+Neq*0, Neq*Ngrid-1)
      RTOL = 1.0E-4
      ATOL = 1.0E-4
      IPRT = 1
      If(IPRT.EQ.0)IPRT=Ngrid
      If(IPRT.GT.Ngrid)IPRT=Ngrid
!
!:Calculate the Grid Point Sequence
```

```
!
      Xalpha = 0
      Xbeta = 1
      Xgrid(1)=Xalpha
      Xgrid(Ngrid)=Xbeta
      Xbreak(1)=Xalpha
      Xbreak(Nbreak)=Xbeta
      dXgrid = (Xbeta - Xalpha)
      Do J=2,Ngrid-1
       Xgrid(J)=Xalpha+dXgrid*(Float(J-1)/Float(Ngrid-1))**1
      End Do
!
!:Info(1..18) Array
!
      Info(01) = 0
      Info(02) = 0
      Info(03) = 0
      Info(04) = 0
      Info(05) = 0
      Info(06) = 1
      Info(07) = 0
      Info(08) = 0
      RWORK(3) = 0
      Info(09) = 1
      IWORK(3) = 5
      Info(10) = 0
      Info(11) = 1
      RWORK(44) = 0
      Info(12) = Npar
      Info(13) = 2
      Info(14) = 1
      Info(15) = 0
      Info(16) = 0
      USTOP(1-1)=0.5
      Info(17) = Neq * 32 - Neq + 4
      RWORK(42) = USTOP(0)
      RWORK(43) = 1.0E-6
      Info(18) = 0
      Info(26) = 1
      Info(28) = 0
      Info(29) = 1
      Info(30) = 2
      Info(31) = 0
      Info(19) = 0
      Info(20) = 0
      Info(21) = 1
      Info(22) = 30
      Info(23) = Nbreak - 2
      IWORK(17) = 30
      IWORK(18) = 5
      IWORK(21) = 1000
!
!:Calculate Initial Values for PDAPLUS
!
      Do Igrid=1,Ngrid
       IPARLOC = 1
```

```
      Call ISUBP(Tini,Xgrid(Igrid),Neq,U,Igrid,IPARLOC,Ngrid,Npar,RPAR,IPAR,Ieform)
     End Do
!
!:Print Some Input Information
!
     Write(LUN,'(A35,I5)')' Number of State Equations.........',Neq
     Write(LUN,'(A35,I5)')' Number of Sensitivity Parameters..',Npar
     Write(LUN,'(A35,I5)')' Number of Discretization Points...',Ngrid
     Write(LUN,'(A35,I5)')' Number of Integration Points......',NPTS
     Write(LUN,'(A1)')' '
!
!:CALL PDAPLUS Integrator and Print Results
!
100   Continue
     Do I=1,NPTS
      Iloop = I
     If(IWELL.EQ.2)Then
     PWELL=BOB
     EndIf
      Call PDAPLUS(Tini,Tout(I),Xalpha,Ngrid,Xgrid,Icord,Neq,U,UPRIME,
    *             RTOL,ATOL,Info,RWORK,
    *             LRW,IWORK,LIW,RPAR,IPAR,Idid,LUNERR,Ieform,
    *             FPSUBP,EPSUBP,DPSUBP,GPSUBP)
     II=5
     LOGR=(log((Xgrid(II)+RW/RE)/(Xgrid(1)+RW/RE))-CC+SKIN)
     If(QB.EQ.2)Then
     QGDARCY=QGDARCY1/RW*(U(2,II)-U(2,1))/LOGR
     QGDA11=QGDA111/RW*(U(3,II)-U(3,1))/LOGR
     QGDA12=QGDA121/RW*(U(2,II)-U(2,1))/LOGR
     QGDA1=(QGDA11+QGDA12)
     QGDA21=QGDA211/RW*(U(3,II)-U(3,1))/LOGR
     QGDA22=QGDA221/RW*(U(2,II)-U(2,1))/LOGR
     QGDA2=(QGDA21+QGDA22)
     QGRSW11=QGRSW111/RW*(U(2,II)-U(2,1))/LOGR
     QGRSW12=QGRSW121/RW*(U(3,II)-U(3,1))/LOGR
     QGRSW1=(QGRSW11+QGRSW12)
     QGRSW21=QGRSW211/RW*(U(2,II)-U(2,1))/LOGR
     QGRSW22=QGRSW221/RW*(U(3,II)-U(3,1))/LOGR
     QGRSW2=(QGRSW21+QGRSW22)
     QWDARCY1=QWDARCY11/RW*(U(2,II)-U(2,1))/LOGR
     QWDARCY2=QWDARCY21/RW*(U(3,II)-U(3,1))/LOGR
     QWDARCY=(QWDARCY1+QWDARCY2)
     QG1=(QGDARCY+QGDA2+QGRSW2)
     QW1=QWDARCY
     EndIf
     If(IWELL.EQ.2)Then
     XR1=(QGDARCY1+QGDA221+QGRSW211+ALFA1*QWDARCY11)
     XR2=QGDA21+QGRSW22+ALFA1*QWDARCY2
     BOB=U(2,II)-(QTSP-XR2)/XR1*RW*LOGR
     Info(1)=0
     EndIf
     If(BOB.LT.25)Then
     BOB=25.0
     ElseIf(BOB.GT.PGI)Then
     BOB=PGI
     EndIf
```

```
      If(Iloop.GT.1)Then
      ZAMAN(I)=Tini
      QGIN(I)=abs(QG1)/1000.0
      QWIN(I)=abs(QW1)
      QGCUM(I)=QGCUM(I-1)+abs(QG1)/1.0E6*dT
      QWCUM(I)=QWCUM(I-1)+abs(QW1)/1.0E3*dT
      QGPRO(I)=ADSRATE1
      QWPRO(I)=ADSRATE2
      PWELL1(I)=PGL
      EndIf
!
!:Print Modeling results
!
       If(I.EQ.1.AND.Ieform.EQ.0)Then
        Write(LUN,'(A231)')'  Time Var      Space Var      U(1)         U(2)         U(3)
     * U(4)         U(5)         U(6)         U(7)         U(8)         U(9)
     *         U(10)        U(11)        U(12)        U(13)        U(14)
     *    U(15)        U(16)'
       EndIf
       Write(LUN,'(1X,1PE12.5,2X,1PE12.5,3X,16(1PE12.5,1X))')Tini,Xgrid(1),(U(J1,1),J1=1,Neq)
       Do J2=2,Ngrid-1,IPRT
        Write(LUN,'(1X,12X,   2X,1PE12.5,3X,16(1PE12.5,1X))')Xgrid(J2),(U(J1,J2),J1=1,Neq)
       End Do
       Write(LUN,'(1X,12X,    2X,1PE12.5,3X,16(1PE12.5,1X))')Xgrid(Ngrid),(U(J1,Ngrid),J1=1,Neq)
       If(Idid.LT.0)GoTo 60
       If(Info(17).GT.0 .AND. Idid.EQ.4)GoTo 80
       If(Info(04).GT.0 .AND. Idid.EQ.5)GoTo 95
      End Do
      GoTo 60
80    Continue
95    Continue
60    Continue
!
!:Exit Code and Integration Run Time Statistics
!
      Write(LUN,'(A1)')' '
      If(Idid.GE.0)Write(LUN,'(A49,I5)')' EXIT PDAPLUS: SOLUTION SUCCESSFUL with IDID.....',Idid
      If(Idid.LT.0)Write(LUN,'(A49,I5)')' EXIT PDAPLUS: SOLUTION HAS FAILED with IDID.....',Idid
      Write(LUN,'(A49,I5)')            ' Number of Steps Taken Thus far..................',IWORK(11)
      Write(LUN,'(A49,I5)')            ' Number of Function Evaluations..................',IWORK(12)
      Write(LUN,'(A49,I5)')            ' Number of Jacobian Evaluations..................',IWORK(13)
      Write(LUN,'(A49,I5)')            ' Number of Jacobian Factorizations...............',IWORK(23)
!
!:User Customized Output
!
      ADSCO2=Pi*RE**2*DZ*(1.0-PORO)*VL10*R*(460+TSC)/PSC/MW1/1.0E6
      ADSCH4=Pi*RE**2*DZ*(1.0-PORO)*VL20*R*(460+TSC)/PSC/MW2/1.0E6
      GASCOMP=1
      Call COMPFACTOR(U,Ieform,RPAR)
      Z1=ZZ
      TEMP=TEMP-460
      GASCOMP=2
      Call COMPFACTOR(U,Ieform,RPAR)
      Z2=ZZ
      TEMP=TEMP-460
      BULKCO2=Y11*Pi*RE**2*DZ*PORO*SGI*PGI/(Z1*R*TEMP)*R*(460+TSC)/PSC/1.0E6
```

```
      BULKCH4=(1.0-Y11)*Pi*RE**2*DZ*PORO*SGI*PGI/(Z2*R*TEMP)*R*(460+TSC)/PSC/1.0E6
      CO2IN=ADSCO2+BULKCO2
      CH4IN=ADSCH4+BULKCH4
      H2OIN=Pi*RE**2*DZ*PORO*(1.0-SGI)/1.0/ALFA1/1.0E3
      Write(6,*)'         ','        TIME VAR        U(1)        U(2)        U(3)        U(4)'
      Do J1=1,1002
      Write(6,'(1X,12X,
2X,1PE12.5,3X,7(1PE12.5,1X))')ZAMAN(J1),QGIN(J1),QWIN(J1),QGCUM(J1),QWCUM(J1),QGPRO(J1),QWP
RO(J1),PWELL1(J1)
      EndDo
      Write(6,*)
      Write(6,*)
      Write(6,*)
      Write(6,*) '---------------------------------------------------------------------'
      Write(6,*)'FORMATION PROPERTIES'
      Write(6,*) '---------------------------------------------------------------------'
      Write(6,'(A48,F10.2,A12)')'RESERVOIR AREA..............................=',Pi*(RE*0.3048/1000)**2, '(KM)2'
      Write(6,'(A48,F10.2,A12)')'AVERAGE RESERVOIR DEPTH.....................=',DEPTH*0.3048, 'M'
      Write(6,'(A48,F10.2,A12)')'FORMATION THICKNESS.........................=',DZ*0.3048, 'M'
      Write(6,'(A48,F10.2,A12)')'EFFECTIVE POROSITY..........................=',POROI*100.0,'%'
      Write(6,'(A48,F10.2,A12)')'ABSOLUTE PERMEABILITY.......................=',KABSI,'MD'
      Write(6,'(A48,D10.2,A12)')'FORMATION COMPRESSIBILITY...................=',CP*14.696/0.101325, '1/MPA'
      Write(6,'(A48,F10.2,A12)')'COAL DENSITY................................=',ROC,'GR/CM3'
      Write(6,'(A48,F10.2,A12)')'FORMATION TEMPERATURE.......................=',(TEMP+460)*0.556-273.15, 'OC'
      Write(6,'(A48,F10.2,A12)')'INITIAL FORMATION PRESSURE..................=',PGI*0.101325/14.696, 'MPA'
      Write(6,'(A48,F10.2,A12)')'INITIAL WATER SATURATION....................=',(1.0-SGI),'FRACTION'
      Write(6,*)
      Write(6,*)'INITIAL GAS AND WATER IN PLACE'
      Write(6,*) '---------------------------------------------------------------------'
      Write(6,'(A48,F10.2,A12)')'CO2 IN ADSORBED PHASE......................=',Y11*ADSCO2*0.028317,
'SM3*10**6'
      Write(6,'(A48,F10.2,A12)')'CH4 IN ADSORBED PHASE......................=',ADSCH4*0.028317, 'SM3*10**6'
      Write(6,'(A48,F10.2,A12)')'COMPOSITION FOR CO2 IN BULK GAS PHASE......=',Y11,'FRACTION'
      Write(6,'(A48,F10.2,A12)')'COMPOSITION FOR CH4 IN BULK GAS PHASE......=',1.0-Y11,'FRACTION'
      Write(6,'(A48,F10.2,A12)')'CO2 IN BULK GAS PHASE......................=',BULKCO2*0.028317*10**3,
'SM3*10**3'
      Write(6,'(A48,F10.2,A12)')'CH4 IN BULK GAS PHASE......................=',BULKCH4*0.028317*10**3,
'SM3*10**3'
      Write(6,'(A48,F10.2,A12)')'TOTAL CO2-IN-PLACE.........................=',CO2IN*0.028317, 'SM3*10**6'
      Write(6,'(A48,F10.2,A12)')'TOTAL CH4-IN-PLACE.........................=',CH4IN*0.028317, 'SM3*10**6'
      Write(6,'(A48,F10.2,A12)')'TOTAL H2O-IN-PLACE.........................=',H2OIN*0.15899, 'SM3*10**3'
      Write(6,*)
      Write(6,*)'WELLBORE PROPERTIES'
      Write(6,*) '---------------------------------------------------------------------'
      Write(6,'(A48,F10.2,A12)')'WELL RADIUS.................................=',RW*0.3048*100, 'CM'
      Write(6,'(A48,F10.2,A12)')'WELLBORE PRESSURE...........................=',PWELL*0.101325/14.696, 'MPA'
      Write(6,'(A48,F10.2,A12)')'SKIN FACTOR.................................=',SKIN
      Write(6,*)
      Write(6,*)'ADSORPTION ISOTHERMS'
      Write(6,*) '---------------------------------------------------------------------'
      Write(6,'(A48,F10.2,A12)')'ADSORPTION CAPACITY FOR CO2.................=',VL1*R*TSC/MW1/PSC/ROC,
'SM3/TON'
      Write(6,'(A48,F10.2,A12)')'ADSORPTION CAPACITY FOR CH4.................=',VL2*R*TSC/MW1/PSC/ROC,
'SM3/TON'
      Write(6,'(A48,F10.2,A12)')'LANGMUIR PRESSURE FOR CO2...................=',PL1**0.101325/14.696, 'MPA'
      Write(6,'(A48,F10.2,A12)')'LANGMUIR PRESSURE FOR CH4...................=',PL2*0.101325/14.696, 'MPA'
```

```
      Write(6,*)
      Write(6,*)'TRANSPORT PARAMETERS'
      Write(6,*) '--------------------------------------------------------------------'
      Write(6,'(A48,F10.2,A12)')'CLEAT SPACING.............................=',CLSP*0.3048*100, 'CM'
      Write(6,'(A48,D10.2,A12)')'MICROPORE DIFFUSION COEFFICIENT............=',DI*0.0929, 'M2/DAY'
      Write(6,'(A48,F10.2,A12)')'SORPTION TIME CONSTANT......................=',TAO,'DAY'
      Write(6,'(A48,F10.2,A12)')'CRITICAL WATER CONTENT (SWC)................=',SWIRR,'FRACTION'
      Write(6,'(A48,F10.2,A12)')'CRITICAL GAS CONTENT (SGC).................=',SGIRR,'FRACTION'
      Write(6,'(A48,F10.2,A12)')'RELATIVE PERMEABILITY TO WATER AT SGC.......=',KRCW,'MD'
      Write(6,'(A48,F10.2,A12)')'RELATIVE PERMEABILITY TO GAS AT SWC.........=',KRCG,'MD'
      Write(6,*) '--------------------------------------------------------------------'
      Write(6,*)
!
!:End of MAIN Program
!
      End

      Subroutine ISUBP(T, X, Neq, U, Igrid, JPAR, Ngrid, Npar, RPAR, IPAR, Ieform)
      Implicit Real*8(A-H,O-Z)
      Integer NCP
      Integer NPE
      Parameter (NCP=2,NPE=NCP+2)
      Parameter (NCMAX=10,Zero=0.0D0,One=1.0D0,Pi=3.141592653589793D0)
!
!:Variable Declaration Statements section
!
      Dimension U(Neq,Ngrid,1),RPAR(0:*),IPAR(0:*)
      Real*8 R,ALFA,PSC,TSC,DEPTH,DZ,CP,CM,ROC,POROI,KABSI,CLSP,PW,PGRAD,TGRAD,OBGR
     *      AD,TRES,POB,VL1,PL1,PC1,TC1,CONV1,CONV2,CONV3,CONV4,VL2,PL2,PC2,TC2,PM
     *      AX,VMAX,V,H,KRGC,KRWC,QG1,QW1,QG2,QW2,SG2,ROSC,CW,KRCW,KRCG,SWIRR,SGIR
     *      R,RW,RE,SKIN,TEMP,PGI,S,LOGR,PWELL,SWELL,PCGW,PORO,KABS,SWN,KRG,KRW,DV
     *      T,DVP,BG,BW,DA,BOB,MW,MW1,MW2,Z,ZZ,Z1,Z2,DZDPG,RO,KK1,XK1,YK1,VISG,VIS
     *      W,A,B,SG1,QGSP,QWSP,QTSP,A11,A12,A13,A21,A22,A23,VL3,VL3IRR,PO,CBET,PC
     *      ,TC,VIRR,TAO,DI,AA1,AA2,AA3,Y11,AB1,BB1,BB2,BB3,BB4,BB5,BB6,BB7,BB8,CO
     *      EFF1,COEFF2,DPGDR,DVP1,DBW,DPORO,DBG,CG,CG1,CG2,ALFA1,FLOWGP,FLOWWP,SG
     *      P,DSGDR,VL10,VL20,VL30,PGQ,ADSA,K1,K2,FLOWGI,FLOWWI,SGI,PG1,XG1,DPOROD
     *
PG,DKABSDPORO,DSWNDSG,DSWNDSW,DKRGDSWN,DKRWDSWN,EU,DZFAC,DZFAC1,DZFAC2
     *      ,D2ZDPG2,D2ZDPG21,D2ZDPG22,D2ZDPG2T,DPCGWDSW,DPCGW2DSW2,DBWDPW,DBGDPG,
     *
DVISGDROG,DROGDPG,DVISWDPW,DRSWDPG,D2BGDPG2,ADSCO2,ADSCH4,BULKCO2,BULK
     *      CH4,CO2IN,CH4IN,H2OIN,EKO01,EKO02,EKO03,EKO04,EKO05,EKO06,EKO07,EKO08,
     *      EKO09,EKO10,EKO11,EKO12,EKO13,EKO14,EKO15,EKO16,EKO17,EKO18,EKO19,EKO2
     *      0,EKO21,EKO22,EKO23,EKO24,EKO25,EKO26,EKO27,EKO28,EKO29,EKO30,DAE01,DA
     *      E02,DAE03,DAE04,DAE05,DAE06,DAE07,DAE08,DAE09,DAE10,DAE11,DAE12,DAE13,
     *      DAE14,DAE15,DAE16,DAE17,DAE18,DAE19,DAE20,RSWE01,RSWE02,RSWE03,RSWE04,
     *      RSWE05,RSWE06,RSWE07,RSWE08,RSWE09,RSWE10,RSWE11,RSWE12,RSWE13,RSWE14,
     *      RSWE15,RSWE16,RSWE17,RSWE18,RSWE19,RSWE20,RSWE21,RSWE22,RSWE23,RSWE24,
     *      RSWE25,RSWE26,RSWE27,RSWE28,RSWE29,RSWE30,RSWE31,RSWE32,RSWE33,RSWE34,
     *      RSWE35,RSWE36,C11,C12,C13,C14,C15,C16,C17,C21,C22,C23,C24,C25,C26,C27,
     *      C31,C32,C33,C34,C35,C36,C37,FM1,FM2,FM3,FM4,CE11,CE12,CE13,CE21,CE22,C
     *      E23,CE31,CE32,CE33,CE41,CE42,CE43,CE51,CE52,CE53,RSW1,RSW2,DRSW1DPG,DR
     *
SW2DPG,QGDARCY,QWDARCY,QWDARCY1,QGDARCY1L,QWDARCY2,QGDA1,QGDA2,QGDA11,
     *      QGDA12,QGDA21,QGDA22,QGDA1R,QGDA2R,QGDA11R,QGDA12R,QGDA21R,QGDA22R,QGR
     *      SW1,QGRSW2,QGRSW11,QGRSW12,QGRSW21,QGRSW22,QGRSW1R,QGRSW2R,QGRSW11R,QG
```

```
    *      RSW12R,QGRSW21R,QGRSW22R,QGDARCY1,QWDARCY11,QWDARCY21,QGDA111,QGDA121,
    *      QGDA211,QGDA221,QGRSW111,QGRSW121,QGRSW211,QGRSW221,QGDARCY1R,QWDARCY1
    *      1R,QWDARCY21R,QGDA111R,QGDA121R,QGDA211R,QGDA221R,QGRSW111R,QGRSW121R,
    *      QGRSW211R,QGRSW221R,ALI,ALI1,ALI11,ALI2,ALI22,ALI3,ALI4,XR1,XR2,XRN,MO
    *      ISTURE,ASH,MULTIPLIER,WI1,WI2,QSP,CC,QWELL,PGL,SGL,PGR,PG,SG,Y1,ZAMAN(
    *      1002),QGIN(1002),QWIN(1002),QGPRO(1002),QWPRO(1002),ADSRT1(1002),ADSRT
    *      2(1002),ADSRT3(1002),PWELL1(1002),QGCUM(1002),QWCUM(1002),ADSRATE1,ADS
    *      RATE2,ADSRATE3,QG1ATWELL,RR,PWW,UP(3,4),UPX(3,4),UPXX(3,4),ZOC(10),WOC
    *      (10),AOC(10,10),BOC(10,10)
     Integer GASCOMP,FLAG1,J1,J5,ITER1,Iloop,BC,IWELL,QB,II,NSUB,ISYM
!
!:External Declarations, Common Blocks and Data Statements
!
     Common/USRI00P/ IOFSET
     Common/WEIGHTS/ PROOT(NCMAX),WQ(NCMAX),AX(NCMAX,NCMAX),BXX(NCMAX,NCMAX)
     Common/USRR01P/
R,ALFA,PSC,TSC,DEPTH,DZ,CP,CM,ROC,POROI,KABSI,CLSP,PW,PGRAD,TGRAD,OBGR
    *           AD,TRES,POB,VL1,PL1,PC1,TC1,CONV1,CONV2,CONV3,CONV4,VL2,PL2,PC2,TC2,PM
    *
AX,VMAX,V,H,KRGC,KRWC,QG1,QW1,QG2,QW2,SG2,ROSC,CW,KRCW,KRCG,SWIRR,SGIR
    *           R,RW,RE,SKIN,TEMP,PGI,S,LOGR,PWELL,SWELL,PCGW,PORO,KABS,SWN,KRG,KRW,DV
    *           T,DVP,BG,BW,DA,BOB,MW,MW1,MW2,Z,ZZ,Z1,Z2,DZDPG,RO,KK1,XK1,YK1,VISG,VIS
    *           W,A,B,SG1,QGSP,QWSP,QTSP,A11,A12,A13,A21,A22,A23,VL3,VL3IRR,PO,CBET,PC
    *           ,TC,VIRR,TAO,DI,AA1,AA2,AA3,Y11,AB1,BB1,BB2,BB3,BB4,BB5,BB6,BB7,BB8,CO
    *           EFF1,COEFF2,DPGDR,DVP1,DBW,DPORO,DBG,CG,CG1,CG2,ALFA1,FLOWGP,FLOWWP,SG
    *           P,DSGDR,VL10,VL20,VL30,PGQ,ADSA,K1,K2,FLOWGI,FLOWWI,SGI,PG1,XG1,DPOROD
    *
PG,DKABSDPORO,DSWNDSG,DSWNDSW,DKRGDSWN,DKRWDSWN,EU,DZFAC,DZFAC1,DZFAC2
    *
,D2ZDPG2,D2ZDPG21,D2ZDPG22,D2ZDPG2T,DPCGWDSW,DPCGW2DSW2,DBWDPW,DBGDPG,
    *
DVISGDROG,DROGDPG,DVISWDPW,DRSWDPG,D2BGDPG2,ADSCO2,ADSCH4,BULKCO2,BULK
    *           CH4,CO2IN,CH4IN,H2OIN,EKO01,EKO02,EKO03,EKO04,EKO05,EKO06,EKO07,EKO08,
    *           EKO09,EKO10,EKO11,EKO12,EKO13,EKO14,EKO15,EKO16,EKO17,EKO18,EKO19,EKO2
    *           0,EKO21,EKO22,EKO23,EKO24,EKO25,EKO26,EKO27,EKO28,EKO29,EKO30,DAE01,DA
    *           E02,DAE03,DAE04,DAE05,DAE06,DAE07,DAE08,DAE09,DAE10,DAE11,DAE12,DAE13,
    *           DAE14,DAE15,DAE16,DAE17,DAE18,DAE19,DAE20,RSWE01,RSWE02,RSWE03,RSWE04,
    *           RSWE05,RSWE06,RSWE07,RSWE08,RSWE09,RSWE10,RSWE11,RSWE12,RSWE13,RSWE14,
    *           RSWE15,RSWE16,RSWE17,RSWE18,RSWE19,RSWE20,RSWE21,RSWE22,RSWE23,RSWE24,
    *           RSWE25,RSWE26,RSWE27,RSWE28,RSWE29,RSWE30,RSWE31,RSWE32,RSWE33,RSWE34,
    *           RSWE35,RSWE36,C11,C12,C13,C14,C15,C16,C17,C21,C22,C23,C24,C25,C26,C27,
    *           C31,C32,C33,C34,C35,C36,C37,FM1,FM2,FM3,FM4,CE11,CE12,CE13,CE21,CE22,C
    *           E23,CE31,CE32,CE33,CE41,CE42,CE43,CE51,CE52,CE53,RSW1,RSW2,DRSW1DPG,DR
    *
SW2DPG,QGDARCY,QWDARCY,QWDARCY1,QGDARCY1L,QWDARCY2,QGDA1,QGDA2,QGDA11,
    *
QGDA12,QGDA21,QGDA22,QGDA1R,QGDA2R,QGDA11R,QGDA12R,QGDA21R,QGDA22R,QGR
    *
SW1,QGRSW2,QGRSW11,QGRSW12,QGRSW21,QGRSW22,QGRSW1R,QGRSW2R,QGRSW11R,QG
    *
RSW12R,QGRSW21R,QGRSW22R,QGDARCY1,QWDARCY11,QWDARCY21,QGDA111,QGDA121,
    *
QGDA211,QGDA221,QGRSW111,QGRSW121,QGRSW211,QGRSW221,QGDARCY1R,QWDARCY1
    *
1R,QWDARCY21R,QGDA111R,QGDA121R,QGDA211R,QGDA221R,QGRSW111R,QGRSW121R,
    *           QGRSW211R,QGRSW221R,ALI,ALI1,ALI11,ALI2,ALI22,ALI3,ALI4,XR1,XR2,XRN,MO
```

```
     *         ISTURE,ASH,MULTIPLIER,WI1,WI2,QSP,CC,QWELL,PGL,SGL,PGR,PG,SG,Y1,ZAMAN
     *         ,QGIN ,QWIN ,QGPRO ,QWPRO ,ADSRT1 ,ADSRT2 ,ADSRT3 ,PWELL1 ,QGCUM ,QWCU
     *         M ,ADSRATE1,ADSRATE2,ADSRATE3,QG1ATWELL,RR,PWW,UP ,UPX ,UPXX ,ZOC ,WOC
     *         ,AOC ,BOC
      Common/USRI01P/ GASCOMP,FLAG1,J1,J5,ITER1,Iloop,BC,IWELL,QB,II,NSUB,ISYM
!
!:Model Equations Section: Initial Values
!:Retrieve the Sensitivity Parameters
!
      U(1,Igrid,1)=PGI
      U(2,Igrid,1)=PGI
      U(3,Igrid,1)=SGI
      U(4,Igrid,1)=Y11
      Do J=1,NPE
      U(4+J,Igrid,1)=VL1*K1*Y11*PGI/(1.0+K1*Y11*PGI+K2*(1.0-Y11)*PGI)
      U(8+J,Igrid,1)=VL2*K2*(1.0-Y11)*PGI/(1.0+K1*Y11*PGI+K2*(1.0-Y11)*PGI)
      U(12+J,Igrid,1)=VL3
      EndDo
      If(JPAR.EQ.1)Return
!
!:End of Subroutine ISUBP
!
      Return
      End

      Subroutine FPSUBP(T,Xgrid,X,Neq,Ugrid,U,Ux,Uxx,F,RPAR,IPAR,Ieform,Ires,Ielem,Igrid,Ngrid)
      Implicit Real*8(A-H,O-Z)
      Integer NCP
      Integer NPE
      Parameter (NCP=2,NPE=NCP+2)
      Parameter (NCMAX=10,Zero=0.0D0,One=1.0D0,Pi=3.141592653589793D0)
!
!:Variable Declaration Statements section
!
      Dimension F(Neq),U(Neq),Ux(Neq),Uxx(Neq),RPAR(0:*),IPAR(0:*)
      Dimension Xgrid(*),Ugrid(Neq,*)
      Real*8 R,ALFA,PSC,TSC,DEPTH,DZ,CP,CM,ROC,POROI,KABSI,CLSP,PW,PGRAD,TGRAD,OBGR
     *    AD,TRES,POB,VL1,PL1,PC1,TC1,CONV1,CONV2,CONV3,CONV4,VL2,PL2,PC2,TC2,PM
     *    AX,VMAX,V,H,KRGC,KRWC,QG1,QW1,QG2,QW2,SG2,ROSC,CW,KRCW,KRCG,SWIRR,SGIR
     *    R,RW,RE,SKIN,TEMP,PGI,S,LOGR,PWELL,SWELL,PCGW,PORO,KABS,SWN,KRG,KRW,DV
     *    T,DVP,BG,BW,DA,BOB,MW,MW1,MW2,Z,ZZ,Z1,Z2,DZDPG,RO,KK1,XK1,YK1,VISG,VIS
     *    W,A,B,SG1,QGSP,QWSP,QTSP,A11,A12,A13,A21,A22,A23,VL3,VL3IRR,PO,CBET,PC
     *    ,TC,VIRR,TAO,DI,AA1,AA2,AA3,Y11,AB1,BB1,BB2,BB3,BB4,BB5,BB6,BB7,BB8,CO
     *    EFF1,COEFF2,DPGDR,DVP1,DBW,DPORO,DBG,CG,CG1,CG2,ALFA1,FLOWGP,FLOWWP,SG
     *    P,DSGDR,VL10,VL20,VL30,PGQ,ADSA,K1,K2,FLOWGI,FLOWWI,SGI,PG1,XG1,DPOROD
     *
PG,DKABSDPORO,DSWNDSG,DSWNDSW,DKRGDSWN,DKRWDSWN,EU,DZFAC,DZFAC1,DZFAC2
     *    ,D2ZDPG2,D2ZDPG21,D2ZDPG22,D2ZDPG2T,DPCGWDSW,DPCGW2DSW2,DBWDPW,DBGDPG,
     *
DVISGDROG,DROGDPG,DVISWDPW,DRSWDPG,D2BGDPG2,ADSCO2,ADSCH4,BULKCO2,BULK
     *    CH4,CO2IN,CH4IN,H2OIN,EKO01,EKO02,EKO03,EKO04,EKO05,EKO06,EKO07,EKO08,
     *    EKO09,EKO10,EKO11,EKO12,EKO13,EKO14,EKO15,EKO16,EKO17,EKO18,EKO19,EKO2
     *    0,EKO21,EKO22,EKO23,EKO24,EKO25,EKO26,EKO27,EKO28,EKO29,EKO30,DAE01,DA
     *    E02,DAE03,DAE04,DAE05,DAE06,DAE07,DAE08,DAE09,DAE10,DAE11,DAE12,DAE13,
     *    DAE14,DAE15,DAE16,DAE17,DAE18,DAE19,DAE20,RSWE01,RSWE02,RSWE03,RSWE04,
     *    RSWE05,RSWE06,RSWE07,RSWE08,RSWE09,RSWE10,RSWE11,RSWE12,RSWE13,RSWE14,
```

```
   *     RSWE15,RSWE16,RSWE17,RSWE18,RSWE19,RSWE20,RSWE21,RSWE22,RSWE23,RSWE24,
   *     RSWE25,RSWE26,RSWE27,RSWE28,RSWE29,RSWE30,RSWE31,RSWE32,RSWE33,RSWE34,
   *     RSWE35,RSWE36,C11,C12,C13,C14,C15,C16,C17,C21,C22,C23,C24,C25,C26,C27,
   *     C31,C32,C33,C34,C35,C36,C37,FM1,FM2,FM3,FM4,CE11,CE12,CE13,CE21,CE22,C
   *     E23,CE31,CE32,CE33,CE41,CE42,CE43,CE51,CE52,CE53,RSW1,RSW2,DRSW1DPG,DR
   *
SW2DPG,QGDARCY,QWDARCY,QWDARCY1,QGDARCY1L,QWDARCY2,QGDA1,QGDA2,QGDA11,
   *     QGDA12,QGDA21,QGDA22,QGDA1R,QGDA2R,QGDA11R,QGDA12R,QGDA21R,QGDA22R,QGR
   *     SW1,QGRSW2,QGRSW11,QGRSW12,QGRSW21,QGRSW22,QGRSW1R,QGRSW2R,QGRSW11R,QG
   *     RSW12R,QGRSW21R,QGRSW22R,QGDARCY1,QWDARCY11,QWDARCY21,QGDA111,QGDA121,
   *     QGDA211,QGDA221,QGRSW111,QGRSW121,QGRSW211,QGRSW221,QGDARCY1R,QWDARCY1
   *     1R,QWDARCY21R,QGDA111R,QGDA121R,QGDA211R,QGDA221R,QGRSW111R,QGRSW121R,
   *     QGRSW211R,QGRSW221R,ALI,ALI1,ALI11,ALI2,ALI22,ALI3,ALI4,XR1,XR2,XRN,MO
   *     ISTURE,ASH,MULTIPLIER,WI1,WI2,QSP,CC,QWELL,PGL,SGL,PGR,PG,SG,Y1,ZAMAN(
   *     1002),QGIN(1002),QWIN(1002),QGPRO(1002),QWPRO(1002),ADSRT1(1002),ADSRT
   *     2(1002),ADSRT3(1002),PWELL1(1002),QGCUM(1002),QWCUM(1002),ADSRATE1,ADS
   *     RATE2,ADSRATE3,QG1ATWELL,RR,PWW,UP(3,4),UPX(3,4),UPXX(3,4),ZOC(10),WOC
   *     (10),AOC(10,10),BOC(10,10)
      Integer GASCOMP,FLAG1,J1,J5,ITER1,Iloop,BC,IWELL,QB,II,NSUB,ISYM
!
!:External Declarations, Common Blocks and Data Statements
!
      Common/USRI00P/ IOFSET
      Common/WEIGHTS/ PROOT(NCMAX),WQ(NCMAX),AX(NCMAX,NCMAX),BXX(NCMAX,NCMAX)
      Common/USRR01P/
R,ALFA,PSC,TSC,DEPTH,DZ,CP,CM,ROC,POROI,KABSI,CLSP,PW,PGRAD,TGRAD,OBGR
   *           AD,TRES,POB,VL1,PL1,PC1,TC1,CONV1,CONV2,CONV3,CONV4,VL2,PL2,PC2,TC2,PM
   *
AX,VMAX,V,H,KRGC,KRWC,QG1,QW1,QG2,QW2,SG2,ROSC,CW,KRCW,KRCG,SWIRR,SGIR
   *           R,RW,RE,SKIN,TEMP,PGI,S,LOGR,PWELL,SWELL,PCGW,PORO,KABS,SWN,KRG,KRW,DV
   *           T,DVP,BG,BW,DA,BOB,MW,MW1,MW2,Z,ZZ,Z1,Z2,DZDPG,RO,KK1,XK1,YK1,VISG,VIS
   *           W,A,B,SG1,QGSP,QWSP,QTSP,A11,A12,A13,A21,A22,A23,VL3,VL3IRR,PO,CBET,PC
   *           ,TC,VIRR,TAO,DI,AA1,AA2,AA3,Y11,AB1,BB1,BB2,BB3,BB4,BB5,BB6,BB7,BB8,CO
   *           EFF1,COEFF2,DPGDR,DVP1,DBW,DPORO,DBG,CG,CG1,CG2,ALFA1,FLOWGP,FLOWWP,SG
   *           P,DSGDR,VL10,VL20,VL30,PGQ,ADSA,K1,K2,FLOWGI,FLOWWI,SGI,PG1,XG1,DPOROD
   *
PG,DKABSDPORO,DSWNDSG,DSWNDSW,DKRGDSWN,DKRWDSWN,EU,DZFAC,DZFAC1,DZFAC2
   *
,D2ZDPG2,D2ZDPG21,D2ZDPG22,D2ZDPG2T,DPCGWDSW,DPCGW2DSW2,DBWDPW,DBGDPG,
   *
DVISGDROG,DROGDPG,DVISWDPW,DRSWDPG,D2BGDPG2,ADSCO2,ADSCH4,BULKCO2,BULK
   *           CH4,CO2IN,CH4IN,H2OIN,EKO01,EKO02,EKO03,EKO04,EKO05,EKO06,EKO07,EKO08,
   *           EKO09,EKO10,EKO11,EKO12,EKO13,EKO14,EKO15,EKO16,EKO17,EKO18,EKO19,EKO2
   *           0,EKO21,EKO22,EKO23,EKO24,EKO25,EKO26,EKO27,EKO28,EKO29,EKO30,DAE01,DA
   *           E02,DAE03,DAE04,DAE05,DAE06,DAE07,DAE08,DAE09,DAE10,DAE11,DAE12,DAE13,
   *           DAE14,DAE15,DAE16,DAE17,DAE18,DAE19,DAE20,RSWE01,RSWE02,RSWE03,RSWE04,
   *           RSWE05,RSWE06,RSWE07,RSWE08,RSWE09,RSWE10,RSWE11,RSWE12,RSWE13,RSWE14,
   *           RSWE15,RSWE16,RSWE17,RSWE18,RSWE19,RSWE20,RSWE21,RSWE22,RSWE23,RSWE24,
   *           RSWE25,RSWE26,RSWE27,RSWE28,RSWE29,RSWE30,RSWE31,RSWE32,RSWE33,RSWE34,
   *           RSWE35,RSWE36,C11,C12,C13,C14,C15,C16,C17,C21,C22,C23,C24,C25,C26,C27,
   *           C31,C32,C33,C34,C35,C36,C37,FM1,FM2,FM3,FM4,CE11,CE12,CE13,CE21,CE22,C
   *           E23,CE31,CE32,CE33,CE41,CE42,CE43,CE51,CE52,CE53,RSW1,RSW2,DRSW1DPG,DR
   *
SW2DPG,QGDARCY,QWDARCY,QWDARCY1,QGDARCY1L,QWDARCY2,QGDA1,QGDA2,QGDA11,
   *
QGDA12,QGDA21,QGDA22,QGDA1R,QGDA2R,QGDA11R,QGDA12R,QGDA21R,QGDA22R,QGR
```

```
    *
SW1,QGRSW2,QGRSW11,QGRSW12,QGRSW21,QGRSW22,QGRSW1R,QGRSW2R,QGRSW11R,QG
    *
RSW12R,QGRSW21R,QGRSW22R,QGDARCY1,QWDARCY11,QWDARCY21,QGDA111,QGDA121,
    *
QGDA211,QGDA221,QGRSW111,QGRSW121,QGRSW211,QGRSW221,QGDARCY1R,QWDARCY1
    *
1R,QWDARCY21R,QGDA111R,QGDA121R,QGDA211R,QGDA221R,QGRSW111R,QGRSW121R,
    *            QGRSW211R,QGRSW221R,ALI,ALI1,ALI11,ALI2,ALI22,ALI3,ALI4,XR1,XR2,XRN,MO
    *            ISTURE,ASH,MULTIPLIER,WI1,WI2,QSP,CC,QWELL,PGL,SGL,PGR,PG,SG,Y1,ZAMAN
    *            ,QGIN ,QWIN ,QGPRO ,QWPRO ,ADSRT1 ,ADSRT2 ,ADSRT3 ,PWELL1 ,QGCUM ,QWCU
    *            M ,ADSRATE1,ADSRATE2,ADSRATE3,QG1ATWELL,RR,PWW,UP ,UPX ,UPXX ,ZOC ,WOC
    *            ,AOC ,BOC
    Common/USRI01P/ GASCOMP,FLAG1,J1,J5,ITER1,Iloop,BC,IWELL,QB,II,NSUB,ISYM
!
!:Model Equations Section
!:Retrieve Sensitivity Parameters
!
    PORO=POROI-POROI*(CP*(POB-U(2)))
    DPORODPG=POROI*CP
    KABS=KABSI*(PORO/POROI)**3
    DKABSDPORO=3*KABS/PORO
    SW=1.0-U(3)
    SWN=(SW-SWIRR)/(1-SGIRR-SWIRR)
    DSWNDSW=1.0/(1-SGIRR-SWIRR)
    KRG=KRCG*(1-SWN**2)*(1-SWN)**2
    KRW=KRCW*SWN**4
    If (KRG.LE.0.0.OR.KRW.LE.0.0) Then
    KRG=0.0
    KRW=0.0
    EndIf
    If (KRG.GE.1.0.OR.KRW.GE.1.0) Then
    KRG=1.0
    KRW=1.0
    EndIf
    DKRGDSWN=-2.0*KRG*(2.0*SWN+1.0)/(1.0-SWN*SWN)
    DKRWDSWN=4.0*KRW/SWN
    If (SW.LE.SWIRR) Then
    SW=1.001*SWIRR
    EndIf
    PCGW=1.0/(13.448*(SW-SWIRR))**0.5
    DPCGWDSW=-0.5*13.448/(13.448*(SW-SWIRR))**1.5
    DPCGW2DSW2=0.5*1.5*13.448*13.448/(13.448*(SW-SWIRR))**2.5
    PW=U(2)-PCGW
    DVT=-1.0001E-02+1.33391E-04*TEMP+5.50654E-07*TEMP*TEMP
    DVP=-1.95301E-9*PW*TEMP-1.72834E-13*PW**2*TEMP-3.58922E-7*PW-2.25341E-10*PW**2
    BW=(1+DVT)*(1+DVP)
    DBWDPW=(1+DVT)*(-1.95301E-9*TEMP-2.0*1.72834E-13*PW*TEMP-3.58922E-7-2.0*2.25341E-10*PW)
    GASCOMP=1
    Call COMPFACTOR(U,Ieform,RPAR)
    Z1=ZZ
    MW1=MW
    CG1=CG
    DZFAC1=DZFAC
    D2ZDPG21=D2ZDPG2
    TEMP=TEMP-460
```

```
    GASCOMP=2
    Call COMPFACTOR(U,Ieform,RPAR)
    Z2=ZZ
    MW2=MW
    CG2=CG
    DZFAC2=DZFAC
    D2ZDPG22=D2ZDPG2
    Z=U(4)*Z1+(1.0-U(4))*Z2
    MW=U(4)*MW1+(1.0-U(4))*MW2
    CG=U(4)*CG1+(1.0-U(4))*CG2
    DZDPG=U(4)*DZFAC1+(1.0-U(4))*DZFAC2
    D2ZDPG2T=U(4)*D2ZDPG21+(1.0-U(4))*D2ZDPG22
    BG=PSC*Z*(TEMP)/((TSC+460)*U(2))
    DBGDPG=-BG*CG
    D2BGDPG2=BG*CG**2+BG/(U(2)*U(2))-BG/(Z*Z)*DZDPG**2+BG/Z*D2ZDPG2T
    TEMP=TEMP-460
    TEMP=TEMP+460
    RO=1.4935E-3*U(2)*MW/(Z*TEMP)
    KK1=(9.4+0.02*MW)*TEMP**1.5/(209+19*MW+TEMP)
    XK1=3.5+986/TEMP+0.01*MW
    YK1=2.4-0.2*XK1
    VISG=1.0E-4*KK1*exp(XK1*RO**YK1)
    DROGDPG=RO*CG
    DVISGDROG=VISG*XK1*YK1*RO**(YK1-1.0)
    TEMP=TEMP-460
    A=109.574-8.40564*S+0.313314*S**2+8.72213E-3*S**3
    B=-1.12166+2.63951E-2*S-6.79461E-4*S**2-5.47119E-5*S**3+1.55586E-6*S**4
    VISW=A*TEMP**B*(0.9994+4.0295E-5*PW+3.1062E-9*PW**2)
    DVISWDPW=A*TEMP**B*(4.0295E-5+2.0*3.1062E-9*PW)
    AT1=8.15839-6.12265E-2*TEMP+1.91663E-4*TEMP**2-2.1654E-7*TEMP**3
    AT2=1.01021E-2-7.44241E-5*TEMP+3.05553E-7*TEMP**2-2.94883E-10*TEMP**3
    AT3=-1.0E-7*(9.02505-0.130237*TEMP+8.53425E-4*TEMP**2-2.34122E-6*TEMP**3+2.37049E-
9*TEMP**4)
    RSW1=U(4)*(AT1+AT2*(U(2))+AT3*(U(2))**2)
    RSW2=(1.0-U(4))*(AT1+AT2*(U(2))+AT3*(U(2))**2)
    DRSW1DPG=U(4)*(AT2+2.0*AT3*U(2))
    DRSW2DPG=(1.0-U(4))*(AT2+2.0*AT3*U(2))
    EKO01=(U(4)*ALFA*ALFA1*KABS*KRG)/(VISG*BG*RE*RE)
    EKO02=(U(4)*ALFA*ALFA1*KRG)/(VISG*BG*RE*RE)*DKABSDPORO*DPORODPG
    EKO03=(U(4)*ALFA*ALFA1*KABS*KRG)/(VISG*VISG*BG*RE*RE)*DVISGDROG*DROGDPG
    EKO04=(U(4)*ALFA*ALFA1*KABS*KRG)/(VISG*BG*BG*RE*RE)*DBGDPG
    EKO05=(EKO02-EKO03-EKO04)
    EKO06=(U(4)*ALFA*ALFA1*KABS)/(VISG*BG*RE*RE)*DKRGDSWN*DSWNDSW
    EKO07=(ALFA*ALFA1*KABS*KRG)/(VISG*BG*RE*RE)
    EKO08=((1.0-U(4))*ALFA*ALFA1*KABS*KRG)/(VISG*BG*RE*RE)
    EKO09=((1.0-U(4))*ALFA*ALFA1*KRG)/(VISG*BG*RE*RE)*DKABSDPORO*DPORODPG
    EKO10=((1.0-U(4))*ALFA*ALFA1*KABS*KRG)/(VISG*VISG*BG*RE*RE)*DVISGDROG*DROGDPG
    EKO11=((1.0-U(4))*ALFA*ALFA1*KABS*KRG)/(VISG*BG*BG*RE*RE)*DBGDPG
    EKO12=(EKO09-EKO10-EKO11)
    EKO13=((1.0-U(4))*ALFA*ALFA1*KABS)/(VISG*BG*RE*RE)*DKRGDSWN*DSWNDSW
    EKO14=(ALFA*ALFA1*KABS*KRG)/(VISG*BG*RE*RE)
    EKO15=FM1*(ALFA*KABS*KRW)/(VISW*BW*RE*RE)
    EKO16=FM1*(ALFA*KRW)/(VISW*BW*RE*RE)*DKABSDPORO*DPORODPG
    EKO17=FM1*(ALFA*KABS*KRW)/(VISW*VISW*BW*RE*RE)*DVISWDPW
    EKO18=FM1*(ALFA*KABS*KRW)/(VISW*BW*BW*RE*RE)*DBWDPW
    EKO19=FM1*(EKO16-EKO17-EKO18)
```

```
    EKO20=FM1*(ALFA*KRW)/(VISW*BW*RE*RE)*DKABSDPORO*DPORODPG*DPCGWDSW
    EKO21=FM1*(ALFA*KABS)/(VISW*BW*RE*RE)*DKRWDSWN*DSWNDSW
    EKO22=FM1*2.0*DPCGWDSW*(ALFA*KABS*KRW)/(VISW*VISW*BW*RE*RE)*DVISWDPW
    EKO23=FM1*2.0*DPCGWDSW*(ALFA*KABS*KRW)/(VISW*BW*BW*RE*RE)*DBWDPW
    EKO24=FM1*(EKO20-EKO21-EKO22-EKO23)
    EKO25=FM1*(ALFA*KABS*KRW)/(VISW*VISW*BW*RE*RE)*DVISWDPW*DPCGWDSW**2
    EKO26=FM1*(ALFA*KABS*KRW)/(VISW*BW*BW*RE*RE)*DBWDPW*DPCGWDSW**2
    EKO27=FM1*(ALFA*KABS)/(VISW*BW*RE*RE)*DKRWDSWN*DSWNDSW*DPCGWDSW
    EKO28=FM1*(ALFA*KABS*KRW)/(VISW*BW*RE*RE)*DPCGW2DSW2
    EKO29=FM1*(EKO25+EKO26+EKO27+EKO28)
    EKO30=FM1*(ALFA*KABS*KRW)/(VISW*BW*RE*RE)*DPCGWDSW
    DAE01=FM2*U(4)*DA*U(3)/(BG*BG*RE*RE)*DBGDPG
    DAE02=FM2*2.0*U(4)*DA*U(3)/(BG*RE*RE)*DBGDPG**2
    DAE03=FM2*U(4)*DA*U(3)/(BG*BG*RE*RE)*D2BGDPG2
    DAE04=FM2*(DAE02-DAE03)
    DAE05=FM2*U(4)*DA/(BG*BG*RE*RE)*DBGDPG
    DAE06=FM2*U(4)*DA/(BG*BG*RE*RE)*DBGDPG
    DAE07=FM2*(DAE05+DAE06)
    DAE08=FM2*DA*U(3)/(BG*BG*RE*RE)*DBGDPG
    DAE09=FM2*DA/(BG*RE*RE)
    DAE10=FM2*U(4)*DA/(BG*RE*RE)
    DAE11=FM2*(1.0-U(4))*DA*U(3)/(BG*BG*RE*RE)*DBGDPG
    DAE12=FM2*2.0*(1.0-U(4))*DA*U(3)/(BG*RE*RE)*DBGDPG**2
    DAE13=FM2*(1.0-U(4))*DA*U(3)/(BG*BG*RE*RE)*D2BGDPG2
    DAE14=FM2*(DAE12-DAE13)
    DAE15=FM2*(1.0-U(4))*DA/(BG*BG*RE*RE)*DBGDPG
    DAE16=FM2*(1.0-U(4))*DA/(BG*BG*RE*RE)*DBGDPG
    DAE17=FM2*(DAE15+DAE16)
    DAE18=FM2*DA*U(3)/(BG*BG*RE*RE)*DBGDPG
    DAE19=FM2*DA/(BG*RE*RE)
    DAE20=FM2*(1.0-U(4))*DA/(BG*RE*RE)
    RSWE01=FM3*FM1*(RSW1*ALFA*KABS*KRW)/(VISW*BW*RE*RE)
    RSWE02=FM3*FM1*(ALFA*KABS*KRW)/(VISW*BW*RE*RE)*DRSW1DPG
    RSWE03=FM3*FM1*(RSW1*ALFA*KRW)/(VISW*BW*RE*RE)*DKABSDPORO*DPORODPG
    RSWE04=FM3*FM1*(RSW1*ALFA*KABS*KRW)/(VISW*VISW*BW*RE*RE)*DVISWDPW
    RSWE05=FM3*FM1*(RSW1*ALFA*KABS*KRW)/(VISW*BW*BW*RE*RE)*DBWDPW
    RSWE06=FM3*FM1*(RSWE02+RSWE03-RSWE04-RSWE05)
    RSWE07=FM3*FM1*(ALFA*KABS*KRW)/(VISW*BW*RE*RE)*DRSW1DPG*DPCGWDSW

RSWE08=FM3*FM1*(RSW1*ALFA*KRW)/(VISW*BW*RE*RE)*DKABSDPORO*DPORODPG*DPCGWDS
W
    RSWE09=FM3*FM1*(RSW1*ALFA*KABS)/(VISW*BW*RE*RE)*DKRWDSWN*DSWNDSW

RSWE10=FM3*FM1*2.0*DPCGWDSW*(RSW1*ALFA*KABS*KRW)/(VISW*VISW*BW*RE*RE)*DVISWD
PW

RSWE11=FM3*FM1*2.0*DPCGWDSW*(RSW1*ALFA*KABS*KRW)/(VISW*BW*BW*RE*RE)*DBWDPW
    RSWE12=FM3*FM1*(RSWE07+RSWE08-RSWE09-RSWE10-RSWE11)

RSWE13=FM3*FM1*(RSW1*ALFA*KABS*KRW)/(VISW*VISW*BW*RE*RE)*DVISWDPW*DPCGWDSW*
*2

RSWE14=FM3*FM1*(RSW1*ALFA*KABS*KRW)/(VISW*BW*BW*RE*RE)*DBWDPW*DPCGWDSW**2

RSWE15=FM3*FM1*(RSW1*ALFA*KABS)/(VISW*BW*RE*RE)*DKRWDSWN*DSWNDSW*DPCGWDSW
    RSWE16=FM3*FM1*(RSW1*ALFA*KABS*KRW)/(VISW*BW*RE*RE)*DPCGW2DSW2
```

```
      RSWE17=FM3*FM1*(RSWE13+RSWE14+RSWE15+RSWE16)
      RSWE18=FM3*FM1*(RSW1*ALFA*KABS*KRW)/(VISW*BW*RE*RE)*DPCGWDSW
      RSWE19=FM3*FM1*(RSW2*ALFA*KABS*KRW)/(VISW*BW*RE*RE)
      RSWE20=FM3*FM1*(ALFA*KABS*KRW)/(VISW*BW*RE*RE)*DRSW2DPG
      RSWE21=FM3*FM1*(RSW2*ALFA*KRW)/(VISW*BW*RE*RE)*DKABSDPORO*DPORODPG
      RSWE22=FM3*FM1*(RSW2*ALFA*KABS*KRW)/(VISW*VISW*BW*RE*RE)*DVISWDPW
      RSWE23=FM3*FM1*(RSW2*ALFA*KABS*KRW)/(VISW*BW*BW*RE*RE)*DBWDPW
      RSWE24=FM3*FM1*(RSWE20+RSWE21-RSWE22-RSWE23)
      RSWE25=FM3*FM1*(ALFA*KABS*KRW)/(VISW*BW*RE*RE)*DRSW2DPG*DPCGWDSW

RSWE26=FM3*FM1*(RSW2*ALFA*KRW)/(VISW*BW*RE*RE)*DKABSDPORO*DPORODPG*DPCGWDS
W
      RSWE27=FM3*FM1*(RSW2*ALFA*KABS)/(VISW*BW*RE*RE)*DKRWDSWN*DSWNDSW

RSWE28=FM3*FM1*2.0*DPCGWDSW*(RSW2*ALFA*KABS*KRW)/(VISW*VISW*BW*RE*RE)*DVISWD
PW

RSWE29=FM3*FM1*2.0*DPCGWDSW*(RSW2*ALFA*KABS*KRW)/(VISW*BW*BW*RE*RE)*DBWDPW
      RSWE30=FM3*FM1*(RSWE25+RSWE26-RSWE27-RSWE28-RSWE29)

RSWE31=FM3*FM1*(RSW2*ALFA*KABS*KRW)/(VISW*VISW*BW*RE*RE)*DVISWDPW*DPCGWDSW*
*2

RSWE32=FM3*FM1*(RSW2*ALFA*KABS*KRW)/(VISW*BW*BW*RE*RE)*DBWDPW*DPCGWDSW**2

RSWE33=FM3*FM1*(RSW2*ALFA*KABS)/(VISW*BW*RE*RE)*DKRWDSWN*DSWNDSW*DPCGWDSW
      RSWE34=FM3*FM1*(RSW2*ALFA*KABS*KRW)/(VISW*BW*RE*RE)*DPCGW2DSW2
      RSWE35=FM3*FM1*(RSWE31+RSWE32+RSWE33+RSWE34)
      RSWE36=FM3*FM1*(RSW2*ALFA*KABS*KRW)/(VISW*BW*RE*RE)*DPCGWDSW
      C11=EKO01-DAE01-RSWE01
      C12=EKO05+DAE04-RSWE06
      C13=-EKO06-DAE07-RSWE12
      C14=EKO07-DAE08+0.0
      C15=0.0+DAE09+0.0
      C16=0.0+0.0+RSWE17
      C17=0.0+DAE10-RSWE18
      C21=EKO08-DAE11-RSWE19
      C22=EKO12+DAE14-RSWE24
      C23=-EKO13-DAE17-RSWE30
      C24=-EKO14+DAE18+0.0
      C25=0.0-DAE19+0.0
      C26=0.0+0.0+RSWE35
      C27=0.0+DAE20-RSWE36
      C31=EKO15+0.0+0.0
      C32=EKO19+0.0+0.0
      C33=EKO24+0.0+0.0
      C34=0.0+0.0+0.0
      C35=0.0+0.0+0.0
      C36=-EKO29+0.0+0.0
      C37=EKO30+0.0+0.0
      Do J=1,NPE
      UP(1,J)=U(4+J)
      UP(2,J)=U(8+J)
      UP(3,J)=U(12+J)
      EndDo
      Call UsrEvalUx(NSUB,NCP,ISYM,UP,UPX,AOC)
```

```
      Call UsrEvalUxx(NSUB,NCP,ISYM,UP,UPXX,BOC)
      ADSRATE1=-(1.0-PORO)*A11*UPX(1,NPE)
      ADSRATE2=-(1.0-PORO)*A12*UPX(2,NPE)
      ADSRATE3=-(1.0-PORO)*A13*UPX(3,NPE)
      F(1)=Ux(1)

F(2)=C11*Uxx(2)+C12*Ux(2)**2+C13*Ux(2)*Ux(3)+C14*Ux(2)*Ux(4)+C15*Ux(3)*Ux(4)+C16*Ux(3)**2+C1
7*Uxx(3)+ADSRATE1

F(3)=C21*Uxx(2)+C22*Ux(2)**2+C23*Ux(2)*Ux(3)+C24*Ux(2)*Ux(4)+C25*Ux(3)*Ux(4)+C26*Ux(3)**2+C2
7*Uxx(3)+ADSRATE2

F(4)=C31*Uxx(2)+C32*Ux(2)**2+C33*Ux(2)*Ux(3)+C34*Ux(2)*Ux(4)+C35*Ux(3)*Ux(4)+C36*Ux(3)**2+C3
7*Uxx(3)
      F(4+1)=UPX(1,1)
      F(8+1)=UPX(2,1)
      F(12+1)=UPX(3,1)
      Do J=2, NCP+1
      F(4+J)=A21*UPXX(1,J)
      F(8+J)=A22*UPXX(2,J)
      F(12+J)=A23*UPXX(3,J)
      EndDo
      F(4+NPE)=UP(1,NPE)-VL1*K1*U(4)*U(2)/(1.0+K1*U(4)*U(2)+K2*(1.0-U(4))*U(2))
      F(8+NPE)=UP(2,NPE)-VL2*K2*(1.0-U(4))*U(2)/(1.0+K1*U(4)*U(2)+K2*(1.0-U(4))*U(2))
      F(12+NPE)=UP(3,NPE)-VL3
!
!:End of Subroutine FPSUBP
!
      Return
      End

      Subroutine GPSUBP(T,Xgrid,X,Neq,Ugrid,U,Ux,G,RPAR,IPAR,Ieform,Ires,IBNRY,Ielem,Igrid,Ngrid)
      Implicit Real*8(A-H,O-Z)
      Integer NCP
      Integer NPE
      Parameter (NCP=2,NPE=NCP+2)
      Parameter (NCMAX=10,Zero=0.0D0,One=1.0D0,Pi=3.141592653589793D0)
!
!:Variable Declaration Statements section
!
      Dimension G(Neq),U(Neq),Ux(Neq),RPAR(0:*),IPAR(0:*)
      Dimension Xgrid(*),Ugrid(Neq,*)
      Real*8 R,ALFA,PSC,TSC,DEPTH,DZ,CP,CM,ROC,POROI,KABSI,CLSP,PW,PGRAD,TGRAD,OBGR
     *      AD,TRES,POB,VL1,PL1,PC1,TC1,CONV1,CONV2,CONV3,CONV4,VL2,PL2,PC2,TC2,PM
     *      AX,VMAX,V,H,KRGC,KRWC,QG1,QW1,QG2,QW2,SG2,ROSC,CW,KRCW,KRCG,SWIRR,SGIR
     *      R,RW,RE,SKIN,TEMP,PGI,S,LOGR,PWELL,SWELL,PCGW,PORO,KABS,SWN,KRG,KRW,DV
     *      T,DVP,BG,BW,DA,BOB,MW,MW1,MW2,Z,ZZ,Z1,Z2,DZDPG,RO,KK1,XK1,YK1,VISG,VIS
     *      W,A,B,SG1,QGSP,QWSP,QTSP,A11,A12,A13,A21,A22,A23,VL3,VL3IRR,PO,CBET,PC
     *      ,TC,VIRR,TAO,DI,AA1,AA2,AA3,Y11,AB1,BB1,BB2,BB3,BB4,BB5,BB6,BB7,BB8,CO
     *      EFF1,COEFF2,DPGDR,DVP1,DBW,DPORO,DBG,CG,CG1,CG2,ALFA1,FLOWGP,FLOWWP,SG
     *      P,DSGDR,VL10,VL20,VL30,PGQ,ADSA,K1,K2,FLOWGI,FLOWWI,SGI,PG1,XG1,DPOROD
     *
PG,DKABSDPORO,DSWNDSG,DSWNDSW,DKRGDSWN,DKRWDSWN,EU,DZFAC,DZFAC1,DZFAC2
     *      ,D2ZDPG2,D2ZDPG21,D2ZDPG22,D2ZDPG2T,DPCGWDSW,DPCGW2DSW2,DBWDPW,DBGDPG,
     *
DVISGDROG,DROGDPG,DVISWDPW,DRSWDPG,D2BGDPG2,ADSCO2,ADSCH4,BULKCO2,BULK
```

```
    *     CH4,CO2IN,CH4IN,H2OIN,EKO01,EKO02,EKO03,EKO04,EKO05,EKO06,EKO07,EKO08,
    *     EKO09,EKO10,EKO11,EKO12,EKO13,EKO14,EKO15,EKO16,EKO17,EKO18,EKO19,EKO2
    *     0,EKO21,EKO22,EKO23,EKO24,EKO25,EKO26,EKO27,EKO28,EKO29,EKO30,DAE01,DA
    *     E02,DAE03,DAE04,DAE05,DAE06,DAE07,DAE08,DAE09,DAE10,DAE11,DAE12,DAE13,
    *     DAE14,DAE15,DAE16,DAE17,DAE18,DAE19,DAE20,RSWE01,RSWE02,RSWE03,RSWE04,
    *     RSWE05,RSWE06,RSWE07,RSWE08,RSWE09,RSWE10,RSWE11,RSWE12,RSWE13,RSWE14,
    *     RSWE15,RSWE16,RSWE17,RSWE18,RSWE19,RSWE20,RSWE21,RSWE22,RSWE23,RSWE24,
    *     RSWE25,RSWE26,RSWE27,RSWE28,RSWE29,RSWE30,RSWE31,RSWE32,RSWE33,RSWE34,
    *     RSWE35,RSWE36,C11,C12,C13,C14,C15,C16,C17,C21,C22,C23,C24,C25,C26,C27,
    *     C31,C32,C33,C34,C35,C36,C37,FM1,FM2,FM3,FM4,CE11,CE12,CE13,CE21,CE22,C
    *     E23,CE31,CE32,CE33,CE41,CE42,CE43,CE51,CE52,CE53,RSW1,RSW2,DRSW1DPG,DR
    *
SW2DPG,QGDARCY,QWDARCY,QWDARCY1,QGDARCY1L,QWDARCY2,QGDA1,QGDA2,QGDA11,
    *     QGDA12,QGDA21,QGDA22,QGDA1R,QGDA2R,QGDA11R,QGDA12R,QGDA21R,QGDA22R,QGR
    *     SW1,QGRSW2,QGRSW11,QGRSW12,QGRSW21,QGRSW22,QGRSW1R,QGRSW2R,QGRSW11R,QG
    *     RSW12R,QGRSW21R,QGRSW22R,QGDARCY1,QWDARCY11,QWDARCY21,QGDA111,QGDA121,
    *     QGDA211,QGDA221,QGRSW111,QGRSW121,QGRSW211,QGRSW221,QGDARCY1R,QWDARCY1
    *     1R,QWDARCY21R,QGDA111R,QGDA121R,QGDA211R,QGDA221R,QGRSW111R,QGRSW121R,
    *     QGRSW211R,QGRSW221R,ALI,ALI1,ALI11,ALI2,ALI22,ALI3,ALI4,XR1,XR2,XRN,MO
    *     ISTURE,ASH,MULTIPLIER,WI1,WI2,QSP,CC,QWELL,PGL,SGL,PGR,PG,SG,Y1,ZAMAN(
    *     1002),QGIN(1002),QWIN(1002),QGPRO(1002),QWPRO(1002),ADSRT1(1002),ADSRT
    *     2(1002),ADSRT3(1002),PWELL1(1002),QGCUM(1002),QWCUM(1002),ADSRATE1,ADS
    *     RATE2,ADSRATE3,QG1ATWELL,RR,PWW,UP(3,4),UPX(3,4),UPXX(3,4),ZOC(10),WOC
    *     (10),AOC(10,10),BOC(10,10)
    Integer GASCOMP,FLAG1,J1,J5,ITER1,Iloop,BC,IWELL,QB,II,NSUB,ISYM
!
!:External Declarations, Common Blocks and Data Statements
!
    Common/USRI00P/ IOFSET
    Common/WEIGHTS/ PROOT(NCMAX),WQ(NCMAX),AX(NCMAX,NCMAX),BXX(NCMAX,NCMAX)
    Common/USRR01P/
R,ALFA,PSC,TSC,DEPTH,DZ,CP,CM,ROC,POROI,KABSI,CLSP,PW,PGRAD,TGRAD,OBGR
    *          AD,TRES,POB,VL1,PL1,PC1,TC1,CONV1,CONV2,CONV3,CONV4,VL2,PL2,PC2,TC2,PM
    *
AX,VMAX,V,H,KRGC,KRWC,QG1,QW1,QG2,QW2,SG2,ROSC,CW,KRCW,KRCG,SWIRR,SGIR
    *          R,RW,RE,SKIN,TEMP,PGI,S,LOGR,PWELL,SWELL,PCGW,PORO,KABS,SWN,KRG,KRW,DV
    *          T,DVP,BG,BW,DA,BOB,MW,MW1,MW2,Z,ZZ,Z1,Z2,DZDPG,RO,KK1,XK1,YK1,VISG,VIS
    *          W,A,B,SG1,QGSP,QWSP,QTSP,A11,A12,A13,A21,A22,A23,VL3,VL3IRR,PO,CBET,PC
    *          ,TC,VIRR,TAO,DI,AA1,AA2,AA3,Y11,AB1,BB1,BB2,BB3,BB4,BB5,BB6,BB7,BB8,CO
    *          EFF1,COEFF2,DPGDR,DVP1,DBW,DPORO,DBG,CG,CG1,CG2,ALFA1,FLOWGP,FLOWWP,SG
    *          P,DSGDR,VL10,VL20,VL30,PGQ,ADSA,K1,K2,FLOWGI,FLOWWI,SGI,PG1,XG1,DPOROD
    *
PG,DKABSDPORO,DSWNDSG,DSWNDSW,DKRGDSWN,DKRWDSWN,EU,DZFAC,DZFAC1,DZFAC2
    *
,D2ZDPG2,D2ZDPG21,D2ZDPG22,D2ZDPG2T,DPCGWDSW,DPCGW2DSW2,DBWDPW,DBGDPG,
    *
DVISGDROG,DROGDPG,DVISWDPW,DRSWDPG,D2BGDPG2,ADSCO2,ADSCH4,BULKCO2,BULK
    *          CH4,CO2IN,CH4IN,H2OIN,EKO01,EKO02,EKO03,EKO04,EKO05,EKO06,EKO07,EKO08,
    *          EKO09,EKO10,EKO11,EKO12,EKO13,EKO14,EKO15,EKO16,EKO17,EKO18,EKO19,EKO2
    *          0,EKO21,EKO22,EKO23,EKO24,EKO25,EKO26,EKO27,EKO28,EKO29,EKO30,DAE01,DA
    *          E02,DAE03,DAE04,DAE05,DAE06,DAE07,DAE08,DAE09,DAE10,DAE11,DAE12,DAE13,
    *          DAE14,DAE15,DAE16,DAE17,DAE18,DAE19,DAE20,RSWE01,RSWE02,RSWE03,RSWE04,
    *          RSWE05,RSWE06,RSWE07,RSWE08,RSWE09,RSWE10,RSWE11,RSWE12,RSWE13,RSWE14,
    *          RSWE15,RSWE16,RSWE17,RSWE18,RSWE19,RSWE20,RSWE21,RSWE22,RSWE23,RSWE24,
    *          RSWE25,RSWE26,RSWE27,RSWE28,RSWE29,RSWE30,RSWE31,RSWE32,RSWE33,RSWE34,
    *          RSWE35,RSWE36,C11,C12,C13,C14,C15,C16,C17,C21,C22,C23,C24,C25,C26,C27,
```

```
   *          C31,C32,C33,C34,C35,C36,C37,FM1,FM2,FM3,FM4,CE11,CE12,CE13,CE21,CE22,C
   *          E23,CE31,CE32,CE33,CE41,CE42,CE43,CE51,CE52,CE53,RSW1,RSW2,DRSW1DPG,DR
   *
SW2DPG,QGDARCY,QWDARCY,QWDARCY1,QGDARCY1L,QWDARCY2,QGDA1,QGDA2,QGDA11,
   *
QGDA12,QGDA21,QGDA22,QGDA1R,QGDA2R,QGDA11R,QGDA12R,QGDA21R,QGDA22R,QGR
   *
SW1,QGRSW2,QGRSW11,QGRSW12,QGRSW21,QGRSW22,QGRSW1R,QGRSW2R,QGRSW11R,QG
   *
RSW12R,QGRSW21R,QGRSW22R,QGDARCY1,QWDARCY11,QWDARCY21,QGDA111,QGDA121,
   *
QGDA211,QGDA221,QGRSW111,QGRSW121,QGRSW211,QGRSW221,QGDARCY1R,QWDARCY1
   *
1R,QWDARCY21R,QGDA111R,QGDA121R,QGDA211R,QGDA221R,QGRSW111R,QGRSW121R,
   *          QGRSW211R,QGRSW221R,ALI,ALI1,ALI11,ALI2,ALI22,ALI3,ALI4,XR1,XR2,XRN,MO
   *          ISTURE,ASH,MULTIPLIER,WI1,WI2,QSP,CC,QWELL,PGL,SGL,PGR,PG,SG,Y1,ZAMAN
   *          ,QGIN ,QWIN ,QGPRO ,QWPRO ,ADSRT1 ,ADSRT2 ,ADSRT3 ,PWELL1 ,QGCUM ,QWCU
   *          M ,ADSRATE1,ADSRATE2,ADSRATE3,QG1ATWELL,RR,PWW,UP ,UPX ,UPXX ,ZOC ,WOC
   *          ,AOC ,BOC
   Common/USRI01P/ GASCOMP,FLAG1,J1,J5,ITER1,Iloop,BC,IWELL,QB,II,NSUB,ISYM
!
!:Boundary Value Functions Section
!:Retrieve the Sensitivity Parameters
!

   Select Case (IBNRY)
   Case(1)
   PORO=POROI-POROI*(CP*(POB-U(2)))
   DPORODPG=POROI*CP
   KABS=KABSI*(PORO/POROI)**3
   DKABSDPORO=3*KABS/PORO
   SW=1.0-U(3)
   SWN=(SW-SWIRR)/(1-SGIRR-SWIRR)
   DSWNDSW=1.0/(1-SGIRR-SWIRR)
   KRG=KRCG*(1-SWN**2)*(1-SWN)**2
   KRW=KRCW*SWN**4
   If (KRG.LE.0.0.OR.KRW.LE.0.0) Then
   KRG=0.0
   KRW=0.0
   EndIf
   If (KRG.GE.1.0.OR.KRW.GE.1.0) Then
   KRG=1.0
   KRW=1.0
   EndIf
   DKRGDSWN=-2.0*KRG*(2.0*SWN+1.0)/(1.0-SWN*SWN)
   DKRWDSWN=4.0*KRW/SWN
   If (SW.LE.SWIRR) Then
   SW=1.001*SWIRR
   EndIf
   PCGW=1.0/(13.448*(SW-SWIRR))**0.5
   DPCGWDSW=-0.5*13.448/(13.448*(SW-SWIRR))**1.5
   DPCGW2DSW2=0.5*1.5*13.448*13.448/(13.448*(SW-SWIRR))**2.5
   PW=U(2)-PCGW
   DVT=-1.0001E-02+1.33391E-04*TEMP+5.50654E-07*TEMP*TEMP
   DVP=-1.95301E-9*PW*TEMP-1.72834E-13*PW**2*TEMP-3.58922E-7*PW-2.25341E-10*PW**2
   BW=(1+DVT)*(1+DVP)
```

```
      DBWDPW=(1+DVT)*(-1.95301E-9*TEMP-2.0*1.72834E-13*PW*TEMP-3.58922E-7-2.0*2.25341E-10*PW)
      GASCOMP=1
      Call COMPFACTOR(U,Ieform,RPAR)
      Z1=ZZ
      MW1=MW
      CG1=CG
      DZFAC1=DZFAC
      D2ZDPG21=D2ZDPG2
      TEMP=TEMP-460
      GASCOMP=2
      Call COMPFACTOR(U,Ieform,RPAR)
      Z2=ZZ
      MW2=MW
      CG2=CG
      DZFAC2=DZFAC
      D2ZDPG22=D2ZDPG2
      Z=U(4)*Z1+(1.0-U(4))*Z2
      MW=U(4)*MW1+(1.0-U(4))*MW2
      CG=U(4)*CG1+(1.0-U(4))*CG2
      DZDPG=U(4)*DZFAC1+(1.0-U(4))*DZFAC2
      D2ZDPG2T=U(4)*D2ZDPG21+(1.0-U(4))*D2ZDPG22
      BG=PSC*Z*(TEMP)/((TSC+460)*U(2))
      DBGDPG=-BG*CG
      D2BGDPG2=BG*CG**2+BG/(U(2)*U(2))-BG/(Z*Z)*DZDPG**2+BG/Z*D2ZDPG2T
      TEMP=TEMP-460
      TEMP=TEMP+460
      RO=1.4935E-3*U(2)*MW/(Z*TEMP)
      KK1=(9.4+0.02*MW)*TEMP**1.5/(209+19*MW+TEMP)
      XK1=3.5+986/TEMP+0.01*MW
      YK1=2.4-0.2*XK1
      VISG=1.0E-4*KK1*exp(XK1*RO**YK1)
      DROGDPG=RO*CG
      DVISGDROG=VISG*XK1*YK1*RO**(YK1-1.0)
      TEMP=TEMP-460
      A=109.574-8.40564*S+0.313314*S**2+8.72213E-3*S**3
      B=-1.12166+2.63951E-2*S-6.79461E-4*S**2-5.47119E-5*S**3+1.55586E-6*S**4
      VISW=A*TEMP**B*(0.9994+4.0295E-5*PW+3.1062E-9*PW**2)
      DVISWDPW=A*TEMP**B*(4.0295E-5+2.0*3.1062E-9*PW)
      AT1=8.15839-6.12265E-2*TEMP+1.91663E-4*TEMP**2-2.1654E-7*TEMP**3
      AT2=1.01021E-2-7.44241E-5*TEMP+3.05553E-7*TEMP**2-2.94883E-10*TEMP**3
      AT3=-1.0E-7*(9.02505-0.130237*TEMP+8.53425E-4*TEMP**2-2.34122E-6*TEMP**3+2.37049E-
   9*TEMP**4)
      RSW1=U(4)*(AT1+AT2*(U(2))+AT3*(U(2))**2)
      RSW2=(1.0-U(4))*(AT1+AT2*(U(2))+AT3*(U(2))**2)
      DRSW1DPG=U(4)*(AT2+2.0*AT3*U(2))
      DRSW2DPG=(1.0-U(4))*(AT2+2.0*AT3*U(2))
      G(1)=U(1)-PGI
      G(2)=U(2)-PWELL
      G(3)=U(3)-(1.0-1.0E-10)
      G(4)=U(4)-(1.0-1.0E-20)
      Do J=1,NPE
      UP(1,J)=U(4+J)
      UP(2,J)=U(8+J)
      UP(3,J)=U(12+J)
      EndDo
      Call UsrEvalUx(NSUB,NCP,ISYM,UP,UPX,AOC)
```

```
Call UsrEvalUxx(NSUB,NCP,ISYM,UP,UPXX,BOC)
G(4+1)=UPX(1,1)
G(8+1)=UPX(2,1)
G(12+1)=UPX(3,1)
Do J=2, NCP+1
G(4+J)=A21*UPXX(1,J)
G(8+J)=A22*UPXX(2,J)
G(12+J)=A23*UPXX(3,J)
EndDo
G(4+NPE)=UP(1,NPE)-VL1*K1*U(4)*U(2)/(1.0+K1*U(4)*U(2)+K2*(1.0-U(4))*U(2))
G(8+NPE)=UP(2,NPE)-VL2*K2*(1.0-U(4))*U(2)/(1.0+K1*U(4)*U(2)+K2*(1.0-U(4))*U(2))
G(12+NPE)=UP(3,NPE)-VL3
PGL=U(2)
QGDARCY1=(2*Pi*RW*DZ*ALFA*KABS)*(ALFA1*KRG)/(VISG*BG)
QGDARCY1L=(2*Pi*RW*DZ*ALFA*KABS)*(ALFA1)/(VISG*BG)
QGDA111=FM2*(2*Pi*RW*DZ*DA/(BG))
QGDA121=-FM2*(2*Pi*RW*DZ*DA*U(3)/(BG*BG)*DBGDPG)
QGDA211=FM2*(2*Pi*RW*DZ*DA/(BG))
QGDA221=-FM2*(2*Pi*RW*DZ*DA*U(3)/(BG*BG)*DBGDPG)
QGRSW111=FM3*FM1*(2*Pi*RW*DZ*RSW1*ALFA*KABS)*(KRW)/(VISW*BW)
QGRSW121=FM3*FM1*(2*Pi*RW*DZ*RSW1*ALFA*KABS)*(KRW)/(VISW*BW)*DPCGWDSW
QGRSW211=FM3*FM1*(2*Pi*RW*DZ*RSW2*ALFA*KABS)*(KRW)/(VISW*BW)
QGRSW221=FM3*FM1*(2*Pi*RW*DZ*RSW2*ALFA*KABS)*(KRW)/(VISW*BW)*DPCGWDSW
QWDARCY11=FM1*(2*Pi*RW*DZ*ALFA*KABS)*(KRW)/(VISW*BW)
QWDARCY21=FM1*(2*Pi*RW*DZ*ALFA*KABS)*(KRW)/(VISW*BW)*DPCGWDSW
If(QB.EQ.1)Then
QGDARCY1=(2*Pi*RW*DZ*ALFA*KABS)*(ALFA1*KRG)/(VISG*BG)
QGDARCY1L=(2*Pi*RW*DZ*ALFA*KABS)*(ALFA1)/(VISG*BG)
QGDA111=FM2*(2*Pi*RW*DZ*DA/(BG))
QGDA121=-FM2*(2*Pi*RW*DZ*DA*U(3)/(BG*BG)*DBGDPG)
QGDA211=FM2*(2*Pi*RW*DZ*DA/(BG))
QGDA221=-FM2*(2*Pi*RW*DZ*DA*U(3)/(BG*BG)*DBGDPG)
QGRSW111=FM3*FM1*(2*Pi*RW*DZ*RSW1*ALFA*KABS)*(KRW)/(VISW*BW)
QGRSW121=FM3*FM1*(2*Pi*RW*DZ*RSW1*ALFA*KABS)*(KRW)/(VISW*BW)*DPCGWDSW
QGRSW211=FM3*FM1*(2*Pi*RW*DZ*RSW2*ALFA*KABS)*(KRW)/(VISW*BW)
QGRSW221=FM3*FM1*(2*Pi*RW*DZ*RSW2*ALFA*KABS)*(KRW)/(VISW*BW)*DPCGWDSW
QWDARCY11=FM1*(2*Pi*RW*DZ*ALFA*KABS)*(KRW)/(VISW*BW)
QWDARCY21=FM1*(2*Pi*RW*DZ*ALFA*KABS)*(KRW)/(VISW*BW)*DPCGWDSW
QGDARCY=QGDARCY1*Ux(2)
QGDA11=QGDA111*Ux(3)
QGDA12=QGDA121*Ux(2)
QGDA1=(QGDA11+QGDA12)
QGDA21=QGDA211*Ux(3)
QGDA22=QGDA221*Ux(2)
QGDA2=(QGDA21+QGDA22)
QGRSW11=QGRSW111*Ux(2)
QGRSW12=QGRSW121*XR1*Ux(3)
QGRSW1=(QGRSW11+QGRSW12)
QGRSW21=QGRSW211*Ux(2)
QGRSW22=QGRSW221*Ux(3)
QGRSW2=(QGRSW21+QGRSW22)
QWDARCY1=QWDARCY11*Ux(2)
QWDARCY2=QWDARCY21*Ux(3)
QWDARCY=(QWDARCY1+QWDARCY2)
QG1=(QGDARCY+QGDA2+QGRSW2)
QW1=QWDARCY
```

```
EndIf
Case(2)
QGDARCY1R=(2*Pi*RW*DZ*ALFA*KABS)*(ALFA1*KRG)/(VISG*BG)
QGDA111R=FM2*(2*Pi*RW*DZ*DA/(BG))
QGDA121R=-FM2*(2*Pi*RW*DZ*DA*U(3)/(BG*BG)*DBGDPG)
QGDA211R=FM2*(2*Pi*RW*DZ*DA/(BG))
QGDA221R=-FM2*(2*Pi*RW*DZ*DA*U(3)/(BG*BG)*DBGDPG)
QGRSW111R=FM3*FM1*(2*Pi*RW*DZ*RSW1*ALFA*KABS)*(KRW)/(VISW*BW)
QGRSW121R=FM3*FM1*(2*Pi*RW*DZ*RSW1*ALFA*KABS)*(KRW)/(VISW*BW)*DPCGWDSW
QGRSW211R=FM3*FM1*(2*Pi*RW*DZ*RSW2*ALFA*KABS)*(KRW)/(VISW*BW)
QGRSW221R=FM3*FM1*(2*Pi*RW*DZ*RSW2*ALFA*KABS)*(KRW)/(VISW*BW)*DPCGWDSW
QWDARCY11R=FM1*(2*Pi*RW*DZ*ALFA*KABS)*(KRW)/(VISW*BW)
QWDARCY21R=FM1*(2*Pi*RW*DZ*ALFA*KABS)*(KRW)/(VISW*BW)*DPCGWDSW
If(QB.EQ.1)Then
QGDARCYR=QGDARCY1R*Ux(2)
QGDA11R=QGDA111R*Ux(3)
QGDA12R=QGDA121R*Ux(2)
QGDA1R=FM2*(QGDA11R+QGDA12R)
QGDA21R=QGDA211R*Ux(3)
QGDA22R=QGRSW221R*Ux(2)
QGDA2R=(QGDA21R+QGDA22R)
QGRSW11R=QGRSW111R*Ux(2)
QGRSW12R=QGRSW121R*Ux(3)
QGRSW1R=(QGRSW11R+QGRSW12R)
QGRSW21R=QGRSW211R*Ux(2)
QGRSW22R=QGRSW221R*Ux(3)
QGRSW2R=(QGRSW21R+QGRSW22R)
QWDARCY1R=QWDARCY11R*Ux(2)
QWDARCY2R=QWDARCY21R*Ux(3)
QWDARCYR=(QWDARCY1R+QWDARCY2R)
QG1R=QGDARCYR+QGDA2R+QGRSW2R
QW1R=QWDARCYR
EndIf
G(1)=U(1)-PGI
If(Ieform.EQ.0)G(2)=U(2)-25.0
If(Ieform.EQ.1)G(2)=Ux(2)-0.0
G(3)=Ux(3)-0.0
G(4)=Ux(4)-0.0
Do J=1,NPE
UP(1,J)=U(4+J)
UP(2,J)=U(8+J)
UP(3,J)=U(12+J)
EndDo
Call UsrEvalUx(NSUB,NCP,ISYM,UP,UPX,AOC)
Call UsrEvalUxx(NSUB,NCP,ISYM,UP,UPXX,BOC)
G(4+1)=UPX(1,1)
G(8+1)=UPX(2,1)
G(12+1)=UPX(3,1)
Do J=2, NCP+1
G(4+J)=A21*UPXX(1,J)
G(8+J)=A22*UPXX(2,J)
G(12+J)=A23*UPXX(3,J)
EndDo
G(4+NPE)=UP(1,NPE)-VL1*K1*U(4)*U(2)/(1.0+K1*U(4)*U(2)+K2*(1.0-U(4))*U(2))
G(8+NPE)=UP(2,NPE)-VL2*K2*(1.0-U(4))*U(2)/(1.0+K1*U(4)*U(2)+K2*(1.0-U(4))*U(2))
G(12+NPE)=UP(3,NPE)-VL3
```

```
      ALI3=(2*Pi*DZ*ALFA*ALFA1*KABS*KRG)/(VISG*BG)
      ALI4=(2*Pi*DZ*ALFA*KABS*KRW)/(VISW*BW)
      QG2=ALI3*Ux(2)
      QW2=ALI4*(Ux(2)+DPCGWDSW*Ux(3))
      PGR=U(2)
      End Select
!
!:End of Subroutine GPSUBP
!
      Return
      End

      Subroutine DPSUBP(T,Xgrid,X,Neq,Ugrid,U,D,RPAR,IPAR,Ieform,Ires,Ielem,Igrid,Ngrid)
      Implicit Real*8(A-H,O-Z)
      Integer NCP
      Integer NPE
      Parameter (NCP=2,NPE=NCP+2)
      Parameter (NCMAX=10,Zero=0.0D0,One=1.0D0,Pi=3.141592653589793D0)
!
!:Variable Declaration Statements section
!
      Dimension D(Neq,*),U(Neq),RPAR(0:*),IPAR(0:*)
      Dimension Xgrid(*),Ugrid(Neq,*)
      Real*8 R,ALFA,PSC,TSC,DEPTH,DZ,CP,CM,ROC,POROI,KABSI,CLSP,PW,PGRAD,TGRAD,OBGR
     *      AD,TRES,POB,VL1,PL1,PC1,TC1,CONV1,CONV2,CONV3,CONV4,VL2,PL2,PC2,TC2,PM
     *      AX,VMAX,V,H,KRGC,KRWC,QG1,QW1,QG2,QW2,SG2,ROSC,CW,KRCW,KRCG,SWIRR,SGIR
     *      R,RW,RE,SKIN,TEMP,PGI,S,LOGR,PWELL,SWELL,PCGW,PORO,KABS,SWN,KRG,KRW,DV
     *      T,DVP,BG,BW,DA,BOB,MW,MW1,MW2,Z,ZZ,Z1,Z2,DZDPG,RO,KK1,XK1,YK1,VISG,VIS
     *      W,A,B,SG1,QGSP,QWSP,QTSP,A11,A12,A13,A21,A22,A23,VL3,VL3IRR,PO,CBET,PC
     *      ,TC,VIRR,TAO,DI,AA1,AA2,AA3,Y11,AB1,BB1,BB2,BB3,BB4,BB5,BB6,BB7,BB8,CO
     *      EFF1,COEFF2,DPGDR,DVP1,DBW,DPORO,DBG,CG,CG1,CG2,ALFA1,FLOWGP,FLOWWP,SG
     *      P,DSGDR,VL10,VL20,VL30,PGQ,ADSA,K1,K2,FLOWGI,FLOWWI,SGI,PG1,XG1,DPOROD
     *
PG,DKABSDPORO,DSWNDSG,DSWNDSW,DKRGDSWN,DKRWDSWN,EU,DZFAC,DZFAC1,DZFAC2
     *      ,D2ZDPG2,D2ZDPG21,D2ZDPG22,D2ZDPG2T,DPCGWDSW,DPCGW2DSW2,DBWDPW,DBGDPG,
     *
DVISGDROG,DROGDPG,DVISWDPW,DRSWDPG,D2BGDPG2,ADSCO2,ADSCH4,BULKCO2,BULK
     *      CH4,CO2IN,CH4IN,H2OIN,EKO01,EKO02,EKO03,EKO04,EKO05,EKO06,EKO07,EKO08,
     *      EKO09,EKO10,EKO11,EKO12,EKO13,EKO14,EKO15,EKO16,EKO17,EKO18,EKO19,EKO2
     *      0,EKO21,EKO22,EKO23,EKO24,EKO25,EKO26,EKO27,EKO28,EKO29,EKO30,DAE01,DA
     *      E02,DAE03,DAE04,DAE05,DAE06,DAE07,DAE08,DAE09,DAE10,DAE11,DAE12,DAE13,
     *      DAE14,DAE15,DAE16,DAE17,DAE18,DAE19,DAE20,RSWE01,RSWE02,RSWE03,RSWE04,
     *      RSWE05,RSWE06,RSWE07,RSWE08,RSWE09,RSWE10,RSWE11,RSWE12,RSWE13,RSWE14,
     *      RSWE15,RSWE16,RSWE17,RSWE18,RSWE19,RSWE20,RSWE21,RSWE22,RSWE23,RSWE24,
     *      RSWE25,RSWE26,RSWE27,RSWE28,RSWE29,RSWE30,RSWE31,RSWE32,RSWE33,RSWE34,
     *      RSWE35,RSWE36,C11,C12,C13,C14,C15,C16,C17,C21,C22,C23,C24,C25,C26,C27,
     *      C31,C32,C33,C34,C35,C36,C37,FM1,FM2,FM3,FM4,CE11,CE12,CE13,CE21,CE22,C
     *      E23,CE31,CE32,CE33,CE41,CE42,CE43,CE51,CE52,CE53,RSW1,RSW2,DRSW1DPG,DR
     *
SW2DPG,QGDARCY,QWDARCY,QWDARCY1,QGDARCY1L,QWDARCY2,QGDA1,QGDA2,QGDA11,
     *      QGDA12,QGDA21,QGDA22,QGDA1R,QGDA2R,QGDA11R,QGDA12R,QGDA21R,QGDA22R,QGR
     *      SW1,QGRSW2,QGRSW11,QGRSW12,QGRSW21,QGRSW22,QGRSW1R,QGRSW2R,QGRSW11R,QG
     *      RSW12R,QGRSW21R,QGRSW22R,QGDARCY1,QWDARCY11,QWDARCY21,QGDA111,QGDA121,
     *      QGDA211,QGDA221,QGRSW111,QGRSW121,QGRSW211,QGRSW221,QGDARCY1R,QWDARCY1
     *      1R,QWDARCY21R,QGDA111R,QGDA121R,QGDA211R,QGDA221R,QGRSW111R,QGRSW121R,
     *      QGRSW211R,QGRSW221R,ALI,ALI1,ALI11,ALI2,ALI22,ALI3,ALI4,XR1,XR2,XRN,MO
```

```
     *      ISTURE,ASH,MULTIPLIER,WI1,WI2,QSP,CC,QWELL,PGL,SGL,PGR,PG,SG,Y1,ZAMAN(
     *      1002),QGIN(1002),QWIN(1002),QGPRO(1002),QWPRO(1002),ADSRT1(1002),ADSRT
     *      2(1002),ADSRT3(1002),PWELL1(1002),QGCUM(1002),QWCUM(1002),ADSRATE1,ADS
     *      RATE2,ADSRATE3,QG1ATWELL,RR,PWW,UP(3,4),UPX(3,4),UPXX(3,4),ZOC(10),WOC
     *      (10),AOC(10,10),BOC(10,10)
      Integer GASCOMP,FLAG1,J1,J5,ITER1,Iloop,BC,IWELL,QB,II,NSUB,ISYM
!
!:External Declarations, Common Blocks and Data Statements
!
      Common/USRI00P/ IOFSET
      Common/WEIGHTS/ PROOT(NCMAX),WQ(NCMAX),AX(NCMAX,NCMAX),BXX(NCMAX,NCMAX)
      Common/USRR01P/
R,ALFA,PSC,TSC,DEPTH,DZ,CP,CM,ROC,POROI,KABSI,CLSP,PW,PGRAD,TGRAD,OBGR
     *           AD,TRES,POB,VL1,PL1,PC1,TC1,CONV1,CONV2,CONV3,CONV4,VL2,PL2,PC2,TC2,PM
     *
AX,VMAX,V,H,KRGC,KRWC,QG1,QW1,QG2,QW2,SG2,ROSC,CW,KRCW,KRCG,SWIRR,SGIR
     *           R,RW,RE,SKIN,TEMP,PGI,S,LOGR,PWELL,SWELL,PCGW,PORO,KABS,SWN,KRG,KRW,DV
     *           T,DVP,BG,BW,DA,BOB,MW,MW1,MW2,Z,ZZ,Z1,Z2,DZDPG,RO,KK1,XK1,YK1,VISG,VIS
     *           W,A,B,SG1,QGSP,QWSP,QTSP,A11,A12,A13,A21,A22,A23,VL3,VL3IRR,PO,CBET,PC
     *           ,TC,VIRR,TAO,DI,AA1,AA2,AA3,Y11,AB1,BB1,BB2,BB3,BB4,BB5,BB6,BB7,BB8,CO
     *           EFF1,COEFF2,DPGDR,DVP1,DBW,DPORO,DBG,CG,CG1,CG2,ALFA1,FLOWGP,FLOWWP,SG
     *           P,DSGDR,VL10,VL20,VL30,PGQ,ADSA,K1,K2,FLOWGI,FLOWWI,SGI,PG1,XG1,DPOROD
     *
PG,DKABSDPORO,DSWNDSG,DSWNDSW,DKRGDSWN,DKRWDSWN,EU,DZFAC,DZFAC1,DZFAC2
     *
,D2ZDPG2,D2ZDPG21,D2ZDPG22,D2ZDPG2T,DPCGWDSW,DPCGW2DSW2,DBWDPW,DBGDPG,
     *
DVISGDROG,DROGDPG,DVISWDPW,DRSWDPG,D2BGDPG2,ADSCO2,ADSCH4,BULKCO2,BULK
     *           CH4,CO2IN,CH4IN,H2OIN,EKO01,EKO02,EKO03,EKO04,EKO05,EKO06,EKO07,EKO08,
     *           EKO09,EKO10,EKO11,EKO12,EKO13,EKO14,EKO15,EKO16,EKO17,EKO18,EKO19,EKO2
     *           0,EKO21,EKO22,EKO23,EKO24,EKO25,EKO26,EKO27,EKO28,EKO29,EKO30,DAE01,DA
     *           E02,DAE03,DAE04,DAE05,DAE06,DAE07,DAE08,DAE09,DAE10,DAE11,DAE12,DAE13,
     *           DAE14,DAE15,DAE16,DAE17,DAE18,DAE19,DAE20,RSWE01,RSWE02,RSWE03,RSWE04,
     *           RSWE05,RSWE06,RSWE07,RSWE08,RSWE09,RSWE10,RSWE11,RSWE12,RSWE13,RSWE14,
     *           RSWE15,RSWE16,RSWE17,RSWE18,RSWE19,RSWE20,RSWE21,RSWE22,RSWE23,RSWE24,
     *           RSWE25,RSWE26,RSWE27,RSWE28,RSWE29,RSWE30,RSWE31,RSWE32,RSWE33,RSWE34,
     *           RSWE35,RSWE36,C11,C12,C13,C14,C15,C16,C17,C21,C22,C23,C24,C25,C26,C27,
     *           C31,C32,C33,C34,C35,C36,C37,FM1,FM2,FM3,FM4,CE11,CE12,CE13,CE21,CE22,C
     *           E23,CE31,CE32,CE33,CE41,CE42,CE43,CE51,CE52,CE53,RSW1,RSW2,DRSW1DPG,DR
     *
SW2DPG,QGDARCY,QWDARCY,QWDARCY1,QGDARCY1L,QWDARCY2,QGDA1,QGDA2,QGDA11,
     *
QGDA12,QGDA21,QGDA22,QGDA1R,QGDA2R,QGDA11R,QGDA12R,QGDA21R,QGDA22R,QGR
     *
SW1,QGRSW2,QGRSW11,QGRSW12,QGRSW21,QGRSW22,QGRSW1R,QGRSW2R,QGRSW11R,QG
     *
RSW12R,QGRSW21R,QGRSW22R,QGDARCY1,QWDARCY11,QWDARCY21,QGDA111,QGDA121,
     *
QGDA211,QGDA221,QGRSW111,QGRSW121,QGRSW211,QGRSW221,QGDARCY1R,QWDARCY1
     *
1R,QWDARCY21R,QGDA111R,QGDA121R,QGDA211R,QGDA221R,QGRSW111R,QGRSW121R,
     *           QGRSW211R,QGRSW221R,ALI,ALI1,ALI11,ALI2,ALI22,ALI3,ALI4,XR1,XR2,XRN,MO
     *           ISTURE,ASH,MULTIPLIER,WI1,WI2,QSP,CC,QWELL,PGL,SGL,PGR,PG,SG,Y1,ZAMAN
     *           ,QGIN ,QWIN ,QGPRO ,QWPRO ,ADSRT1 ,ADSRT2 ,ADSRT3 ,PWELL1 ,QGCUM ,QWCU
     *           M ,ADSRATE1,ADSRATE2,ADSRATE3,QG1ATWELL,RR,PWW,UP ,UPX ,UPXX ,ZOC ,WOC
     *           ,AOC ,BOC
```

```
      Common/USRI01P/ GASCOMP,FLAG1,J1,J5,ITER1,Iloop,BC,IWELL,QB,II,NSUB,ISYM
!
!:Diffusion Coefficient Section:Initialize
!
      Do JEQ=1, Neq
       Do IEQ=1, Neq
        D(JEQ,IEQ)=0.0
       End Do
      End Do
      Do IEQ=1, Neq
       D(IEQ,IEQ)=1.0
      End Do
!
!:End of Subroutine DPSUBP
!
      Return
      End

      Subroutine EPSUBP(T,Xgrid,X,Neq,Ugrid,U,E,RPAR,IPAR,Ieform,Ires,JLOC,Ielem,Igrid,Ngrid)
      Implicit Real*8(A-H,O-Z)
      Integer NCP
      Integer NPE
      Parameter (NCP=2,NPE=NCP+2)
      Parameter (NCMAX=10,Zero=0.0D0,One=1.0D0,Pi=3.141592653589793D0)
!
!:Declaration Statements section
!
      Dimension E(Neq,*),U(Neq),RPAR(0:*),IPAR(0:*)
      Dimension Xgrid(*),Ugrid(Neq,*)
      Real*8 R,ALFA,PSC,TSC,DEPTH,DZ,CP,CM,ROC,POROI,KABSI,CLSP,PW,PGRAD,TGRAD,OBGR
     *      AD,TRES,POB,VL1,PL1,PC1,TC1,CONV1,CONV2,CONV3,CONV4,VL2,PL2,PC2,TC2,PM
     *      AX,VMAX,V,H,KRGC,KRWC,QG1,QW1,QG2,QW2,SG2,ROSC,CW,KRCW,KRCG,SWIRR,SGIR
     *      R,RW,RE,SKIN,TEMP,PGI,S,LOGR,PWELL,SWELL,PCGW,PORO,KABS,SWN,KRG,KRW,DV
     *      T,DVP,BG,BW,DA,BOB,MW,MW1,MW2,Z,ZZ,Z1,Z2,DZDPG,RO,KK1,XK1,YK1,VISG,VIS
     *      W,A,B,SG1,QGSP,QWSP,QTSP,A11,A12,A13,A21,A22,A23,VL3,VL3IRR,PO,CBET,PC
     *      ,TC,VIRR,TAO,DI,AA1,AA2,AA3,Y11,AB1,BB1,BB2,BB3,BB4,BB5,BB6,BB7,BB8,CO
     *      EFF1,COEFF2,DPGDR,DVP1,DBW,DPORO,DBG,CG,CG1,CG2,ALFA1,FLOWGP,FLOWWP,SG
     *      P,DSGDR,VL10,VL20,VL30,PGQ,ADSA,K1,K2,FLOWGI,FLOWWI,SGI,PG1,XG1,DPOROD
     *
PG,DKABSDPORO,DSWNDSG,DSWNDSW,DKRGDSWN,DKRWDSWN,EU,DZFAC,DZFAC1,DZFAC2
     *      ,D2ZDPG2,D2ZDPG21,D2ZDPG22,D2ZDPG2T,DPCGWDSW,DPCGW2DSW2,DBWDPW,DBGDPG,
     *
DVISGDROG,DROGDPG,DVISWDPW,DRSWDPG,D2BGDPG2,ADSCO2,ADSCH4,BULKCO2,BULK
     *      CH4,CO2IN,CH4IN,H2OIN,EKO01,EKO02,EKO03,EKO04,EKO05,EKO06,EKO07,EKO08,
     *      EKO09,EKO10,EKO11,EKO12,EKO13,EKO14,EKO15,EKO16,EKO17,EKO18,EKO19,EKO2
     *      0,EKO21,EKO22,EKO23,EKO24,EKO25,EKO26,EKO27,EKO28,EKO29,EKO30,DAE01,DA
     *      E02,DAE03,DAE04,DAE05,DAE06,DAE07,DAE08,DAE09,DAE10,DAE11,DAE12,DAE13,
     *      DAE14,DAE15,DAE16,DAE17,DAE18,DAE19,DAE20,RSWE01,RSWE02,RSWE03,RSWE04,
     *      RSWE05,RSWE06,RSWE07,RSWE08,RSWE09,RSWE10,RSWE11,RSWE12,RSWE13,RSWE14,
     *      RSWE15,RSWE16,RSWE17,RSWE18,RSWE19,RSWE20,RSWE21,RSWE22,RSWE23,RSWE24,
     *      RSWE25,RSWE26,RSWE27,RSWE28,RSWE29,RSWE30,RSWE31,RSWE32,RSWE33,RSWE34,
     *      RSWE35,RSWE36,C11,C12,C13,C14,C15,C16,C17,C21,C22,C23,C24,C25,C26,C27,
     *      C31,C32,C33,C34,C35,C36,C37,FM1,FM2,FM3,FM4,CE11,CE12,CE13,CE21,CE22,C
     *      E23,CE31,CE32,CE33,CE41,CE42,CE43,CE51,CE52,CE53,RSW1,RSW2,DRSW1DPG,DR
     *
SW2DPG,QGDARCY,QWDARCY,QWDARCY1,QGDARCY1L,QWDARCY2,QGDA1,QGDA2,QGDA11,
```

```
     *      QGDA12,QGDA21,QGDA22,QGDA1R,QGDA2R,QGDA11R,QGDA12R,QGDA21R,QGDA22R,QGR
     *      SW1,QGRSW2,QGRSW11,QGRSW12,QGRSW21,QGRSW22,QGRSW1R,QGRSW2R,QGRSW11R,QG
     *      RSW12R,QGRSW21R,QGRSW22R,QGDARCY1,QWDARCY11,QWDARCY21,QGDA111,QGDA121,
     *      QGDA211,QGDA221,QGRSW111,QGRSW121,QGRSW211,QGRSW221,QGDARCY1R,QWDARCY1
     *      1R,QWDARCY21R,QGDA111R,QGDA121R,QGDA211R,QGDA221R,QGRSW111R,QGRSW121R,
     *      QGRSW211R,QGRSW221R,ALI,ALI1,ALI11,ALI2,ALI22,ALI3,ALI4,XR1,XR2,XRN,MO
     *      ISTURE,ASH,MULTIPLIER,WI1,WI2,QSP,CC,QWELL,PGL,SGL,PGR,PG,SG,Y1,ZAMAN(
     *      1002),QGIN(1002),QWIN(1002),QGPRO(1002),QWPRO(1002),ADSRT1(1002),ADSRT
     *      2(1002),ADSRT3(1002),PWELL1(1002),QGCUM(1002),QWCUM(1002),ADSRATE1,ADS
     *      RATE2,ADSRATE3,QG1ATWELL,RR,PWW,UP(3,4),UPX(3,4),UPXX(3,4),ZOC(10),WOC
     *      (10),AOC(10,10),BOC(10,10)
      Integer GASCOMP,FLAG1,J1,J5,ITER1,Iloop,BC,IWELL,QB,II,NSUB,ISYM
!
!:External Declarations, Common Blocks and Data Statements
!
      Common/USRI00P/ IOFSET
      Common/WEIGHTS/ PROOT(NCMAX),WQ(NCMAX),AX(NCMAX,NCMAX),BXX(NCMAX,NCMAX)
      Common/USRR01P/
R,ALFA,PSC,TSC,DEPTH,DZ,CP,CM,ROC,POROI,KABSI,CLSP,PW,PGRAD,TGRAD,OBGR
     *           AD,TRES,POB,VL1,PL1,PC1,TC1,CONV1,CONV2,CONV3,CONV4,VL2,PL2,PC2,TC2,PM
     *
AX,VMAX,V,H,KRGC,KRWC,QG1,QW1,QG2,QW2,SG2,ROSC,CW,KRCW,KRCG,SWIRR,SGIR
     *           R,RW,RE,SKIN,TEMP,PGI,S,LOGR,PWELL,SWELL,PCGW,PORO,KABS,SWN,KRG,KRW,DV
     *           T,DVP,BG,BW,DA,BOB,MW,MW1,MW2,Z,ZZ,Z1,Z2,DZDPG,RO,KK1,XK1,YK1,VISG,VIS
     *           W,A,B,SG1,QGSP,QWSP,QTSP,A11,A12,A13,A21,A22,A23,VL3,VL3IRR,PO,CBET,PC
     *           ,TC,VIRR,TAO,DI,AA1,AA2,AA3,Y11,AB1,BB1,BB2,BB3,BB4,BB5,BB6,BB7,BB8,CO
     *           EFF1,COEFF2,DPGDR,DVP1,DBW,DPORO,DBG,CG,CG1,CG2,ALFA1,FLOWGP,FLOWWP,SG
     *           P,DSGDR,VL10,VL20,VL30,PGQ,ADSA,K1,K2,FLOWGI,FLOWWI,SGI,PG1,XG1,DPOROD
     *
PG,DKABSDPORO,DSWNDSG,DSWNDSW,DKRGDSWN,DKRWDSWN,EU,DZFAC,DZFAC1,DZFAC2
     *
,D2ZDPG2,D2ZDPG21,D2ZDPG22,D2ZDPG2T,DPCGWDSW,DPCGW2DSW2,DBWDPW,DBGDPG,
     *
DVISGDROG,DROGDPG,DVISWDPW,DRSWDPG,D2BGDPG2,ADSCO2,ADSCH4,BULKCO2,BULK
     *           CH4,CO2IN,CH4IN,H2OIN,EKO01,EKO02,EKO03,EKO04,EKO05,EKO06,EKO07,EKO08,
     *           EKO09,EKO10,EKO11,EKO12,EKO13,EKO14,EKO15,EKO16,EKO17,EKO18,EKO19,EKO2
     *           0,EKO21,EKO22,EKO23,EKO24,EKO25,EKO26,EKO27,EKO28,EKO29,EKO30,DAE01,DA
     *           E02,DAE03,DAE04,DAE05,DAE06,DAE07,DAE08,DAE09,DAE10,DAE11,DAE12,DAE13,
     *           DAE14,DAE15,DAE16,DAE17,DAE18,DAE19,DAE20,RSWE01,RSWE02,RSWE03,RSWE04,
     *           RSWE05,RSWE06,RSWE07,RSWE08,RSWE09,RSWE10,RSWE11,RSWE12,RSWE13,RSWE14,
     *           RSWE15,RSWE16,RSWE17,RSWE18,RSWE19,RSWE20,RSWE21,RSWE22,RSWE23,RSWE24,
     *           RSWE25,RSWE26,RSWE27,RSWE28,RSWE29,RSWE30,RSWE31,RSWE32,RSWE33,RSWE34,
     *           RSWE35,RSWE36,C11,C12,C13,C14,C15,C16,C17,C21,C22,C23,C24,C25,C26,C27,
     *           C31,C32,C33,C34,C35,C36,C37,FM1,FM2,FM3,FM4,CE11,CE12,CE13,CE21,CE22,C
     *           E23,CE31,CE32,CE33,CE41,CE42,CE43,CE51,CE52,CE53,RSW1,RSW2,DRSW1DPG,DR
     *
SW2DPG,QGDARCY,QWDARCY,QWDARCY1,QGDARCY1L,QWDARCY2,QGDA1,QGDA2,QGDA11,
     *
QGDA12,QGDA21,QGDA22,QGDA1R,QGDA2R,QGDA11R,QGDA12R,QGDA21R,QGDA22R,QGR
     *
SW1,QGRSW2,QGRSW11,QGRSW12,QGRSW21,QGRSW22,QGRSW1R,QGRSW2R,QGRSW11R,QG
     *
RSW12R,QGRSW21R,QGRSW22R,QGDARCY1,QWDARCY11,QWDARCY21,QGDA111,QGDA121,
     *
QGDA211,QGDA221,QGRSW111,QGRSW121,QGRSW211,QGRSW221,QGDARCY1R,QWDARCY1
```

```
     *
1R,QWDARCY21R,QGDA111R,QGDA121R,QGDA211R,QGDA221R,QGRSW111R,QGRSW121R,
     *          QGRSW211R,QGRSW221R,ALI,ALI1,ALI11,ALI2,ALI22,ALI3,ALI4,XR1,XR2,XRN,MO
     *          ISTURE,ASH,MULTIPLIER,WI1,WI2,QSP,CC,QWELL,PGL,SGL,PGR,PG,SG,Y1,ZAMAN
     *          ,QGIN ,QWIN ,QGPRO ,QWPRO ,ADSRT1 ,ADSRT2 ,ADSRT3 ,PWELL1 ,QGCUM ,QWCU
     *          M ,ADSRATE1,ADSRATE2,ADSRATE3,QG1ATWELL,RR,PWW,UP ,UPX ,UPXX ,ZOC ,WOC
     *          ,AOC ,BOC
      Common/USRI01P/ GASCOMP,FLAG1,J1,J5,ITER1,Iloop,BC,IWELL,QB,II,NSUB,ISYM
!
!:JLOC=0 Indicates an Interior Point
!:JLOC=1 Indicates Left Boundary
!:JLOC=2 Indicates Right Boundary
!
      Select Case (JLOC)
      Case(1)
       Do I=1,Neq
        Do J=1,Neq
         E(I,J)=0.0
        End Do
       End Do
      E(06,06)=1.0
      E(07,07)=1.0
      E(10,10)=1.0
      E(11,11)=1.0
      E(14,14)=1.0
      E(15,15)=1.0
      Case(0)
       Do I=1,Neq
        Do J=1,Neq
         E(I,J)=0.0
        End Do
       End Do
      PORO=POROI-POROI*(CP*(POB-U(2)))
      DPORODPG=POROI*CP
      KABS=KABSI*(PORO/POROI)**3
      DKABSDPORO=3*KABS/PORO
      SW=1.0-U(3)
      SWN=(SW-SWIRR)/(1-SGIRR-SWIRR)
      DSWNDSW=1.0/(1-SGIRR-SWIRR)
      KRG=KRCG*(1-SWN**2)*(1-SWN)**2
      KRW=KRCW*SWN**4
      If (KRG.LE.0.0.OR.KRW.LE.0.0) Then
      KRG=0.0
      KRW=0.0
      EndIf
      If (KRG.GE.1.0.OR.KRW.GE.1.0) Then
      KRG=1.0
      KRW=1.0
      EndIf
      DKRGDSWN=-2.0*KRG*(2.0*SWN+1.0)/(1.0-SWN*SWN)
      DKRWDSWN=4.0*KRW/SWN
      If (SW.LE.SWIRR) Then
      SW=1.001*SWIRR
      EndIf
      PCGW=1.0/(13.448*(SW-SWIRR))**0.5
      DPCGWDSW=-0.5*13.448/(13.448*(SW-SWIRR))**1.5
```

```
    DPCGW2DSW2=0.5*1.5*13.448*13.448/(13.448*(SW-SWIRR))**2.5
    PW=U(2)-PCGW
    DVT=-1.0001E-02+1.33391E-04*TEMP+5.50654E-07*TEMP*TEMP
    DVP=-1.95301E-9*PW*TEMP-1.72834E-13*PW**2*TEMP-3.58922E-7*PW-2.25341E-10*PW**2
    BW=(1+DVT)*(1+DVP)
    DBWDPW=(1+DVT)*(-1.95301E-9*TEMP-2.0*1.72834E-13*PW*TEMP-3.58922E-7-2.0*2.25341E-10*PW)
    GASCOMP=1
    Call COMPFACTOR(U,Ieform,RPAR)
    Z1=ZZ
    MW1=MW
    CG1=CG
    DZFAC1=DZFAC
    D2ZDPG21=D2ZDPG2
    TEMP=TEMP-460
    GASCOMP=2
    Call COMPFACTOR(U,Ieform,RPAR)
    Z2=ZZ
    MW2=MW
    CG2=CG
    DZFAC2=DZFAC
    D2ZDPG22=D2ZDPG2
    Z=U(4)*Z1+(1.0-U(4))*Z2
    MW=U(4)*MW1+(1.0-U(4))*MW2
    CG=U(4)*CG1+(1.0-U(4))*CG2
    DZDPG=U(4)*DZFAC1+(1.0-U(4))*DZFAC2
    D2ZDPG2T=U(4)*D2ZDPG21+(1.0-U(4))*D2ZDPG22
    BG=PSC*Z*(TEMP)/((TSC+460)*U(2))
    DBGDPG=-BG*CG
    D2BGDPG2=BG*CG**2+BG/(U(2)*U(2))-BG/(Z*Z)*DZDPG**2+BG/Z*D2ZDPG2T
    TEMP=TEMP-460
    TEMP=TEMP+460
    RO=1.4935E-3*U(2)*MW/(Z*TEMP)
    KK1=(9.4+0.02*MW)*TEMP**1.5/(209+19*MW+TEMP)
    XK1=3.5+986/TEMP+0.01*MW
    YK1=2.4-0.2*XK1
    VISG=1.0E-4*KK1*exp(XK1*RO**YK1)
    DROGDPG=RO*CG
    DVISGDROG=VISG*XK1*YK1*RO**(YK1-1.0)
    TEMP=TEMP-460
    A=109.574-8.40564*S+0.313314*S**2+8.72213E-3*S**3
    B=-1.12166+2.63951E-2*S-6.79461E-4*S**2-5.47119E-5*S**3+1.55586E-6*S**4
    VISW=A*TEMP**B*(0.9994+4.0295E-5*PW+3.1062E-9*PW**2)
    DVISWDPW=A*TEMP**B*(4.0295E-5+2.0*3.1062E-9*PW)
    AT1=8.15839-6.12265E-2*TEMP+1.91663E-4*TEMP**2-2.1654E-7*TEMP**3
    AT2=1.01021E-2-7.44241E-5*TEMP+3.05553E-7*TEMP**2-2.94883E-10*TEMP**3
    AT3=-1.0E-7*(9.02505-0.130237*TEMP+8.53425E-4*TEMP**2-2.34122E-6*TEMP**3+2.37049E-
9*TEMP**4)
    RSW1=U(4)*(AT1+AT2*(U(2))+AT3*(U(2))**2)
    RSW2=(1.0-U(4))*(AT1+AT2*(U(2))+AT3*(U(2))**2)
    DRSW1DPG=U(4)*(AT2+2.0*AT3*U(2))
    DRSW2DPG=(1.0-U(4))*(AT2+2.0*AT3*U(2))
    CE11=((U(4)*U(3)/BG*DPORODPG)-(U(4)*PORO*U(3)/(BG*BG)*DBGDPG))
    CE12=(U(4)*PORO/BG)
    CE13=(PORO*U(3)/BG)
    CE21=((((1.0-U(4))*U(3)/BG*DPORODPG)-((1.0-U(4))*PORO*U(3)/(BG*BG)*DBGDPG)))
    CE22=((1.0-U(4))*PORO/BG)
```

```
      CE23=(PORO*U(3)/BG)
      CE31=FM1*(((1.0-U(3))/(ALFA1*BW)*DPORODPG)-(PORO*(1.0-U(3))/(ALFA1*BW*BW)*DBWDPW))
      CE32=FM1*(((PORO/(ALFA1*BW))+(PORO*(1.0-U(3))/(ALFA1*BW*BW)*DBWDPW*DPCGWDSW)))
      CE33=FM1*0.0
      CE41=FM3*FM1*((PORO*(1.0-U(3))/(ALFA1*BW)*DRSW1DPG)+(RSW1*(1.0-
U(3))/(ALFA1*BW)*DPORODPG)-(RSW1*PORO*(1.0-U(3))/(ALFA1*BW*BW)*DBWDPW))
      CE42=FM3*FM1*((RSW1*PORO*(1.0-
U(3))/(ALFA1*BW*BW)*DBWDPW*DPCGWDSW)+(RSW1*PORO/(ALFA1*BW)))
      CE43=FM3*FM1*0.0
      CE51=FM3*FM1*((PORO*(1.0-U(3))/(ALFA1*BW)*DRSW2DPG)+(RSW2*(1.0-
U(3))/(ALFA1*BW)*DPORODPG)-(RSW2*PORO*(1.0-U(3))/(ALFA1*BW*BW)*DBWDPW))
      CE52=FM3*FM1*((RSW2*PORO*(1.0-
U(3))/(ALFA1*BW*BW)*DBWDPW*DPCGWDSW)+(RSW2*PORO/(ALFA1*BW)))
      CE53=FM3*FM1*0.0
      E(2,2)=CE11+CE41
      E(2,3)=CE12-CE42
      E(2,4)=CE13+0.0
      E(3,2)=CE21+CE51
      E(3,3)=CE22-CE51
      E(3,4)=-CE23+0.0
      E(4,2)=CE31+0.0
      E(4,3)=-CE32+0.0
      E(06,06)=1.0
      E(07,07)=1.0
      E(10,10)=1.0
      E(11,11)=1.0
      E(14,14)=1.0
      E(15,15)=1.0
      Case(2)
       Do I=1,Neq
        Do J=1,Neq
         E(I,J)=0.0
        End Do
       End Do
      E(06,06)=1.0
      E(07,07)=1.0
      E(10,10)=1.0
      E(11,11)=1.0
      E(14,14)=1.0
      E(15,15)=1.0
      End Select
!
!:End of Subroutine EPSUBP
!
      Return
      End

      Subroutine CompFactor(U,Ieform,Rpar)
      Implicit Real*8(A-H,O-Z)
      Integer NCP
      Integer NPE
      Parameter (NCP=2,NPE=NCP+2)
      Parameter (NCMAX=10,Zero=0.0D0,One=1.0D0,Pi=3.141592653589793D0)
!
!:Variable Declaration Statements section
!
```

```
      Real*8 RPAR(0:*),U(*),YY,VALF,DERVALF,SE1,SE2,SE3,SE4,SE5,SE6,TTR
      Real*8 R,ALFA,PSC,TSC,DEPTH,DZ,CP,CM,ROC,POROI,KABSI,CLSP,PW,PGRAD,TGRAD,OBGR
     *      AD,TRES,POB,VL1,PL1,PC1,TC1,CONV1,CONV2,CONV3,CONV4,VL2,PL2,PC2,TC2,PM
     *      AX,VMAX,V,H,KRGC,KRWC,QG1,QW1,QG2,QW2,SG2,ROSC,CW,KRCW,KRCG,SWIRR,SGIR
     *      R,RW,RE,SKIN,TEMP,PGI,S,LOGR,PWELL,SWELL,PCGW,PORO,KABS,SWN,KRG,KRW,DV
     *      T,DVP,BG,BW,DA,BOB,MW,MW1,MW2,Z,ZZ,Z1,Z2,DZDPG,RO,KK1,XK1,YK1,VISG,VIS
     *      W,A,B,SG1,QGSP,QWSP,QTSP,A11,A12,A13,A21,A22,A23,VL3,VL3IRR,PO,CBET,PC
     *      ,TC,VIRR,TAO,DI,AA1,AA2,AA3,Y11,AB1,BB1,BB2,BB3,BB4,BB5,BB6,BB7,BB8,CO
     *      EFF1,COEFF2,DPGDR,DVP1,DBW,DPORO,DBG,CG,CG1,CG2,ALFA1,FLOWGP,FLOWWP,SG
     *      P,DSGDR,VL10,VL20,VL30,PGQ,ADSA,K1,K2,FLOWGI,FLOWWI,SGI,PG1,XG1,DPOROD
     *
PG,DKABSDPORO,DSWNDSG,DSWNDSW,DKRGDSWN,DKRWDSWN,EU,DZFAC,DZFAC1,DZFAC2
     *      ,D2ZDPG2,D2ZDPG21,D2ZDPG22,D2ZDPG2T,DPCGWDSW,DPCGW2DSW2,DBWDPW,DBGDPG,
     *
DVISGDROG,DROGDPG,DVISWDPW,DRSWDPG,D2BGDPG2,ADSCO2,ADSCH4,BULKCO2,BULK
     *      CH4,CO2IN,CH4IN,H2OIN,EKO01,EKO02,EKO03,EKO04,EKO05,EKO06,EKO07,EKO08,
     *      EKO09,EKO10,EKO11,EKO12,EKO13,EKO14,EKO15,EKO16,EKO17,EKO18,EKO19,EKO2
     *      0,EKO21,EKO22,EKO23,EKO24,EKO25,EKO26,EKO27,EKO28,EKO29,EKO30,DAE01,DA
     *      E02,DAE03,DAE04,DAE05,DAE06,DAE07,DAE08,DAE09,DAE10,DAE11,DAE12,DAE13,
     *      DAE14,DAE15,DAE16,DAE17,DAE18,DAE19,DAE20,RSWE01,RSWE02,RSWE03,RSWE04,
     *      RSWE05,RSWE06,RSWE07,RSWE08,RSWE09,RSWE10,RSWE11,RSWE12,RSWE13,RSWE14,
     *      RSWE15,RSWE16,RSWE17,RSWE18,RSWE19,RSWE20,RSWE21,RSWE22,RSWE23,RSWE24,
     *      RSWE25,RSWE26,RSWE27,RSWE28,RSWE29,RSWE30,RSWE31,RSWE32,RSWE33,RSWE34,
     *      RSWE35,RSWE36,C11,C12,C13,C14,C15,C16,C17,C21,C22,C23,C24,C25,C26,C27,
     *      C31,C32,C33,C34,C35,C36,C37,FM1,FM2,FM3,FM4,CE11,CE12,CE13,CE21,CE22,C
     *      E23,CE31,CE32,CE33,CE41,CE42,CE43,CE51,CE52,CE53,RSW1,RSW2,DRSW1DPG,DR
     *
SW2DPG,QGDARCY,QWDARCY,QWDARCY1,QGDARCY1L,QWDARCY2,QGDA1,QGDA2,QGDA11,
     *      QGDA12,QGDA21,QGDA22,QGDA1R,QGDA2R,QGDA11R,QGDA12R,QGDA21R,QGDA22R,QGR
     *      SW1,QGRSW2,QGRSW11,QGRSW12,QGRSW21,QGRSW22,QGRSW1R,QGRSW2R,QGRSW11R,QG
     *      RSW12R,QGRSW21R,QGRSW22R,QGDARCY1,QWDARCY11,QWDARCY21,QGDA111,QGDA121,
     *      QGDA211,QGDA221,QGRSW111,QGRSW121,QGRSW211,QGRSW221,QGDARCY1R,QWDARCY1
     *      1R,QWDARCY21R,QGDA111R,QGDA121R,QGDA211R,QGDA221R,QGRSW111R,QGRSW121R,
     *      QGRSW211R,QGRSW221R,ALI,ALI1,ALI11,ALI2,ALI22,ALI3,ALI4,XR1,XR2,XRN,MO
     *      ISTURE,ASH,MULTIPLIER,WI1,WI2,QSP,CC,QWELL,PGL,SGL,PGR,PG,SG,Y1,ZAMAN(
     *      1002),QGIN(1002),QWIN(1002),QGPRO(1002),QWPRO(1002),ADSRT1(1002),ADSRT
     *      2(1002),ADSRT3(1002),PWELL1(1002),QGCUM(1002),QWCUM(1002),ADSRATE1,ADS
     *      RATE2,ADSRATE3,QG1ATWELL,RR,PWW,UP(3,4),UPX(3,4),UPXX(3,4),ZOC(10),WOC
     *      (10),AOC(10,10),BOC(10,10)
      Integer GASCOMP,FLAG1,J1,J5,ITER1,Iloop,BC,IWELL,QB,II,NSUB,ISYM
!
!:Executable Code and Common Blocks Section
!
      Common/USRI00P/ IOFSET
      Common/WEIGHTS/ PROOT(NCMAX),WQ(NCMAX),AX(NCMAX,NCMAX),BXX(NCMAX,NCMAX)
      Common/USRR01P/
R,ALFA,PSC,TSC,DEPTH,DZ,CP,CM,ROC,POROI,KABSI,CLSP,PW,PGRAD,TGRAD,OBGR
     *          AD,TRES,POB,VL1,PL1,PC1,TC1,CONV1,CONV2,CONV3,CONV4,VL2,PL2,PC2,TC2,PM
     *
AX,VMAX,V,H,KRGC,KRWC,QG1,QW1,QG2,QW2,SG2,ROSC,CW,KRCW,KRCG,SWIRR,SGIR
     *          R,RW,RE,SKIN,TEMP,PGI,S,LOGR,PWELL,SWELL,PCGW,PORO,KABS,SWN,KRG,KRW,DV
     *          T,DVP,BG,BW,DA,BOB,MW,MW1,MW2,Z,ZZ,Z1,Z2,DZDPG,RO,KK1,XK1,YK1,VISG,VIS
     *          W,A,B,SG1,QGSP,QWSP,QTSP,A11,A12,A13,A21,A22,A23,VL3,VL3IRR,PO,CBET,PC
     *          ,TC,VIRR,TAO,DI,AA1,AA2,AA3,Y11,AB1,BB1,BB2,BB3,BB4,BB5,BB6,BB7,BB8,CO
     *          EFF1,COEFF2,DPGDR,DVP1,DBW,DPORO,DBG,CG,CG1,CG2,ALFA1,FLOWGP,FLOWWP,SG
     *          P,DSGDR,VL10,VL20,VL30,PGQ,ADSA,K1,K2,FLOWGI,FLOWWI,SGI,PG1,XG1,DPOROD
```

```
     *
PG,DKABSDPORO,DSWNDSG,DSWNDSW,DKRGDSWN,DKRWDSWN,EU,DZFAC,DZFAC1,DZFAC2
     *
,D2ZDPG2,D2ZDPG21,D2ZDPG22,D2ZDPG2T,DPCGWDSW,DPCGW2DSW2,DBWDPW,DBGDPG,
     *
DVISGDROG,DROGDPG,DVISWDPW,DRSWDPG,D2BGDPG2,ADSCO2,ADSCH4,BULKCO2,BULK
     *          CH4,CO2IN,CH4IN,H2OIN,EKO01,EKO02,EKO03,EKO04,EKO05,EKO06,EKO07,EKO08,
     *          EKO09,EKO10,EKO11,EKO12,EKO13,EKO14,EKO15,EKO16,EKO17,EKO18,EKO19,EKO2
     *          0,EKO21,EKO22,EKO23,EKO24,EKO25,EKO26,EKO27,EKO28,EKO29,EKO30,DAE01,DA
     *          E02,DAE03,DAE04,DAE05,DAE06,DAE07,DAE08,DAE09,DAE10,DAE11,DAE12,DAE13,
     *          DAE14,DAE15,DAE16,DAE17,DAE18,DAE19,DAE20,RSWE01,RSWE02,RSWE03,RSWE04,
     *          RSWE05,RSWE06,RSWE07,RSWE08,RSWE09,RSWE10,RSWE11,RSWE12,RSWE13,RSWE14,
     *          RSWE15,RSWE16,RSWE17,RSWE18,RSWE19,RSWE20,RSWE21,RSWE22,RSWE23,RSWE24,
     *          RSWE25,RSWE26,RSWE27,RSWE28,RSWE29,RSWE30,RSWE31,RSWE32,RSWE33,RSWE34,
     *          RSWE35,RSWE36,C11,C12,C13,C14,C15,C16,C17,C21,C22,C23,C24,C25,C26,C27,
     *          C31,C32,C33,C34,C35,C36,C37,FM1,FM2,FM3,FM4,CE11,CE12,CE13,CE21,CE22,C
     *          E23,CE31,CE32,CE33,CE41,CE42,CE43,CE51,CE52,CE53,RSW1,RSW2,DRSW1DPG,DR
     *
SW2DPG,QGDARCY,QWDARCY,QWDARCY1,QGDARCY1L,QWDARCY2,QGDA1,QGDA2,QGDA11,
     *
QGDA12,QGDA21,QGDA22,QGDA1R,QGDA2R,QGDA11R,QGDA12R,QGDA21R,QGDA22R,QGR
     *
SW1,QGRSW2,QGRSW11,QGRSW12,QGRSW21,QGRSW22,QGRSW1R,QGRSW2R,QGRSW11R,QG
     *
RSW12R,QGRSW21R,QGRSW22R,QGDARCY1,QWDARCY11,QWDARCY21,QGDA111,QGDA121,
     *
QGDA211,QGDA221,QGRSW111,QGRSW121,QGRSW211,QGRSW221,QGDARCY1R,QWDARCY1
     *
1R,QWDARCY21R,QGDA111R,QGDA121R,QGDA211R,QGDA221R,QGRSW111R,QGRSW121R,
     *          QGRSW211R,QGRSW221R,ALI,ALI1,ALI11,ALI2,ALI22,ALI3,ALI4,XR1,XR2,XRN,MO
     *          ISTURE,ASH,MULTIPLIER,WI1,WI2,QSP,CC,QWELL,PGL,SGL,PGR,PG,SG,Y1,ZAMAN
     *          ,QGIN ,QWIN ,QGPRO ,QWPRO ,ADSRT1 ,ADSRT2 ,ADSRT3 ,PWELL1 ,QGCUM ,QWCU
     *          M ,ADSRATE1,ADSRATE2,ADSRATE3,QG1ATWELL,RR,PWW,UP ,UPX ,UPXX ,ZOC ,WOC
     *          ,AOC ,BOC
      Common/USRI01P/ GASCOMP,FLAG1,J1,J5,ITER1,Iloop,BC,IWELL,QB,II,NSUB,ISYM
!
!:Enter the User's Statement Section
!:Retrieve the Sensitivity Parameters
!
      If (GASCOMP.EQ.1) Then
      PC=1100
      TC=64.4
      MW=44.01
      ElseIf (GASCOMP.EQ.2) Then
      PC=673.1
      TC=-116.7
      MW=16
      ElseIf (GASCOMP.EQ.0)Then
      Write (*,*) '*******NO GAS COMPONENTS?******'
      EndIf
      TEMP=TEMP+460
      TC=TC+460
      TTR=TC/TEMP
      YY=0.001
      Do J=1,100
      SE1=-0.06125/PC*TTR*exp(-1.2*(1-TTR)**2)
```

```
      SE2=14.76*TTR-9.76*TTR**2+4.58*TTR**3
      SE3=90.7*TTR-242.2*TTR**2+42.4*TTR**3
      SE4=2.18+2.82*TTR
      SE5=29.52*TTR-19.52*TTR**2+9.16*TTR**3
      SE6=1.18+2.82*TTR
      DERVALF=-SE5*YY+SE4*SE3*YY**SE6+(1.0+4*YY+4.0*YY**2-4.0*YY**3+YY**4)/(1.0-YY)**4
      VALF=SE1*U(2)-SE2*YY**2+SE3*YY**SE4+YY*(1.0+YY+YY**2-YY**3)/(1.0-YY)**3
      If (abs(VALF).LT.1.0E-4)Then
      ZZ=-(SE1*U(2))/YY
      DZFAC=ZZ/U(2)+ZZ*SE1/YY/DERVALF
      CG=1.0/U(2)-DZFAC/ZZ
      D2ZDPG2=-ZZ*CG/U(2)+(SE1/YY/DERVALF)*DZFAC
      Return
      EndIf
      YY=YY-VALF/DERVALF
      EndDo
!
!:End of User Procedure
!
      Return
      End
```

REFERENCES

1. Hansen, J., Sato, M., Ruedy, R., Lacis, A., and Oinas, V., "Global warming in the twenty-first century: An alternative scenario", Proc.Natl.Acad.Sci., (1997), pp.9875-9880.
2. Halmann, M. M. and Steinberg, M., "Greenhouse gas carbon dioxide mitigation: Science and technology", Lewis Publishers, Boca Raton-FL, (1999).
3. Intergovernmental Panel on Climate Change (IPCC), "Climate change 1995: The science of climate change", Cambridge University Press, (1996).
4. Bryant, E., "Climate process and change", Cambridge University Press, Cambridge-UK, (1997).
5. Bolin, B., "The Kyoto negotiations on climate change: A science perspective", Science, (1998), pp.330-331.
6. Reichle, D., Houghton, J., Kane, B., and Ekmann, J. et al., "Carbon sequestration: Research and development", U.S. DOE report, (1999).
7. Herzog, H. J. and Drake, E. M., "Carbon dioxide recovery and disposal from large energy systems", Annual Review of Energy and the Environment, Vol.21 (1996), pp.145-166.
8. Bachu, S., "Sequestration of CO_2 in geological media: criteria and approach for site selection in response to climate change", Energy Convers.Manage., Vol.41, (2000), pp.953-970.
9. Gentzis, T., "Subsurface sequestration of carbon dioxide- an overview from an Alberta (Canada) perspective", Int.J.Coal Geol., Vol.43 (2000), pp.287-305.
10. White, C. M., Straeisar, B. R., Granite, E. J., Hoffman, J. S., and Pennline, H. W., "Separation and capture of CO_2 from large stationary sources and sequestration in geological formations", J.Air & Waste Manag.Assoc., Vol.53 (2003), pp.645-715.
11. Kolesar, J. E., Ertekin, T., and Obut, S. T., "The unsteady-state nature of sorption and diffusion phenomena in the micropore structure of coal: Part 2: Solution", SPE Formation Evaluation, (1990), pp.81-88.

12. Meyers, R. A., "Coal Structure", Academic Press, N.Y., (1982).

13. Gamson, P. D., Beamish, B. B., and Johnson, D. P., "Coal microstructure and micropermeability and their effects on natural gas recovery", Fuel, Vol.72 (1993), pp.87-99.

14. Collins, R. E., "New theory for gas adsorption and transport in coal", Proc. of the 1991 Coalbed Methane Symposium, Tuscaloosa, May 13-16, (1991).

15. Ozdemir, E., Schroeder, K., and Morsi, B. I., "Global warming: Carbon dioxide sequestration in coal seams", Proc. of. Am. Chem. Soc., Vol.42 (2002), pp.310-317.

16. Toda, Y., "Densities of coals measured with various liquids", Fuel, Vol.51 (1972), pp.108-112.

17. Lucht, L. M., Larson, J. M., and Peppas, N. A., "Macromolecular structure of coals: 9. Molecular structure and glass transition temperature", Energy & Fuels, Vol.1 (1987), pp.56-58.

18. Shimizu, K., Takanohashi, T., and Iino, M., "Sorption behaviors of various organic vapors to Argonne Premium coal samples", Energy & Fuels, Vol.12 (1998), pp.891-896.

19. Khan, M. R. and Jenkins, R. G., "Thermoplastic properties of coal at elevated pressures: effects of gas atmospheres", PennState University, State College, PA, (1985).

20. Ceglarska-Stefanska, G. and Czaplinski, A., "Correlation between sorption and dilatometric processes in hard coals", Fuel, Vol.72 (1993), pp.413-417.

21. Shimizu, K., Takanohashi, T., and Iino, M., "Sorption behaviors of various organic vapors to Argonne Premium coal samples", Energy & Fuels, Vol.12 (1998), pp.891-896.

22. Takanohashi, T., Terao, Y., Yoshida, T., and Iino, M., "Adsorption and diffusion of alcohol vapors by Argonne Premium coals", Energy & Fuels, Vol.14 (2000), pp.915-919.

23. Walker, P. L. J. and Mahajan, O. P., "Pore structure in coals", Energy & Fuels, Vol.7 (1993), pp.559-560.

24. Larsen, J. W., Hall, P., and Wernett, P. C., "Pore structure of Argonne Premium coals", Energy & Fuels, Vol.9 (1995), pp.324-330.

25. Larsen, J. W. and Wernett, P. C., "The Argonne coals do not have an extended inter-connected pore network", Preprints of Papers, Am. Chem. Soc., Div. of Fuel Chem., Vol.37 (1992), pp.849-855.

26. Mahajan, O. P., "Coal porosity", In: Meyers, R. A, "Coal structure", Academic Press, N.Y., (1982), pp.51-86.

27. Marsh, H., "Adsorption methods to study microporosity in coals and carbons - a critique", Carbon, Vol.25 (1987), pp.49-58.

28. Larsen, J. W. and Wernett, P., "Pore structure of Illinois No. 6 coal", Energy & Fuels, Vol.2 (1988), pp.719-720.

29. Gan, H., Nandi, S. P., and Walker, P. L. Jr., "Nature of the porosity in American coals", Fuel, Vol.51 (1972), pp.272-277.

30. Walker Jr., P. L. and Kini, K. A., "Measurement of the ultrafine surface area of coals", Fuel, Vol.44 (1965), pp.453

31. Medek, J., "Possibility of micropore analysis of coal and coke from the carbon dioxide isotherm", Fuel, Vol.56 (1977), pp.131-133.

32. Milewska-Duda, J., Duda, J., Nodzenski, A., and Lakatos, J., "Absorption and adsorption of methane and carbon dioxide in hard coal and active carbon", Langmuir, Vol.16 (2000), pp.5458-5466.

33. Takanohashi, T., Terao, Y., Yoshida, T., and Iino, M., "Adsorption and diffusion of alcohol vapors by Argonne Premium coals", Energy & Fuels, Vol.14 (2000), pp.915-919.

34. Grzybek, T., Jodlowski, G. S., Kreiner, K., Milewska-Duda, J., and Zyla, M., "Surface changes in coals after oxidation. 2. H_2O Sorption Studies", Langmuir, Vol. 13 (5), (2002), pp.1123-1127.

35. Reucroft, P. J. and Patel, K. B., "Surface area and swellability of coal", Fuel, Vol.62 (1983), pp.279-284.

36. Reucroft, P. J. and Sethuraman, A. R., "Effect of pressure on carbon dioxide induced coal swelling", Energy & Fuels, Vol.1 (1987), pp.72-75.

37. St.George, J. D. and Barakat, M. A., "The Change in effective stress associated with shrinkage from gas desorption in coal", International Journal of Coal Geology, Vol.45 (2001), pp.105-113.

38. Milewska-Duda, J. and Duda, J., "Hard coal surface heterogeneity in the sorption process", Langmuir, Vol.13 (1997), pp.1286-1296.

39. Joubert, J. I., Grein, C. T., and Bienstock, D., "Sorption of methane in moist coal", Fuel, Vol.52 (1972), pp.185.

40. Joubert, J. I., Grein, C. T., and Bienstock, D., "Effect of moisture on the methane capacity of American coals", Fuel, Vol.53 (1974), pp.186-190.

41. Levy, J. H., Day, S. J., and Killingley, J. S., "Methane capacities of Bowen Basin coals related to coal properties", Fuel, Vol.76 (1997), pp.813-819.

42. Bustin, M., "Research activities on CO_2, H_2S, and SO_2 sequestration at UBC", Coal Seq. I Symp., Huston, TX, March 14-15, (2002).

43. Schroeder, K., Ozdemir, E., and Morsi, B. I., "Sequestration of carbon dioxide in coal seams", First National Carbon Seq. Conf., U.S.DOE/NETL, (2001), pp.1-10.

44. Bustin, R. M. and Clarkson, C. R., "Geological controls on coalbed methane reservoir capacity and gas content.", Int.J.Coal Geol., Vol.38 (1998), pp.3-26.

45. Crosdale, P. J., Basil Beamish, B., and Valix, M., "Coalbed methane sorption related to coal composition", International Journal of Coal Geology, Vol.35 (1998), pp.147-158.

46. Ruppel, T. C., Grein, C. T., and Bienstock, D., "Adsorption of methane/ethane mixture on dry coal at elevated pressure", Fuel, Vol.51 (1972), pp.297-303.

47. Yang, R. T. and Saunders, J. T., "Adsorption of gases on coals and heat-treated coals at elevated temperature and pressure 1.Adsorption from hydrogen and methane as single gases", Fuel, Vol.64 (1985), pp.616-620.

48. Saunders, J. T., Tsai, B. M. C., and Yang, R. T., "Adsorption of gases on coals and heat-treated coals at elevated temperature and pressure 2.Adsorption from hydrogen-methane mixtures", Fuel, Vol.64 (1985), pp.621-626.

49. Yong, Z., Mata, V., and Rodrigues, A. E., "Adsorption of carbon dioxide at high temperature-a review", Seperation and Purification Technology, Vol.26 (2002), pp.195-205.

50. Nodzenski, A., "Sorption and desorption of gases (CH_4,CO_2) on hard coal and active carbon at elevated pressures", Fuel, Vol.77 (1998), pp.1243-1246.

51. Clarkson, C. R. and Bustin, R. M., "The Effect of pore structure and gas pressure upon the transport properties of coal: a laboratory and modeling study. 1. Isotherms and pore volume distributions.", Fuel, Vol.78 (1999), pp.1333-1344.

52. Clarkson, C. R., "The effect of coal composition, moisture content, and pore volume distribution upon single and binary gas equilibrium and nonequilibrium adsorption: implications for gas content determination", Ph.D. Dissertation, Univ. of British Columbia, Canada,. (1998).

53. Al-hawaree, M., "Geomechanics of CO_2 Sequestration in Coalbed Methane Reservoirs", M.S. Thesis, Univ. of Alberta, Canada, (1999).

54. Hall, F. E., Zhou, C., and Gasem, K. A. M., "Adsorption of pure methane, nitrogen, and carbon dioxide and their binary mixtures on wet Fruitland coal", SPE 29194, SPE Eastern Regional Conf. and Exhib., Charleston, WV, Nov. 8-10, (1994), pp.329-344.

55. Zhou, C., "Modeling and prediction of pure and multicomponent gas adsorption", Ph.D. Dissertation, Oklahoma State Univ., (1994).

56. Krooss, B. M., van Bergen, F., Gensterblum, Y., Siemons, N., Pagnier, H. J. M., and David, P., "High-pressure methane and carbon dioxide adsorption on dry and moisture-equilibrated Pennsylvanian coals", Int.J.Coal Geol., Vol.51 (2002), pp.69-92.

57. Stevens, S. H., Kuuskraa, V. A., Spector, D., and Riemer, P., "CO_2 sequestration in deep coal seams : Pilot results and worldwide potential (1999), pp.175-180.

58. Van Krevelen, D. W., "Coal", Elsevier, N.Y., (1961).

59. Smith, K. L., Smooth, L. D., Fletcher, T. H., and Pugmire, R. J., "The Structure and reaction processes of coal", Plenium Press, N.Y., (1994).

60. Haenel, M. W., "Recent progress in coal structure research", Fuel, Vol.71 (1992), pp.1211-1223.

61. Meyers, R. A., "Coal Handbook", Marcel Dekker, N.Y., (1981).

62. Doyle, B. R., "Hazardous gases underground: Application to tunnel engineering", Marcel Dekker, N.Y., (2001).

63. Rogers, R. E., "Coalbed methane: Principles and practice", Prentice Hall, New Jersey, (1994).

64. Clayton, J. L., "Geochemistry of coalbed gas - A review", International Journal of Coal Geology, Vol.35 (1998), pp.159-173.

65. Schobert, H. H., "The Chemistry of hydrocarbon fuels", Butterworth & Co., N.Y., (1990).

66. Bratek, K., Bratek, W., Gerus-Piasecka, I., Jaseinko, S., and Wilk, P., "Properties and structure of different rank anthracites", Fuel, Vol.81 (2002), pp.97-108.

67. Gorbaty, M. L., "Prominent frontiers of coal science: past, present and future", Fuel, Vol.73 (1994), pp.1819-1828.

68. Jones, J. M., Pourkashanian, M., Rena, C. D., and Williams, A., "Modeling the relationship of coal structure to char porosity", Fuel, Vol.78 (1999), pp.1737-1744.

69. Given, P. H., "The distribution of hydrogen in coals and its relation to coal structure", Fuel, Vol.39 (1960), pp.147.

70. Wiser, W. H., In: Proceeding of the EPRI Conference on Coal Catalysis, Conference Proceedings, Pola Alto, CA, (1973), pp.3.

71. Nakamura, K., "A Model structure of Zao Zhuang bituminous coal", Energy & Fuels, Vol.9 (1995), pp.1003-1010.

72. Ohkawa, T., Sasai, T., and Komoda, N., "Computer-aided construction of coal molecular structure using construction knowledge and partial structure evaluation", Energy & Fuels, Vol.11 (1997), pp.937-944.

73. Mathews, J. P., Hatcher, P. G., and Scaroni, A. W., "Proposed model structures for Upper Freeport and Lewiston-Stockton vitrinites", Energy & Fuels, Vol.15 (2001), pp.863-873.

74. Shinn, J. H., "From coal to single-stage and two-stage products: A reactive model of coal structure", Fuel, Vol.63 (1984), pp.1187.

75. Marzec, A., "Macromolecular and molecular model of coal structure", Fuel Process.Technol., Vol.14 (1986), pp.39-46.

76. Miura, K., Mae, K., Li, W., Kusakawa, T., Morozumi, F., and Kumano, A., "Estimation of hydrogen bond distribution in coal through the analysis of OH stretching bands in diffuse reflectance infrared spectrum measured by in-situ technique", Energy & Fuels, Vol.15 (2001), pp.599-610.

77. Takanohashi, T., Kudo, T., and Iino, M., "Coal gels formed by coal-solvent interactions", Energy & Fuels, Vol.12 (1998), pp.470-475.

78. Khan, M. R. and Jenkins, R. G., "Thermoplastic properties of coal at elevated pressures 1. Evaluation of a high-pressure microdilatometer", Fuel, Vol.63 (1984), pp.109-115.

79. Larsen, J. W., Flowers, R. A., Hall, P. J., and Carlson, G., "Structural rearrangement of strained coals", Energy & Fuels, Vol.11 (1997), pp.998-1002.

80. Cody, G. D. J., Larsen, J. W., and Siskin, M., "Anisotropic solvent swelling of coals", Energy & Fuels, Vol.2 (1988), pp.340-344.

81. Haward, R. N., "The physics of glassy polymers", Wiley, N.Y., (1973).

82. Peppas, N. A., "Swelling and dissolution of the macromolecular structure of bituminous coals", Polymer, Vol.38 (1997), pp.3425-3427.

83. Cartz, L., Diamond, R., and Hirsch, P. B., Nature, Vol.177 (1956), pp.500.

84. Sharma, S., Kyotani, T., and Tomita, A., "Direct observation of layered structure of coals by a transmission electron microscope", Energy & Fuels, Vol.14 (2000), pp.515-516.

85. Sharma, A., Kyotani, T., and Tomita, A., "Direct observation of raw coals in lattice fringe mode using high-resolution transmission electron microscopy", Energy & Fuels, Vol.14 (2000), pp.1219-1225.

86. Wertz, D. L. and Quin, J. L., "Wide angle X-ray scattering study of the layering in three of the Argonne Premium coals", Fuel, Vol.79 (2000), pp.1981-1989.

87. International Union of Pure and Applied Chemistry (IUPAC), "Manuals of symbols and terminology for physico chemical quantities and units", Butterworth, Londan, U.K.,. (1972).

88. Wernett, P. C., Larsen, J. W., Yamada, O., and Hong J. Y., "Determination of the average micropore diameter of an Illinois No. 6 coal by ^{129}Xe NMR", Energy & Fuels, Vol.4 (1990), pp.412-413.

89. Tsiao, C. and Botto, R. E., "^{129}Xe NMR investigation of coal micropores", Energy & Fuels, Vol.5 (1991), pp.87-92.

90. Amarasekera, G., Scarlett, M. J., and Mainwaring, D. E., "Micropore size distributions and specific interactions in coals", Fuel, Vol.74 (1995), pp.115-118.

91. Hayashi, J., Norinaga, K., Kudo, N., and Chiba, T., "Estimation of size and shape of pores in moist coal utilizing sorbed water as a molecular probe", Energy & Fuels, Vol.15 (2001), pp.903-909.

92. Radovic, L. R., Menon, V. C., Leon, C. A., Kyotani, T., Danner, R. P., Anderson, S., and Hatcher, P. G., "On the porous structure of coals: Evidence for an interconnected but constricted micropore system and implications for coalbed methane recovery", Adsorption, Vol.3 (1997), pp.221-232.

93. Mahajan, O. P. and Walker, P. L. J., "Porosity of coals and coal products", Report, PennState Univ., State College, PA, (1978).

94. Mahajan, O. P., "Coal porosity", In: Meyers, R. A., "Coal structure", Academic Press, N.Y., (1982), pp.51-86.

95. Grimes, W. R., Gorbaty, M. L., Larsen, J. W., and Wender, I., "The physical structure of coal: Coal science", Volume 1 (1982), pp.21-42.

96. Jones, A. H., Bell, G. J., and Schraufnagel, R. A., "A review of the physical and mechanical properties of coal with implications for coal-bed methane well completion and production", (1988), pp.169-181.

97. Senel, I. G., Guruz, A. G., Yucel, H., Kandas, A. W., and Sarofim, A. F., "Characterization of pore structure of Turkish coals", Energy & Fuels, Vol.15 (2001), pp.331-338.

98. Huang, H., Wang, K., Bodily, D. M., and Hucka, V. J., "Density measurements of Argonne Premium coal samples", Energy & Fuels, Vol.9 (1995), pp.20-24.

99. Walker, P. L., Jr., Verma, S. K., Rivera-Utrilla, J., and Davis, A., "Densities, porosities and surface areas of coal macerals as measured by their interaction with gases, vapors and liquids", Fuel, Vol.67 (1988), pp.1615-1623.

100. King, J. G. and Wilkins, E. T., Proc. Conf. Ultrafine Structure of Coals, Bcura, London, U.K., (1944), pp.46.

101. Walker, P. L., Verma, S. K., Rivera-Utrilla, J., and Khan, R., "A direct measurement of expansion in coals and macerals induced by carbon dioxide and methanol", Fuel, Vol.67 (1988), pp.719-726.

102. Alexeev, A. D., Vasilensko, T. A., and Ulyanova, E. V., "Closed porosity in fossil coals", Fuel, Vol.78 (1999), pp.635-638.

103. Gregg, S. J. and Sing, K. S. W., "Adsorption, surface area and porosity", Academic Press, N.Y., (1982).

104. Nandi, A. P. and Walker, P. L. Jr., "Surface areas of coals", Fuel, Vol.47 (1968), pp.322-324.

105. Nandi, S. P. and Walker, P. L. Jr., "Activated diffusion of methane in coal", Fuel, Vol.49 (1970), pp.309-323.

106. Anderson, R. B., Bayer, J., and Hofer, L. J. E., "Determining surface areas from CO_2 adsorption isotherms at -78 ^oC", Fuel, Vol.44 (1965), pp.443-452.

107. Walker, P. L. and Geller, I., "Change in surface of anthracite on heat treatment", Nature, Vol.178 (1956), pp.1001-1001.

108. Anderson, R. B., Hall, W. K., Lecky, J. A., and Stein, K. C., "Sorption studies on American coals", J.Phys.Chem., Vol.60 (1956), pp.1548-1558.

109. Mahajan, O. P., "CO_2 surface area of coals: The 25-year paradox", Carbon, Vol.29 (1991), pp.735-742.

110. Walker, P. L., "Microporosity in coal: its characterization and its implications for coal utilization", Philos.Trans.R.Soc.London, Ser.A, Vol.300 (1981), pp.65-81.

111. Astakhov, A. V., Bunin, A. V., and Khazov, S. P., "Capillary condensation of gases adsorbed in coal pores", Khimiya Tverdogo Topliva (Leningrad) (USSR), Vol.4 (1991), pp.47-49.

112. Gan, H., Nandi, S. P., and Walker, P. L. Jr., "Nature of the porosity in American coals", Fuel, Vol.51 (1972), pp.272-277.

113. Reucroft, P. J. and Patel, H., "Gas-induced swelling in coal", Fuel, Vol.65 (1986), pp.816-820.

114. Walker, P. L. J., Davis, A., Verma, S. K., Rivera-Utrilla, J., and Khan, M. R., "Data base for the analysis of compositional characteristics of coal seams and macerals", Final report, PennState university, State College, PA, (1984).

115. Astakhov, A. V. and Shirochin, D. L., "Capillary-like condensation of sorbed gases in coals", Fuel, Vol.70 (1991), pp.51-56.

116. Bustin, R. M. and Clarkson, C. R., "Geological controls on coalbed methane reservoir capacity and gas content", Int.J.Coal Geol., Vol.38 (1998), pp.3-26.

117. Diamond, W. P. and Schatzel, S. J., "Measuring the gas content of coal: A review", Int.J.Coal Geol., Vol.35 (1998), pp.311-331.

118. Clarkson, C. R., Bustin, R. M., and Levy, J. H., "Application of the mono/multilayer and adsorption potential theories to coal methane adsorption isotherms at elevated temperature and pressure", Carbon, Vol.35 (1997), pp.1689-1705.

119. IUPAC, "Manual of Symbols and Terminology, Appendix 2, Colloid and Surface Chemistry", Pure Appl.Chem., Vol.31 (1972), pp.578

120. Choi, J., Do, D. D., and Do, H. D., "Surface diffusion of adsorbed molecules in porous media: Monolayer, multilayer, and capillary condensation regimes", Ind.Eng.Chem.Res., Vol.40 (2001), pp.4005-4031.

121. Langmuir, I., "The adsorption of gases on plane surfaces of glass, mica and platinum", J.Am.Chem.Soc., Vol.40 (1918), pp.1361

122. Brunauer, S., Emmett, P. H., and Teller, E., J.Am.Chem.Soc., Vol.60 (1938), pp.309.

123. Aranovich, G. L. and Donohue, M. D., "Adsorption isotherms for microporous adsorbents", Carbon, Vol.33 (1995), pp.1369-1375.

124. Gil, A. and Grange, P., "Application of the Dubinin-Radushkevich and Dubinin-Astakhov equations in the characterization of microporous solids", Colloids and Surfaces A, Vol.113 (1996), pp.39-50.

125. Polanyi, M., Trans.Faraday Soc., Vol.28 (1932), pp.316.

126. Dubinin, M. M., "Porous structure and adsorption properties of active carbons", In: Walker P.L., "Chemistry and physics of carbon", Marcel Dekker, N.Y.,(1966), pp.51-120.

127. Sircar, S., "Gibbsian surface excess for gas adsorption-revisited", Ind.Eng.Chem.Res., Vol.38 (1999), pp.3670-3682.

128. Relch, R., Zlegler, W. T., and Rogers, K. A., "Adsorption of methane, ethane, and ethylene gases and their binary and ternary mixtures and carbon dioxide on activated carbon at 212-301 K and pressures to 35 atmospheres", Ind.Eng.Chem.Process Des.Dev., Vol.19 (1980), pp.336-344.

129. Dubinin, M. M., "The potential theory of adsorption of gases and vapors for adsorbents with energetically nonuniform surfaces", Chem.Rev., Vol.60 (1960), pp.234-241.

130. Murata, K., El-Merraoui, M., and Kaneko, K., "A new determination method of absolute adsorption isotherm of supercritical gases under high pressure with a special relevance to density-functional theory study", J.Chem.Phys., Vol.114 (2001), pp.4196-4205.

131. Salem, M. M. K., Braeuer, P., Szombathely, M., Heuchel, M., Harting, P., and Quitzsch, K., "Thermodynamics of high-pressure adsorption of argon, nitrogen, and methane on microporous adsorbents", Langmuir, Vol.14 (1998), pp.3376-3389.

132. Wakasugi, Y., Ozawa, S., and Ogino, Y., "Physical adsorption of gases at high pressure V. An extension of a generalized adsorption equation to systems with polar adsorbents", J.Colloid.Interface Sci., Vol.79 (1981), pp.399-409.

133. Humayun, R. and Tomasko, D. L., "High-resolution adsorption isotherms of supercritical carbon dioxide on activated carbon", A.I.Ch.E.J., Vol.46 (2000), pp.2065-2075.

134. Chaback, J. J., Morgan, W. D., and Yee, D., "Sorption of nitrogen, methane, carbon dioxide and their mixtures on bituminous coals at in-situ conditions", Fluid Phase Equilibria, Vol.117 (1996), pp.289-296.

135. Do, D. D., "Adsorption analysis: Equilibria and kinetics", Imperial College Press, London, U.K., (1998).

136. Suzuki, M., "Adsorption engineering", Elsevier, N.Y., (1990).

137. Reid, R. C., Prausnitz, J. M., and Sherwood, T. K., "The Properties of gases and liquids", McGraw Hill, N.Y., 3rd Ed. (1977).

138. Kamiuto, K., Ermalina, and Ihara, K., "CO_2 adsorption equilibria of the honeycomb zeolite beds", Applied Energy, Vol.69 (2001), pp.285-292.

139. Amankwah, K. A. G. and Schwarz, J. A., "A modified approach for estimating pseudo-vapor pressures in the application of the Dubinin-Astakhov equation", Carbon, Vol.33 (1995), pp.1313-1319.

140. Sobolik, J. l., Ludlow, D. K., and Hesevich, W. L., "Parametric sensitivity comparison of the BET and Dubinin-Radushkevich models for determining char surface area by CO_2 adsorption", Fuel, Vol.71 (1992), pp.1195-1202.

141. Clarkson, C. R., Bustin, R. M., and Levy, J. H., "Application of the mono/multilayer and adsorption potential theories to coal methane adsorption isotherms at elevated temperature and pressure", Carbon, Vol.35 (1997), pp.1689-1705.

142. Bradley, R. H. and Rand, B., "On the physical adsorption of vapors by microporous carbon", J.Colloid.Interface Sci., Vol.169 (1995), pp.168-176.

143. Paulsen, P. D., Moore, B. C., and Cannon, F. S., "Applicability of adsorption equations to argon, nitrogen, and volatile organic compound adsorption onto activated carbon", Carbon, Vol.37 (1999), pp.1843-1853.

144. Martin-Martinez, J. M., Torregrosa-Marcia, R., and Mittelmeijer-Hazeleger, M. C., "Mechanisms of adsorption of CO_2 in the micropores of activated anthracite", Fuel, Vol.74 (1995), pp.111-114.

145. DeGance, A. E., Morgan, W. D., and Yee, D., "High pressure adsorption of methane, nitrogen and carbon dioxide on coal substrates", Fluid Phase Equilibria, Vol.82 (1993), pp.215-224.

146. Payne, H. K., Sturdevant, G., and Leland, T., "Improved two-dimensional equation of state to predict adsorption of pure and mixed hydrocarbons", I&EC Fund., Vol.7 (1968), pp.363-374.

147. Myers, A. L. and Prausnitz, J. M., "Thermodynamics of mixed-gas adsorption", AIChE J., Vol.11 (1965), pp.121-127.

148. Ruthven, D. M., "Principles of adsorption and adsorption processes", Wiley, N.Y., (1984).

149. Toda, Y. and Toyoda, S., "Experimental relation between Dubinin-Polanyi equation and Langmuir equation", Carbon, Vol.10 (1972), pp.231-238.

150. Ettinger, I., Eremin, I., Zimakov, B., and Yanovskaya, M., "Natural factors influencing coal sorption properties I - Petrography and the sorption properties of coals", Fuel, Vol.45 (1966), pp.267-275.

151. Toda, Y., Hatami, M., Toyoda, S., Yoshida, Y., and Honda, H., "Micropore structure of coal", Fuel, Vol.50 (1971), pp.187-200.

152. Spitzer, Z., Biba, V., Bohac, F., and Malkova, E., "Micropore structure analysis of coal from adsorption isotherms of methanol", Fuel, Vol.56 (1977), pp.313-318.

153. Debelak, K. A. and Schrodt, J. T., "Comparison of pore structure in Kentucky coals by mercury penetration and carbon dioxide adsorption", Fuel, Vol.58 (1979), pp.732-736.

154. Lu, X.-C., Li, F.-C., and Watson, A. T., "Adsorption measurements in Devonian Shales", Fuel, Vol.74 (1995), pp.599-603.

155. Salame, I. I. and Bandosz, T. J., "Study of diethyl ether adsorption on activated carbon using IGC at finite concentration", Langmuir, Vol.17 (2001), pp.4967-4972.

156. Ozdemir, E., Morsi, B. I., and Schroeder, K., "Importance of volume effects to adsorption isotherms of carbon dioxide on coals", Langmuir, Vol.19 (2003), pp.9764-9773.

157. Starzewski, P. and Grillet, Y., "Thermochemical studies of adsorption of He and CO_2 on coals at ambient temperature", Fuel, Vol.68 (1989), pp.375-379.

158. Stauffer, D. B., Hirschenhofer, J. H., and White, J. S., "Carbon dioxide capture for emerging energy technologies", Recent advances in coal utilization technology (1994), pp.139-146.

159. Kumar, M. and Hari Shankar, R., "Removal of ash from Indian Assam Coking coal using sodium hydroxide and acid solutions", Energy Sources, Vol.22 (2000), pp.187-196.

160. Hayashi, J., Takeuchi, K., Kusakabe, K., and Morooka, S., "Removal of calcium from low rank coals by treatment with CO_2 dissolved in water", Fuel, Vol.70 (1991), pp.1181-1186.

161. Labuschagne, B. C. J., "Relationships between oil and agglomeration and surface properties of coal: Effect of pH and oil composition", Coal Preparation, Vol.3 (1986), pp.1-13.

162. Sakanishi, K., Watanabe, I., Nonaka, T., Kishino, M., and Mochida, I., "Effects of organic acid pretreatment on the structure and pyrolysis reactivity of coals", Fuel, Vol.80 (2001), pp.273-281.

163. Harvey, R. D. and Ruch, R. R., "Mineral matter in Illinois and other U.S. coals", In: Vorres, K.S., "Mineral matter and ash in coal", ACS, Washington, DC, (1986), pp.10-40.

164. Hendricks, T. A., "The origin of coal", In: Lowry, H.H., "Chemistry of coal utilization", (1945), pp.1-24.

165. Finkelman, R. B. and Stanton, R. W., "Identification and significance of accessory minerals from a bituminous coal", Fuel, Vol.57 (1978), pp.763-768.

166. Thiessen, G., "Forms of sulphur in coal", In: Lowry, H.H., "Chemistry of coal utilization", (1945), pp.425-449.

167. Joseph, J. T. and Forrai, T. R., "Effect of exchangeable cations on liquefaction of low rank coals", Fuel, Vol.71 (1992), pp.75-80.

168. Kirner W.R., "The occurrence of nitrogen in coal", In: Lowry, H.H., "Chemistry of coal utilization", (1945), pp.450-484.

169. Larsen, J. W., Green, T. K., and Kovac, J., "Nature of the macromolecular network structure of bituminous coals", J.Org.Chem., Vol.50 (11-29-1985), pp.4729-4735.

170. Chen, C., Gao, J., and Yan, Y., "Role of noncovalent bonding in swelling of coal", Energy & Fuels, Vol.12 (1998), pp.1328-1334.

171. Mahajan, O. P. and Walker, P. L. Jr., "Effect of inorganic matter removal from coals and chars on their surface areas", Fuel, Vol.58 (1979), pp.333-337.

172. Nishino, J., "Adsorption of water vapor and carbon dioxide at carboxylic functional groups on the surface of coal", Fuel, Vol.80 (2001), pp.757-764.

173. Larsen, J. W., Pan C.S., and Shinn, J. H., "Effect of demineralization on the macromolecular structure of coals", Energy & Fuels, Vol.3 (1989), pp.557-561.

174. Mahajan, O. P. and Walker, P. L. Jr., "Effect of Inorganic Matter Removal from Coals and Chars on Their Surface Areas", Fuel, Vol.58 (2002), pp.333-337.

175. Kim, A. G. and Kissell, F. N., "Methane formation and migration in coalbeds", In: Duel, M, Kim, A.G., "Methane control research: Summary of results", U.S. Dept. of Interior, Breau of Mines, bulletin 687, (1986), pp.18-25.

176. Kuuskraa, V. and Brandenburg, C. F., "Coalbed methane sparks a new energy industry", Oil and Gas Journal, Vol.87 (1989), pp.49-56.

177. Amy, P. and Haldeman, D. L., "The microbiology of the terrestrial deep subsurface", CRC Press, N.Y., (1997).

178. Chen, J. H., Wong, D. S. H., Tan, S. S., Subramanian, R., Lira, C. T., and Orth, M., "Adsorption and desorption of carbon dioxide onto and from activated carbon at high pressures", Ind.Eng.Chem.Res., Vol.36 (1997), pp.2808-2815.

179. Milewska-Duda, J. J. and Milewska-Duda, J., "Analysis of structure of vitrains and durains on the basis of a dual sorption model", Langmuir, Vol.9 (1993), pp.3558-3561.

180. King, G. R. and Ertekin, T., "A survey of mathematical models related to methane production from coal seams, Part I: Empirical & equilibrium sorption models", Proc. of the 1989 Coalbed methane Symp., Tuscaloosa, AL, (1989).

181. King, G. R. and Ertekin, T., "A survey of mathematical models related to methane production from coal seams, Part II: Non-equilibrium sorption models", Proc. of the 1989 Coalbed methane Symp., Tuscaloosa, AL, (1989).

182. King, G. R. and Ertekin, T., "State-of-the-art, modeling for unconventional gas recovery", SPE 29575, Rocky mountain Regional Low Permeability Reservoir Symp., Denver, CO, March 20-22, (1991), pp.289-312.

183. King, G. R. and Ertekin, T., "State-of-the-art modeling for unconventional gas recovery, Part II: Recent developments (1989-1994)", SPE 18947, (1995).

184. Kohler, T. E., "Development and application of a compositional coalbed methane production model", Ph.D. Dissertation, PennState Univ., State College, PA, (1999).

185. Goktas, B., "Development and application of a local grid refinement technique for accurate representation of cavity-completed wells in reservoir simulators", Ph.D. Dissertation, PennState Univ., State College, PA, (1999).

186. Reeves, S. R., "Geological sequestration of CO2 in deep, unmineable coalbeds: An integrated research and commercial- scale field demonstration project",SPE 26894, Eastern Regional Conf. and Exhib., Pittsburgh, PA, Nov. 2-4, (2001), pp. 83-92

187. Bertheux, W. B., "Enhanced coalbed methane production by carbon dioxide injection in water saturated coal; experiments, image analysis, and simulations", M.S. Thesis, Delft Univ. and Technol., Netherlands, (2000).

188. Tsiao, C. and Botto, R. E., "sup 129 Xe NMR investigation of coal micropores", Energy & Fuels, Vol.5 (1991), pp.87-92.

189. King, G. R., Ertekin, T., and Schwerer, F. C., "Numerical simulation of the transient behavior of coal-seam degasification wells", SPE Form.Eval., (1986), pp.165-183.

190. Laubach, S. E., Marrett, R. A., Olson, J. E., and Scott, A. R., "Characteristics and origins of coal cleat-A review", Int.J.Coal Geol., Vol.35 (1998), pp.175-207.

191. Close, J. C., Law, B. E., and Rice, D. D., "Natural fractures in coal", AAPG studies in geology, No.38 (1993), pp.119-132.

192. Su, X., Feng, Y., Chen, J., and Pan, J., "The characteristics and origins of cleat in coal from Western North China", Int.J.Coal Geol., Vol.47 (2001), pp.51-62.

193. Karacan, C. Ö. and Okandan, E., "Fracture / Cleat analysis of coals from Zonguldak Basin (Northwestern Turkey) relative to the potential of coalbed methane production", International Journal of Coal Geology, Vol.44 (2000), pp.109-125.

194. Law, B. E., "The relationship between coal rank and cleat spacing: Implications for the prediction of permeability in coal", (1993), pp.435-442.

195. Massarotto, P., Rudolph, V., Golding, S., and Glikson, M., "4-D coal permeability for geological sequestration of CO_2", 2001 Pittsburgh Coal Conference (2001), pp.1-9.

196. Puri, R. and Seidle, J. P., "Measurement of stress-dependent permeability in coal and its influence on coalbed methane production", Fuel, Vol.16 (1992), pp.183-202.

197. Gash, B. W., "Measurement of 'rock properties' in coal for coalbed methane production", SPE 22909, 66th Ann. tech. Conf. and Exhib., Dallas, TX, Oct. 6-9, (1991), pp. 221-230.

198. Harpalani, S. and Chen, G., "Estimation of changes in fracture porosity of coal with gas emission", Fuel, Vol.74 (1995), pp.1491-1498.

199. Weishauptova, Z. and Medek, J., "Bound forms of methane in the porous system of coal", Fuel, Vol.77 (1998), pp.71-76.

200. Remner, D. J., Ertekin, T., Sung, W., and King, G. R., "A parametric study of the effects of coal seam properties on gas drainage efficiency", SPE Res., (1986), pp.633-646.

201. Ertekin, T., King, G. R., and Schwerer, F. C., "Dynamic gas slippage: A unique dual-mechanism approach to the flow of gas in tight formations", SPE Form.Eval., (1986), pp.43-52.

202. McKee, C. R., Bumb, A. C., and Koenig, R. A., "Stress-dependent permeability and porosity of coal and other geologic formations", SPE Formation Evaluation, (1988), pp.81-91.

203. Reznik, A. A., Singh, P. K., and Foley, W. L., "An Analysis of the Effect of CO_2 Injection on the Recovery of In-Situ Methane From Bituminous Coal: An Experimental Simulation", SPE Journal, (1984), pp.521-528.

204. Puri, R. and Yee, D., "Enhanced Coalbed Methane Recovery", SPE 20732, 65th Annual technical Conf. and Exhib., New Orleans, LA, Sept. 23-26, (1990), pp. 193-202

205. Arri, L. E., Yee, D., Morgan, W. D., and Jeansonne, M. W., "Modeling coalbed methane production with binary gas sorption", SPE 24363, Rocky Mountain Regional Meeting, Casper, Wyoming, May 18-21, (1992), pp.459-472.

206. Reeves, S., "Geologic sequestration of CO_2 in deep, unmineable coalbeds: An integrated research and commercial-scale field demonstration project", First National Carbon Sequestration Conference, U.S.DOE/NETL, (2001), pp.1-12.

207. Vorres, K. S., "User's Handbook for the Argonne Premium Coal Sample Program", Argonne National Lab. Pub. Illinois, (1993).

208. Vorres, K. S., "The Argonne Premium Coal Sample Program", Energy & Fuels, Vol.4 (1990), pp.420-426.

209. Schmidt, L. D., "Changes in coal during storage", In: Lowry, H.H., " Chemistry of coal utilization", (1945), pp.627-676.

210. Span, R. and Wagner, W., "A new equation of state for carbon dioxide covering the fluid region from the triple-point temperature to 1100 K at pressures up to 800 MPa", Journal of Physical and Chemical Reference Data, Vol.25 (1996), pp.1509-1596.

211. Zhou, L., Zhou, Y., Li, M., Chen, P., and Wang, Y., "Experimental and modeling study of the adsorption of supercritical methane on a high surface activated carbon", Langmuir, Vol.16 (2000), pp.5955-5959.

212. Bell, G. J. and Rakop, K. C., "Hysteresis of methane/coal sorption isotherms", SPE 15454, 61st Ann. tech. Conf. and Exhib., new Orleans, LA, Oct. 5-8, (1986).

213. Conforti, R. M. and Barbari, T. A., "A thermodynamic analysis of gas sorption-desorption hysteresis in glassy polymers", Macromolecules, Vol.26 (1993), pp.5209-5212.

214. Press, W. H., Flannery, B. P., Teukolsky, S. A., and Vetterling, W. T., "Numerical recipes", Cambridge Univ. Press, Cambridge, U.K., (1986).

215. Deevi, S. C. and Suuberg, E. M., "Physical changes accompanying drying of western US lignites", Fuel, Vol.66 (1987), pp.454-460.

216. Butterfield, I. M. and Thomas, K. M., "Some aspects of changes in the macromolecular structure of coals in relation to thermoplastic properties", Fuel, Vol.74 (1995), pp.1780-1785.

217. Abramov, F. A., Repka, V. V., and Andreev, S. Yu., "Experimental determination of moisture distribution in porous structure of extracted coal", Izv.Vyssh.Uchebn.Zaved., Gorn.Zh.(USSR), Vol.3 (1982), pp.58-60.

218. Suuberg, E. M., Otake, Y., Yun, Y., and Deevil, S. C., "Role of moisture in coal structure and the effects of drying upon the accessibility of coal structure", Energy & Fuels, Vol.7 (1993), pp.384-392.

219. Otake, Y. and Suuberg, E. M., "Solvent swelling rates of low rank coals and implications regarding their structure", Fuel, Vol.77 (1998), pp.901-904.

220. Neimark, A. and Ravikovitch, P. I., "Calibration of pore volume in adsorption experiments and theoretical models", Langmuir, Vol.13 (1997), pp.5148-5160.

221. Malbrunot, P., Vidal, D., and Vermesse, J., "Adsorbent helium density measurement and its effect on adsorption isotherms at high pressure", Langmuir, Vol.13 (1997), pp.539-544.

222. Sircar, S., "Measurement of Gibbsian surface excess", AIChE J., Vol.47 (2001), pp.1169-1176.

223. Menon, P. G., "Adsorption at high pressures", Chem.Rev., Vol.68 (1968), pp.277-294.

224. Moffat, D. H. and Weale, K. E., "Sorption by coal of methane at high pressures", Fuel, Vol.54 (1955), pp.449-462.

225. Fleming, G. K. and Koros, W. J., "Dilation of polymers by sorption of carbon dioxide at elevated pressures: 1. Silicone rubber and unconditioned polycarbonate", Macromolecules, Vol.19 (1986), pp.2285-2291.

226. Greenkorn, R. A., "Flow phenomena in porous media", Marcel Dekker, N.Y., (1983).

227. Toth, J., "Some consequences of the applications of incorrect gas/solid adsorption isotherm equations", J.Colloid.Interface Sci., Vol.185 (1997), pp.228-235.

228. Aoshima, M., Fukasawa, K., and Keneko, K., "Micropore filling of supercritical Xe in micropores of activated carbon fibers", J.Colloid.Interface Sci., Vol.222 (2000), pp.179-183.

229. Marsh, H., "The determination of surface areas of coals - some physicochemical considerations", Fuel, Vol.44 (1965), pp.253-268.

230. Harpalani, S., "Permeability changes resulting from gas desorption. Final report, May 1988-June 1989", Arizona Univ. Tucson, AZ, (1989).

231. Glass, A. S. and Larsen, J. W., "Coal surface properties. specific and nonspecific interactions for polar molecules and surface tensions for hydrocarbons at the surface of Illinois No. 6 coal", Energy & Fuels, Vol.8 (1994), pp.629-636.

232. Norinaga, K., Kumagai, H., Hayashi, J., and Chiba, T., "Classification of water sorbed in coal on the basis of congelation characteristics", Energy & Fuels, Vol.12 (1998), pp.574-579.

233. Painter, P. C., Graf, J., and Coleman, M. M., "Coal solubility and swelling. 3. A model for coal swelling", Energy & Fuels, Vol.4 (1990), pp.393-397.

234. Larsen, J. W., Lee, D., and Shawver, S. E., "Coal macromolecular structure and reactivity", Fuel Process.Technol., Vol.12 (1986), pp.51-62.

235. Mahajan, O. P., "Adsorption and pore structure and coal-water interactions", In: Klein, R., "Sample selection, aging, and reactivity of coal", Wiley, N.Y., (1989).

236. Larsen, J. W. and Jones, J., "Rates of reaction of Wyodak Rawhide coal hydroxyl groups with tetra-alkylammonium hydroxides and rates of the concomitant swelling", Energy & Fuels, Vol.15 (2001), pp.769-775.

237. Iwai, Y., Amiya, M., Murozono, T., and Arai, Y., "Drying of coals by using supercritical carbon dioxide", Ind.Eng.Chem.Res., Vol.37 (1998), pp.2893-2896.

238. Stumm, W. and Morgan, J. J., "Aquatic chemistry: chemical equilibria and their rates in natural waters", John Willey & Sons, N.Y., (1996).

239. Archer, J. S. and Wall, C. G., "Petroleum Engineering: Principles and Practice", Graham and Trotman, Meryland, (1986).

240. Archer, D., Kheshgi, H., and Maier-Reimer, E., "Multiple timescales for neutralization of fossil fuel CO2", Geophys.Res.Lett., Vol.24 (1997), pp.405-408.

241. Donohue, M. D. and Aranovich, G. L., "Classification of Gibbs adsorption isotherms", Advances in Colloid and Interface Science, Vol.76-77 (1998), pp.137-152.

242. Ozdemir, E., Morsi, B. I., and Schroeder, K., "CO_2 Adsorption Capacity of Argonne Premium Coals", Fuel, Vol.83 (2004), pp.1085-1094.

243. Wiebe, R. and Gaddy, V. L., "The solubility of carbon dioxide in water at various temperatures from 12 to 40^o and pressures to 500 atmospheres", J.Am.Chem.Soc., Vol.62 (1940), pp.815-817.

244. Prutton, C. F. and Savage, R. L., "The solubility of carbon dioxide in calcium chloride-water solutions at 75, 100, 120^o and high pressures", J.Am.Chem.Soc., Vol.67 (1945), pp.1550-1554.

245. White, C. M., "An initial set of working hypotheses concerning some chemical and physical events when CO_2 is injected into a coalbed", Amer.Chem.Soc.Div.Fuel Chem.Preprints, Vol.46 (2003), pp.114-116.

246. Giddings, J. C., Myers, M. N., and King, J. W., "Dense gas chromatography at pressures to 2000 atmospheres", J.Chromatogr.Sci., Vol.7 (1969), pp.276-283.

247. Kolesar, J. E., Ertekin, T., and Obut, S. T., "The unsteady-state nature of sorption and diffusion phenomena in the micropore structure of coal: Part I- Theory and mathematical formulation", SPE Formation Evaluation, (1990), pp.81-88.

248. Athena, "Athena Visual Workbench: Modeling, Optimization and Nonlinear Parameter Estimation for Scientists and Engineers", http://www.athenavisual.com/, (2002).

249. Craft, B. C., Hawkins, M. F., and Terry, R. E., "Applied petroleum reservoir engineering", Englewood Cliffs, New Jersey, (1991).

250. Munka, M. and Papay, J., "4D numerical modeling of petroleum reservoir recovery", Akademiai Kiado, Budapest, (2001).

251. Sung, W., "Development, testing and application of a multi-well numerical coal seam degasification simulator", Ph.D. Dissertation, PennState Univ., State College, PA, (1987).

252. Sung, W. M., Huh, D. G., Ryu, B. J., and Lee, H. S., "Development and application of gas hydrate reservoir simulator based on depressurizing mechanism", Korean J.Chem.Eng., Vol.17 (2000), pp.344-350.

253. Manik, J., "Compositional modeling of enhanced coalbed methane recovery", Ph.D. Dissertation, PennState Univ., State College, PA, (1999).

254. McKee, C. R. and Bumb, A. C., "Flow-testing coalbed methane production wells in the presence of water and gas", SPE Formation Evaluation, (1987), pp.599-608.

255. Peng, D. Y. and Robinson, D. B., "A new two-constant equation of state", Ind.Eng.Chem.Fundam., Vol.15 (1976), pp.59-64.

256. Angus, S., Armstrong, B., and de Reuck, K. M., "Carbon Dioxide", Pergamon Press, N.Y., (1976).

257. Box, G. E. P., Hunter, W. G., and Hunter, J. S., "Statistics for experimenters: An introduction to design, data analysis, and model building", John Wiley & Sons, N.Y., (1978).

258. Sawyer, W. K., Zuber, M. D., Kuuskraa, V. A., and Horner, D. M., "Using reservoir simulation and field data to define mechanisms controlling coalbed methane production", Proceedings of the 1987 coalbed methane symposium, (1988).

259. Gray, I., "Reservoir engineering in coal seams: Part 1-The physical process of gas storage and movement in coal seams", SPE 12514, (1987).

260. Durucan, S. and Edwards, J. S., "The effects of stress and fracturing on permeability of coal", Min.Sci.Technol., Vol.3 (1986), pp.205-216.

261. Young, G. B. C., "Coal reservoir characteristics from simulation of the Cedar Hill Field San Juan basin", Quarterly Review of Methane from Coal Seams Technology, Vol.10 (1992), pp.6-10.

262. Crichlow, H. B., "Modern reservoir engineering - A simulation approach", Englewood Cliffs, New Jersey, (1977).

263. McCain, W. D., "The properties of petroleum fluids", Pennwell Publishing Co., Tulsa, OK, 2nd Ed., (1988).

264. Dake, L. P., "Fundamentals of reservoir engineering", Elsevier, N.Y., (1978).